Influence des électrolytes et leurs additifs sur la stabilité d'une électrode Mg et sur les processus interfaciaux dans les batteries Mg-air

Yaqing Zhou

PSL UNIVERSITÉ PARIS

THÈSE DE DOCTORAT
DE L'UNIVERSITÉ PSL

Préparée à Chimie ParisTech

Influence of electrolytes and their additives on the stability of Mg electrode and the interfacial processes in Mg-air batteries

Soutenue par
Yaqing ZHOU
Le 8 septembre 2022

Ecole doctorale n° 388
Chimie physique et chimie analytique de Paris centre

Spécialité
Chimie Physique

Composition du jury :

Mme Nadine Pébère Directrice de recherche, Université de Toulouse	*Présidente*
M. Eric de Vito Directeur de recherche, CEA (LITEN)	*Rapporteur*
Mme Cristina Iojoiu Directrice de recherche, Université Grenoble Alpes	*Rapporteur*
M. Philippe Marcus Directeur de recherche émérite, Chimie ParisTech	*Co-encadrant*
Mme Jolanta Świątowska Directrice de recherche, Chimie ParisTech	*Directrice de thèse*

Chimie Paris ParisTech | PSL

Abstract

The world has witnessed the increasing demand for non-fossil fuel power sources with large capacity, high power, low cost and reliable safety. Among different new energy storage systems, metal-air batteries have a greater power storage capacity, a few times more than the best performing lithium-ion batteries. Metal-air batteries such as Li-air, Zn-air, Mg-air and Al-air batteries are promising to be applied to the next generation of electric vehicles (EVs).

Among various types of metal-air batteries, Mg-air batteries have attracted significant attention due to their high theoretical specific capacity (2200 Ah/kg), specific energy density (6.8 kWh/kg), volumetric capacity of Mg (3833 mAh/cm^3), and theoretical voltage (3.09 V). Furthermore, by application the Mg-air batteries, the weight of battery can be significantly reduced (due to the low density of Mg anode 1.74 g/cm^3). Moreover, Mg is also environmentally friendly, non-toxic and an abundant element.

However, in aqueous electrolytes, Mg undergoes self-corrosion and a large amount of H_2 is generated. Low coulombic efficiency and low operating voltages are the major drawbacks of Mg-air batteries. Moreover, the negative difference effect (NDE), during which, the cathodic and anodic currents increase with the imposed potential, accelerates the corrosion of Mg anode during Mg-air batteries discharge and leads to a hydrogen evolution. To overcome these problems, this thesis mainly focusses on the electrolyte modifications in order to improve the discharge performance of Mg-air batteries. Besides, the surface analyses, by means of X-ray photoelectron spectroscopy (XPS) and time-of-flight secondary ion mass spectrometry (ToF-SIMS), combined with the morphological characterizations using microscopic techniques, such as scanning electron microscopy (SEM), optical microscopy (OM) and three-dimensional laser scanning microscope (3D-LSM) were used to better understand the reactivity of Mg anode and the surface modifications induced by corrosion or discharge tests in different electrolytes and their additives. Various electrochemical techniques and galvanostatic discharge tests were employed to elucidate the corrosion mechanisms of pure Mg (99.9 wt. %) and the discharge performances of full Mg-air battery.

The first part of the work aimed at applying an organic/inorganic hybrid electrolyte in Mg-air battery to reduce the corrosion of pure Mg anode and improve the battery performance. Herein, the effect of different ethanol to water fractions mixed with 0.6 M NaCl on magnesium

corrosion behavior and battery discharge performances are demonstrated. The significant corrosion inhibition in a high content of ethanol (≥ 20 vol. %) was attributed to formation of more corrosion protective surface layer enriched in magnesium oxide as demonstrated by SEM, XPS and ToF-SIMS. However, this layer was revealed to be not optimized for application in Mg-air batteries due to a decrease of discharge potential. Within several lower ethanol contents, 0.5 vol % was demonstrated to be the most performant for Mg-air batteries which shown a limited corrosion rate, improved discharge performance and battery lifetime.

In a second part, we employed sodium 5-sulfosalicylate (5-S-Sal) corrosion inhibitor into aqueous NaCl electrolyte to improve the discharge performance of Mg-air battery and decrease the side reactions of Mg anode. XPS and ToF-SIMS analyses show that the presence of 5-S-Sal inhibitor leads to a lower quantity of $Mg(OH)_2$ in a corrosion resistant layer than in pure NaCl electrolyte. The surface enrichment in S-like species originating from inhibitor molecule could have an important effect on Mg corrosion decrease and H_2 evolution downturn. The discharge voltage of full Mg-air battery improves of over 200 mV, and the discharge lifetime is extended sevenfold.

In the last part, the conventional NaCl solute was replaced by $NaNO_3$, then a trace of acetic acid as an inhibitor was added into the aqueous electrolyte. The resulting Mg-air batteries based on an optimized electrolyte shows an improved discharge voltage. The lifetime of full Mg-air batteries is drastically prolonged to more than 360 hours in modified electrolyte compared to only ~17 hours in NaCl electrolyte. TEM demonstrates that the typical flake-like $Mg(OH)_2$ morphology changes to the lamellar-like as a function of acetic acid addition. The surface chemical analyses by XPS and ToF-SIMS show that with the addition of acetic acid, the nitrate/nitrites can be formed and adsorb together with carboxylic acid leading to formation of more robust and corrosion resistant layer, but sufficiently permeable for ion diffusion. This layer allows for improved electrochemical performance of Mg anode in Mg-air battery.

Table of contents

Chapter I State-of-the-art and objectives of the thesis

I-1 Research background

Since 1970, the traditional energy sources such as coal, oil, and natural gas are increasingly close to exhaustion and our societies are facing different major challenges: the worldwide energy crisis and a wide range of environmental problems [1-3]. Nowadays, the worldwide consciousness of green energy that produced less CO_2 emission and sustainable concept greatly promote the developing of renewable clean energy sources [4, 5].

The most of renewable energy sources such as solar energy, tidal or wind energy need to be converted to the electric energy, which causes the lower utilization. Besides, the renewable energy sources are also intermittent and depend on the weather conditions [1, 6]. For these reasons, the electrochemical power sources such as batteries and fuel cells are necessary for energy conversion and efficient energy storage [7]. The electrochemical energy storage system can be characterized by numbers of desirable features, like a long life cycle, pollution free operation, low maintenance and high round trip efficiency [6]. Thus, over the years, various electrical energy storages have been investigated, such as different types of batteries (lead (Pb)-acid, nickel-chromium (Ni-Cr), nickel-metal hydride (Ni-MH), zinc/halogen, redox/hybrid flow, lithium-ion, sodium sulfur (NAS), etc. [8]). However, due to different drawbacks of these kinds of batteries (Table I-1) such as, the high cost per kWh and low energy density or safety issues, their further application have been restricted, thus the next generation of new storage technologies are required to be developed [9, 10]. Although lithium-ion batteries have been one kind of widely commercially available energy storage technologies, the energy density of 150-250 Wh/kg is limited to provide the extended use for large stationary applications [11]. Therefore, the safe and high-energy-density energy storage systems are extremely desired.

Among different new energy storage systems, metal-air batteries are interesting alternatives due to their high-power storage capacities, few times higher than the best performing lithium-ion batteries and their large theoretical energy density (Fig. I-1 b). Especially in recent years, metal-oxygen/air batteries are frequently recommended to replace current battery technologies for using in electric vehicles or grid energy storage systems [12-14]. The metal-oxygen/air batteries are composed of a metal anode and an air-breathing cathode in aqueous or non-aqueous

electrolyte [15]. Normally, they can be classified to aqueous and non-aqueous metal batteries which depend on the nature of the anode employed (schema is shown in Fig. I-1 a).

Table I-1. Electrochemical energy-storage technologies for stationary applications [16].

technology	typical power (MW)	discharge time	storage capacity cost ($/kWh)	life time (cycle/years)	efficiency (%)	drawbacks
supercapacitors	0.25	<1 min	500–3000	500000/20	>90	explosion hazard, low energy density, cost
regenerative fuel cells with hydrogen storage	10[a]	>5 h		13	40–50	low-density storage, high cost, safety
lead-acid batteries	0.5–20	3–5 h	65–120	1000–1200/3–4	70–80	low energy density, short lifetime, temperature sensitive
Li-ion batteries		1–5 h	400–600	750–3000/6–8	80–90	cost, safety, short lifetime, self-discharge, temperature sensitive
NAS battery	0.25–1	6–8 h	360–500	2500–4500/6–12	87	cost, high-temperature operation, safety
flow battery (VRB)	0.5–12	10 h	150–2500	500–2000/10	70	low energy density

[a]Projected.

The non-aqueous air batteries consist of alkali metal as anode , and it can be lithium (Li-air), sodium (Na-air), or potassium (K-air) [17-19]. The working mechanism is illustrated in Fig. I-1 a, the anodic reaction of metal (Me) dissolution (I-1) and the cathodic reactions leading to formation of oxide, superoxide and peroxide (I-2) [20, 21]. However, the solubility of superoxide and peroxide are limited in the electrolyte and then they can be deposited on the air cathode surface which gradually block the cathode and leads to the battery failure.

$$Me \leftrightarrow Me^{n+} + ne^- \quad \text{(I-1)}$$

$$n Me^+ + n O_2 + ne^- \leftrightarrow n Me_n O_2 \ (n \text{ is 1 or 2}) \quad \text{(I-2)}$$

The aqueous metal-air batteries are mainly composed of multi-valent earth metal such as Mg (Mg-air), or first-row transition metals such as Fe (Fe-air) and Zn (Zn-air), or Al (Al-air) batteries [12]. The reaction mechanism is based on the oxidation of the metal at the anode while the O_2 passes through the air cathode, then reduces to OH^- by reacting with H_2O as show in Fig. I-1 a and the equations (I-3) and (I-4) [12].

$$Me \leftrightarrow Me^{n+} + ne^- \quad \text{(I-3)}$$

$$2H_2O + O_2 + 4e^- \leftrightarrow 4OH^- \quad \text{(I-4)}$$

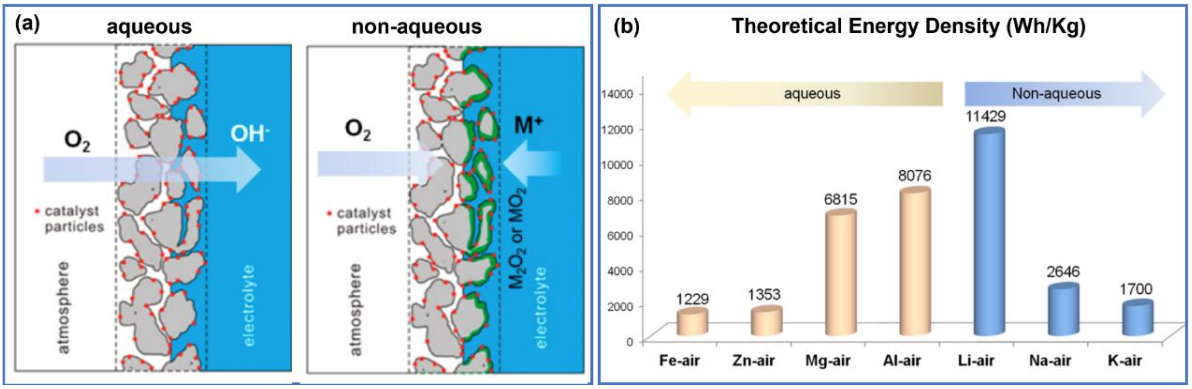

Fig. I-1 (a) Schema of aqueous and non-aqueous metal-air batteries; (b) theoretical energy densities for different types of metal-air batteries [12].

Comparing to the non-aqueous metal-air batteries (monovalent alkali metals, Li- [22], Na- [23], or K-air batteries [24]), the aqueous metal-air batteries (multivalent metals, such as Zn-, Mg- or Al-air batteries) [25, 26] are very interesting for the electrochemical energy storage devices due to their high volumetric energy density (with an exception for Li-air). Multivalent-ion batteries can, in principle, provide a higher energy density than monovalent. Besides, Zn-air, Mg-air and Al-air batteries are promising candidates for the application in the next generation electric vehicles (EVs). An intensive research and development have been performed on Zn-air batteries [27, 28], but the theoretical energy density of Zn-air batteries (as shown in Fig. I-1, 1353 Wh/kg) is far less than Mg-air batteries (6815 Wh/kg). Fig. I-2 presents different metals as candidates for anodes [29-32]. Mg owns well-balanced properties like highly negative redox potential, higher volumetric capacity, great chemical stability and low cost.

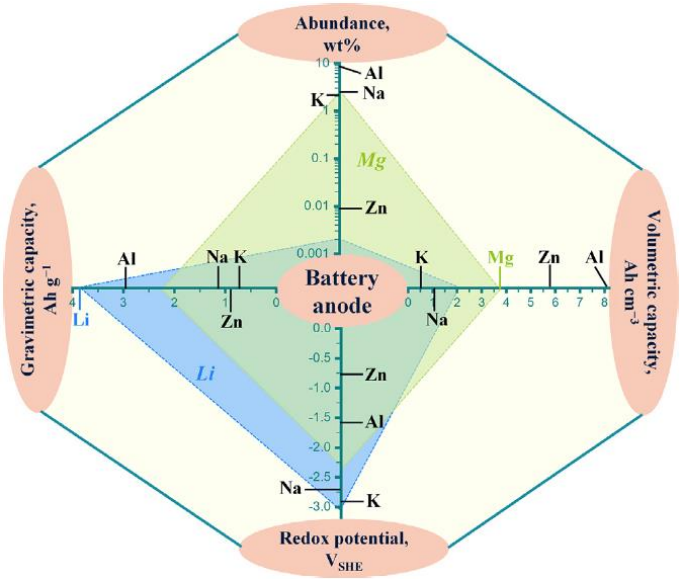

Fig. I-2 Key features of traditional and emerging metallic anodes for energy strong. Abundance represents the occurrence as weight fraction of each element in Earth's crust [29].

I-2 Introduction to Mg-air batteries

I-2.1 Secondary and primary Mg-air batteries

In principle, all the batteries can be classified into primary and secondary batteries. Correspondingly, Mg metal can also act as anode for both primary Mg-air batteries and rechargeable (secondary) Mg-O_2 (air) batteries. The rechargeable Mg-air batteries normally work only with non-aqueous electrolytes according to the previous studies [33-37]. However, the research activities are limited due to several fundamental scientific difficulties listed hereafter [38]. Firstly, the initial discharge process produces MgO or MgO_2 forming an insulating film with very poor thermodynamic and kinetics properties, hardly converting back into the metallic Mg. Secondly, the improvement of energy conversion efficiency and high-rate stability of rechargeable Mg-air batteries need the efficient electrocatalysts for $4e^-$ oxygen reduction reaction and the high ionic conductivity of the organic electrolyte. The groups of Shiga and Siegel [34, 35] devoted their research to thoroughly understand the free energy evolutions of the secondary Mg-air batteries by first principle calculation and investigation of some new polymers such as 2,2,6,6-tetramethylpiperidine-oxyl (TEMPO)-anion complex to catalyze the decomposition of MgO [33, 35, 36]. Even though, the results showed very low round-trip efficiencies of MgO intermediate and very large overvoltage drops. Besides, these

non-aqueous electrolytes are corrosive and sensitive to the air humidity and can cause several safety issues.

After slowing down the efforts on research and development of secondary Mg-air batteries, the primary Mg-air batteries have been attracted interests. The number of citations and publications shows a great increase in recent years (Fig. I-3 a), but still significantly lower than other metal-air batteries (Fig. I-3 b).

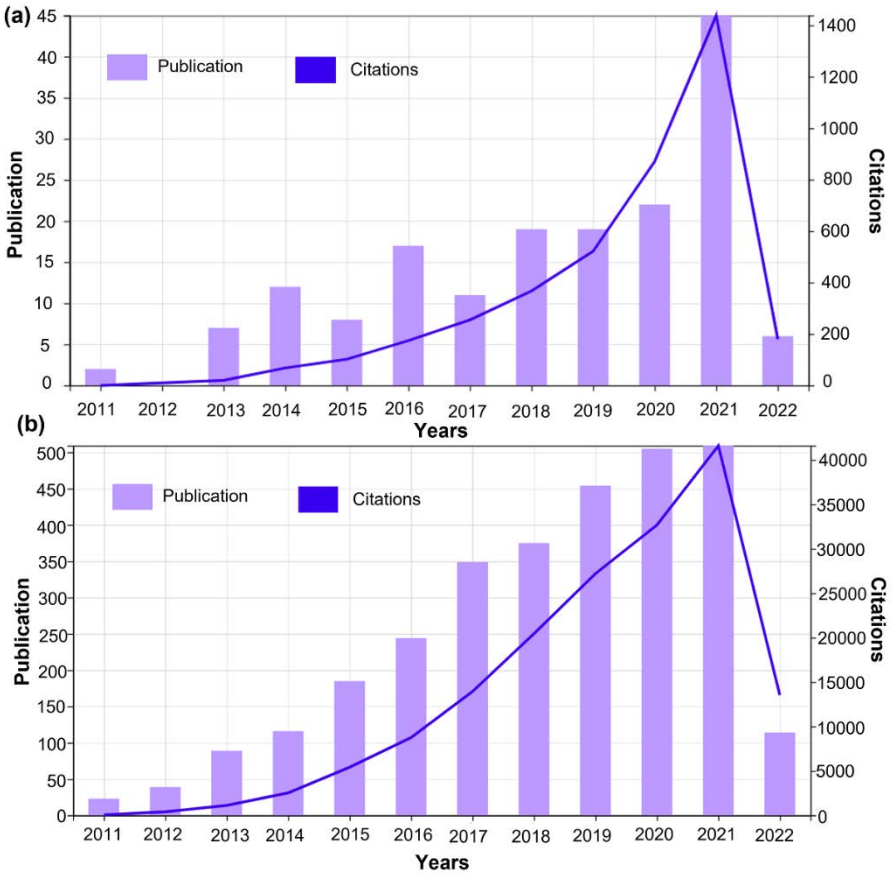

Fig. I-3 Number of citations and publications over time regarding (a) “Mg-air batteries”; (b) “Metal-air batteries” as derived from ISI Web of Knowledge in 2011-06/2022.

The present Mg-air batteries, which can be commercialized are the primary Mg-air batteries. Compared to the secondary Mg-air batteries, the primary batteries are much safer due to application of the aqueous-based electrolytes such as the seawater. They can have an open cell construction and consume oxygen from air. Mg metal as anode can be replaced by new Mg plate when the Mg metal is exhausted, thus the Mg-air batteries can be “refuelable” [4].

Compared to the other metal-air batteries, as illustrates Table I-2, Mg-air batteries have a high theoretical specific (faradic) capacity (2200 Ah/kg), specific energy density (6.8 kWh/kg, volumetric capacity of Mg anode (3833 mAh/cm^3) and also a high theoretical voltage (3.09 V) [39-41]. Furthermore, the weight of battery systems can be significantly reduced due to the low density of Mg anode 1.74 g/cm^3. Mg is also environmentally friendly [42], non-toxic and it is the eight most abundant element which constitutes about 2% of the Earth's crust.

Table I-2. Important parameters for different types of metal-air batteries [15, 43-46].

Batteries	Invented year	Theoretical working voltage (V)	Theoretical specific capacity (Ah / kg)	Theoretical energy density (Wh / kg)
Mg-air	1966	3.09	920	2843
Zn-air	1878	1.65	658	1085
Li-air	1996	2.96	1170	3463
Al-air	1962	2.71	1030	2791
Na-air	2012	2.33	687	1600
K-air	2013	2.48	377	935

The primary Mg-air batteries have already been used in many practical applications. In 2013, Korea Institute of Science and Technology (KIST) demonstrated an electric car equipped with full Mg-air batteries [47] with a range 800 km (the five times higher energy density battery compared to a similar size lithium-ion battery). Furthermore, the commercial application of magnesium-air fuel cells (MAFC) in different areas has been recently demonstrated (Fig. I-4). The Magpower systems Inc. of Canada [48] has developed one kind of commercialized MAFC product (Fig. I-4 a), which can be applied to lifeboats, homes, schools and hospitals. Fig. I-4 b shows the Mg-air battery type of AM-180, which was designed by Dalian Institute of Chemical Physics, Chinese Academy of Science. It can be used for LED light and mobile phones charging via an 5 V USB with energy of 180 Wh. The weight of the battery is only 428 g without electrolyte and can be stored for 10 years with working life of about 1200 h at the temperature of -20 ℃ to 55 ℃ [49, 50]. The Furukawa Battery Co., Ltd. of Japan [51] has developed a small and portable emergency MAFC (Fig. I-4 c) called MgBOX, which can be stored for long

periods, easily transported due to the light weight (only 1.6 kg). It can be activated by simply adding fresh or salt water, and it could provide a source of electricity for five days via an USB port. The IONS LAB of Korea has developed a seawater battery GOODiON [52], which can supply 5 and 10 W of power complete with 5 V/ 2A USB port (Fig. I-4 d) which can be also used for smartphone charging.

Fig. I-4 The examples of the commercial applications of Mg-air batteries: (a) MAFC by MagPower Systems Inc., Canada [48, 53]; (b) AM-180 developed by DICP, CAS, China [49]; (c) MgBox by Furukawa Battery Co., Ltd, Japan [51]; [d] Seawater Battery GOODiON by IONS LAB, Korea [52].

I-2.3 Working mechanisms of Mg-air batteries

The schematic diagram of Mg-air batteries is shown in Fig. I-5 (where Mg-air batteries is to primary Mg-air batteries). The metallic anode can be the pure Mg (commercial Mg or Nano/mesoscale) or Mg alloys (Mg/Al/Zn, AZ31, AZ61, AZ91; Mg/Al/Mn, AM50, AM60; MA8M06 and Mg/Li). The electrolytes can be the aqueous solutions of NaCl, $KHCO_3$, NH_4NO_3, $NaNO_3$, HNO_3, $NaNO_2$, $Mg(NO_3)_2 \cdot 6H_2O$ + $NaNO_2$, Na_2SO_4, $MgCl_2$, $MgBr_2$, phosphonium chloride, ionic liquids and so on [54]. The air cathode is composed of oxygen from the air combined with the waterproof breathable layer, gas diffusion layer and the catalyst layer

deposited on the current collector.

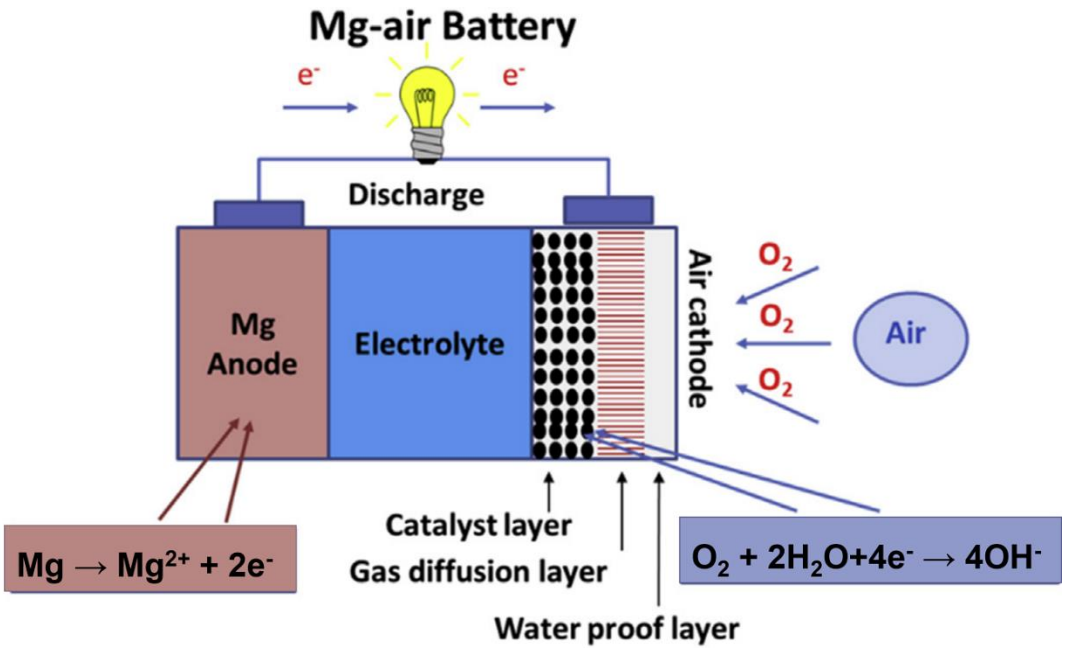

Fig. I-5 The structure and working principle of Mg-air battery [54].

The overall reaction of Mg-air batteries is as the following equation:

$$2\ Mg + O_2 + 2\ H_2O \rightarrow 2\ Mg\ (OH)_2 \qquad E° = -3.09\ V\ vs.\ SHE \qquad (I\text{-}5)$$

The anode Mg is oxidized to Mg^{2+}, producing two electrons (Fig. I-5), O_2 passes through the air cathode and adsorbs on the catalyst surface, then react with H_2O to produce OH^- and the electrons [55]. The efficient electrocatalysts for $4e^-$ oxygen reduction is desirable due to its high energy efficiency [38] as shown by the following anodic and cathodic equations, respectively [56]:

$$2\ Mg \rightarrow 2\ Mg^{2+} + 4e^- \qquad E° = -2.69V\ vs.\ SHE \qquad (I\text{-}6)$$

$$O_2 + 2\ H_2O + 4e^- \rightarrow 4\ (OH)^- \qquad E° = 0.4V\ vs.\ SHE \qquad (I\text{-}7)$$

The $2e^-$ pathway is unfavorable since the produced peroxide species are corrosive and can cause premature degradation of the electrochemical cell. As shown the equations I-(8-10) [54], the

two-electron reaction of oxygen firstly generates OH^- and HO_2^- and then reduction to OH^- occurs on the cathode side:

$$O_2 + H_2O + 2\,e^- \rightarrow OH^- + HO_2^- \quad \text{(I-8)}$$

$$H_2O + HO_2^- + 2e^- \rightarrow 3\,OH^- \quad \text{(I-9)}$$

$$2\,HO_2^- \rightarrow 2\,OH^- + O_2 \quad \text{(I-10)}$$

I-2.4 Challenges of primary Mg-air batteries

Although numerous advantages of Mg-air batteries have been listed, there are still some challenges for their widespread application. Low coulombic efficiency and low operating voltages (comparing to the theoretical values) are the major drawbacks of Mg-air batteries.

Mg anode can suffer the severe self-corrosion from the micro-galvanic corrosion (due to the presence of some metallic impurities in Mg) and the chunk effect (which is caused by the detachment of metallic particles) [57]. Moreover, the negative difference effect (NDE) [58-63], during which, the cathodic and anodic currents increase with the imposed potential, accelerates corrosion during Mg-air batteries discharge and leads to a hydrogen evolution. Due to the Mg corrosion, the discharge products such as MgO, $Mg(OH)_2$ and $MgCO_3$ can accumulate on the Mg surface [64-66] and form a passivating layer leading to impediment of the Mg reactivity and the reduction of the reaction area. Thus, the sluggish anodic reaction kinetic of Mg anode can cause the unstable low discharge voltage and the poor intermittent discharge behavior [67, 68]. Another issue of Mg-air batteries is the slow sluggish kinetics of oxygen reduction reaction (ORR) in the air cathode, which is related to the catalyst [44]. The catalytic activity can directly influence the depth and rate of discharge process [69]. As a result, the working voltage and actual discharge performances of Mg-air batteries are greatly lower than their theoretical values. The coulombic efficiency and utilization efficiency of Mg anode are significantly lower and the practical specific energy of full Mg-air batteries is reduced [55].

To overcome these problems, a better understanding of working mechanisms of different Mg-air battery components (Mg anode, air-cathode and the electrolyte) and increase their performances are of great interests.

I-3 Understanding the corrosion mechanism and the self-discharge of Mg anode

I-3.1 Corrosion mechanism of Mg anode

The high chemical and electrochemical activity of Mg anode and the poor protection surface film in aqueous electrolytes lead to the severe corrosion of Mg, which results in the side reactions in Mg-air batteries and greatly hinders their development [70-72]. Thus, it is important to understand the corrosion mechanisms of Mg in aqueous-based electrolytes and the formation of the corrosion products on the Mg surface.

One important phenomenon related to the Mg corrosion is the negative difference effect (NDE) firstly proposed in 1866 [73]. During the anodic polarization and corrosion of Mg, the hydrogen evolution can occur, and they increase as the applied anodic potential increases. The corrosion behavior of Mg anode is complex and there are still several mechanisms debated [70, 74-81].

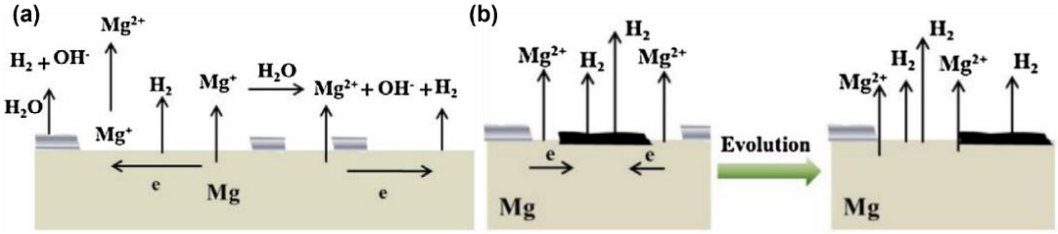

Fig. I-6 Schematic illustration of (a) incomplete film univalent Mg^{+} ion mechanism; (b) enhanced cathodic catalytic model [82].

A widely accepted mechanism is the "incomplete film univalent Mg^{+} ion mechanism" [72] (shown in Fig. I-6 a), which is based on the partially protective film mechanism [74]. Firstly, the film-free areas of Mg surface with Mg electrochemically oxidizes to the univalent Mg^{+}, then some of the Mg^{+} ions further oxidize to Mg^{2+}, and finally, the remaining Mg^{+} ions react with water and finally convert into Mg^{2+} releasing H_2 [58, 83, 84]. Another mechanism of Mg corrosion mostly admitted by researchers [77, 83, 85], is the enhanced catalytic activity model (Fig. I-6 b) based on the assumptions proposed by Frankel *et al.* [77].

I-3.2 Surface film on Mg exposed into aqueous electrolytes

The surface film play an important role on Mg corrosion in aqueous electrolytes [86, 87]. In fact, the Mg is very thermodynamically active and can even corrode in the pure water. According to the E-pH Pourbaix diagram in Fig. I-8 a [84], Mg can be oxidized at the wide ranges of pH (neutral and acidic) and potentials. The $Mg(OH)_2$ is stable only at the pH > 11. Even though, the intermediate active magnesium ion can further react with water and produce H_2, which involves the micro-galvanic coupling between cathodic and anodic areas [88]. As shown in Fig. I-7, the small metallic impurities present in the Mg metal can form the second phases. The Mg matrix behaves as an anode because it has a corrosion potential lower than the second phases, which can involve the micro-galvanic corrosion and increase the H_2 evolution.

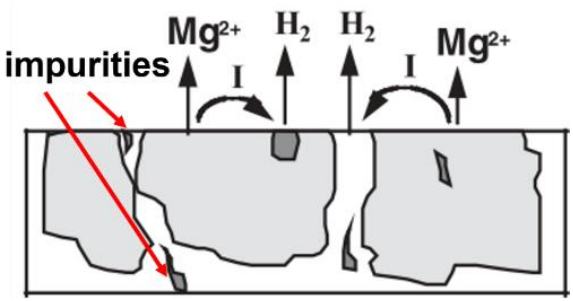

Fig. I-7 Schematic representation of micro-galvanic corrosion of Mg containing the metallic impurities [88].

Besides, a filiform or pitting corrosion in NaCl electrolyte can occur. Then, the corrosion will lead to different surface modifications which depend on the used electrolyte. As shown in Fig. I-8 b and c, the shallow pits can be formed on the Mg surface and deep growth defects can be observed in the areas of hydrogen bubble presence, which is related to the hydrogen evolution reaction (HER). The HER is also significantly accelerated by the Mg anode polarization.

At first, a film is formed on Mg surface during the sample preparation, which will be destroyed by the immersion of Mg into electrolyte and a new steady state surface film will be formed. The surface film is consisting of an inner MgO layer and outer layer of $Mg(OH)_2$ [78, 89, 90]. The outer layer of $Mg(OH)_2$ is very porous and loose in a corrosive electrolyte such as NaCl, while the inner MgO is denser and more corrosion resistant to the metal substrate. The polarization current can easily pass through the electrolyte in the pores of the outer surface film. The outer

layer can grow through the migration and combination of the Mg^{2+} and OH^- in the outer surface film and the deposition of the supersaturated Mg^{2+} and OH^- from the solution. However, the breakdown of the surface film can be induced by the severe HER, and lead to the formation of cracks, pores or gaps [91]. Dark areas are usually formed as observed by Song's group [74, 92], and they are related to the Mg dissolution and HER [58, 92]. The hydrogen bubbles can be seen in the dark areas, which increase with time and HER. The initially isolated dark areas merge and the fraction of dark areas increase.

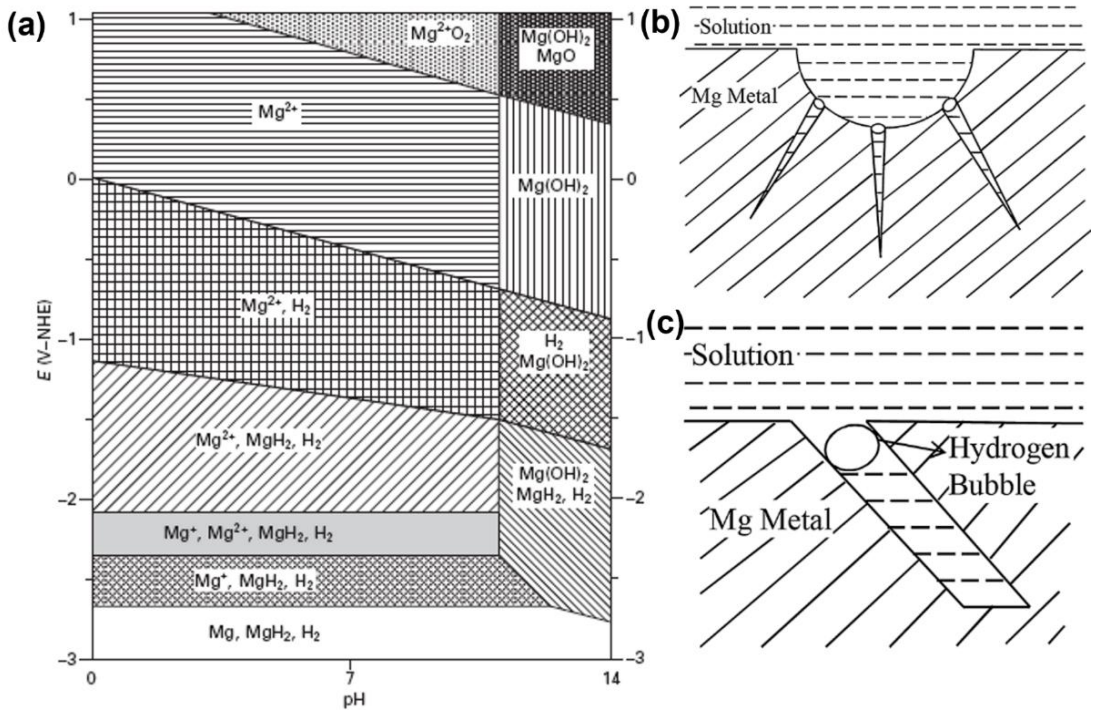

Fig. I-8 (a) E-pH diagram of Mg anode in aqueous environments [84]; (b) and (c) schematic of the filiform corrosion for pure Mg in 3.5% NaCl aqueous electrolyte [72].

I-4 Improvement of Mg-air battery performances

There are different ways of improving the discharge performances of Mg-air batteries:

1) The modification of Mg-based anode material by alloying of Mg with the other elements (Al, Li, Mn, or Zn) and decreasing the self-corrosion of anode is one of most popular ways.
2) The modification of air cathode based on enhancing its catalytic activity and increasing

the oxide reduction reaction (ORR) activity.

3) The modification of electrolyte by decreasing its high reactivity (*e.g.* the self-corrosion) with Mg-based anode and better control the electrode/electrolyte interface.

The details will be introduced in the following section.

I-4.1 Mg anode modifications

With regard to the Mg anode of Mg-air batteries, Tong *et al.* [93] schematized the main issues and the activities of Mg-anode as shown in Fig. I-9. The principal side reaction, which is the self-corrosion of Mg anode, can lead to the Mg anode dissolution and energy loss, which leads to the low anodic efficiency and low discharge voltage in the Mg-air batteries. The self-corrosion is highly dependent on the presence of defects, intermetallic particles and metallic impurities, such as Fe, Ni or Cu [94-97]. The metallic impurities with a nobler standard potential than Mg are likely to activate the cathodic reaction. The reactivity of Mg can be strongly influenced by the amount of metallic impurities in Mg [98-100]. The areas with the metallic impurities or intermetallic particles are hard to transfer Mg^{2+}, which leads to lower discharge performance of Mg-air batteries.

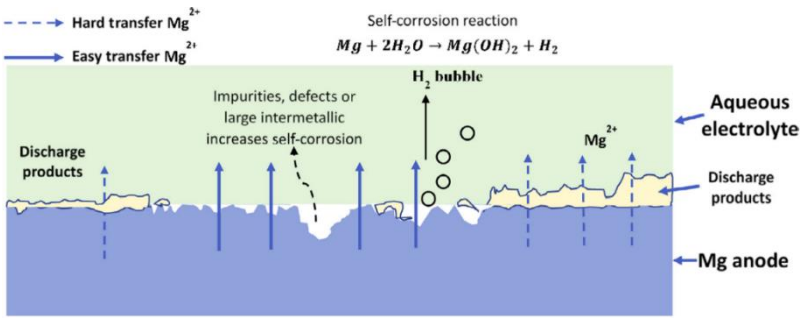

Fig. I-9 The main activities of Mg anode in Mg-air batteries [93].

The chunk effect is caused by the detachment of particles and leads to the inhomogeneous dissolution of Mg anode. Furthermore, the discharge/corrosion products covering the Mg surface, lead to the anode polarization. These side reactions greatly decrease the anodic utilization efficiency and consequently reduce the discharge capacity of Mg-air batteries. Thus, the chunk effect should be minimized, and more homogenous dissolution should be favorized to improve the battery performance (discharge behavior).

High-purity Mg (>99.99%) as anode for Mg-air batteries shows a good discharge performance, but the application is limited due to its high-cost. Lower purity Mg usually contains several metallic impurities such as Fe, Ni, etc. [70, 96], which can result in high corrosion rate of Mg anode. Therefore, alloying of Mg with the suitable metal elements is a very common method to improve the performance of full cells. The commercial Mg alloys (AZ31, AZ61, AZ91 and AP65) have been used as anode materials in Mg-air batteries since 1960 s [101-103].

Recently, the research studies on the suitable alloys for application in Mg-air batteries have been intensified. Al alloyed with Mg forms the secondary phase (i.e., $Mg_{17}Al_{12}$ [88, 104]) that can reduce anodic reaction kinetics and increase the corrosion resistance. Ma *et al.* [102] studied the high concentration of Al (~9 wt. %) added into AZ91 and showed that the discharge activation of Mg-air batteries can be greatly increased. Moreover, the formation of $Mg_{17}Al_{12}$ can prevent discharge product peeling out [105]. Besides, the addition of 3 wt. % [94] or 6 wt. % [106] of Al to pure Mg also showed a higher discharge capacity and anodic efficiency of Mg-based anode. Zn is another very common element used in Mg alloys. A dissolution of discharge products (such as $Mg(OH)_2$) can be accelerated due to the pH decrease by the hydrolyzation of dissolved Zn^{2+} in seawater-based electrolyte [107]. The Mg-Al-Zn series alloys showed a good mechanical properties and much higher corrosion resistance, however the anodic efficiency and discharge capacity in Mg-air batteries can be hindered. Some other alloying elements added into AZ series alloys have been investigated. Liu *et al.* [108] reported adding Ca, Sm and La into the AZ91 alloys. The full Mg-air batteries can lead, in this case, to a stable discharge voltage, high discharge capacity of 1381 Ah/kg and anodic efficiency of 61.9 %. The AP series alloys, which are Mg-Al alloys with Pb (Mg-Al Pb alloy), have a very negative OCP and can provide a high discharge voltages for Mg-air batteries [8]. Based on the activation mechanism of Mg-Al-Pb alloy reported by Wang *et al.* [105], the precipitated lead oxides on the surface of the alloy can facilitate the precipitation of $Al(OH)_3$, which also benefit to the peel-off the $Mg(OH)_2$ film and activate the magnesium substrate leading to the better discharge performances of Mg-air batteries [105, 109]. Wang *et al.* [110] reported an improvement of utilization efficiency (0.1 wt. % at 180 mA/cm^2) and reduced self-discharge in Mg-air batteries by adding 0.1 wt. % of In to AP65 alloy anode. Feng *et al.* investigated the discharge performance of the Mg-Al-Pb-Ce-Y anode in Mg-air batteries (3.5 wt. % NaCl as electrolyte) and showed that the anodic efficiency reached to 60.5% at a current density of 10 mA/cm^2. The other Mg-Al-based alloys such as Mg-Al-Mn (AM) [109, 111, 112], Mg-Al-Sn (AT) [111, 113], Mg-Al-rare-earth element

(In, Ga, Ce) [106, 114, 115] also has been recently investigated.

Mg-Li alloys are also commonly studied for the application in Mg-air batteries due to their lightest structure, extremely negative OCP and good faradic capacities. The content of Li in Mg alloys is very important. For low Li content (< 11 wt. %), Mg-Li alloys show poor corrosion behavior due to the increased cathodic kinetics between α- Mg and β- Li [116]. However, for high Li content (~11 wt. %), the alloy structure can convert from HCP to BCC, which results in reduction of the anodic dissolution kinetics [117, 118]. Yang *et al.* [119] compared the discharge performance of Mg-air batteries by employing the LAZ131 (Mg Bal wt% -3 wt. % Li-3 wt. %Al-1 wt. % Zn) and LAZ531 (Mg Bal wt. % -5 wt. % Li-3 wt. %Al-1 wt. % Zn) alloys as anode, the results showed that the LAZ531 alloy possesses high and steady discharge voltage (1.48 V at 2.3 mA/cm^2 and 1.37 V at 10 mA/cm^2). Moreover, the addition of elements, like Ce and Y into the LAZ, can enhance the anodic efficiency [120] and form an easy peel-off layer [121, 122]. Wang *et al.* [68] reported that the application of Mg-Li-Al-Ce-Y-Zn alloy as the anode in Mg-air battery, can lead to the improvement of anodic efficiency, which reaches to 60.6% and which is significantly higher than those obtained for AP65 Mg alloy.

The other Mg alloys such as Mg-Ca [67, 122], Mg-Bi [123, 124], Mg-Sn [111, 125] and Mg-RE alloys (*e.g.*, Mg- Zn-Gd-Nd-Zr) [126, 127] were also investigated for potential applications as anode materials for Mg-air batteries. Deng *et al.* [29, 128] (Fig. I-10 a) presents the maximum energy densities of Mg-air batteries based on diverse alloy anodes. The Ca-based alloys show the superior energy densities. Fig. I-10 b summarizes the anodic efficiency as a function of OCP for Mg-air batteries and it can be concluded that the Mg-Li-Al alloys demonstrate the highest anodic efficiency.

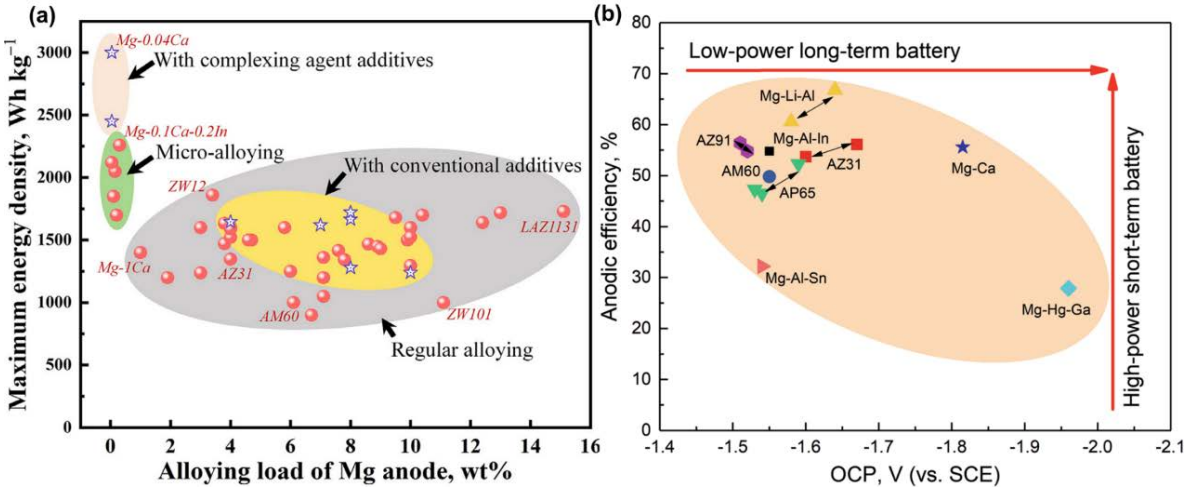

Fig. I-10 Mg-air batteries with selected alloy anodes tested at current density of 10 mA/cm^2 in 3.5 wt. % NaCl electrolyte (a) maximum energy density vs. adopting diverse alloy anodes [29]; (b) anodic efficiency as a function of OCP for different Mg alloy anodes [128].

Regarding Mg-based anode modification, microstructure tuning like heat treatment and wrought process (rolling and extrusion) can be also employed to improve the performance of Mg-air batteries. Wang *et al.* [129] studied the wrought Mg-Al-Pb-RE alloys showing the enhanced discharge voltage and anodic efficiency up to 64.1 % at current density of 10 mA/cm^2. Gu *et al.* [130] reported that Mg-0.5 Sn-0.5 Mn-0.5Ca (wt. %) alloys by casting and extrusion can exhibit a better discharge activity and higher specific energy.

Although the Mg alloys or the post-treatments of Mg-based anode materials can enhance the performances of Mg-air batteries, it can lead to more expensive or not eco-compatible or safe materials processing (for example due to the application of toxic elements such as Pb or Li, respectively), thus, hinder their industrial application and development of Mg-air batteries. For these reasons, it is necessary to think about the modifications and/or optimizations of other battery components such as the electrolyte.

I-4.2 Choice of electrolyte

Electrolyte is one part of the Mg-air batteries, which plays a critical role in the reaction efficiency and the ionic transport. It can determine the utilization efficiency of Mg anode and composition of discharge products. A suitable electrolyte can effectively reduce the self-corrosion rate of Mg and improve the discharge performance of the full Mg-air battery. An ideal electrolyte should have a high ionic and electronic conductivity which can reduce the influence of ohmic drop (IR-drop). Besides, the high chemical and electrochemical stability, environmental friendless and low price are also important factors, which should be taken into account during the electrolyte design [131]. Aqueous electrolytes are commonly used for primary Mg-air batteries. For the aqueous electrolyte, the selection of solute is critical, and the most frequently used solute is NaCl. The modifications of electrolyte can be done by adding additives. Another way to modify the electrolyte can be a solvent improvement by mixing the organic and inorganic solvents.

I-4.3 Development of electrolytes

The solutes such as NaC1, $KHCO_3$, NH_4NO_3, $NaNO_3$, $NaNO_2$, Na_2SO_4, $MgCl_2$, $MgBr_2$ or $Mg(ClO_4)_2$ in aqueous solvent were proposed as electrolytes for Mg-air batteries by Sathyanarayana *et al.* in 1981 [132]. They have demonstrated a novel type of Mg-air battery showing a long service-life capability. A higher corrosion resistance (higher open circuit voltage) of Mg anode in alkaline than acidic or natural electrolytes (as show in Table I-2 [55]) was attributed to the formation of thick $Mg(OH)_2$ film protecting the Mg surface and leading to better working efficiency of Mg-air battery.

Table I-2. Open circuit voltages (E_{ocp}) of Mg anode in aqueous electrolytes with different salts [55, 133].

Electrolyte	E_{OCP} (V vs. NHE)
NaCl	–1.72
Na_2SO_4	–1.75
HCl	–1.68
HNO_3	–1.49
NaOH	–1.47
NH_3	–1.43

Since 2011 [134], the neutral NaCl aqueous electrolyte has been rapidly developed for Mg-air batteries due to its high ionic conductivity, low price and environmental friendliness. Different concentrations of NaCl for Mg seawater batteries have been studied by Zhao *et al.* [135]. A higher content of NaCl can enhance the discharge current values at a specific voltage plateau stage. It can be associated with the high Cl^-, which can accelerate the self-peel of discharge products and increase the anodic dissolution rate [136]. Acharya *et al.* [137] reported that high concentration of NaCl can destroy the $Mg(OH)_2$ film. Although the NaCl solution is widely used for Mg-air batteries, it has also many drawbacks, such as a higher self-corrosion or an elevated anodic polarization of Mg anode. As demonstrated by Yao [138] *et al.*, due to a high surface hydrophilic properties of Mg anode, the Cl^- can easily spread over the surface of Mg anode and accelerate the corrosion of Mg. It also was proved by Cao *et al.* [139] that the high

quantity of Cl^- can breakdown the surface film.

Chen's group [138] has shown that the NO_3^- or NO_2^- ions are less aggressive to the Mg anode than Cl^- and SO_4^{2-} [101] and concluded that the mixed of $Mg(NO_3)_2$ and $NaNO_2$ are well compatible with Mg-air batteries. Furthermore, Richey *et al.* [140] compared the discharge behaviour of Mg-air batteries in electrolytes with different salts (NaCl, $NaNO_3$, $NaPO_4$, and a NaCl/$NaPO_4$ mixture). Fig. I-11 [140] illustrates that the H_2 evolution in the nitrate-based electrolyte was the lowest among different salts used in aqueous electrolytes. In $NaNO_3$ electrolyte, a dominant cathodic reaction is a reduction of NO_3^- to NO_2^- instead of H_2 evolution:

$$NO_3^- + H_2O + e^- \rightarrow NO_2 + 2OH^- \qquad \text{(I-12)}$$

However, a decrease of the faradaic efficiency (related to formation of Mg^{2+}) can be also observed.

Furthermore, a mixture of NaCl / HNa_2PO_4 in aqueous solvent was employed in Mg-air battery [140]. It was shown that the pure HNa_2PO_4 can efficiently decrease the H_2 evolution but also increase the charge transfer resistance significantly hindering the anodic Mg^+ dissolution and limiting a discharge voltage. Thus, by mixing NaCl with Na_2HPO_4, the corrosion of Mg can be slowed down and the discharge potential can still be relatively high (only 0.04 V lower than in pure NaCl electrolyte).

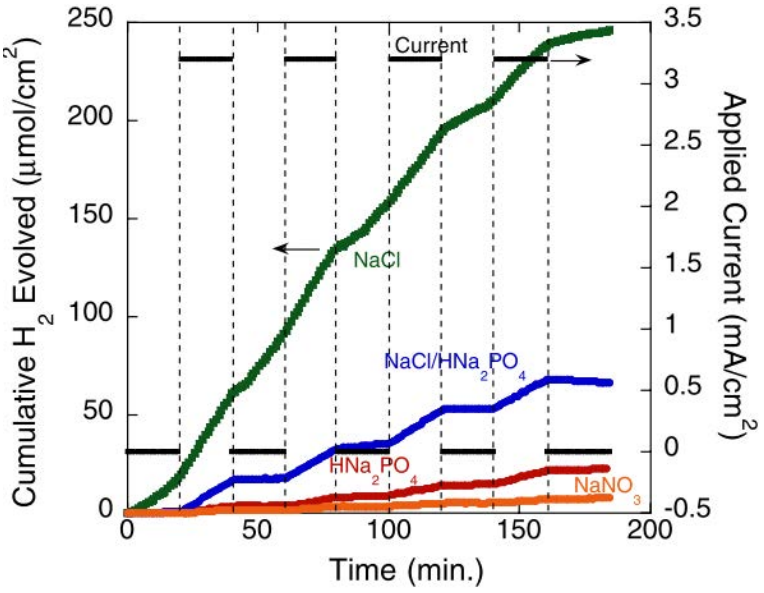

Fig. I-11 The comparation of H_2 evolution for Mg anode in different electrolytes (the anodic chronopotentiometric scans at 3.2 mA/cm^2) [140].

For developing a less corrosive electrolyte, the ionic liquids or mixture of ionic liquids and water electrolytes can be proposed. There are few bibliographic data about the reactivity of ionic liquids with Mg or Mg alloys and their application in Mg-air batteries. The application of phosphonium chloride ionic liquid mixed with water as electrolyte for Mg-air batteries was reported by Khoo *et al.* [42]. It can be concluded that an amorphous gel-like interface was formed on Mg anode allowing for a good passivation and leading to a stable galvanostatic discharge. Besides Mega *et al.* [141] demonstrated cycling of Mg using a novel alkoxyammonium ionic liquids and discussed the working mechanism of this electrolyte with Mg, supporting it by DFT calculations. The ionic liquid of 1-ethyl-3-methylimidazolium bis(trifluoromethylsulfonyl)imide with an applied additive of butyl acetate improved significantly the ionic conductivity of the electrolyte and thus led to the enhanced battery performance [142].

Recently, Antrens' group [143] compared the discharge performance of Mg in electrolyte of 3.5 wt. % NaCl and simulated urine (SU) for Mg-air batteries, and demonstrated the lower discharge voltage in SU due to the low conductivity of SU and high solution resistance. Ying Liew *et al.* [144] reported an eco-friendly water-soluble graphene-incorporated agar gel electrolyte for Mg-air batteries, which shown that the discharge capacity and energy density can reach 1010 Ah/kg and 1.41 KWh/kg, respectively, which was attributed to the high ionic conductivity of this electrolyte.

Summarizing, it can be concluded that the electrolyte modifications and the electrode/electrolyte interface reactivity understanding are the important steps in development of Mg-air battery performances.

I-4.4 Electrolyte modifications

In order to enhance the discharge performances of Mg-air batteries, the modifications of solutes and the solvents can be performed. At the same time, the electrolyte pH and temperature should be also considered. The modifications of solutes can rely on application of mixture of different salts in aqueous electrolyte and utilization of electrolyte additives. The objective of additives is to decrease the HER, so they can be called corrosion inhibitors. Concerning the solvents, the

aqueous and non-aqueous reagents can be used. It should be noted that the electrolyte modifications/formulation is not restricted to the above cited combinations. For example, here, the application of ionic liquids or mixture of ionic liquids with aqueous electrolytes will not be discussed.

I-4.4.1 Application of electrolyte additives

The most popular electrolyte modification is the addition of additive. The self-corrosion of Mg and the low anodic efficiency of Mg-air battery are the main drawbacks, thus, the additives, which attract much attention are the electrolyte inhibitors. Lamaka *et al.* [95] have systematically screened the Mg corrosion inhibitors and the efficiency of selected top 15 corrosion inhibitors is shown in Table I-3. Notably, the sodium salts of pyridine-dicarboxylic acids and several derivatives of salicylic acids show one of the highest inhibiting efficiencies among other inhibitors. Besides, quinaldates and nitrates with fumarates and nitrobarbiturates with good inhibition efficiency were also tested. Although there are many types of inhibitors that can greatly decrease the corrosion of Mg anode, the discharge performances (such as the utilization of Mg anode and discharge voltage) of Mg-air batteries can be unfortunately also decreased. It is attributed to the decrease of the anodic reaction kinetics and the lower ionic conductivity.

Table I-3. Inhibiting efficiency (η, %) of 15 corrosion inhibitors for commercial purity (CP) Mg (impurities: 220 ppm) and high purity (HP) Mg (impurities: 51 ppm and 50 ppm) [95].

Rank	CP-Mg-220ppm	η, %	HP-Mg-51 ppm	η, %	HP-Mg-50 ppm	η, %
1	Salicylaldehide	98	2, 5-Pyridinedicarboxylate Na	92	2,5-Pyridinedicarboxylate Na	99
2	3-Methylsalicylate Na	97	Folate Na	89	2,6-Pyridinedicarboxylate Na	99
3	KNO_3	97	Na_2CrO_4	85	2,3-Pyridinedicarboxylate Na	98
4	8-Hydroxyquinoline	95	3,5-Dinitrosalicylate Na	81	3,4-Pyridinedicarboxylate Na	97
5	KCN	94	2,6-Pyridinedicarboxylate Na	75	KNO_3	97
6	Dodecylbenzene Sulfonate Na	93	Fumarate Na	73	2-Hydroxy-1,4-Naphtoquinone	97
7	Na_3PO_4	93	Quinaldate Na	70	Fumarate Na	95
8	Salicylate Na	92	2,3-Pyridinedicarboxylate Na	70	3-MethylSalicylate Na	94
9	$Ce(NO_3)_3$	92	3,4-Pyridinedicarboxylate Na	64	4-Isopropylbenzoate Na	94
10	2,6-Pyridinedicarboxylate Na	90	2-Thenoyltrifluoroacetone	63	5-MethylSalicylate Na	93
11	$La(NO_3)_3$	88	5-Methylsalicylate Na	61	NaF	93
12	5-Aminosalicylate Na	86	4-Isopropylbenzoate Na	51	Succinate Na	93
13	Oxalate Na	86	2-Hydroxy-1,4Naphtoquinone	48	Diglycolate Na	93
14	Diglycolate Na	86	Benzoate Na	48	Oxalate Na	93
15	Thiosalicylate Na	86	N-Lauroylsarcosine Na	47	$Ce(NO_3)_3$	90
Cr(VI) ranked	**50**	61	**3**	85	**62**	56

As the nitrates are effective corrosion inhibitors, they were widely used for Mg-air batteries [56, 145]. The NO_3^- can remarkably prolong the protection of Mg surface film in Cl^--containing electrolyte, but the inhibiting mechanism is not clear [146]. Snihirova *et al.* [145] reported the higher impedance in electrolyte of NO_3^- + NaCl compared to the pure NaCl and an utilization efficiency of 82 %, due to the formation of a more corrosion protective film on Mg surface [145]. The mixed additives of $NaNO_3$ and salicylate can both strongly influence the redeposition and oxidation of Fe. It is widely known that the metallic impurities, such Fe impurities (discussed in 1.4.1), [62, 95, 96, 147] can promote the self-corrosion and thus lead to the low utilization of Mg anode. Therefore, the mixed $NaNO_3$ and salicylate additives greatly improve the discharge performance of Mg-air.

The effect of phosphate and vanadate as the electrolyte additives were investigated by Zhao *et al.* [148], and it was demonstrated that the anodic efficiency of Mg-air batteries was well improved, while the phosphate demonstrated to have a stronger inhibiting effect due to the formation of a more porous discharge product film on the Mg surface allowing for an easy transfer of Mg^{2+} from the substrate through the layer. Besides, the investigation of sodium phosphate and sodium dodecylbenzenesulfonate as electrolyte additives for Mg-air batteries were performed by Li *et al.* [149]. They also demonstrated that the addition of sodium phosphate can reduce the self-corrosion of Mg anode, increase the anodic utilization (95.2 %)

and improve the discharge voltage of Mg-air batteries. These effects were attributed to the reduced formation of discharge products formed on Mg anode surface.

Another interesting additive is the catalyst material such as water soluble graphene (WSG) [149], which can be used not only as a catalyst for the cathode electrode but also as an electrolyte additive used as a corrosion inhibitor. As reported, the WSG-based electrolyte improved the discharge capacity of Mg-air batteries due to its higher electrical conductivity. Besides, the longer battery service time was also observed which was attributed to the reduced corrosion rate of Mg anode. The catalyst material of MoS_2 (water dispersible nano MoS_2 sheets) was also investigated as an inhibitor in $MgCl_2$ electrolyte for Mg-air batteries [150]. The maximum discharge capacity of 1170 Ah/kg was achieved leading to limited Mg breakdown during self-discharge. The catalysis materials favoured a more negative potential of Mg electrode, OER (oxygen evolution reaction) kinetics of air cathode.

Oxyanion corrosion inhibitor as electrolyte additive for Mg-air batteries were reported by Zhao *et al.* [151], who studied the addition of Li_2CrO_4 in 3.5 wt. % NaCl solution. The anode efficiency of the Mg-air battery increased by 28.4 % and the corrosion current density of Mg anode was greatly decreased. These increased performances were also attributed to the loose product film formation during a discharge test and lower self-corrosion rate of Mg anode. .

A series of complexing agents as electrolyte additives were reported by Zheludkevich's group [152, 153]. The objective of the complexing agents is to form a complex with Fe^{3+} to prevent the Fe-re-deposition and formation of a soluble complex with Mg^{2+} which benefit to the anodic utilization. The first work by Vaghefinazari *et al.* [152] demonstrated that the nitrilotriacetic acid (NTA) and 1,2-Dihydroxybenzene-3,5-disulfonic acid (Tiron) can provide a more negative potentials of discharge. The results showed a formation of a layer over the Fe-rich impurities and deactivating these cathodic micro-sites. It can keep the Mg surface active and fresh at the same time, which can prevent the formation of $Mg(OH)_2$ precipitation. Wang *et al.* [153] compared the discharge performance of Mg-air batteries by adding complexing agents of citric acid, salicylic acid, 2,6-dihydroxybenzoic acid, 5-sul-fosalicylic acid and 3,4-dihydroxybenzoic acid. The discharge voltage reached 1.86 V with 5-sul-fosalicylic acid at current density of 0.5 mA/cm^2 and the highest specific energy above 3.0 kWh/kg (at 1 mA/cm^2 discharge current density) was observed for 0.1 M citrate.

The decyl glucoside (DG) surfactant as a new type of inhibitor was also used as the electrolyte

additives [154]. The results show that the DG surfactant is an adequate corrosion inhibitor which can adsorb on the Mg anode surface. The inhibition efficiency can reach more than 94% for the concentration of DG surfactant near to critical micelle concentration (2.5 mM). However, the inhibition efficiency of DG surfactant depends on temperature, and thus, it can increase the activation energy of the corrosion process.

I-4.4.2 Modification of the background solvent

Recently, the double solutions were developed for Mg-air batteries, as the illustrated in Fig. I-12 [155, 156]. The organic/inorganic double solutions with an organic part: 0.5 M $Mg(ClO_4)_2$-N,N-dimethylformamide (DMF) or acetonitrile (AN) was used in the Mg-anode side and an inorganic part: 0.6 M NaCl-H_2O was employed in the air cathode side. The cathodic reaction in aqueous NaCl electrolyte can lead to a higher discharge voltage. The organic electrolyte has a function of separating the Mg anode from the corrosive inorganic electrolyte, leading to the higher anodic utilization rate (85 %). However, finally, a lower discharge voltage was obtained in this double-electrolyte system comparing to a pure NaCl aqueous electrolyte, it was due to the lower conductivity of organic electrolytes and the formation of the adsorption layer on the Mg anode surface [157].

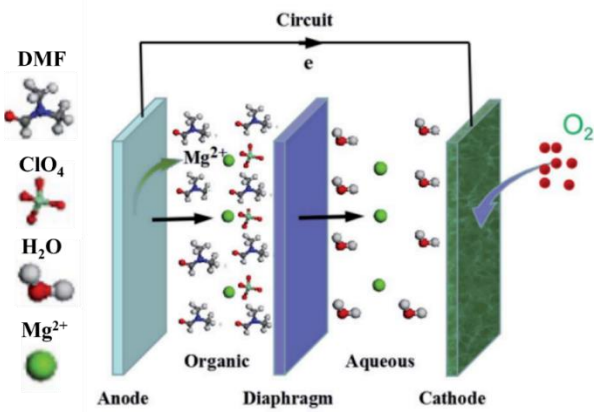

Fig. I-12 Schematic of the Mg-air battery with organic/inorganic double electrolytes [155, 156].

Leong *et al.* [158] employed a dual-electrolyte with an acid-salt configuration to improve the voltage and power performances of Mg-air battery. The sulfuric acid (H_2SO_4) served as a catholyte, and sodium nitrate used as a saline anolyte. The open circuit voltage was improved by 46 % compared to a single-electrolyte system, the energy density achieved 2043 Wh/kg at

20 mA/cm^2, and the discharge capacity 1851 Ah/kg with a coulombic efficiency of 84 % at 50 mA/cm^2. The improvement benefited from the broadened electrochemical window and reduced passivation.

Almost at the same time Li *et al.* [159], published a high-energy-density Mg-air battery based on dual-layer gel electrolyte. At first, they proposed the double-layer gel electrolyte to prevent the corrosion of Mg anode and the formation of dense passive layer. The composition of dual-layer gel electrolyte as shows Fig. I-13 (the central image), was composed of poly (ethylene oxide) (PEO) organic gel and crosslinked polyacrylamide (PAM) hydrogel. The PEO gel exhibited a uniform, dense surface layer with a high ionic conductivity, efficiently preventing the corrosion of Mg anode and benefiting a good Mg^{2+} transfer. Meanwhile, the PAM hydrogel with a porous network structure can lead to the formation of loose needle-like discharge products. For these reasons, the new type of dual-layer electrolyte was employed for Mg-air batteries achieving 99.3 % utilization rate of Mg anode and energy density of 2282 Wh/kg.

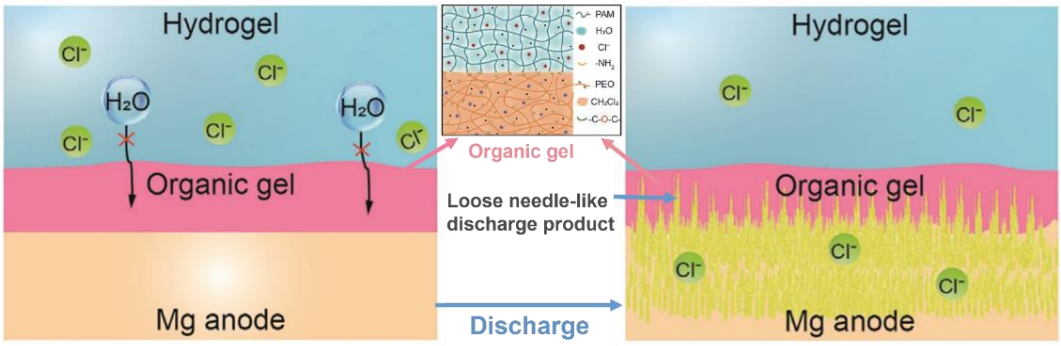

Fig. I-13 The schema of dual-layer gel electrolyte and the corresponding discharge process of Mg-air batteries [159].

There are only few organic/inorganic types of electrolytes that have been used for Mg-air batteries. However, other metal-air batteries show some promising performances in double organic/inorganic electrolytes [160-162]. Lee *et al.* [163] investigated the four organic additives in an electrolyte of 8.5 M KOH solution containing 25 g of ZnO and 3000 ppm of polyethylene glycol in 1 L of water. The objective was to suppress the hydrogen evolution and the dendrite formation during recharging. The results showed a decrease of the hydrogen evolution in the order of tartaric acid > succinic acid > phosphoric acid > citric acid. In the case of prevention

of dendrite formation, the order was citric acid > succinic acid > tartaric acid > phosphoric acid. Ghazvini *et al.* [164] reported the application of 1-ethyl-3-methylimidazolium acetate-water mixtures for Zn-air batteries. The water was used in order to reduce the viscosity and improve the electrolyte conductivity. The authors achieved a coulombic efficiency of 97 % for 50 discharge-charge cycles with a cell voltage of ~ 1.45 V in 20 vol. % water-organic mixture electrolyte. For the Al-air batteries, Palma *et al.* [162] studied the xanthan and κ-carrageenan based alkaline hydrogels as electrolytes, and reported the best performances of Al-air batteries in electrolyte with κ-carrageenan. Besides, the calcium alginate hydrogel based electrolyte can greatly inhibit the self-corrosion of aluminum, as recently demonstrated by Hou *at al.* [165]. The specific capacity of Al-air battery was significantly increased and the best discharge voltage was 1.37 V at current density of 1 mA/cm^2.

I-5 Summary and objectives of the thesis

The Mg-air batteries can be seriously considered as an interesting energy storage device if a solution is found to reach their high theoretical specific and volumetric capacity. The Mg is an interesting anode material because it has the second-most negative electrode potential. Moreover, Mg is also environmentally friendly, non-toxic and abundant. However, the drawbacks of Mg-air batteries such as the high self-corrosion rate, unstable low discharge voltage and insufficient specific energy density greatly hinder their practical applications and commercialization. In order to face the scientific and technical challenges, large numbers of research were devoted to the modification of Mg-based anode materials. Although, the high price and the complexity in conceptualisation and fabrication of Mg alloys, the anode materials need to be developed. However, a development aiming at increasing the electrochemical performances of batteries, can be focused also on other Mg-battery components such as the electrolytes and the anode/electrolyte interface properties. The research and development need to be conducted in parallel on different battery components to fulfil different environmental or energy restrictions. The positive electrode materials cannot be forgotten. It should be noted that the electrolyte modifications have recently drawn attention of researchers. The electrolyte can be modified by application of mixed of salts or addition of additives (inhibitors) or by employing two or more solvents. As introduced in this chapter, the reactivity of Mg can significantly differ as a function of type of solvent, salt or presence of inhibitor. Without being critical, most of the research ascertain the electrochemical behaviour of Mg-air batteries as a

function of electrolyte or electrode modifications by employing the classical microscopic or spectroscopic techniques.

According to our knowledge there is almost no research demonstrating a thorough chemical characterisation of Mg-anode leading to a better understanding of Mg-anode induced by the discharge process. The knowledge about the presence and the nature of species formed on the surface of Mg-based anode after immersion or discharge tests is primordial in the investigation of Mg corrosion behaviour and improving the battery performances. Although the electrolyte has been investigated by some researchers, it is still not enough, and as for Li-ion batteries this aspect has been slightly neglected up to now. It should be emphasized that the electrode/electrolyte interface of Mg-air battery has been seldom reported.

In order to improve the stability of Mg negative electrode and the performances of Mg-air battery, a comprehensive study of the modifications at the electrode/electrolyte interface as a function of the electrolyte composition has been performed. The specific questions that we wanted to address in this work were:

1) Can the improved corrosion properties of Mg be beneficial to the electrochemical behaviour of the Mg negative electrode used in Mg-air battery?
2) Can corrosion inhibitors be used in Mg-air battery systems to improve the longevity of Mg negative electrode or discharge potential?
3) What is the nature and chemical composition of the surface layer formed on the Mg negative electrode responsible for the improved electrochemical properties of Mg-air?
4) How we can tune the electrolyte composition using salt, solvent and additive to customise the electrode/electrolyte interface for Mg-air batteries and how can be explained the working mechanisms of improved Mg-air battery performances?

To do so, this work was focused on the Mg electrode modifications as a function of the electrolyte composition (salt, solvent or additive) induced by electrochemical processes (immersion, polarisation, discharge). To be more complementary with reference to the state-of-the-art, the surface and in-depth composition of Mg electrode were analysed by surface sensitive techniques such as X-ray photoelectron spectroscopy (XPS) and time-of-flight secondary ion mass spectrometry (ToF-SIMS), respectively.

The first part of this work (chapter III) presents a novel method of improving the electrochemical performances of Mg-air battery by employing organic/inorganic hybrid

electrolyte. To do so, a part of the water volume was replaced by ethanol solvent and mixed with 0.6 M NaCl. The presence of water in ethanol leads to improved electrolyte's ionic conductivity. First, the influence of high concentration of ethanol (20 vol. %, 60 vol. %) on corrosion properties of Mg, morphological and surface modifications of Mg by XPS and ToF-SIMS are demonstrated. Then, the discharge behaviour of full Mg-air battery in the high ethanol concentration and trace of ethanol are compared. The optimized composition of inorganic/organic dual electrolyte (≤ 5 vol. % of ethanol) is proposed and series of battery tests at different current densities are performed.

In the second part of the work (Chapter IV), we propose to apply the sodium 5-sulfosalicylate (5-S-Sal) as a corrosion inhibitor in 0.6 M NaCl electrolyte for Mg-air batteries. A pure commercial Mg anode (99.9 %) was used as a model electrode material instead of the Mg alloy in order to discard the interference with the alloying elements in the alloy and better understand the influence of 5-S-Sal inhibitor added to the electrolyte and its working mechanism. Different immersion times of Mg anode in electrolyte with and without inhibitors were applied to elucidate the progress of Mg corrosion and analyze the corrosion of Mg by linear sweep voltammetry and electrochemical impedance spectroscopy. The surface chemical composition of Mg anode was analyzed by XPS and ToF-SIMS. Then, after the corrosion studies, different concentrations of 5-S-Sal were used to compare the discharge behaviors with the objective to tune the best battery performance *i.e.*, the highest discharge voltage and the longest battery lifetime. The composition and morphology of Mg anode was also analyzed after discharge tests to demonstrate its improved performance in electrolyte with presence of inhibitor.

In the third part of this thesis (chapter V), we propose to apply low quantity of acetic acid agent in $NaNO_3$ aqueous electrolyte for Mg-air batteries for enhancing the discharge efficiency. Firstly, the influence of acetic acid on the behaviour of Mg-anode (in full cells) in different electrolytes such as NaCl in H_2O, $NaNO_3$ in H_2O and $NaNO_3$ in H_2O were investigated. The following part demonstrates the improved performance of Mg-air batteries in optimized electrolyte of $NaNO_3$ in H_2O with acetic acid. Transmission electron microscope (TEM) was applied to clarify the differences of the surface layers formed on Mg anode in electrolyte with and without acetic acid. XPS and ToF-SIMS were further used to show the surface chemical composition of Mg anode corrosion products and discharge products.

I-References

[1] T.B. Johansson, Renewable energy: sources for fuels and electricity, Energy Studied Review, 4 (1992) 201-212.

[2] T.H. Oh, S.Y. Pang, S.C. Chua, Energy policy and alternative energy in Malaysia: Issues and challenges for sustainable growth, Renewable and Sustainable Energy Reviews, 14 (2010) 1241-1252.

[3] D.A.a.M. Tatsutani, Sustainable energy for developing countries, journals OpenEdition, 2 (2009) 2.

[4] F. Cheng, J. Chen, Metal-air batteries: from oxygen reduction electrochemistry to cathode catalysts, Chem Soc Rev, 41 (2012) 2172-2192.

[5] R. M. Dell and D. A. J. Rand, Clean Energy, Royal Society of Chemistry, Cambridge (2004).

[6] X.W. Md. Arafat Rahman, and Cuie Wen, High Energy Density Metal-Air Batteries A Review, J Electrochem Soc, 160 (2013) A1759-A1771.

[7] I. Katsounaros, S. Cherevko, A.R. Zeradjanin, K.J. Mayrhofer, Oxygen electrochemistry as a cornerstone for sustainable energy conversion, Angewandte Chemie, 53 (2014) 102-121.

[8] T.B.R. D. Linden, Handbook of Batteries, McGraw-Hill, New York, Handbook of Batteries (2002).

[9] A.J. Mauger, C.M. , Critical review on lithium-ion batteries: Are they safe? sustainable?, Ionics, 23 (2017) 1933–1947.

[10] F.A.a.C.I. Misgina Tilahun Tsehaye Prospects for Anion-Exchange Membranes in Alkali Metal–Air Batteries, energies, 12 (2019) 4702.

[11] X. Feng, M. Ouyang, X. Liu, L. Lu, Y. Xia, X. He, Thermal runaway mechanism of lithium ion battery for electric vehicles: A review, Energy Storage Materials, 10 (2018) 246-267.

[12] Y.G. Li, J. Lu, Metal Air Batteries: Will They Be the Future Electrochemical Energy Storage Device of Choice?, Acs Energy Lett, 2 (2017) 1370-1377.

[13] P.G. Bruce, S.A. Freunberger, L.J. Hardwick, J.M. Tarascon, Li-O2 and Li-S batteries with high energy storage, Nature materials, 11 (2011) 19-29.

[14] B.M.C. G. Girishkumar, A. C. Luntz, S. Swanson, W. Wilcke, Lithium-Air Battery: Promise and Challenges, Journal Physical Chemistry letters, 1 (2010) 2193-2203.

[15] X. Zhang, X.-G. Wang, Z. Xie, Z. Zhou, Recent progress in rechargeable alkali metal–air batteries, Green Energy & Environment, 1 (2016) 4-17.

[16] G.L. Soloveichik, Flow Batteries Current Status and Trends, Chemical Reviews, 115 (2015) 11533-11558.

[17] K.M.J. Abraham, Z. A Polymer Electrolyte-Based Rechargeable Lithium/Oxygen Battery, J. Electrochem. Soc. , 143 (1996) 1-5.

[18] P. Hartmann, C.L. Bender, M. Vracar, A.K. Durr, A. Garsuch, J. Janek, P. Adelhelm, A rechargeable room-temperature sodium superoxide (NaO2) battery, Nature materials, 12 (2013) 228-232.

[19] X. Ren, Y. Wu, A low-overpotential potassium-oxygen battery based on potassium

superoxide, Journal of the American Chemical Society, 135 (2013) 2923-2926.

[20] J. Hassoun, F. Croce, M. Armand, B. Scrosati, Investigation of the O2 electrochemistry in a polymer electrolyte solid-state cell, Angewandte Chemie, 50 (2011) 2999-3002.

[21] L.L. Johnson, C. Liu, Z. Chen, Y. Freunberger, S. A. Ashok, P. C. Praveen, B. B. Dholakia, K. Tarascon, J.-M. Bruce, P. G. , The Role of LiO2 Solubility in O2 Reduction in Aprotic Solvents and Its Consequences for Li-O2 Batteries, Nat. Chem. , 6 (2014).

[22] J. Ma, W. Zhang, X. Wang, M. Tang, Z. Huang, J. Li, H. Zhang, X. Yang, Z. Guo, Y. Wang, Revealing the mechanism of saturated ether electrolyte for improving the long-cycling stability of Na-O2 batteries, Nano Energy, 84 (2021) 105927.

[23] X. Chi, M. Li, J. Di, P. Bai, L. Song, X. Wang, F. Li, S. Liang, J. Xu, J. Yu, A highly stable and flexible zeolite electrolyte solid-state Li-air battery, Nature, 592 (2021) 551-557.

[24] L. Qin, L. Schkeryantz, J. Zheng, N. Xiao, Y. Wu, Superoxide-Based K-O2 Batteries: Highly Reversible Oxygen Redox Solves Challenges in Air Electrodes, Journal of the American Chemical Society, 142 (2020) 11629-11640.

[25] M.A. Deyab, Effect of nonionic surfactant as an electrolyte additive on the performance of aluminum-air battery, J Power Sources, 412 (2019) 520-526.

[26] J. Fu, Z.P. Cano, M.G. Park, A. Yu, M. Fowler, Z. Chen, Electrically Rechargeable Zinc-Air Batteries: Progress, Challenges, and Perspectives, Advanced materials, 29 (2017).

[27] C. Gu, X.-Q. Xie, Y. Liang, J. Li, H. Wang, K. Wang, J. Liu, M. Wang, Y. Zhang, M. Li, H. Kong, C.-S. Liu, Small molecule-based supramolecular-polymer double-network hydrogel electrolytes for ultra-stretchable and waterproof Zn–air batteries working from −50 to 100 °C, Energy & Environmental Science, 14 (2021) 4451-4462.

[28] Y.P. Chen, S.Y. Lin, R.M. Sun, A.J. Wang, L. Zhang, X. Ma, J.J. Feng, FeCo/FeCoP encapsulated in N, Mn-codoped three-dimensional fluffy porous carbon nanostructures as highly efficient bifunctional electrocatalyst with multi-components synergistic catalysis for ultra-stable rechargeable Zn-air batteries, Journal of colloid and interface science, 605 (2022) 451-462.

[29] L.W. Min Deng , Bahram Vaghefinazari, Wen Xu, Christian Feiler, Sviatlana V. Lamaka, Daniel Höche, Mikhail L. Zheludkevich, Darya Snihirova, High-energy and durable aqueous magnesium batteries: Recent advances and perspectives, Energy Storage Materials, 43 (2021) 238-247.

[30] J. Xiang, L. Yang, L. Yuan, K. Yuan, Y. Zhang, Y. Huang, J. Lin, F. Pan, Y. Huang, Alkali-Metal Anodes: From Lab to Market, Joule, 3 (2019) 2334-2363.

[31] C. Wei, Y. Tao, H. Fei, Y. An, Y. Tian, J. Feng, Y. Qian, Recent advances and perspectives in stable and dendrite-free potassium metal anodes, Energy Storage Materials, 30 (2020) 206-227.

[32] Y. Tian, Y. An, C. Liu, S. Xiong, J. Feng, Y. Qian, Reversible zinc-based anodes enabled by zincophilic antimony engineered MXene for stable and dendrite-free aqueous zinc batteries, Energy Storage Materials, 41 (2021) 343-353.

[33] G. Vardar, E.G. Nelson, J.G. Smith, J. Naruse, H. Hiramatsu, B.M. Bartlett, A.E.S. Sleightholme, D.J. Siegel, C.W. Monroe, Identifying the Discharge Product and Reaction Pathway for a Secondary Mg/O2 Battery, Chemistry of Materials, 27 (2015) 7564-7568.

[34] J.G. Smith, J. Naruse, H. Hiramatsu, D.J. Siegel, Theoretical Limiting Potentials in Mg/O2 Batteries, Chemistry of Materials, 28 (2016) 1390-1401.

[35] T. Shiga, Y. Hase, Y. Kato, M. Inoue, K. Takechi, A rechargeable non-aqueous Mg-O2 battery, Chemical communications, 49 (2013) 9152-9154.

[36] Y.H. T. Shiga, Y. Yagi, N. Takahashi, K. Takechi, , Catalytic Cycle Employing TEMPO-Anion Complex to Obtain Secondary Mg-O2 Battery, J. Phys. Chem, 5 (2014) 1648.

[37] C.B. P. Reinsberg, H. Baltruschat, Mechanistic investigation of the oxygen reduction in magnesium ion- containing dimethyl sulfoxide, Electrochim. Acta 200 (2016) 214.

[38] Y.S. Chun-Sheng Li, Florian Gebert, and Shu-Lei Chou, Current Progress on Rechargeable Magnesium–Air Battery, Adv. Energy Mater, 7 (2017) 1700869.

[39] X. Liu, J. Xue, The role of Al2Gd cuboids in the discharge performance and electrochemical behaviors of AZ31-Gd anode for Mg-air batteries, Energy, 189 (2019) 116314.

[40] X. Liu, S. Liu, J. Xue, Discharge performance of the magnesium anodes with different phase constitutions for Mg-air batteries, J Power Sources, 396 (2018) 667-674.

[41] Y. Li, X. Zhang, H.-B. Li, H.D. Yoo, X. Chi, Q. An, J. Liu, M. Yu, W. Wang, Y. Yao, Mixed-phase mullite electrocatalyst for pH-neutral oxygen reduction in magnesium-air batteries, Nano Energy, 27 (2016) 8-16.

[42] T. Khoo, P.C. Howlett, M. Tsagouria, D.R. MacFarlane, M. Forsyth, The potential for ionic liquid electrolytes to stabilise the magnesium interface for magnesium/air batteries, Electrochimica Acta, 58 (2011) 583-588.

[43] Y. Liu, Q. Sun, W. Li, K.R. Adair, J. Li, X. Sun, A comprehensive review on recent progress in aluminum–air batteries, Green Energy & Environment, 2 (2017) 246-277.

[44] Y.L. Xiaomeng Zhang , Min Jiang, Jianxu Wei, Xinxin Ding, Changyan Zhu, Hao Heg, Hongchang Lai , Junyu Shi, Engineering the coordination environment in atomic Fe/Ni dual-sites for efficient oxygen electrocatalysis in Zn-air and Mg-air batteries, Chemical Engineering Journal, 426 (2021) 130758.

[45] K.M. Abraham, A Brief History of Non-Aqueous Metal-Air Batteries, ECS Transactions, 3 (2008) 67-71.

[46] N.S. Hazri, S. Basri, S.K. Kamarudin, A.M. Zainoodin, Critical review on development of magnesium alloy as anode in

Mg‐Air

fuel cell and additives in electrolyte, International Journal of Energy Research, 45 (2021) 15739-15759.

[47] C. Byung-wo, http://www.electric-vehiclenews.com/2013/01/kist-develop-magnesium-air-battery-with.html, [Cited January, 2013], (2013).

[48] MAGPOWER, http://www.magpowersystems.com/.

[49] http://www.dafc.dicp.ac.cn/yanjiufangxiang/2010040759.html, (Accessed Jan 2019).

[50] Z.P. Q. Liu, W. Wang, L. An, G. Sun, Aqueous metal-air batteries: Fundamentals and Applications, Energy Storage Materials, 27 (2019) 478-505.

[51] M.M.A. Battery, 2019, https://www.ecomarinepower.com/en/mgbox-air-battery, ([cited

2020 September]).

[52] S.b. GOODiON, Research and development of metal-air fuel cells., http://www.ionslab.co.kr., ([September 2020]).

[53] E. Wang, Z. Yan, Q. Liu, J. Gao, M. Liu, G. Sun, Research and Development of Metal-Air Fuel Cells, 63 (2018) 285-323.

[54] L. Zhang, Q. Shao, J. Zhang, An overview of non-noble metal electrocatalysts and their associated air cathodes for Mg-air batteries, Materials Reports: Energy, 1 (2021) 100002.

[55] T. Zhang, Z. Tao, J. Chen, Magnesium–air batteries: from principle to application, Mater. Horiz., 1 (2014) 196-206.

[56] W. Li, C. Li, C. Zhou, H. Ma, J. Chen, Metallic magnesium nano/mesoscale structures: their shape-controlled preparation and mg/air battery applications, Angewandte Chemie, 45 (2006) 6009-6012.

[57] M. Esmaily, J.E. Svensson, S. Fajardo, N. Birbilis, G.S. Frankel, S. Virtanen, R. Arrabal, S. Thomas, L.G. Johansson, Fundamentals and advances in magnesium alloy corrosion, Progress in Materials Science, 89 (2017) 92-193.

[58] G. Song, Recent Progress in Corrosion and Protection of Magnesium Alloys, Advanced Energy Materials, 7 (2005) 563-586.

[59] J. Li, B. Zhang, Q. Wei, N. Wang, B. Hou, Electrochemical behavior of Mg-Al-Zn-In alloy as anode materials in 3.5 wt.% NaCl solution, Electrochimica Acta, 238 (2017) 156-167.

[60] M. Curioni, The behaviour of magnesium during free corrosion and potentiodynamic polarization investigated by real-time hydrogen measurement and optical imaging, Electrochimica Acta, 120 (2014) 284-292.

[61] G. Williams, N. Birbilis, H.N. McMurray, The source of hydrogen evolved from a magnesium anode, Electrochemistry Communications, 36 (2013) 1-5.

[62] K.A. Yasakau, A. Maltseva, S.V. Lamaka, D. Mei, H. Orvi, P. Volovitch, M.G.S. Ferreira, M.L. Zheludkevich, The effect of carboxylate compounds on Volta potential and corrosion inhibition of Mg containing different levels of iron, Corros Sci, 194 (2022) 109937.

[63] R.M.S. Arthur E. Martell, Critical Stability Constants, Springer, Second supplement (1989).

[64] X. Chen, S. Ning, Q. Le, H. Wang, Q. Zou, R. Guo, J. Hou, Y. Jia, A. Atrens, F. Yu, Effects of external field treatment on the electrochemical behaviors and discharge performance of AZ80 anodes for Mg-air batteries, Journal of Materials Science & Technology, 38 (2020) 47-55.

[65] M. Deng, L. Wang, D. Höche, S.V. Lamaka, D. Snihirova, B. Vaghefinazari, M.L. Zheludkevich, Clarifying the decisive factors for utilization efficiency of Mg anodes for primary aqueous batteries, J Power Sources, 441 (2019) 227201.

[66] X. Chen, Y. Jia, Q. Le, H. Wang, X. Zhou, F. Yu, A. Atrens, Discharge properties and electrochemical behaviors of AZ80-La-Gd magnesium anode for Mg-air battery, Journal of Magnesium and Alloys, (2020).

[67] M. Deng, D. Hoche, S.V. Lamaka, D. Snihirova, M.L. Zheludkevich, Mg-Ca binary alloys as anodes for primary Mg-air batteries, J Power Sources, 396 (2018) 109-118.

[68] N.G. Wang, R.C. Wang, Y. Feng, W.H. Xiong, J.C. Zhang, M. Deng, Discharge and and corrosion behaviour of Mg-Li-Al-Ce-Y-Zn alloy as the anode for Mg-air battery, Corros Sci,

112 (2016) 13-24.

[69] Y. Zhang, X. Wu, Y. Fu, W. Shen, X. Zeng, W. Ding, Carbon aerogel supported Pt–Zn catalyst and its oxygen reduction catalytic performance in magnesium-air batteries, Journal of Materials Research, 29 (2014) 2863-2870.

[70] A.A. G.L. Song, Corrosion mechanisms of magnesium alloys, Adv. Eng. Mater. , 1 (1999) 11-33.

[71] S.J. A. Atrens, Z. Shi, M.S. Dargusch, Viewpoint - Understanding Mg corrosion in the body for biodegradable medical implants, Scr. Mater, 154 (2018) 92-100.

[72] A. Atrens, G. Song, M. Liu, Z. Shi, F. Cao, M.S. Dargusch, Review of Recent Developments in the Field of Magnesium Corrosion, Advanced Energy Materials, 17 (2015) 400-453.

[73] W. Beetz, XXXIV. On the development of hydrogen from the anode, The London, Edinburgh, and Dublin Philosophical Magazine and Journal of Science, 32 (2009) 269-278.

[74] A.A. G. Song, D. Stjohn, J. Nairn, Y. Li, The electrochemical corrosion of pure magnesium in 1 N NaCl, Corros. Sci. , 39 (1997) 855-875.

[75] G.G. Perrault, Potentionstatic study of the magnesium electrode in aqueous soultion J. Electroanal. Chem. Int. Electrochem, 27 (1970) 47-58.

[76] B.B. M. Straumanis, Disintegration of magnesium while dissolving anodically in neutral and acidic solutions, J. Electrochem. Soc. , 110 (1963) 357-360.

[77] G.S. Frankel, A. Samaniego, N. Birbilis, Evolution of hydrogen at dissolving magnesium surfaces, Corros Sci, 70 (2013) 104-111.

[78] G.v. Baril, G. Galicia, C. Deslouis, N. e, B. Tribollet, V. Vivier, An Impedance Investigation of the Mechanism of Pure Magnesium Corrosion in Sodium Sulfate Solutions, J Electrochem Soc, 154 (2007) C108.

[79] J.X. Jia, A. Atrens, G. Song, T.H. Muster, Simulation of galvanic corrosion of magnesium coupled to a steel fastener in NaCl solution, Materials and Corrosion, 56 (2005) 468-474.

[80] M. Taheri, J.R. Kish, N. Birbilis, M. Danaie, E.A. McNally, J.R. McDermid, Towards a Physical Description for the Origin of Enhanced Catalytic Activity of Corroding Magnesium Surfaces, Electrochimica Acta, 116 (2014) 396-403.

[81] C.D. Taylor, A First-Principles Surface Reaction Kinetic Model for Hydrogen Evolution under Cathodic and Anodic Conditions on Magnesium, J Electrochem Soc, 163 (2016) C602-C608.

[82] G.-L.S. Jufeng Huang, Andrej Atrens, Matthew Dargusch, What activates the Mg surface—A comparison of Mg dissolution mechanisms, Journal of Materials Science & Technology, 54 (2020) 207-220.

[83] Z. Shi, M. Liu, A. Atrens, Measurement of the corrosion rate of magnesium alloys using Tafel extrapolation, Corros Sci, 52 (2010) 579-588.

[84] G.-L. Song, Corrosion electrochemistry of magnesium (Mg) and its alloys, Corrosion of Magnesium Alloys, Woodhead (2011) 3-65.

[85] S. Fajardo, G.S. Frankel, Effect of impurities on the enhanced catalytic activity for hydrogen evolution in high purity magnesium, Electrochimica Acta, 165 (2015) 255-267.

[86] A.A. G. L. Song, D. S. John, X. Wu, J. Nairn, , The anodic dissolution of magnesium in chloride and sulphate solutions, Corros. Sci. , 39 (1997) 1981-2004.

[87] K.A. Unocic, H.H. Elsentriecy, M.P. Brady, H.M. Meyer, G.L. Song, M. Fayek, R.A. Meisner, B. Davis, Transmission Electron Microscopy Study of Aqueous Film Formation and Evolution on Magnesium Alloys, J Electrochem Soc, 161 (2014) C302-C311.

[88] G.S.a.A. Atrens, Understanding Magnesium Corrosion—A Framework for Improved Alloy Performance, Adv. Eng. Mater., 5 (2003) 837-858.

[89] M. Santamaria, F. Di Quarto, S. Zanna, P. Marcus, Initial surface film on magnesium metal: A characterization by X-ray photoelectron spectroscopy (XPS) and photocurrent spectroscopy (PCS), Electrochimica Acta, 53 (2007) 1314-1324.

[90] M. Liu, S. Zanna, H. Ardelean, I. Frateur, P. Schmutz, G. Song, A. Atrens, P. Marcus, A first quantitative XPS study of the surface films formed, by exposure to water, on Mg and on the Mg–Al intermetallics: Al3Mg2 and Mg17Al12, Corros Sci, 51 (2009) 1115-1127.

[91] N. Hara, Y. Kobayashi, D. Kagaya, N. Akao, Formation and breakdown of surface films on magnesium and its alloys in aqueous solutions, Corros Sci, 49 (2007) 166-175.

[92] D.S. G. Song, The effect of zirconium grain refinement on the corrosion behaviour of magnesium-rare earth alloy MEZ, J. Light Met, 2 (2002) 1-16.

[93] F. Tong, S. Wei, X. Chen, W. Gao, Magnesium alloys as anodes for neutral aqueous magnesium-air batteries, Journal of Magnesium and Alloys, 9 (2021) 1861-1883.

[94] S.V. Lamaka, D. Höche, R.P. Petrauskas, C. Blawert, M.L. Zheludkevich, A new concept for corrosion inhibition of magnesium: Suppression of iron re-deposition, Electrochemistry Communications, 62 (2016) 5-8.

[95] S.V. Lamaka, B. Vaghefinazari, D. Mei, R.P. Petrauskas, D. Hoche, M.L. Zheludkevich, Comprehensive screening of Mg corrosion inhibitors, Corros Sci, 128 (2017) 224-240.

[96] D. Hoche, C. Blawert, S.V. Lamaka, N. Scharnagl, C. Mendis, M.L. Zheludkevich, The effect of iron re-deposition on the corrosion of impurity-containing magnesium, Phys Chem Chem Phys, 18 (2016) 1279-1291.

[97] D. Mercier, J. Światowska, E. Protopopoff, S. Zanna, A. Seyeux, P. Marcus, Inhibition of Mg Corrosion by Sulfur Blocking of the Hydrogen Evolution Reaction on Iron Impurities, J Electrochem Soc, 167 (2020) 121504.

[98] M. Liu, P.J. Uggowitzer, A.V. Nagasekhar, P. Schmutz, M. Easton, G.-L. Song, A. Atrens, Calculated phase diagrams and the corrosion of die-cast Mg–Al alloys, Corros Sci, 51 (2009) 602-619.

[99] M.A.I.M.E. J. D. Hanawalt, C. E. Nelson, and J. A. Peloubet, Trans. Am. Inst. Min. Metall. Eng., 147, 273–298 (1942). Corrosion Studies of Magnesium and Its Alloys, Trans. Am. Inst. Min. Metall. Eng., 147 (1942) 273-298.

[100] G.L.M.a.J. Kruger, Corrosion of magnesium, International Materials Reviews, 38 (1993) 138-153.

[101] E.C.J. R. P. Hamlen, J. C. Ruzzo, and E. G. Siwek, Anodes for Refuelable Magnesium-Air Batteries, J Electrochem Soc, 116 (1969) 1588-1592.

[102] J. Ma, G. Wang, Y. Li, F. Ren, A.A. Volinsky, Electrochemical performance of Mg-air

batteries based on AZ series magnesium alloys, Ionics, 25 (2018) 2201-2209.

[103] J. Li, K. Wan, Q. Jiang, H. Sun, Y. Li, B. Hou, L. Zhu, M. Liu, Corrosion and Discharge Behaviors of Mg-Al-Zn and Mg-Al-Zn-In Alloys as Anode Materials, Metals, 6 (2016) 65.

[104] G. Song, A. Atrens, M. Dargusch, Influence of microstructure on the corrosion of diecast AZ91D, Corros Sci, 41 (1998) 249-273.

[105] N.-G. Wang, R.-C. Wang, C.-Q. Peng, Y. Feng, X.-Y. Zhang, Influence of aluminium and lead on activation of magnesium as anode, Transactions of Nonferrous Metals Society of China, 20 (2010) 1403-1411.

[106] J.M. Yaqiong Li, Guangxin Wang, Fengzhang Ren, YujieZhu, Yongfa Song, Jingli Zhang, Effect by adding Ce and In to Mg–6Al Alloy as anode on performance of Mg-air batteries, Mater. Res. Express, 6 (2019) 066315.

[107] N. Wang, R. Wang, C. Peng, Y. Feng, B. Chen, Effect of hot rolling and subsequent annealing on electrochemical discharge behavior of AP65 magnesium alloy as anode for seawater activated battery, Corros Sci, 64 (2012) 17-27.

[108] X. Liu, J. Xue, P. Zhang, Z. Wang, Effects of the combinative Ca, Sm and La additions on the electrochemical behaviors and discharge performance of the as-extruded AZ91 anodes for Mg-air batteries, J Power Sources, 414 (2019) 174-182.

[109] M. Yuasa, X.S. Huang, K. Suzuki, M. Mabuchi, Y. Chino, Discharge properties of Mg-Al-Mn-Ca and Mg-Al-Mn alloys as anode materials for primary magnesium-air batteries, J Power Sources, 297 (2015) 449-456.

[110] N. Wang, R. Wang, C. Peng, B. Peng, Y. Feng, C. Hu, Discharge behaviour of Mg-Al-Pb and Mg-Al-Pb-In alloys as anodes for Mg-air battery, Electrochimica Acta, 149 (2014) 193-205.

[111] H. Xiong, K. Yu, X. Yin, Y. Dai, Y. Yan, H. Zhu, Effects of microstructure on the electrochemical discharge behavior of Mg-6wt%Al-1wt%Sn alloy as anode for Mg-air primary battery, J Alloy Compd, 708 (2017) 652-661.

[112] N.N. Aung, W. Zhou, Effect of grain size and twins on corrosion behaviour of AZ31B magnesium alloy, Corros Sci, 52 (2010) 589-594.

[113] T.X. Zheng, Y.B. Hu, Y.X. Zhang, S.W. Yang, F.S. Pan, Composition optimization and electrochemical properties of Mg-Al-Sn-Mn alloy anode for Mg-air batteries, Mater Design, 137 (2018) 245-255.

[114] S.Q. Yuan, H.M. Lu, Z.G. Sun, L. Fan, X.Y. Zhu, W. Zhang, Electrochemical Performance of Mg-3Al Modified with Ga, In and Sn as Anodes for Mg-Air Battery, J Electrochem Soc, 163 (2016) A1181-A1187.

[115] Y. Song, J. Ma, Y. Li, G. Wang, C. Qin, H.-R. Stock, Effects of second phases in anode materials on discharge performance of Mg-air batteries, Ionics, 25 (2019) 5899-5906.

[116] Y. Song, D. Shan, R. Chen, E.-H. Han, Corrosion characterization of Mg–8Li alloy in NaCl solution, Corros Sci, 51 (2009) 1087-1094.

[117] W. Xu, N. Birbilis, G. Sha, Y. Wang, J.E. Daniels, Y. Xiao, M. Ferry, A high-specific-strength and corrosion-resistant magnesium alloy, Nature materials, 14 (2015) 1229-1235.

[118] L. Hou, M. Raveggi, X.-B. Chen, W. Xu, K.J. Laws, Y. Wei, M. Ferry, N. Birbilis, Investigating the Passivity and Dissolution of a Corrosion Resistant Mg-33at.%Li Alloy in

Aqueous Chloride Using Online ICP-MS, J Electrochem Soc, 163 (2016) C324-C329.

[119] L.W. Huabao Yang, Bin Jiang, Wenjun Liu, Jiangfeng Song, Guangsheng Huang, Dingfei Zhang, Fusheng Pan, Clarifying the roles of grain boundary and grain orientation on the corrosion and discharge processes of α-Mg based Mg-Li alloys for primary Mg-air batteries, Journal of Materials Science & Technology, 62 (2021) 128-138.

[120] D. Cao, L. Wu, Y. Sun, G. Wang, Y. Lv, Electrochemical behavior of Mg–Li, Mg–Li–Al and Mg–Li–Al–Ce in sodium chloride solution, J Power Sources, 177 (2008) 624-630.

[121] Y. Lv, M. Liu, Y. Xu, D. Cao, J. Feng, R. Wu, M. Zhang, The electrochemical behaviors of Mg–8Li–0.5Y and Mg–8Li–1Y alloys in sodium chloride solution, J Power Sources, 239 (2013) 265-268.

[122] D.H. M. Deng, S.V. Lamaka, L. Wang, M.L. Zheludkevich, Revealing the impact of second phase morphology on discharge properties, Corros. Sci, 153 (2019) 225-235.

[123] H.Y. Tok, E. Hamzah, H.R. Bakhsheshi-Rad, The role of bismuth on the microstructure and corrosion behavior of ternary Mg–1.2Ca–xBi alloys for biomedical applications, J Alloy Compd, 640 (2015) 335-346.

[124] W. Zhou, N.N. Aung, Y. Sun, Effect of antimony, bismuth and calcium addition on corrosion and electrochemical behaviour of AZ91 magnesium alloy, Corros Sci, 51 (2009) 403-408.

[125] M. Song, T. Zhang, J. Niu, H. Gao, Y. Shi, Y. Zhang, W. Ma, Z. Zhang, Boosting electrochemical reactivity of tin as an anode for Mg ion batteries through introduction of second phase, J Power Sources, 451 (2020) 227735.

[126] N. Shrestha, K.S. Raja, V. Utgikar, Mg-RE Alloy Anode Materials for Mg-Air Battery Application, J Electrochem Soc, 166 (2019) A3139-A3153.

[127] J.M.Z. N. Shrestha, V. Utgikar, K.S. Raja, Design Strategies for Anode of Mg-Air Batteries and Hydrogen Evolution Reactions on Mg-RE Alloys, ECS Transactions, 13 (2018) 95-107.

[128] M. Deng, Novel Mg-Ca-based alloys as anode materials for primary aqueous Mg-air battery, Chapter 1 (2020) P 293.

[129] N. Wang, W. Li, Y. Huang, G. Wu, M. Hu, G. Li, Z. Shi, Wrought Mg-Al-Pb-RE alloy strips as the anodes for Mg-air batteries, J Power Sources, 436 (2019) 226855.

[130] W.C. Xiongjie Gu, Shiming Cheng, Yanhui Liu, Zhifeng Wang, Hui Yu, Ze-qin Cui, Li-fei Wang, Hong-xia Wang, Tailoring the microstructure and improving the discharge properties of dilute Mg-Sn-Mn-Ca alloy as anode for Mg-air battery through homogenization prior to extrusion, Journal of Materials Science & Technology, 60 (2021) 77-89.

[131] S. Hosseini, S.J. Han, A. Arponwichanop, T. Yonezawa, S. Kheawhom, Ethanol as an electrolyte additive for alkaline zinc-air flow batteries, Scientific reports, 8 (2018) 11273.

[132] N.M. S. Sathyanarayana, A new magnesium-air cell for long-life applications, Journal of Applied Electrochemistry, 11 (1981) 33-39.

[133] W.P.J. H. P. Godard, M. R. Bothwell and R. L. Lane, The Corrosion of Light Metals, John Wiley & Sons, (1967).

[134] Y. Ma, N. Li, D. Li, M. Zhang, X. Huang, Performance of Mg–14Li–1Al–0.1Ce as anode

for Mg-air battery, J Power Sources, 196 (2011) 2346-2350.

[135] B.P. ZHAO Hongyang, JU Dongying Electrochemical performance of magnesium alloy and its application on the sea water battery, Journal of Environmental Sciences, 21 (2009) S88-S91.

[136] M.C. Merino, A. Pardo, R. Arrabal, S. Merino, P. Casajús, M. Mohedano, Influence of chloride ion concentration and temperature on the corrosion of Mg–Al alloys in salt fog, Corros Sci, 52 (2010) 1696-1704.

[137] M.G. Acharya, A.N. Shetty, The corrosion behavior of AZ31 alloy in chloride and sulfate media – A comparative study through electrochemical investigations, Journal of Magnesium and Alloys, 7 (2019) 98-112.

[138] W. Yao, W. Liang, G. Huang, B. Jiang, A. Atrens, F. Pan, Superhydrophobic coatings for corrosion protection of magnesium alloys, Journal of Materials Science & Technology, 52 (2020) 100-118.

[139] F. Cao, C. Zhao, J. You, J. Hu, D. Zheng, G.L. Song, The Inhibitive Effect of Artificial Seawater on Magnesium Corrosion, Advanced Engineering Materials, 21 (2019) 1900363.

[140] F.W. Richey, B.D. McCloskey, A.C. Luntz, Mg Anode Corrosion in Aqueous Electrolytes and Implications for Mg-Air Batteries, J Electrochem Soc, 163 (2016) A958-A963.

[141] M. Kar, Z. Ma, L.M. Azofra, K. Chen, M. Forsyth, D.R. MacFarlane, Ionic liquid electrolytes for reversible magnesium electrochemistry, Chemical communications, 52 (2016) 4033-4036.

[142] J. Zhang, J. Ma, G. Wang, Y. Li, A.A. Volinsky, Electrochemical Performance of 1-Ethyl-3-Methylimidazolium Bis(Trifluoromethylsulfonyl)Imide Ionic Liquid as Electrolyte for Primary Mg-Air Batteries, J Electrochem Soc, 166 (2019) A1103-A1106.

[143] X. Chen, Z. Shi, Q. Le, Q. Zou, N. Yang, M. Zhang, A. Atrens, The feasibility and limitation of urine as the electrolyte for primary Mg-air batteries, Ionics, 27 (2021) 2733-2737.

[144] S.Y. Liew, J.C. Juan, C.W. Lai, G.-T. Pan, T.C.K. Yang, T.K. Lee, An eco-friendly water-soluble graphene-incorporated agar gel electrolyte for magnesium-air batteries, Ionics, 25 (2018) 1291-1301.

[145] D. Snihirova, L. Wang, S.V. Lamaka, C. Wang, M. Deng, B. Vaghefinazari, D. Hoche, M.L. Zheludkevich, Synergistic Mixture of Electrolyte Additives: A Route to a High-Efficiency Mg-Air Battery, The journal of physical chemistry letters, 11 (2020) 8790-8798.

[146] S.Y. Wang, Q. Li, X.K. Zhong, L.Q. Li, F.N. Chen, F. Luo, Y. Dai, H. Gao, F. Liu, H.X. Zhang, Effects of NO−3in NaCl solution on corrosion protection of AZ91D magnesium alloy coated with silane films, Transactions of the IMF, 90 (2013) 78-85.

[147] I.L.M. Emilse M.A. Martini, Characterization of the film formed on iron in borate solution by electrochemical impedance spectroscopy, Corros Sci, 42 (2000) 433-454.

[148] Y. Zhao, G. Huang, C. Zhang, C. Peng, F. Pan, Effect of phosphate and vanadate as electrolyte additives on the performance of Mg-air batteries, Materials Chemistry and Physics, 218 (2018) 256-261.

[149] M. Mayilvel Dinesh, K. Saminathan, M. Selvam, S.R. Srither, V. Rajendran, K.V.I.S. Kaler, Water soluble graphene as electrolyte additive in magnesium-air battery system, J Power Sources, 276 (2015) 32-38.

[150] A. Prabhakaran Shyma, S. Palanisamy, N. Rajendhran, R. Venkatachalam, Enhanced discharge capacity of Mg-air battery with addition of water dispersible nano MoS2 sheet in MgCl2 electrolyte, Ionics, 25 (2018) 583-592.

[151] Y.-C. Zhao, G.-S. Huang, G.-l. Gong, T.-Z. Han, D.-B. Xia, F.-S. Pan, Improving the Intermittent Discharge Performance of Mg–Air Battery by Using Oxyanion Corrosion Inhibitor as Electrolyte Additive, Acta Metallurgica Sinica (English Letters), 29 (2016) 1019-1024.

[152] B. Vaghefinazari, D. Höche, S.V. Lamaka, D. Snihirova, M.L. Zheludkevich, Tailoring the Mg-air primary battery performance using strong complexing agents as electrolyte additives, J Power Sources, 453 (2020) 227880.

[153] L. Wang, D. Snihirova, M. Deng, B. Vaghefinazari, S.V. Lamaka, D. Höche, M.L. Zheludkevich, Tailoring electrolyte additives for controlled Mg-Ca anode activity in aqueous Mg-air batteries, J Power Sources, 460 (2020) 228106.

[154] M.A. Deyab, Decyl glucoside as a corrosion inhibitor for magnesium–air battery, J Power Sources, 325 (2016) 98-103.

[155] P.H. J. Ma, X. Jia, C. Zhanga, G. Wang, Organic/inorganic double solutions for magnesium - air batteries, RSC Advances, 11 (2021) 7502-7510.

[156] J. Ma, X. Jia, M. Ma, C. Zhang, F. Ren, G. Wang, Mg(ClO4)2-N,N-Dimethylformamide (Acetonitrile)/NaCl Double Electrolytes for Magnesium–Air Batteries, Journal of Materials Engineering and Performance, 30 (2021) 1567-1576.

[157] Y.G. D. Aurbach, A. Schechter, O. Chusid, H. Gizbar, Y. Cohen, M. Moshkovich and R. Turgeman, A comparison between the electrochemical behavior of reversible magnesium and lithium electrodes, J. Power Sources, 97–98 (2001) 269–273.

[158] K.W. Leong, Y. Wang, W. Pan, S. Luo, X. Zhao, D.Y.C. Leung, Doubling the power output of a Mg-air battery with an acid-salt dual-electrolyte configuration, J Power Sources, 506 (2021) 230144.

[159] H.C. L. Li, E. He, L. Wang, T. Ye, J. Lu, Y. Jiao, J. Wang, R. Gao, H. Peng, Y. Zhang,, High-Energy-Density Magnesium-Air Battery Based on Dual-Layer Gel Electrolyte, Angew. Chem. Int. Ed, 60 (2021) 15317–15322.

[160] S. Clark, A.R. Mainar, E. Iruin, L.C. Colmenares, J.A. Blázquez, J.R. Tolchard, Z. Jusys, B. Horstmann, Designing Aqueous Organic Electrolytes for Zinc–Air Batteries: Method, Simulation, and Validation, Advanced Energy Materials, 10 (2020) 1903470.

[161] S. Hosseini, S. Masoudi Soltani, Y.-Y. Li, Current status and technical challenges of electrolytes in zinc–air batteries: An in-depth review, Chemical Engineering Journal, 408 (2021) 127241.

[162] T.M. Di Palma, F. Migliardini, D. Caputo, P. Corbo, Xanthan and kappa-carrageenan based alkaline hydrogels as electrolytes for Al/air batteries, Carbohydrate polymers, 157 (2017) 122-127.

[163] C.W. Lee, K. Sathiyanarayanan, S.W. Eom, H.S. Kim, M.S. Yun, Novel electrochemical behavior of zinc anodes in zinc/air batteries in the presence of additives, J Power Sources, 159 (2006) 1474-1477.

[164] M.S. Ghazvini, G. Pulletikurthi, T. Cui, C. Kuhl, F. Endres, Electrodeposition of Zinc from 1-ethyl-3-methylimidazolium acetate-water Mixtures: Investigations on the Applicability

of the Electrolyte for Zn-Air Batteries, J Electrochem Soc, 165 (2018) D354-D363.

[165] X. Hou, Y. Zhang, C. Cui, C. Lin, Y. Li, D. Bu, G. Yan, D. Liu, Q. Wu, X.-M. Song, Photo-assisted Al-air batteries based on gel-state electrolyte, J Power Sources, 533 (2022) 231377.

Chapter II Analytical techniques and experimental conditions

In this chapter, the analytical techniques and experimental conditions will be systematically introduced. Firstly, the design of the Mg-air batteries device (half and full cells) and the electrochemical setup will be shown in detail (section of II-1). The electrochemical measurements such as open circuit potential (OCP), electrochemical impedance spectroscopy (EIS), linear sweep voltammetry (LSV) and galvanostatic discharge have been used in this thesis. The related experimental conditions are described in section of II-2. According to our knowledge, the chemical surface analysis of Mg-based materials used as negative electrodes in Mg-air battery has been rarely reported in literature. However, it should be noted that the knowledge about the chemical composition of the corrosion or discharge products on the surface of Mg anode is very important for the development of Mg-air batteries. The surface analytical technique such as X-ray photoelectron spectroscopy (XPS) is the most adapted and the most frequently used. Time-of-flight secondary ion mass spectrometry (ToF-SIMS) is a complementary method and allows for a fast in-depth chemical characterization of thin layers. The section of II-4 will introduce the working principles of XPS and ToF-SIMS and experimental conditions used in this work.

Surface morphology characterization is an easy way to compare a degradation of Mg anodes induced by corrosion during the electrochemical tests of Mg-air batteries. To do so, scanning electron microscopy (SEM), optical microscope (OM), three-dimensional (3D) laser scanning microscope have been used (section of II-5). The SEM analyzes include the top surface images, cross-sectional and focus ion beam (FIB) SEM. For the insight analysis of the corrosion products of Mg anode in different electrolytes, the TEM analysis has been used (section of II-5). The XRD was only punctually used to analyze the corrosion products, thus, this technique will not be introduced in this chapter.

II-1 Materials

II-1.1 Mg electrode and surface preparation

A plate of pure Mg (≥ 99.9 wt. %, the chemical composition is shown in Table II-1), from a commercial company was cut into several pieces of 15×15×1 mm^3 size. The samples were

ground under water with SiC abrasive papers (#400, #2400, #4000) for the electrochemical measurements and further polished with diamond grinding paste (3, 1 and 0.25 μm) for the surface characterization by X-ray photoelectron spectroscopy (XPS) and time-of-flight secondary ion mass spectrometry (ToF-SIMS). Each sample was rinsed with pure water (resistivity > 18 MΩ·cm) between each step and dried in a flow of compressed air. For the electrochemical tests the samples were only ground with abrasive papers as detailed above.

Table II-1. Chemical composition of the pure Mg (in wt. %).

Chemical Composition (wt. %)										
Mg	Si	Fe	Cu	Mn	Al	Ni	Zn	Sn	Pb	Ti
Bal	0.003	0.002	0.0005	0.002	0.004	0.0005	0.004	0.004	0.001	0.001

II-1.2 Electrolytes

The electrolytes used in this thesis (chapters III, IV and V) are listed in Table II-2.

Table II-2. The chemicals and their corresponding manufactures.

	Chapter III	**Chapter IV**	**Chapter V**
Based electrolyte	0.6 M NaCl / H_2O	0.6 M NaCl / H_2O	0.6 M NaCl / 0.5 M $NaNO_3$ / H_2O
Purity of chemical and supplier	NaCl: AnalaR Normapur, analysis reagent, VMR UP* H_2O: Millipore, resistivity > 18.5 MΩ·cm $NaNO_3$: AnalaR Normapur, analysis reagent, VMR		
Additive (solvent or inhibitor), purity and supplier	Ethanol: > 99.97%, AnalaR Normapur, VMR	Sodium 5-sulfosalicylate acid: Sinopharm Chemical Reagent Co. Ltd	Acetic acid glacial: 100 %, AnalaR Normapur, VMR

* UP ultra pure

II-2 Electrochemical setups

II-2.1 Three-electrode half cell

An EC-Lab SP200 potentiostat (Bio-logic Science Instruments SAS) was used for the OCP, LSV, EIS and half-cell galvanostatic discharge tests. The classical three-electrodes glass cell used for all electrochemical tests was composed of:

- a working electrode (WE): a plate of pure Mg (≥ 99.9 wt. %, with a chemical composition shown in Table II-1), with the area of 1.1 cm^2 delimited by a Viton O-ring,
- a reference electrode (RE): a silver/silver chloride (Ag/AgCl) commercial reference electrode (Radiometer analytical) (similarly to the previous studies [1-4]) composed of a silver wire, immersed in a solution of saturated potassium chloride and silver chloride,
- a counter electrode (CE): a platinum foil with a surface of around 1.1 cm^2; the platinum foil has been chosen instead of a platinum wire in order to minimize the influence of polarization.

II-2.2 Two-electrode full cell

A home-made Mg-air full battery is illustrated in Fig. II-1 a and b. The cell is composed of a Mg anode, an electrolyte (17.5 ml) and an air cathode. It should be noticed that there is no filter material to separate the Mg anode and air cathode because these two electrodes are separated physically by a distance of 5 mm. The following electrodes have been used:

- Mg anode as described above (with the surface of 1.1 cm^2 delimited by a Viton O-ring) with the backside of the electrode connected to a copper foil for the electric contact (Fig. II-1 d).
- an air cathode made of Pt/C (20 wt. % of Pt purchased from Alfa Aesar, France) which was dripped on the surface of commercial air cathode (purchased from Yoteco company, China); the catalyst (Pt/C) loading was 1 mg/cm^2 and the surface area of the cathode was 1.1 cm^2 (the same as the surface of anode), which was embedded by the same size of Viton O-ring used for the Mg anode (Fig. II-1 c).

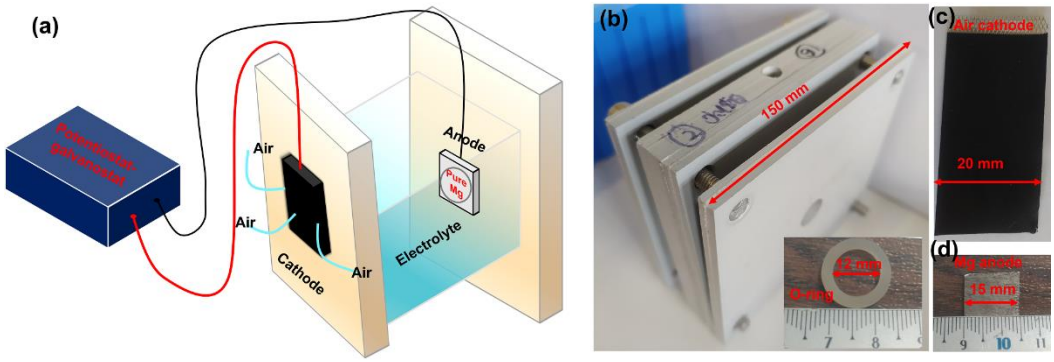

Fig. II-1 (a) Schema of the two-electrode Mg-air battery; (b) home-made device of full Mg-air battery (inset image, Viton O-ring); (c) commercial air cathode; and (d) pure Mg electrode.

II-3 Electrochemical methods

II-3.1 Open circuit potential and H_2 evolution test

a) Open circuit potential (OCP)

The OCP *vs* time refers to the equilibrium potential (also known as the rest potential, or the corrosion potential) between the WE and RE, at which there is no current flow. Although such measurement is very simple, it can be very useful and show the corrosion/electrochemical behavior of the WE. As Mg metal is very active, the OCP measurement is quite meaningful and can reflect differences in the Mg corrosion behavior as a function of the electrolyte. Besides, a more negative OCP of Mg indicates a higher discharge voltage of Mg-air battery [5-8], thus the OCP measurement can be used as a first estimation of the Mg-air battery performance..

b) H_2 evolution test

The Fig. II-2 illustrates a typical homemade H_2 evolution setup. The device comprising an inverted burette with a funnel was used to measure the volume of hydrogen evolution during Mg immersion (area of Mg 1.1 cm^2) in different electrolytes.

The volume of H_2 was measured every 10 min at OCP during 500 min (in Chapters III and IV). The H_2 evolution at OCP can directly reflect the corrosion behavior of Mg anode. In Chapter V, the H_2 evolution was measured under the discharge condition at current density of 5 mA/cm^2. Due to the Mg anode immersion at OCP in the $NaNO_3$ electrolyte (the

experimental electrolyte in Chapter V) a very low volume of H_2 is produced, which leads to a significant experimental error. However, the H_2 evolution test during the galvanostatic discharge conditions was more significant and the results were more reproducible. All experiments were repeated more than three times, and the mean and standard deviation values were calculated.

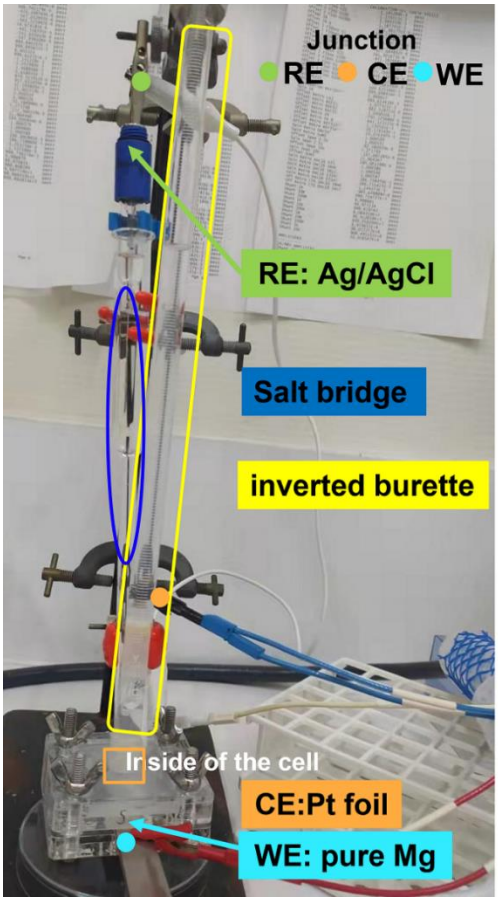

Fig. II-2 Experimental setup for hydrogen evolution measurement.

II-3.2 Electrochemical impedance spectroscopy

The electrochemical impedance spectroscopy (EIS) is a widely used non-destructive method to investigate the corrosion processes or the electrochemical behavior of electrode materials in batteries. The EIS spectra can reflect the interface properties, reaction kinetics, electrolyte resistance by measurements of charge transfer resistance, ohmic conduction, mass transfer, respectively. Additionally, the EIS fitting curve with the suitable equivalent circuit models can illustrate the capacitance of double layer and film resistance.

The EIS spectra are recorded by measuring the cell impedance while applying a periodic small amplitude AC signal at any constant DC potential, over a span of frequencies In this thesis, all of the EIS measurements were performed under a relatively stable OCP. The EIS experiments were performed with the frequency scanned from 100 kHz to 0.1 Hz. They were undertaken after different times of immersion in different electrolytes (specified in each chapter). The obtained EIS spectra were simulated using the EC-lab V11.31 software in Chapter IV and ZSimpDemo 3.3.0d software in Chapter III and V. The reproducibility of the EIS results was verified by repeating each EIS test at least three times.

II-3.3 Linear sweep voltammetry

Linear sweep voltammetry (LSV) is the most used electrochemical techniques for studying the redox reactions. The working potential is swept linearly *vs* time. LSV is a voltammetric method which monitors the current evolution at a working electrode during the change of potential between the working electrode and a reference electrode. At the potential where the species begins to be oxidized or reduced, oxidation or reduction of species is recorded as a peak or trough in the current signal [9, 10]. The LSV, as a potentiodynamic technique, provides useful information such as the corrosion current, the corrosion potential, the polarization resistance.

In the current work, the polarization curves (LSV) were recorded at a scan rate of 1 mV/s from E_{OCP}–0.5 V to E_{OCP} +0.5 V. All experiments were performed after registering stable OCP values (the potential variation of ± 10 mV/hour). EC-lab V11.31 software was used to calculate the corrosion potential and corrosion current densities of Mg anode in different electrolytes.

II-3.4 Galvanostatic discharge test of Mg-air battery

Galvanostatic measurement is based on applying a constant current to the cell (half or full cells) between working electrode and counter electrode to obtain a potential response. As a result, the potential profile *vs* time of discharge or capacity can be obtained. The potential plateaus can be used to analyze the electrochemical process and evaluate the discharge or charge performances. In this work, the discharge performances of the primary Mg-air battery were investigated.

II-3.4.1 Half-cell discharge test

For the discharge performance of half-cell, the conventional tree-electrode cell introduced in II-2.1 was used. The applied current density was usually 2.5, 5, 10, 20 mA/cm^2, more accurate

values are presented in the experimental overviews of the following Chapters III, IV and V. The power density (*P*) can be calculated by the equation (II-1) [11, 12]:

$$P = E\,I \tag{II-1}$$

where the E is the average discharge voltage (V) and the I represent the applied current density (mA/cm^2). Furthermore, the anodic utilization efficiency and specific capacity are the important parameters to estimate discharge performance of Mg-air batteries. The utilization efficiency η (%) and specific capacity Q (Ah/kg) can be calculated by the following formula [13, 14]:

$$\eta = \frac{W_{theo}}{\Delta W} \times 100\% \tag{II-2}$$

$$Q = \frac{I \times t}{\Delta W} \times 1000 \tag{II-3}$$

where ΔW is the practical anode loss mass during discharge test, and it can be measured by the mass of samples before and after discharge test and removal of discharge products. The discharge products can be removed by chromic acid solution (made of 200g/L CrO_3 and 10g/L $AgNO_3$) and the residual discharge products and chromic acid can be further washed by ultrasonic treatment in ethanol. The W_{theo} is the lost mass of theoretical consumption required to transfer charge (g) and it can be calculated using II-4 equation [14, 15]:

$$W_{theo} = \frac{I \times t}{F \times \sum(\frac{xi \times ni}{mi})} \tag{II-4}$$

where the F is Faraday's constant (26.8 Ah / mol), and *xi, ni, and mi* (g / mol) are representing the mass fraction relevant to Mg and each alloying element, number of exchanged electrons and atomic weight, respectively, *I* is the discharge current (A), *t* is the discharge time (h). It should be noticed here that the utilization efficiency, the specific capacity and the loss mass of theoretical consumption were not calculated and presented here due to fundamental character of this research work. However, they should be considered in the future works focused on development of Mg-air batteries.

II-3.4.2 Full-cell discharge test

The discharge tests were performed in a full cell using a home-made full Mg-air battery device (shown in II-2.2). For a reliable comparison of the discharge performance of Mg electrodes, the same thicknesses of Mg plates (15*15*1 mm^3 size) were used in all tests.

The discharge performance of full cells was measured by LAND battery testing system (Landt Instruments Inc., China) at 0.5, 2.5, 5, 10, 20 mA/cm^2 current density (the details of employed current density are further shown in the corresponding Chapters).

II-4 Surface chemical composition

The surface film composition and corrosion products of Mg anode is of great importance to better understand the corrosion of Mg and the discharge behavior of Mg-air batteries as discussed in section of I-3. Here the X-ray photoelectron spectroscopy and time-of-flight secondary ion mass spectrometry are introduced, and the experimental conditions are detailed here.

II-4.1 X-ray photoelectron spectroscopy

The X-ray photoelectron spectroscopy (XPS) is one of the most popular surface analysis techniques with a surface analysis depth of ~10 nm. It is based on the photoelectric effect. It is also called the electron spectroscopy for chemical analysis (ESCA). XPS is a very sensitive surface analysis technique, it can detect all the elements except of H and He, and it can be used for the semi-quantitative analysis with an error below 10%. XPS spectra can provide the information including the chemical state of elements (*e.g.* oxide, metal), the type of bonds and surface composition. XPS is one type of non-destructive analysis techniques expect of the special analysis requirements like the concentration depth profiles using the ion beam etching.

II-4.1.1 Principle of XPS

The photoelectric effect was discovered by Heinrich Hertz [16] and later explained by Albert Einstein [17]. Then, the photoelectric effect was applied in the XPS analysis in the middle 1960s by K. Siegbahn group (University of Uppsala, Sweden). After that, the XPS has been constantly developing and contributing to many great discoveries in surface science.

Fig. II-3 illustrates the schematic diagram of the photoemission process. A photon (energy is

hv) impinges the sample and transfer its energy to an atomic orbital electron in the inner shell, which will produce the emission of the electron with a defined kinetic energy $E_{kin(sp)}$, measured by the XPS spectrometer. A core photoelectron with kinetic energy $E_{kin(sp)}$ can be defined by the following equation [18]:

$$E_{kin(sp)} = hv - E_B - \Phi_{sp} \quad \text{(II-5)}$$

where the *hv* is the energy of incident photon which is caused by the excitation of the equipment (1486.6 eV for Al-Kα and 1253.6 eV for Mg-Kα), E_B is the photoelectron (the binding energy of electron) which relates to the Fermi level of the samples [18], Φ_{sp} is the work function of the spectrometer which is calibrated using gold (this work used Au $4f_{7/2}$) or copper reference [19]. Every element has a set of characteristic peaks with different shapes and intensities in the XPS spectrum, which depend on the different core levels of atoms. Thus, the chemical composition of the sample can be identified. Besides, the relative concentrations of the different compounds can be given based on XPS peak intensities [20].

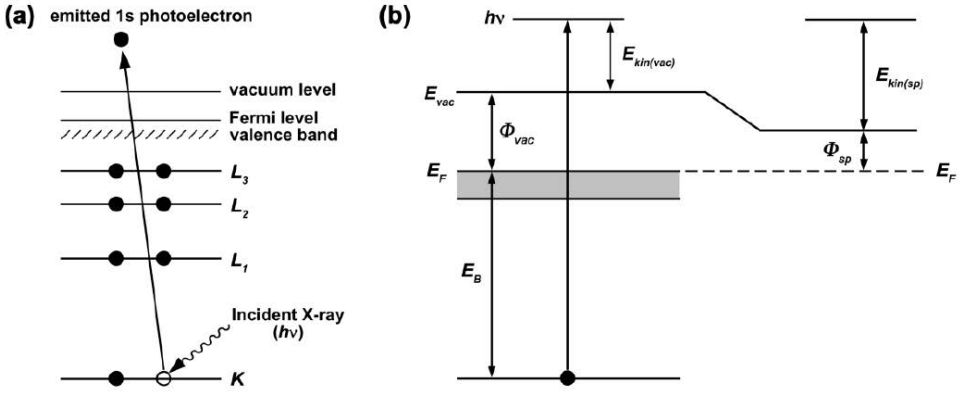

Fig. II-3 (a) Schematic diagram of the photoemission process; (b) and the corresponding energy level diagram [18].

Besides, in other cases an electron jumps and fills the vacancy in the core shell from the outer shell (close to the Fermi level), which ejects an energy that excites the emission of another electron. The ejected electron is called an Auger electron, the Auger process is shown in Fig. II-4.

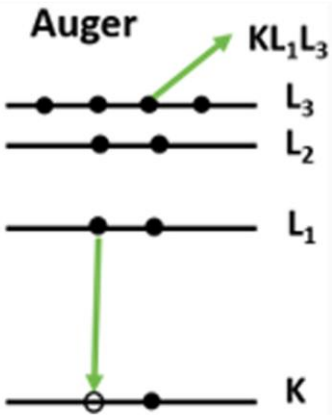

Fig. II-4 Schematic diagram of the Auger process.

II-4.1.2 Thickness and composition calculations

Apart the qualitative information, the semi-quantitative analysis can be performed from the XPS such as the thickness of the surface film and the atomic percentage (ratio) of chemical species.

a) Thickness calculation

In this work, a bilayer MgO/$Mg(OH)_2$ film formation on Mg surface was demonstrated in agreement with the previous studies [21-23]. The oxide surface film consists of a thick external porous layer of hydroxide near to $Mg(OH)_2$, which covers on an inner very thin oxide (MgO). Thus, a bilayer structure model for the thickness of calculations was adopted using the following equation [21, 24]:

$$d = \lambda \sin\theta \ln\left(1 + \frac{I^{ox} D^{met} \lambda^{met}}{I^{met} D^{ox} \lambda^{ox}}\right) \qquad \text{(II-6)}$$

where d is the oxide layer of thickness. It is assumed that the element x is uniformly distributed in both metal (met) and oxide (ox). λ is the inelastic mean free path (IMFP) and it represents the average distance an electron can travel through the material without losing energy. The value of λ depends on the material and the way of the pass which depends on the kinetic energy The values of λ used in this study were assessed by the TPP (Tanuma, Powell, and Perm)-2M formula [25]:

$$\lambda \text{ (IMFP)} = \frac{E}{k_1 \, k_2 \, ln(k_3 E)} \qquad \text{(II-7)}$$

where k_1, k_2 and k_3 are physical parameters and E is the kinetic energy of the photoelectrons and the related values of λ are given in Table II-3. The other parameters are: D — the concentration of the elements or compounds in the matrix and I_{ox} — the intensity of the oxide (ox) in the matrix of the oxide layer (calculated using the equation II-8) [24]:

$$I_{ox} = k\, I_{hv}\, A_\theta\, Y^{ox}\, D^{ox}\, \lambda^{ox} \sin\theta \left(1 - \exp\frac{d^{ox}}{\lambda^{ox} \sin\theta}\right) \exp\left(\frac{-d^{c}}{\lambda^{c} \sin\theta}\right) \qquad \text{(II-8)}$$

where the k is a constant specific of the particular XPS apparatus, I_{hv} is the X-ray intensity at the sample surface, A_θ is the analyzed area and depends on the take-off angle θ (between the sample surface and the direction of the emitted photoelectrons, here in this study $\theta = 90$ °), Y corresponds to the instrument parameters (transmission and detector efficiency) which can be substituted by an experimental photoelectron yield factor. The d^{ox} means an oxide layer of thickness covering a metal substrate and d^{c} is the surface contamination layer.

The I_{met} is the intensity of the photoelectrons emitted by metal in the metallic matrix, which can be expressed as:

$$I_{met} = k_s\, I_{hv}\, A_\theta\, Y^{met}\, D^{met}\, \lambda^{met} \sin\theta \exp\left(\frac{-d^{ox}}{\lambda^{ox} \sin\theta}\right) \exp\left(\frac{-d^{c}}{\lambda^{c} \sin\theta}\right) \qquad \text{(II-9)}$$

b) Composition calculation

The stoichiometry of the compounds can be also calculated. The following equation was used for the calculation of the MgO stoichiometry using the intensity ratio of O 1s and Mg 2p peaks attributed to MgO in the inner part of the surface layer ($R^{O^{2-}\text{in MgO}}_{Mg^{2+}\text{ in MgO}}$):

$$R^{O^{2-} in\, MgO}_{Mg^{2+}\, in\, MgO} = \frac{D^{O^-}_{MgO}}{D^{Mg^{2+}}_{MgO}} = \frac{\lambda^{Mg}_{MgO} T_{Mg} \sigma_{Mg} I^{O^{2-}}_{ox}}{\lambda^{O}_{MgO} T_{O} \sigma_{O} I^{Mg^{2+}}_{ox}} \times$$

$$\frac{1 - exp\left(\frac{-d_{MgO}}{\lambda^{Mg}_{MgO} \sin\theta}\right) exp\left(\frac{-d_{Mg(OH)_2}}{\lambda^{Mg}_{Mg(OH)_2} \sin\theta}\right)}{1 - exp\left(\frac{-d_{MgO}}{\lambda^{O}_{MgO} \sin\theta}\right) exp\left(\frac{-d_{Mg(OH)_2}}{\lambda^{O}_{Mg(OH)_2} \sin\theta}\right)} \qquad \text{(II-10)}$$

The $R^{O^{2-}\text{in MgO}}_{Mg^{2+}\text{ in MgO}}$ value should be theoretically 1 for MgO. σ is the photoionization cross-section, T is a transmission function of the spectrometer, the values of σ and T were given in Table II-3. $I^{O^{2-}}_{ox}$ is the peak area corresponding to oxygen in the oxide layer and $I^{Mg^{2+}}_{ox}$ to the Mg^{2+} in the oxide layer. Furthermore, the stoichiometry of $Mg(OH)_2$ ($R^{O^{2-}\text{in Mg(OH)}_2}_{Mg^{2+}\text{ in Mg(OH)}_2}$) was also calculated using the peak areas of O 1s and Mg 2p corresponding to hydroxide present in the outer hydroxide layer using the equation:

$$R^{O^{2-}\text{in Mg(OH)}_2}_{Mg^{2+}\text{ in Mg(OH)}_2} = \frac{D^{O^-}_{Mg(OH)_2}}{D^{Mg^{2+}}_{Mg(OH)_2}} = \frac{\lambda^{Mg}_{Mg(OH)_2} T_{Mg}\sigma_{Mg} I^{OH^-}_{OH^-}}{\lambda^{O}_{Mg(OH)_2} T_{O}\sigma_{O} I^{Mg^{2+}}_{Mg(OH)_2}} \times \frac{1-\exp\left(\frac{-d_{Mg(OH)_2}}{\lambda^{Mg}_{Mg(OH)_2}\sin\theta}\right)}{1-\exp\left(\frac{-d_{Mg(OH)_2}}{\lambda^{O}_{Mg(OH)_2}\sin\theta}\right)} \quad \text{(II-11)}$$

The theoretical value of this ratio is 2.0. $\lambda^{O}_{MgO}, \lambda^{Mg}_{MgO}$, $\lambda^{O}_{Mg(OH)_2}$ and $\lambda^{Mg}_{Mg(OH)_2}$ correspond to the inelastic mean free paths of photoelectrons emitted by Mg 2p and O 1s core levels in the matrix MgO and $Mg(OH)_2$ given in Table II-3, d_{MgO} and $d_{Mg(OH)_2}$ correspond to the thickness of surface layer of MgO and $Mg(OH)_2$, respectively. If a value is assumed for the quantity of Mg^{2+} in the oxide layer, the value of $I^{Mg^{2+}}_{ox}$ can be calculated by the sum of $I^{Mg^{2+}}_{MgO}$ and $I^{Mg^{2+}}_{Mg(OH)_2}$. Thus, the Mg^{2+} in the $Mg(OH)_2$ layer ($I^{Mg^{2+}}_{Mg(OH)_2}$) can be obtained from the equation:

$$I^{Mg^{2+}}_{Mg(OH)_2} = I^{Mg^{2+}}_{ox} - I^{Mg^{2+}}_{MgO} \quad \text{(II-12)}$$

In theory, the Mg surface film is the bilayer film with the inner MgO and outer porous $Mg(OH)_2$ layer. In practice, the two layers are not ideally distributed in depth and they can be mixed, so the value of $R^{O^{2-}\text{in Mg(OH)}_2}_{Mg^{2+}\text{ in Mg(OH)}_2}$ deviates from 2. The previous results of Marcus's group [22] showed the lower values of the O 1s / Mg 2p ratio varying from 1.82 to 1.87 for Mg immersed in NaCl solution. The different values can reflect the different properties and/or composition of the oxide/hydroxide surface film.

Table II-3. The values of related density elements and the inelastic mean free path (IMFP) used in this work [26].

	IMFP (λ, nm)				Density (mol/cm^3)			σ	T
	met/Mg	into/Mg	into/O	$Mg(OH)_2$/Mg	Mg	MgO	$Mg(OH)_2$		
Mg	2.4	2.6	2.1	4.2	0.07	0.09	0.04	2.93	3349
O						0.09	0.08	0.3335	3435

II-4.1.3 Characterization and experimental conditions

a) Instruments

A Thermo Electron Escalab 250 spectrometer with a monochromated Al Kα radiation (hv = 1486.6 eV) was used for XPS analysis (Fig. II-5 b). A fraction of electrons generated close to the surface leaves the sample into vacuum, then is transferred and collected by the lens system, filtered by a hemispherical sector analyzer and finally recorded by the detector, which measures the electron current as a function of their energy (Fig. II-5 a). As a result, the intensity is plotted *vs* energy as the XPS spectrum.

In current the work, the survey spectra were recorded between 0 and 1350 eV at a pass energy of 50 eV. High resolution spectra were recorded for Mg 2p, O 1s, Cl 2p, C 1s, S 2p, N 1s core levels at pass energy of 20 eV with operating pressure around 10^{-9} mbar. Both spectra (survey and high resolution) were recorded at a take-off angle of 90°. Besides, the spectrometer was calibrated using Au $4f_{7/2}$ at 84.1 eV. Thermo Avantage software (version 5.956) was used for recording and analyzing spectra.

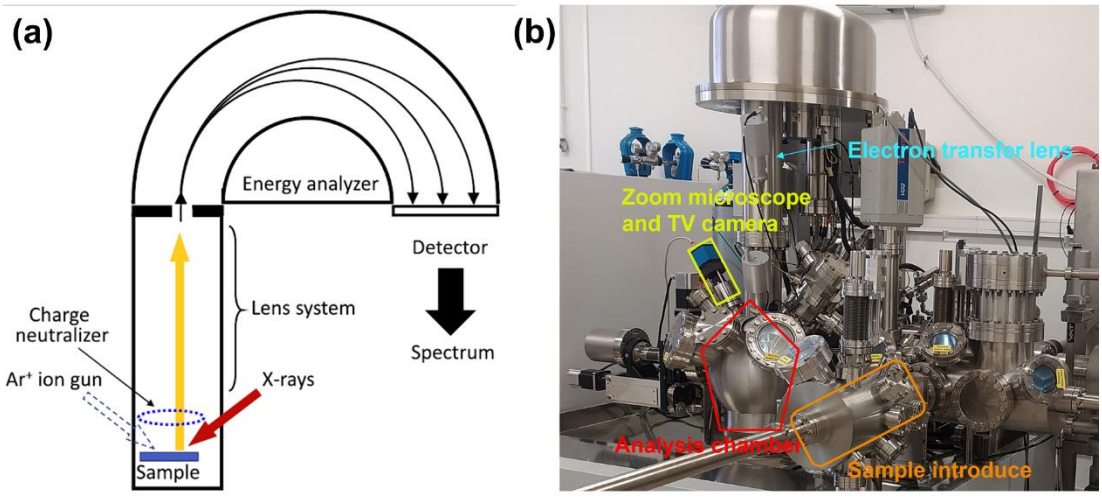

Fig. II-5 (a) The schematic view of the photoelectron spectrometer with the hemispherical

electron energy analyzer; (b) and the photo of the Thermo Electron Escalab 250 spectrometer used in this work.

b) Chemical shift

A chemical shift can be observed in the XPS analysis, which is also called the charge effect. Firstly, the energy levels can be affected by a change of the chemical condition, such as the formation of chemical bonds with other atoms resulting in a change of oxidation state. Normally the binding energy (BE) increase as the elemental oxidation state increases as for some elemental orbitals, such as the O 1s core level of $Mg(OH)_2$ is located at a higher BE than MgO. Secondly, an analyzed atom is more electropositive while the bonded atom is more electronegative, thus the corresponding BE is higher, such as the BE of C-O peak is higher than C-H for C 1s core level.

Besides, the thickness of the oxide surface is also proved to influence the charging effect of BE. Previous works on Mg samples demonstrated that a positive binding energy shift is caused by a charging effect related to formation of a thicker or less conductive surface layer [21, 22].

In this thesis, the binding energy of the elements were corrected using the position of the C 1s signal from hydrocarbons (-CH-CH-) in the contamination layer based on BE of the 286 eV in agreement with the previous study of our group [27].

II-4.2 Time-of-flight secondary ion mass spectrometry

Time-of-Flight Secondary Ion Mass Spectrometry (ToF-SIMS) is a surface analytical technique to analyze the chemical composition of the elements within a solid surface or thin films collecting and measuring the secondary ions with time-of-flight mass analyzer. The ToF-SIMS is a highly sensitive analysis technique which can detect all elements including hydrogen, the detection level can reach ppm of a monolayer for the elements and sub-femtomole for molecules. Besides, the analysis area varies from a few μm to hundreds of μm, and the depth of analysis can be lower than 10 Å. ToF-SIMS can also be used to the elemental or molecular mapping with a high spatial resolution of less than 100 nm, for the new version technology can reached too less than 50 nm..

At the beginning of the 20^{th} century, Thomson [28] observed the release of atoms and ions from a sample surface bombarded with ions. Due to a very fast development of the secondary ion mass spectrometers at that time, Benninghoven [29] has been the first one to be accredited to

develop the ToF-SIMS by introducing a static SIMS, who first achieved chemical analysis of inorganic and organic surfaces and thin films by this technique.

II-4.2.1 Principle of ToF-SIMS

The schematic diagrams in Fig. II-6 illustrate the principle of ToF-SIMS. The primary ion sources normally consist of positive ions of bismuth (Bi_n^+) [30, 31], cesium (Cs^+), oxygen (O_2^+) or negative ions O^- [32, 33] as shown in Fig. II-6 a. As illustrated by Fig. II-6 b combined Fig. II-6 c, a primary ion is employed to bombard the surface of the sample with a kinetic energy of a few keV, and the outermost surface can generate the secondary particles (including electrons, neutral species, ionized atoms, molecules atomic or cluster ions). The secondary ions gain a kinetic energy following the equation:

$$E = qU = \frac{1}{2} mv^2 \qquad \text{(II-13)}$$

where q is the charge of the secondary ions, U is the electric field used to accelerate the produced secondary ions, m and v are the mass and the speed of the secondary ions, respectively. These secondary ions (particles) can be detected and analyzed by a time-of-flight mass analyzer with mass-to-charge ratios [34]. They fly to the detector with a velocity equal to:

$$v = \sqrt{\frac{2qU}{m}} \qquad \text{(II-14)}$$

And the time (t) needed to travel through the analyzer (length L) is a function of the mass of the species, according to equation:

$$t = \frac{L}{v} = L\sqrt{\frac{m}{2qU}} \qquad \text{(II-15)}$$

When the sample is bombarded by the primary ions, the energy can be transferred to the surface by a “collision cascade” sputtering process [35], which happen among the atoms (Fig. II-6 d) [34]. Close to the collision site, the transferred energy is higher than the bonding energy of the molecules and result in extensive fragmentation of molecules and desorption of atoms (or small fragments, as A^+, B^-, C^+ in Fig. II-6 d). But far from the collision site, the transferred energy is

low and can lead to desorption of larger molecular fragments (like AB^+, ABC^+ in Fig. II-6 d) and even of complete molecular species [36]. During the entities desorption process, the charged ions (positively or negatively) are called the secondary ions. The yield secondary ions depend on several factors in the equation described below:

$$I_m^s = I_p y_m \alpha^{\pm} \theta_m \eta \qquad \text{(II-16)}$$

where I_m^s is the secondary ion current of m, the I_p is primary particle flux, y_m the sputter yield, $\alpha^{\pm}$ is the ionization probability to ions (positive or negative), θ_m is the fractional concentration of m species and η is the transmission of the analyzed system.

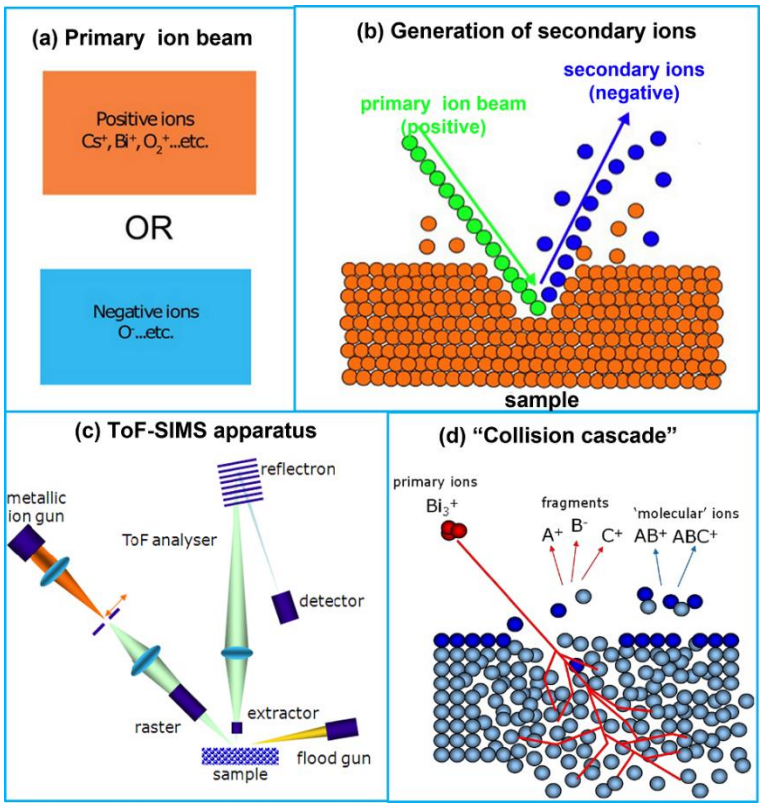

Fig. II-6 (a) The primary ion beam (negative or positive ions) [37, 38]; (b) the primary ion beam strikes the analysis surface during sputtering, producing secondary ions [32]; (c) schema of a ToF-SIMS apparatus [34], (d) "collision cascade" and secondary ion production [34].

II-4.2.2 Characterization and experimental conditions

a) Instrument

In this work, the ToF-SIMS depth profiles were performed using a ToF-SIMS V spectrometer (ION ToF-Munster, Germany, as shown in Fig. II-7) running at an operating pressure of around 10^{-9} mbar. For the analysis a pulsed 25 keV Bi^+ primary ion source delivering a 1.2 pA current was employed over a 100×100 μm^2 area, whereas a 2 keV Cs^+ beam giving a 100 nA target current over 300×300 μm^2 area was used for sputtering. Negative ion depth profiles were recorded due to their better sensitivity to fragments originating from oxides. The Ion-Spec software (version 4.1) was used for data acquisition and processing.

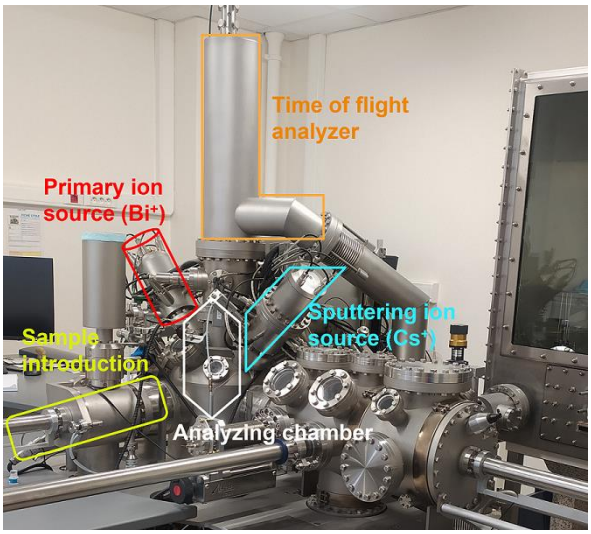

Fig. II-7 The photo of ToF-SIMS V spectrometer used in the current work.

b) Depth profiles

The depth profile combines a static SIMS analysis with a second sputtering beam (such as Cs^+), and a mass spectrum is recorded. The depth profile provides at each level in the sputtered depth, the intensities of selected ions *vs* the sputtering time. Besides the sputtering time can be recalculated to the sputtering depth, and its resolution is less than 1 nm. Thus, the depth profile can provide the information about chemical composition and the ions depth distribution.

In this thesis the commercially available IonToF software was employed to its calibration and data treatment. The negative ions of MgO^-, $MgOH^-$, $MgCl^-$, $MgCO_3^-$, and MgH^- $^{18}OH^-$, $^{18}O^-$, CO_3^-, CO_2^-, were assigned to the oxide film and Mg^- ions were attributed to the pure Mg metallic substrate. The ions of $^{34}S^-$, C^-, Cl^-, NO_2^-, $COOH^-$ were selected for analysis of traces of different electrolytes and their additives (chapter II-V).

II-5. Surface morphology characterization

The morphology characterizations allow to better understand the relationship between the corrosion behavior and performance of Mg as an anode for application in Mg-air batteries. The analyses were performed after immersion and discharge tests in different electrolytes. The main surface morphology analysis techniques are introduced including the scanning electron microscopy (SEM), optical microscope (OM), and three-dimensional (3D) laser scanning microscope.

II-5.1 Scanning electron microscopy

SEM is one of the most widely employed techniques for the surface morphology investigation both in corrosion and battery fields. The cross-sections were also performed using FIB-SEM or mechanical cutting and cross-section polishing.

II-5.1.1 Principle of SEM

SEM uses a focused beam of electrons, also called the primary electrons, which provides energy to the atoms of the sample, which can release secondary electrons. The secondary electron from each point of the sample are collected using a secondary electron detector and form an image [39]. Normally, the electron gun is accelerated by heating or applying high energy in the range from few keV to 50 keV, which produces and emits the primary electrons. Then, these primary electrons are focused and confined to a monochromatic beam by magnetic field lenses and metal slits within a vacuum column [40]. Thus, by scanning coils in a raster pattern with the confined electrons [37, 41, 42], the primary electron beam will interact with the near-surface area of the sample to a certain depth [43]. The SEM system mainly includes the electron gun (thermionic guns and field emission guns) and a column with condenser lens, scanning coil, objective lens, stigmator, sample stage and detector (according to the schema present in Fig. II-8 [44]).

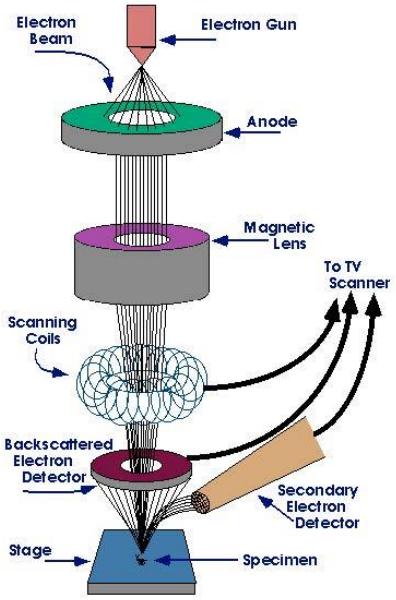

Fig. II-8 Schema of the typical scanning electron microscope (SEM) [44].

Due to Coulomb (electric charge) field interaction of incoming electrons with specimen nucleus and electrons, a variety of signals can be emitted, as shown in the Fig. II-9. These signals include electrons, secondary electrons (SEs, for SEM images analysis), backscattered electrons (BSEs, reflected from the sample by elastic scattering), photons (X-rays, used for elemental analysis) and visible light (cathodoluminescence-CL) [41, 45]. Finally, these signals can be gathered by the detectors (electron collectors), then transformed into images. The secondary electrons are typical for the analysis of the sample morphology and topography and backscattered electrons are normally used to demonstrate the contrasts in multiphase samples composition.

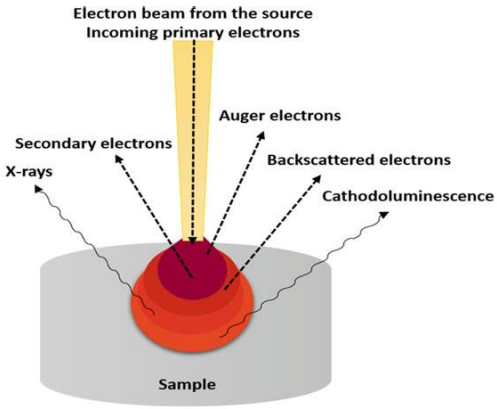

Fig. II-9 Electron–matter interaction volume in the sample and types of generated signals.

II-5.1.2 Instrumentation and experimental conditions

Three different types of emission scanning electron microscope (FE-SEM) were used in this thesis, as shown in Fig. II-10, the main unit was the Zeiss GeminiSEM 500. In this work, the SEM images were performed on the Mg surface with corrosion layer and after removal of the corrosion products by chromic acid (the preparation was described in part of II-3.4.1) to evaluate a degradation of the Mg metallic substrate. Cross-sectional SEM images were obtained by a Zeiss Supra 35. The sample preparation for cross-sectional SEM image was performed by mechanical cutting, then sealing with resin and finally, polishing of the exposed cross-sectional surface with SiC abrasive papers (#400, #2400, #4000). Furthermore, the focused ion beam scanning electron microscope (FIB-SEM) was also used to obtain high resolution cross-sectional SEM images (more information as shown below).

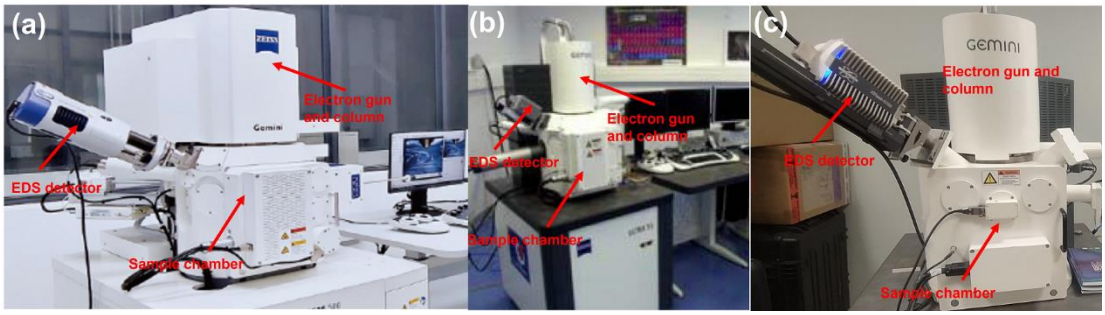

Fig. II-10 FE-SEM used in the current work: (a) Zeiss GeminiSEM 500; (b) Zeiss Ultra 55; (c) Zeiss Supra 35.

II-5.1.3 Focused ion beam scanning electron microscope

As shown in Fig. II-11 a, the ion beam column is fixed at a certain angle relative to the vertical axis of the electron beam. Generally, the ion source is Ga^+ due to its low melting point (29.8°C), low vapor pressure and ease to be distinguished from other elements [46, 47]. The interaction between the target specimen and the Ga^+ ions can offer imaging, milling and deposition. In this study, the milling is used in order to observe the cross-section images of Mg anode. Samples can be microscopically sputtered by ion-atom collisions [48, 49] and if the kinetic energy imparted from an incident ion is sufficient to overcome the binding energy of the target atoms, a surface atom will be expelled [47, 48, 50]. The sputtering rate depends on the accelerating voltage, the angle of incidence and the type of sputtered material [51] [52]. The Fig. II-11 b is

a template image of an Mg anode after the focused ion beam scanning electron microscope (FIB-SEM) analysis.

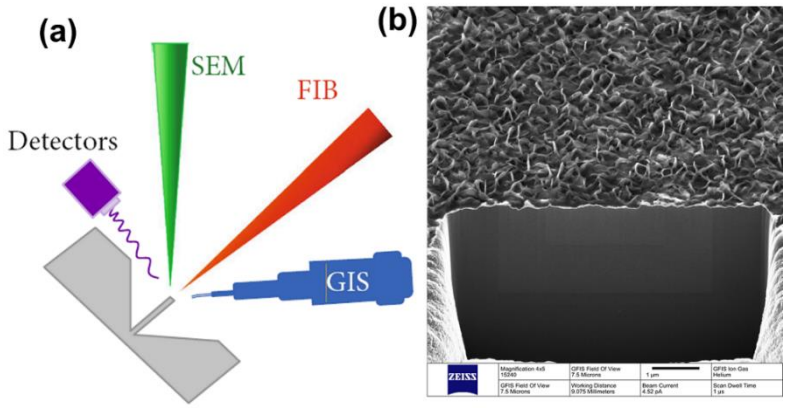

Fig. II-11 (a) Schematic diagram of FIB-SEM system (b) FIB-SEM image of Mg anode.

II-5.2 Optical microscope

Optical microscope (OM) is a type of microscope that uses the visible light and a system of lenses to magnify image of the small specimens. It is one of the most widely used imaging technique due to its great flexibility, reliable design, and low cost. In this work, the surface morphology characterizations of Mg samples before and after electrochemical tests were performed using a digital VHX-500 Keyence optical microscope.

II-5.3 Three-dimensional laser scanning microscope

The three-dimensional laser scanning microscope (3D-LSM) can perform non-contact profile, roughness, and film thickness measurements at a nanometer-level resolution. The working principle of 3D-LSM is based on combination of the white light with the laser light sources, which are used for scanning the sample surface and collect both an optical image and relative high-resolution surface data. The intensity of the returned laser light relative to the z-position of the laser is analyzed, providing the nanometer-level heights. In this work, the three-dimensional laser scanning microscope (VK-X1000 Keyence, Japan) was used to analyze the 3D topography of Mg samples after discharge tests.

II-5.4 Transmission electron microscopy

The high lateral spatial resolution for some of transmission electron microscopy (TEM) instruments can be better than 0.2 nm ‘point-to-point’ thus this microscope can be extremely

powerful to produce high-resolution, two-dimensional images but also to get compositional and crystalline information. TEM technique employs a beam of electrons to transmit through an ultrathin specimen and interact with it resulting in the image formation.

II-5.4.1 Principle of TEM

In TEM, the electron gun emits a focused electron beam to the ultrathin specimen (<200 nm). The signal in the TEM comes from undeflected and deflected electrons penetrating the thickness of the sample. A series of magnetic lenses located at and below the sample position will deliver the signal to a detector (usually a fluorescent screen, a film plate, or a video camera) [53]. Fig. II-12 a illustrates the TEM instrument, showing the principal lenses within a TEM column and the position of specimen. The high spatial resolution of TEM is due to the probe using a highly focused electron beam. The probe can focus on the specimen to a small spot of the size of micron or smaller in diameter. The lateral spatial resolution of TEM instrument can be enhanced by increasing the operating voltage (from 100 kV to 400 kV).

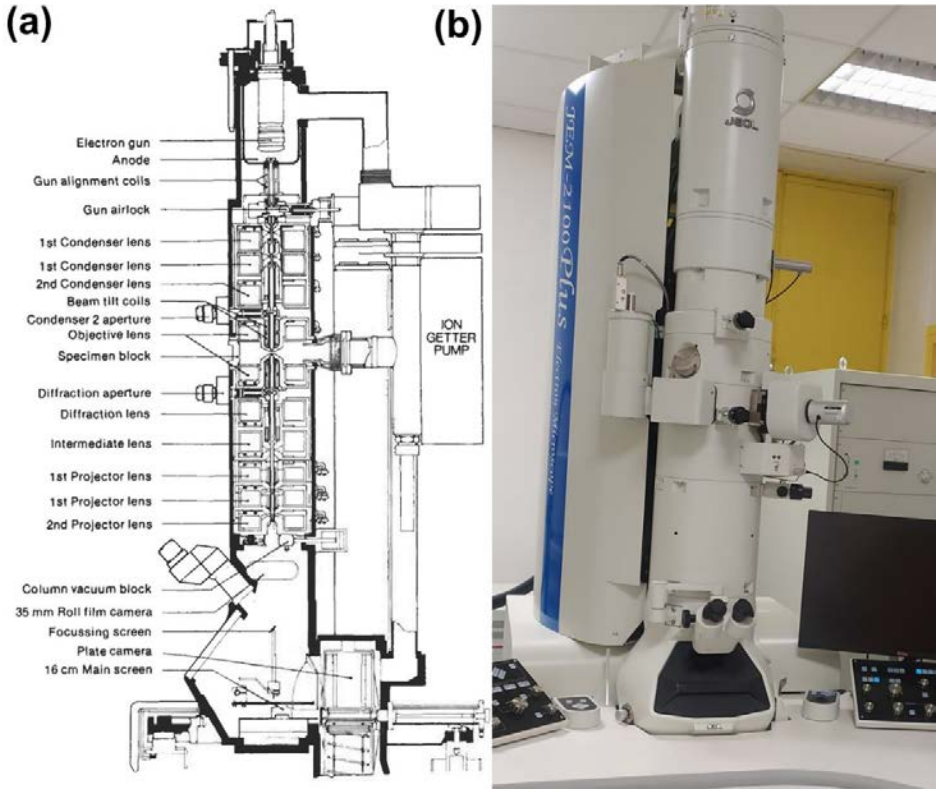

Fig. II-12 (a) Schematic diagram of TEM [53]; (b) JEOL 2100 plus instrument used in the current work.

II-5.4.2 Samples preparation and experimental condition

The ultrathin sample preparation for TEM analysis is very essential. In the current work, the corrosion products of Mg anode after immersion in different electrolytes were scratched by a piece of blade, and then dispersed in the ethanol and loaded on the copper grids. A JEOL 2100 plus transmission electron microscope (TEM) operating at 200 kV (shown in Fig. II-12) was used in the current work.

II-References

[1] X. Zhao, L. Wang, X. Chen, W. Wang, H.L. Xin, X. Du, J. Yang, Ultrafine SmMn2O5-δ electrocatalysts with modest oxygen deficiency for highly-efficient pH-neutral magnesium-air batteries, J Power Sources, 449 (2020) 227482.

[2] K.W. Leong, Y. Wang, W. Pan, S. Luo, X. Zhao, D.Y.C. Leung, Doubling the power output of a Mg-air battery with an acid-salt dual-electrolyte configuration, J Power Sources, 506 (2021) 230144.

[3] M.J. Guangxing Li, Qin Liao, Ruida Ding, Yuanhang Gao, Linwu Jiang, Dina Zhang, Shuguang Chen, Hao He, Directly anchoring Ag single atoms on a-MnO2 nanorods as efficient oxygen reduction catalysts for Mg-air fuel cell, J Alloy Compd, 858 (2021) 157672.

[4] Y. Li, X. Zhang, H.-B. Li, H.D. Yoo, X. Chi, Q. An, J. Liu, M. Yu, W. Wang, Y. Yao, Mixed-phase mullite electrocatalyst for pH-neutral oxygen reduction in magnesium-air batteries, Nano Energy, 27 (2016) 8-16.

[5] L.W. Min Deng, Daniel H¨oche, Sviatlana V. Lamaka, Darya Snihirova, Pingli Jiang, Mikhail L. Zheludkevich, Corrosion and discharge properties of Ca/Ge micro-alloyed Mg anodes for primary aqueous Mg batteries, Corros Sci, 177 (2020) 108958.

[6] X. Liu, J. Xue, P. Zhang, Z. Wang, Effects of the combinative Ca, Sm and La additions on the electrochemical behaviors and discharge performance of the as-extruded AZ91 anodes for Mg-air batteries, J Power Sources, 414 (2019) 174-182.

[7] L. Wang, D. Snihirova, M. Deng, B. Vaghefinazari, S.V. Lamaka, D. Höche, M.L. Zheludkevich, Tailoring electrolyte additives for controlled Mg-Ca anode activity in aqueous Mg-air batteries, J Power Sources, 460 (2020) 228106.

[8] X. Liu, S. Liu, J. Xue, Discharge performance of the magnesium anodes with different phase constitutions for Mg-air batteries, J Power Sources, 396 (2018) 667-674.

[9] R.A.C. Tal M. Nahir, and Edmond F. Bowden, Linear-Sweep Voltammetry of Irreversible Electron Transfer in Surface-Confined Species Using the Marcus Theory, Analytical chemistry, 66 (1994) 2595–2598.

[10] F.J.H. Douglas A. Skoog, Stanley R. Crouch, Principles of Instrumental Analysis. , Cengage Learning (2017) 685.

[11] H.W. Ziyan Li, Junjian Li, Yongpeng Zhuang, Jianzhong Gao, Hang Li, and Weili Cheng, Synergistic Effect of Second Phase and Grain Size on Electrochemical Discharge Performance of Extruded

Mg-9Al-In Alloys as Anodes for Mg-Air Battery, Adv. Eng. Mater., (2020) 1901332.

[12] M.C.LinC.Y.TsaiJ.Y.Uan, Electrochemical behaviour and corrosion performance of Mg–Li–Al–Zn anodes with high Al composition, Corros Sci, 51 (2009) 2463-2472.

[13] Y. Zhou, X. Lu, L. Yang, D. Tie, T. Zhang, F. Wang, Regulating discharge performance of Mg anode in primary Mg-air battery by complexing agents, Electrochimica Acta, 370 (2021) 137805.

[14] B.Y. Bowen Zhang, Wentao Qu, Electrochemical Performance of Mg-air Battery Based on AZ61 Magnesium Alloy with Different Ambient Temperature, Int. J. Electrochem. Sci., 16 (2021) 210258.

[15] F. Tong, S. Wei, X. Chen, W. Gao, Magnesium alloys as anodes for neutral aqueous magnesium-air batteries, Journal of Magnesium and Alloys, 9 (2021) 1861-1883.

[16] H. Hertz, Ueber einen Einfluss des ultravioletten Lichtes auf die electrische Entladung, Annalen der Physik, 267 (1887) 983–1000.

[17] A. Einstein, Über einem die Erzeugung und Verwandlung des Lichtes betreffenden heuristischen Gesichtspunkt, Annalen der Physik, 4 (1905) 132-148.

[18] M.V. Kharlamova, C. Kramberger, Spectroscopy of Filled Single-Walled Carbon Nanotubes, Nanomaterials, 12 (2021).

[19] H. Kuzmany, Solid-State Spectroscopy: An Introduction, Springer, 2nd ed (2009) Berlin/Heidelberg, Germany.

[20] D.G. Briggs, G.T. , Surface Analysis by Auger and X-ray Photoelectron Spectroscopy, IM Publications and Surface Spectra Limited: Chichester, UK, , Perspectives on XPS and AES (2003) 1-30.

[21] M. Santamaria, F. Di Quarto, S. Zanna, P. Marcus, Initial surface film on magnesium metal: A characterization by X-ray photoelectron spectroscopy (XPS) and photocurrent spectroscopy (PCS), Electrochimica Acta, 53 (2007) 1314-1324.

[22] D. Mercier, J. Światowska, E. Protopopoff, S. Zanna, A. Seyeux, P. Marcus, Inhibition of Mg Corrosion by Sulfur Blocking of the Hydrogen Evolution Reaction on Iron Impurities, J Electrochem Soc, 167 (2020) 121504.

[23] D. Hoche, C. Blawert, S.V. Lamaka, N. Scharnagl, C. Mendis, M.L. Zheludkevich, The effect of iron re-deposition on the corrosion of impurity-containing magnesium, Phys Chem Chem Phys, 18 (2016) 1279-1291.

[24] R.H. D. Brune, H. J. Whitlow, O. Hunderi, Surface characterization, Scandinavian Science Publisher, 18 X-ray photoelectron spectroscopy (1997).

[25] C.J.P. S. Tanuma, DR Penn, Calculations of Electron Inelastic Mean Free Paths, Surface and interface analysis, 26 (1993) 165-176.

[26] V. Fournier, P. Marcus, I. Olefjord, Oxidation of magnesium, Surface and Interface Analysis, 34 (2002) 494-497.

[27] M. Santamaria, F. Di Quarto, S. Zanna, P. Marcus, The influence of surface treatment on the anodizing of magnesium in alkaline solution, Electrochimica Acta, 56 (2011) 10533-10542.

[28] J.J. Thomson, XXVI. Rays of positive electricity, The London, Edinburgh, and Dublin Philosophical Magazine and Journal of Science, 21 (1911) 225-249.

[29] A. Benninghoven, Chemical Analysis of Inorganic and Organic Surfaces and Thin Films by Static Time-of-Flight Secondary Ion Mass Spectrometry (TOF-SIMS), Angewandte Chemie International Edition in English, 33 (1994) 1023-1043.

[30] D. Touboul, F. Kollmer, E. Niehuis, A. Brunelle, O. Laprevote, Improvement of biological time-of-flight-secondary ion mass spectrometry imaging with a bismuth cluster ion source, Journal of the American Society for Mass Spectrometry, 16 (2005) 1608-1618.

[31] H. Nygren, K. Borner, B. Hagenhoff, P. Malmberg, J.E. Mansson, Localization of cholesterol, phosphocholine and galactosylceramide in rat cerebellar cortex with imaging TOF-SIMS equipped with a bismuth cluster ion source, Biochimica et biophysica acta, 1737 (2005)

102-110.

[32] E.A. Bonnin, S.O. Rizzoli, Novel Secondary Ion Mass Spectrometry Methods for the Examination of Metabolic Effects at the Cellular and Subcellular Levels, Frontiers in behavioral neuroscience, 14 (2020) 124.

[33] J. Malherbe, F. Penen, M.P. Isaure, J. Frank, G. Hause, D. Dobritzsch, E. Gontier, F. Horreard, F. Hillion, D. Schaumloffel, A New Radio Frequency Plasma Oxygen Primary Ion Source on Nano Secondary Ion Mass Spectrometry for Improved Lateral Resolution and Detection of Electropositive Elements at Single Cell Level, Analytical chemistry, 88 (2016) 7130-7136.

[34] V. Mazel, P. Richardin, ToF-SIMS Study of Organic Materials in Cultural Heritage: Identification and Chemical Imaging, Organic Mass Spectrometry in Art and Archaeology, Chapter 15 (2009) 433-457.

[35] A. Brunelle, D. Touboul, O. Laprevote, Biological tissue imaging with time-of-flight secondary ion mass spectrometry and cluster ion sources, Journal of mass spectrometry : JMS, 40 (2005) 985-999.

[36] A.M. Belu, D.J. Graham, D.G. Castner, Time-of-flight secondary ion mass spectrometry: techniques and applications for the characterization of biomaterial surfaces, Biomaterials, 24 (2003) 3635-3653.

[37] J. Nunez, R. Renslow, J.B. Cliff, 3rd, C.R. Anderton, NanoSIMS for biological applications: Current practices and analyses, Biointerphases, 13 (2017) 03B301.

[38] S. Fearn, Characterisation of biological material with ToF-SIMS: a review, Materials Science and Technology, 31 (2014) 148-161.

[39] S.A.K. Kalsoom Akhtar, Sher Bahadar Khan, and Abdullah M. Asiri, Handbook of Materials Characterization, Springer International Publishing AG, Chapter 4 Scanning Electron Microscopy: Principle and Applications in Nanomaterials Characterization (2018) 113-145.

[40] K. Akhtar, S.A. Khan, S.B. Khan, A.M. Asiri, Scanning Electron Microscopy: Principle and Applications in Nanomaterials Characterization, (2018) 113-145.

[41] A. Alyamani, and Lemine, O. M, FE-SEM Characterization of Some Nanomaterial, Scanning electron microscopy, In V. Kazmiruk (Ed.) InTech. London.

[42] G. McMahon, Analytical instrumentation: A guide to laboratory, portable and miniaturized instruments, Chichester: Wiley. , (2007) (1st ed.p. 296).

[43] J.I. Goldstein, Newbury, D. E., Echlin, P., & Joy, D. C. , Scanning electron microscopy and x-ray microanalysis, (2nd ed.) (1992) New York: Plenum Press.

[44] D.H. Min Deng, Darya Snihirova, Linqian Wang, Bahram Vaghefinazari, Sviatlana V. Lamaka and Mikhail L. Zheludkevich, Magnesium Batteries: Research and Applications, Bibliotheque Sainte Genevieve, CHAPTER 12, Aqueous Mg Batteries (2020) 275-308.

[45] D. Bondeson, Biopolymer-based nanocomposites: Processing and properties. In Department of engineering design and materials Trondheim: Norwegian University of Science and Technology, (2007) p. 114.

[46] L. A. Giannuzzi, Introduction to Focused Ion Beams: Instrumentation, Springer Science & Business Media, in Theory, Techniques and Practice, (2004).

[47] N.Y.a.A. Epstein, Microscopy: Science, Technology, Applications and Education, “Surface nanofabrication using focused ion beam” (2010) 2190–2199.

[48] L. Gu, N. Wang, X. Tang, H.G. Changela, Application of FIB-SEM Techniques for the Advanced Characterization of Earth and Planetary Materials, Scanning, 2020 (2020) 8406917.

[49] C.A.V.a.A.M. Minor, Focused Ion Beam Microscopy and Micromachining, MRS Bulletin, 32 (2007) 389-399.

[50] R. Wirth, Focused Ion Beam (FIB) combined with SEM and TEM: Advanced analytical tools for studies of chemical composition, microstructure and crystal structure in geomaterials on a nanometre scale, Chemical Geology, 261 (2009) 217-229.

[51] S.R.a.R. Puers, A review of focused ion beam applications in microsystem technology, Journal of Micromechanics and Microengineering, 11 (2001) 278-300.

[52] B.T.d.G. N. D. Bassim, A. L. D. Kilcoyne, Keana Scott, Tsengming Chou, S. Wirick, George Cody, and R.M. Stroud, Minimizing damage during FIB-TEM sample preparation of soft materials, Journal of Microscopy, 245 (2012) 288-301.

[53] C.A.E. C. Richard Brundle, Jr., Shaun Wilson, Encyclopedia of Materials Characterization Chapter 2 (1992).

Chapter III Organic/inorganic hybrid electrolyte for enhancing performance of Mg-air batteries

The high self-corrosion rate of Mg in aqueous electrolyte generates H_2, which is the main impediment to restrict the utilization of Mg-air batteries. However, organic/inorganic hybrid electrolyte is prone to reduce the Mg degradation. Herein, the effect of different ethanol fractions in water with 0.6 M NaCl on corrosion behavior of Mg and battery discharge performances is demonstrated. The significant corrosion inhibition in a high content of ethanol (≥ 20 vol. %) in electrolyte is attributed to the formation of a thinner, more corrosion protective layer, enriched in magnesium oxide as demonstrated by scanning electron microscopy, X-ray photoelectron spectroscopy and time-of-flight secondary ion mass spectrometry. Contrarily, in water-based electrolyte a thick, porous and rough layer principally composed of magnesium hydroxide was formed. By varying the ethanol to water fraction in the electrolyte in full battery cells, it is shown that even a small ethanol content (≤ 5 vol. %), can greatly enhance the electrochemical performances of Mg anode. Within several ethanol content, 0.5 vol. % demonstrates the best performances with a limited corrosion rate and greatly improved the discharge performance and the battery lifetime. It is demonstrated here that application of inorganic/organic dual electrolyte is a promising and easy way towards a well-controlled Mg anode reactivity and improved performances of Mg-air battery.

III-1 Objectives and motivation

The influence of electrolyte composition on Mg corrosion is introduced in the section I-3 and I-4.4. To promote a discharge voltage of Mg-air batteries [1-3], the organic additives have been used. So far, very few studies investigated mixed organic-inorganic solvents as electrolytes for Mg-air batteries. Since the proton of ethanol is far less active than that of water, the hydrogen evolution is hindered in this medium. This chapter aims at employing organic (ethanol) / inorganic (water) hybrid electrolyte for Mg-air battery to improve its electrochemical performances.

To do so, a part of water was replaced by ethanol and mixed with 0.6 M NaCl. The influence of high concentration of ethanol (20 vol. %, 60 vol. %) on corrosion properties of Mg were presented in the first part. The XPS and ToF-SIMS were used to study the Mg anode in the electrolyte with and without ethanol. Then, the discharge behaviors of full Mg-air battery with high ethanol concentration and with trace of ethanol are compared. The optimized composition of inorganic/organic dual electrolyte (≤ 5 vol. % of ethanol) is proposed and series of battery tests at different current densities are performed.

III-2 Experimental overview

All details concerning the instruments and experimental conditions were introduced in chapter II. The specific experimental conditions used in this chapter are presented below:

- Electrochemical tests were performed by OCP, LSV and EIS. LSV and EIS were performed after 15 min immersion using a classical 3-electrodes electrochemical cell to study the influence of ethanol concentration (0 %, 20 vol. %, 60 vol. %).
- A hydrogen evolution during Mg immersion in electrolyte with or without ethanol was measured every 10 min at OCP for 500 min.
- The discharge tests of Mg plates (15×15×1 mm^3 size) using LAND battery system were performed using a home-made full Mg-air battery device (present in II-2.2) at 0.5, 2.5, 5, 10 mA/cm^2 current density. It should be noted that the same thickness of Mg plates was used in all tests.
- The surface morphology characterizations were performed by SEM, OM and 3D-LSM. The SEM analyses of Mg samples after the long-time discharge test were performed after removal of the corrosion products by chromic acid.

- The surface chemical composition analyses were performed by ToF-SIMS and XPS for Mg after immersion at OCP for 10 min, and the pristine Mg sample after polishing.

III-3 Results and discussion

III-3.1 Corrosion behavior of Mg in water/ethanol electrolytes

Fig. III-1 a shows the OCP evolution for the pure Mg in 0.6 M NaCl electrolyte as a function of ethanol concentration (0, 20, 60 vol. %). A steep OCP rise (during the first 150 s of immersion), and then an almost steady-state value can be observed for Mg anode in pure water and 20 vol. % ethanol added. The potential increases up to a maximum E_{ds} value which can be defined as the beginning of the formation of dark corrosion spots. The fast potential increase is due to the metal's zero charge potentials that are more negative than their equilibrium potentials, which causes cation adsorption on the electrode surface such as H_3O^+ [4], shifting apparent potential towards a more positive value. In electrolyte with 60 vol. % of ethanol, a more moderate potential increase to E_{ds} (690 s) than in electrolyte without or with 20 vol. % ethanol (150 s) is observed. This indicates that 60 vol. % of ethanol in electrolyte dramatically affects the surface reactivity of Mg, which can be related to the lower reactivity of proton in ethanol than in water. It results in a decreased dissolution of Mg as well as the development of dark corrosion spots.

A slight decrease of potential after dark spots formation (after E_{ds}) and then stabilization at E_{ocp} is noticed. The final E_{ocp} shifts towards negative values with an increase of ethanol concentration (around –15 mV for 20 vol. % and –26 mV for 60 vol. % ethanol) can be attributed to different composition and/or thickness of the surface layer on Mg electrode than those formed in the electrolyte without ethanol. The composition and thickness of the surface layers will be discussed hereafter in section III-3.2.

Electrochemical impedance spectra performed at OCP after 15 min of immersion (at OCP) are shown in Fig. III-1 b, c, d, whereas the equivalent circuits used for fitting are illustrated in Fig. III-1 e. For Mg immersed in electrolyte without and with 20 vol. % of ethanol (Fig. III-1 b), two capacitive loops at the high- and low-frequency range can be distinguished in the Nyquist plots. At the low-frequency range few scattered points can be observed and these data were neglected in the fitting. The presence of two-time constants can be better visible in Bode plots (Fig. III-1 c). The equivalent circuit used for the EIS fitting for these two electrolytes (0 and 20

vol. % of ethanol) is presented in Fig. III-1 e (left-hand). R_s represents the solution resistance. The capacitive loop (CPE_{dl}-double layer capacitance and R_{ct}- charge transfer resistance) at high frequency corresponds to the reactivity in the layer defects at the electrolyte / metallic substrate interface [5-8]. Previous literature studies demonstrated that thick, defective and porous $Mg(OH)_2$ layer can be formed on Mg surface which locally can be coated by MgO layer. The Mg dissolution and formation of Mg^{2+}, occurs in the pores and defects of $Mg(OH)_2$ layer [9]. The second capacitive loop at lower frequencies (in parallel in Fig. III-1 e), with the resistance (R_f) and the capacitance (CPE_f), corresponds to the reactivity of more stable and compact oxide surface film [10]. Depending on the electrolyte used, this layer can be more covering (right-hand schema in Fig. 1e) or less covering showing numerous defect and pores (left-hand schema in Fig. III-1 e). At the lowest frequency range, a poorly resolved inductive loop attributed to the presence of adsorbed corrosion products can be observed [11-13]. However, due to randomly scattered points and difficulties in fitting, this part of the EIS spectra was neglected. A non-ideal capacitive behavior, CPE was adopted for fitting to substitute the capacitor of the electrical double layer (for n equals to 1, the CPE is a pure capacitor) [14, 15]. This deviation from the ideal dielectric behavior can be explained by a heterogenous surface layer formed on the Mg electrode [16-18]. In case of the porous film, a contribution of two capacitances in parallel should be considered. The fraction of the active surface (A) corresponding to the presence of defects and pores in the film plays an important role in the final capacitance value (C), given by Eq. (III-1):

$$C = A \cdot C_{dl} + (1 - A) \cdot C_f \qquad \text{(III-1)}$$

Depending on the film quality, C_{dl} will be predominant for the defective films whereas C_f will be for the better-quality films.

In the case of Mg electrode in 60 vol. % ethanol containing electrolyte, only one capacitive loop in the whole frequency range as shown in the Nyquist plot (Fig. III-1 b) and one time constant in the phase diagram (Bode plot in Fig. III-1 c) can be attributed to the better-quality, more compact and corrosion resistant film. This result can be confirmed by a thorough characterisation of film morphology, structure and composition by ToF-SIMS and SEM shown hereafter in Fig. III-3 and Fig. III-4. Thus, a simplified equivalent circuit (with R_f and CPE_f and predominant contribution of C_f according to Eq. 1) was used for fitting the impedance spectrum

(right-hand schema in Fig. III-1 e [18]) due to a significant activity decrease at the electrolyte / metallic substrate interface ($R_f >> R_{ct}$).

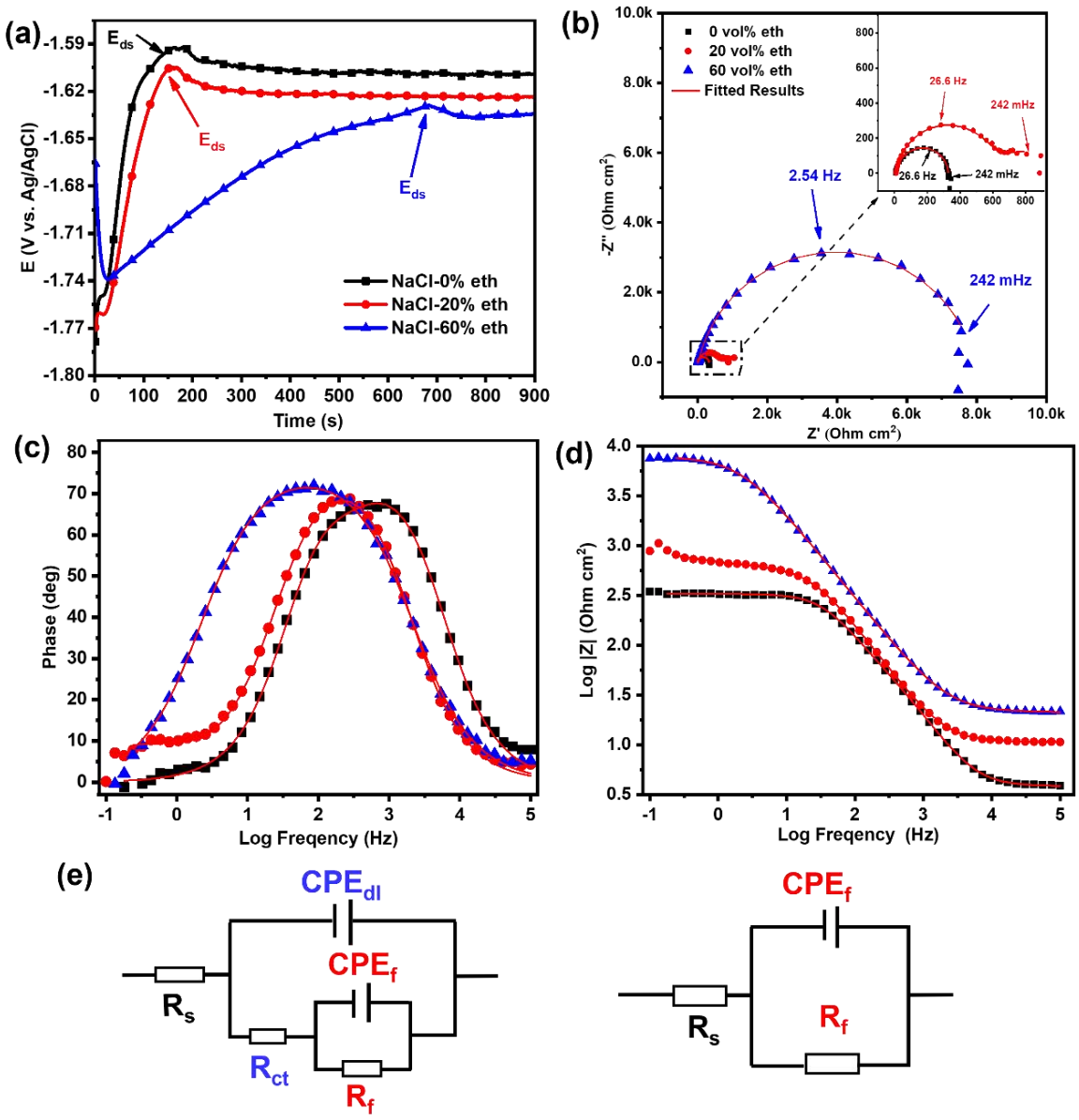

Fig. III-1 (a) Open Circuit Potential (OCP) *vs* time, (b) Electrochemical impedance spectra (Nyquist plots), (c) Bode plots of impedance modulus *vs* log (Freq), (d) Bode plots of phase angle *vs* log (Freq) for Mg samples in NaCl in pure water, 20 vol. % ethanol and 60 vol. % ethanol (e) Equivalent circuits used for fitting impedance spectra obtained for Mg in water and 20 vol. % ethanol (left) and in 60 vol. % of ethanol (right).

The values of fitting parameters are listed in Table III-2. R_{ct} increases a lot with the addition of ethanol (2 times for 20 vol. % ethanol) indicating a decreasing reactivity at the electrolyte / metallic substrate interface. Similarly to R_{ct}, R_f augments from 183 Ω cm^2 in case of electrolyte without ethanol to 393 Ω cm^2 for 20 vol. % and 7917 for 60 vol. % ethanol, which indicates the corrosion inhibition of Mg is markedly improved in the ethanol-containing electrolytes. Besides, the Bode plot in Fig. III-1 d shows that the log $|Z|$ at low frequency increases by 0.5 Ω.cm^2 for 20 vol. % and 1.3 Ω.cm^2 for 60 vol. % ethanol-containing electrolyte, which further confirms that ethanol added to electrolyte facilitates the formation of protective films on the Mg surface. There are very few studies regarding the influence of ethanol or ethanol-water mixed electrolytes on the corrosion of Mg. Compared to blank water, R_s is multiplied almost by ~3 and by ~5 for 20 vol. % ethanol and 60 vol. % ethanol, respectively, meaning that the Mg anode is less conductive in the electrolyte and less electrochemically active (higher R_s). This hypothesis has been previously confirmed by additional SECM experiments allowing to visualize film-free areas over the Mg electrode under immersion in Na_2SO_4 solution [9]. The peak of phase in Bode plots (Fig. III-1 c) moves toward low frequencies and the value of impedance increases with the increase of ethanol fraction in the electrolyte. It further confirms that the corrosion resistance of Mg is higher in the electrolyte containing ethanol.

Table III-2. Parameters obtained from the EIS data fitting for Mg anode tested in 0.6 M NaCl with different fractions of ethanol.

	0 vol. % eth	**20 vol. % eth**	**60 vol. % eth**
R_s (Ω cm^2)	3.8	10.6	21.2
R_{ct} (Ω cm^2)	143	613	-
CPE_{dl} (Ω^{-1} cm^{-2} s^{-1})	13×10^{-6}	16×10^{-6}	-
n_1 (0 < n ⩽ 1)	0.94	0.92	-
R_f (Ω cm^2)	183	393	7917
CPE_f (Ω^{-1} cm^{-2} s^{-1})	9.9×10^{-6}	2.3×10^{-3}	13×10^{-6}
n_2 (0 < n ⩽ 1)	0.97	0.66	0.8

Fig. III-2 a presents potentiodynamic polarization curves obtained for Mg after 15 min of immersion at OCP in 0.6 M NaCl without and with ethanol. The cathodic branch corresponds to the hydrogen evolution reaction according to reaction of III-2,

$$2H_2O + 2e^- \rightarrow H_2 + 2OH^- \qquad \text{(III-2)}$$

and the anodic branch to a dissolution of Mg according to reaction (III-3) [19],

$$Mg \rightarrow Mg^{2+} + 2e^- \qquad \text{(III-3)}$$

However, it should be noted here that hydrogen evolution can also occur during anodic polarisation at active sites of Mg dissolution and it is known as the "anodic hydrogen evolution" [20]. This particular behaviour of Mg is also known as NDE effect [21].

It can be clearly observed that with the increase of the ethanol concentration, the cathodic and anodic current densities decrease, indicating a lower hydrogen evolution and reduced Mg dissolution, respectively. As already mentioned before, the hindered HER in ethanol-based electrolytes may resulted from lower activity of proton in ethanol.

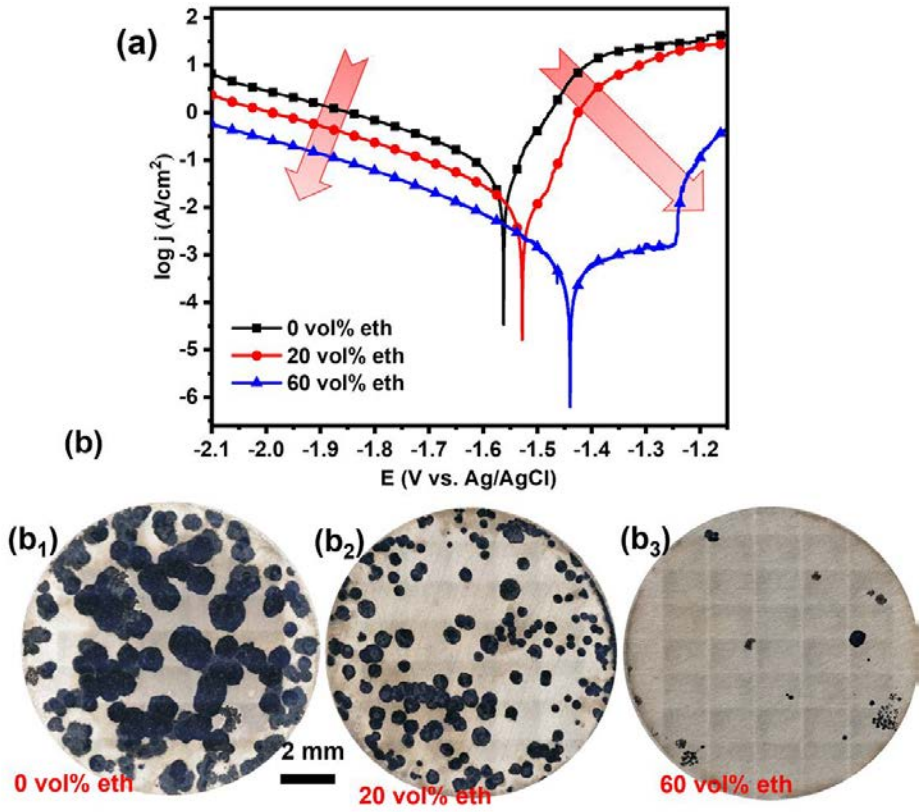

Fig. III-2 (a) Polarization curves of Mg anode in electrolyte of 0.6 M NaCl without or with ethanol (20 vol. % 60 vol. % ethanol) after 15 min OCP, (b) optical microscope images of Mg electrodes after polarization (b_1) without ethanol, (b_2) 20 vol. % ethanol, (b_3) 60 vol. % ethanol.

A dramatic decrease of the anodic current density can be observed in electrolyte with 60 vol. % ethanol. Moreover, a passive domain is observed in the potential range from around –1.4 to –1.25 V. However, above this potential the current density increases rapidly indicating a breakdown of the film and pitting corrosion [22]. It should be noted that the significant decrease of Mg dissolution can lead to the surface lugging by the formation of a corrosion protective layer and thus the activity of Mg as anode in a battery full cell, such as the discharge activity, can be inhibited. A more positive corrosion potential (E_{corr}), a decrease of the corrosion current (I_{corr}) and an increase of polarization resistance (R_p) with addition of ethanol can be observed (Table III-3). It indicates that the corrosion rate is significantly reduced. Moreover, higher R_p implies larger corrosion resistance in agreement with the EIS results (Table III-2).

able III-3. Fitted data of polarization curves of Mg anode in the electrolyte of 0.6 M NaCl with or without ethanol. E_{corr} and I_{corr} with the mean absolute deviation.

	E_{corr} (V)	I_{corr} (µA cm^{-2})	R_p (Ω cm^{-2})
0 vol. % eth	–1.57 ± 0.10	58.1 ± 6.2	296
20 vol. % eth	–1.53 ± 0.02	13.1 ± 3.9	894
60 vol. % eth	–1.42 ± 0.01	0.52 ± 0.1	9763

Fig. III-2 b shows the optical microscopy images of Mg samples after the polarization tests (LSV) in different electrolytes. In electrolyte without ethanol (Fig. III-2 b_1), several large dark spots which cover almost the whole surface can be observed. The size and density of spots decrease with increasing ethanol content in the electrolyte (Fig. III-2 b_2 and b_3). These results are consistent with the polarization and EIS tests and indicate a strong limitation of the growth of dark spots and an effective decrease of the Mg corrosion in electrolyte with ethanol.

Further studies by SEM (Fig. III-3 b) show cracks appearing over the corrosion layer corresponding to the dark corrosion spot on Mg surface exposed to the electrolyte without ethanol. The size of black corrosion spots is reduced to ~1/4 mm^2 for 20 vol. % and few µm^2 for 60 vol. % of ethanol-containing electrolyte (as indicated by the red circle in Fig. III-3 c, d). It was previously demonstrated that the dark areas, assigned to the formation of $Mg(OH)_2$, MgH_2 and/or $MgCl_2$, can catalyse the HER [23, 24], so, this is of great importance to limit their formation.

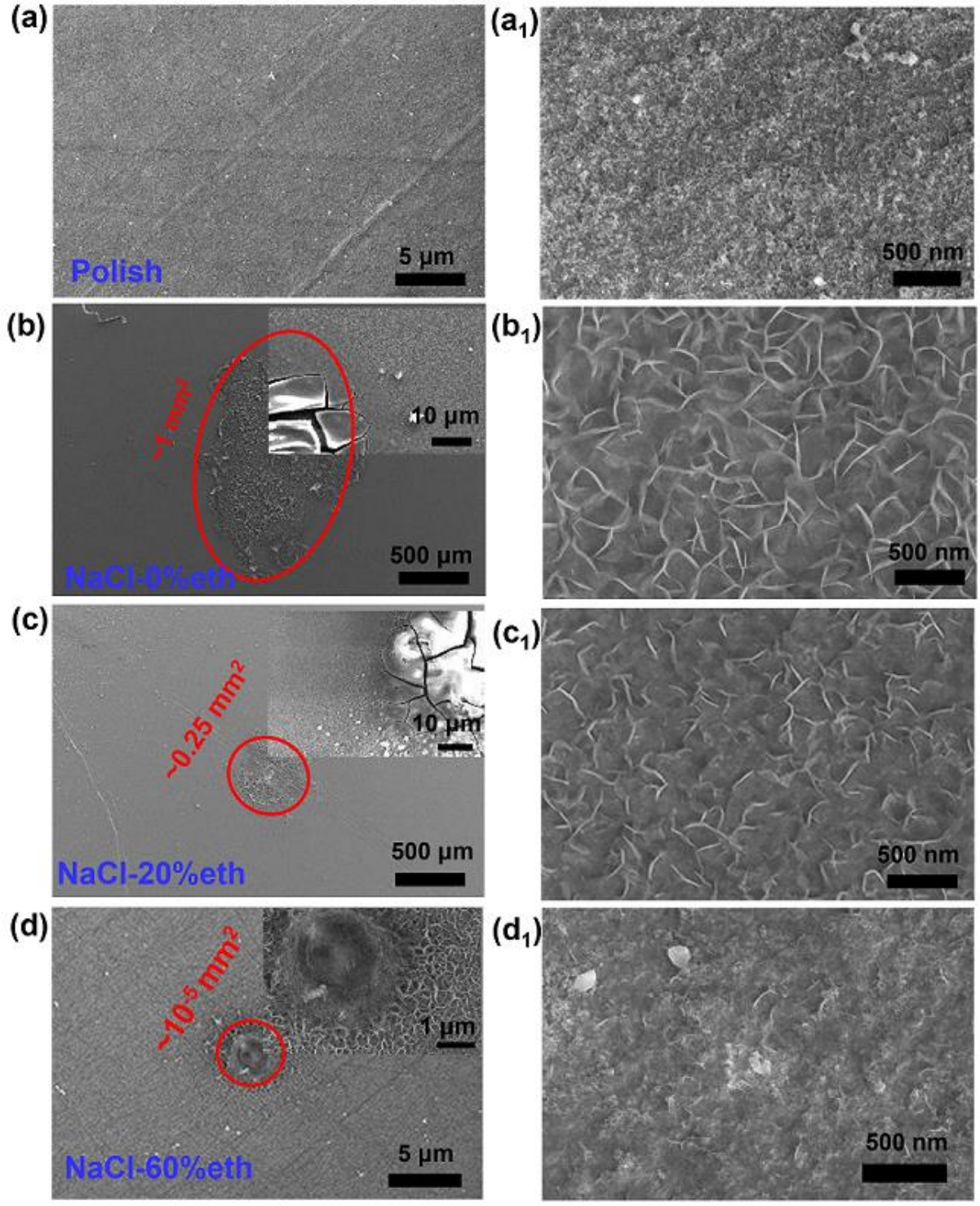

Fig. III-3 SEM images of surface morphologies of Mg anode (a, a1) pristine after polishing, (b, b1); after immersion at OCP for 10 min in 0.6 M NaCl; (b, b1) without ethanol; (c, c1) with 20 vol. % ethanol (d, d1) with 60 vol. % ethanol.

Higher magnification images of areas, out of dark corrosion spots, reveal homogenous flake-like porous structures after immersion in different electrolytes (Fig. III-3 b_1, c_1 and d_1). This typical magnesium oxide-hydroxide morphology was already demonstrated in the literature [25, 26]. A decrease of flake-like porous structure and porosity with increase of ethanol concentration is observed. In 60 vol. % ethanol (Fig. III-3 d and d_1), the surface morphology is similar to the pristine Mg (Fig. III-3 a and a_1). The less and smaller dark spots indicate that the presence of ethanol in electrolyte at sufficiently high concentrations, greatly inhibits the corrosion of Mg and reduces the severe morphological modifications.

III-3.2 Chemical composition of surface layer induced by organic/inorganic electrolyte

To further investigate the influence of ethanol on inhibition of Mg corrosion, chemical surface characterization was performed on Mg anode surfaces (out of dark corrosion spots) by ToF-SIMS negative ion depth profiles (Fig. III-4). MgO^- and $MgOH^-$ ions are characteristic of Mg oxide and Mg hydroxide, respectively. The maximum intensity of $MgOH^-$ signal is observed before MgO^-, indicating a duplex layer structure with an outer Mg hydroxide and an inner Mg oxide layer, as already reported in literature [27, 28]. However, although the duplex structure is clearly visible on pristine sample and on the sample exposed to 60 vol. % ethanol, it is less obvious on samples exposed to pure water and 20 vol. % ethanol. This indicates that high ethanol concentration in electrolyte promotes the Mg oxide formation in the inner layer and inhibits the growth of Mg hydroxide. It should be noted that Mg oxide is known to provide a better corrosion protection than Mg hydroxide [29]. The position of the metal/oxide interface is considered at 80 % of the MgO^- signal intensity decrease. Thus, from the interface position, it can be concluded, that the total oxide-hydroxide layer thickness decreases with increasing ethanol concentration, in the following order: 60 vol. % ethanol < 20 vol. % ethanol < 0 vol. % ethanol. Based on the sputtering rate (0.1 nm/s) estimated from the oxide-hydroxide layer thickness for pristine sample calculated from XPS data (5 nm) [30], the thicknesses for these samples increase respectively, ~17 nm, ~23 nm and ~29 nm. Summarizing, the organic/inorganic hybrid electrolyte has an important influence on the decrease of the quantity of insoluble products formed on the electrode surface as previously demonstrated, [31-33] which can be essential for discharge performance of battery (as discussed in section III-3.3).

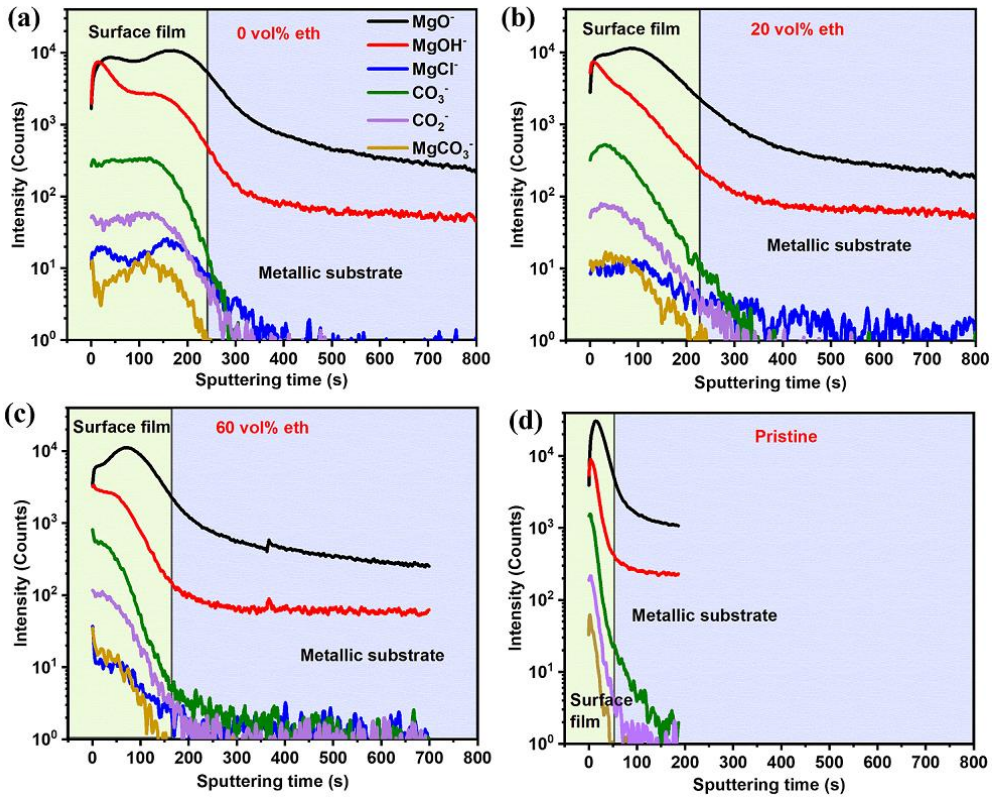

Fig. III-4 ToF-SIMS negative ion depth profiles obtained for Mg (a) after immersion in 0.6 M NaCl without ethanol at OCP for 10 min; (b) with 20 vol. %; (c) 60 vol. % ethanol; and (d) pristine after polishing.

It is worth noting that the $MgCl^-$ profile is similar to MgO^-, which indicates chloride enrichment within the oxide inner layer. Interestingly, with increasing ethanol content, the intensity of $MgCl^-$ signal is slightly reduced, which is consistent with the corrosion decrease. The similar shapes of CO_3^-, CO_2^- and $MgCO_3^-$ signals indicate that carbonates present in the oxide can be attributed to magnesium carbonate. Wang *et al.* have already demonstrated that the carbonates can effectively protect Mg from corrosion [34] while chlorides are highly detrimental to the stability of Mg [35]. However, in cannot be completely ruled out that a small intensity increase of CO_2^- signal with the increase of ethanol concentration originates from decomposition and formation of ethoxy groups. It should be noted that the quantity of carbonates is very low thus it should not be harmful to the efficiency of Mg-air cell.

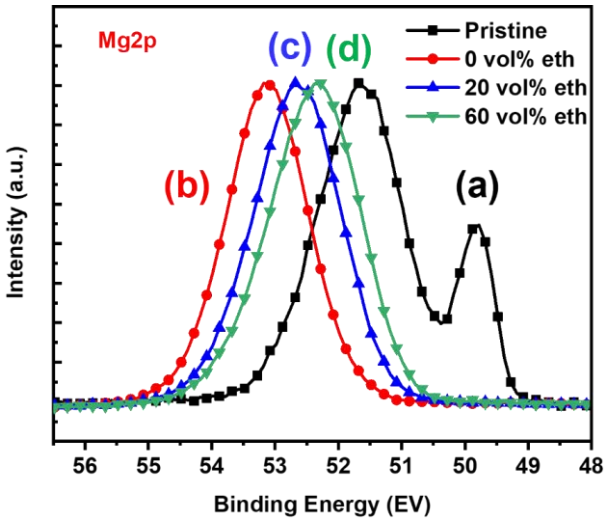

Fig. III-5 XPS spectra of Mg 2p core level for Mg sample (a) Mg pristine after polishing, and after immersion at OCP for 10 min in 0.6 M NaCl (b) without ethanol (c) with 20 vol. % ethanol (d) 60 vol. % ethanol.

The surface chemical composition of Mg electrodes was also analysed by XPS. Mg 2p core level spectra performed on Mg sample after polishing show two peaks at 49.8 and 51.6 eV (Fig. III-5 a), which can be attributed to metallic and oxide/hydroxide, respectively [16, 36]. After immersion in different electrolytes the lower binding energy peak corresponding to the metallic Mg is not detected due to the significant growth of the surface oxide/hydroxide layer and its attenuation. The maximum sampling depth is around 10 nm, which indicates at least the minimum thickness of the layer formed on Mg anode. Only one large peak corresponding to oxide-hydroxide layer is observed (Fig. III-5 b, c and d). This peak shows a shift towards lower binding energy of around 1.6 eV, 1.1 eV and 0.7 eV for 0 vol. %, 20 vol. %, and 60 vol. %, respectively. The positive binding energy shift is caused by charging effect related to the formation of a thicker or less conductive surface layer, as demonstrated in previous works [28, 36]. The thickness growth as a function of the increased ethanol fraction in electrolyte was already demonstrated by ToF-SIMS depth profiles (Fig. III-4). In order to discriminate different species, the fitting of Mg 2p and O1s core level peaks (shown in Fig. III-6) was performed and resulted in presence $Mg(OH)_2$ and $MgCO_3$ [37, 38]. The binding energies and the atomic percentages (calculated from Mg 2p and verified by O 1s peak) of corresponding species are depicted in Table III-4. The presence of very low quantities of MgO or MgOOH species cannot be completely ruled out but the peaks corresponding to these species were not included in the

fitting. In order to correctly assign the magnesium hydroxide, the OH/Mg ratio was calculated from intensities of O 1s (attributed to -OH) and Mg 2p peaks (Fig. III-6), and using the formula presented in previous work [25]. The inelastic mean free paths of the photoelectrons emitted by the O 1s and Mg 2p core levels in the matrix $Mg(OH)_2$ were respectively $\lambda_{O1s}^{Mg(OH)2}$ = 2.4 nm and $\lambda_{Mg2p}^{Mg(OH)2}$ = 4.2 nm [28, 36, 37]. The OH/Mg ratios are 1.89, 1.81 and 1.60 for Mg in electrolyte with 0 vol. %, 20 vol. %, and 60 vol. % ethanol, respectively. The slight decrease of OH/Mg ratio with increasing ethanol fraction is consistent with hydroxide impoverishment on Mg anode surface [39] as already demonstrated by ToF-SIMS results.

Table III-4. Binding energies of Mg 2p, O 1s (eV) for $Mg(OH)_2$ and $MgCO_3$.

Peaks	Species	Binding energy (eV)
O 1s	OH^-	531.8 ± 0.1
	CO_3^{2-}	532.9 ± 0.1
Mg 2p	$Mg(OH)_2$	50.1 ± 0.1
	$MgCO_3$	51.1 ± 0.2

Very low quantity of $MgCO_3$ was detected on the Mg surface after immersion in water-based electrolyte albeit the significant increase from 3 to 26 at. % is observed with increasing ethanol concentration (as shown in Table III-5). Thus, it can be then confirmed that the addition of ethanol induces the surface modifications and favors $MgCO_3$ formation leading to the corrosion inhibition of Mg. The changes in surface reactivity could be also deduced from much lower contact angles measured for samples in the ethanol-rich solvents [40] as shown in Fig. III-S2. This better surface wettability may lead to more efficient surface cleaning and, and in the following stages, to formation of a layer enriched in oxides with a more compact morphology and/or modified thickness as evidenced above by chemical and microscopic analyses.

Table III-5. Atomic % of magnesium compounds calculated from XPS (Mg 2 p) for Mg samples exposed to 0.6 M NaCl electrolyte with different concentration of ethanol.

		Atomic %		
		0 % ethanol	**20 % ethanol**	**60 % ethanol**
Mg 2p	$Mg(OH)_2$	97	93	74
	$MgCO_3$	3	7	26

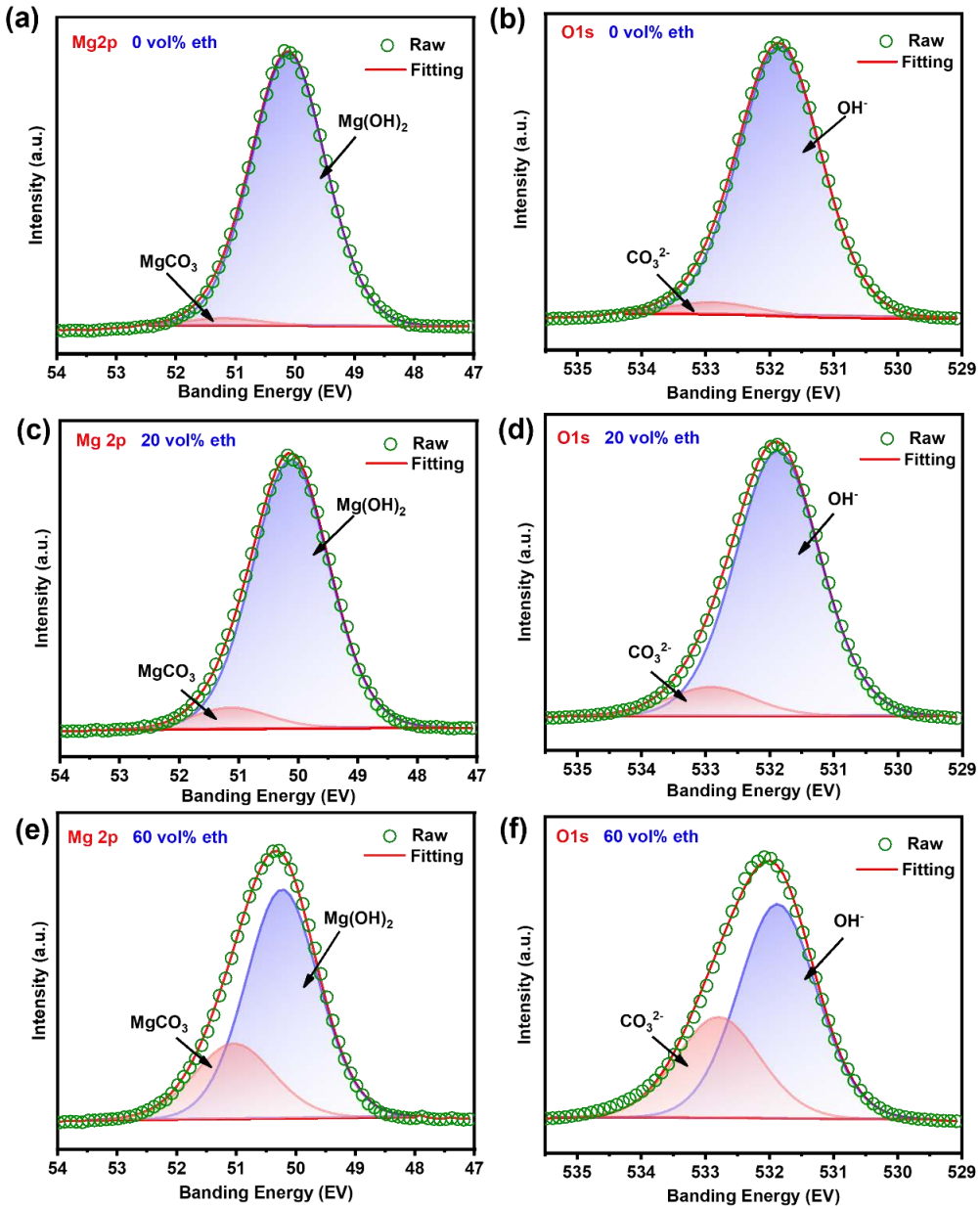

Fig. 6 XPS spectra of Mg 2p and O1s core levels for Mg anode after 15 min OCP test in 0.6 M NaCl with (a) (b) 0 vol. % ethanol; (c) (d) 20 vol. % ethanol; and (e) (f) 60 vol. % ethanol.

III-3.3 Influence of organic/inorganic electrolyte on discharge behavior of full Mg-air battery

The full Mg-air battery discharge tests were performed as a function of time and current densities in various ethanol contents in electrolyte (Fig. III-7). Contrary to the desired result, lower discharge voltage was obtained (Fig. III-7 a) in high-volume concentration of ethanol (20

vol. % and 60 vol. %) compared to blank water-based electrolyte at current density of 0.5 mA/cm^2. With the higher current densities (not shown here) even the lower discharge voltages were observed, which can be attributed to the formation of a blocking layer, hindering the Mg anode reactivity. The formation of a compact, corrosion-protective layer enriched in MgO was discussed and evidenced above by EIS, and ToF-SIMS results. Although the corrosion of Mg can be significantly inhibited in water-ethanol mixed solvent, the high ethanol contents in electrolyte (>20 vol. % of ethanol) are detrimental to the discharge potentials and thus are not suitable for application in Mg-air batteries. A balance between the formation of passivating layer not declining the anodic reaction kinetics and the best discharge performance is compulsory.

After several supplementary tests of much lower ethanol to water fractions (< 5 vol. % of ethanol) as presented hereinbefore by corrosion and surface analyses, it can be concluded that these low concentrations have significant impact on discharge voltage (Fig. III-7 b) and degradation of Mg anode. The discharge voltages reach stable values at around 1 hour. Notably, in electrolyte without ethanol, the discharge voltage declines after 9 hours indicating the failure of Mg anode with the serious black corrosion spots and holes observed after the cell disassembling. With 0.25 vol. % ethanol, the discharge time can be extended up to 13 hours before the end of life of Mg anode. However, in electrolytes with 0.5-5 vol. % ethanol superior voltages (~1.7 V) and better stability after long time (~15 hours) discharge tests. Among them, the highest voltage of around 1.76 V can be noticed for 0.5 vol. % ethanol, which indicates that this is the best organic/inorganic content ratio. The enhanced anode lifetime and working voltage can be attributed to the formation of protective layer not hindering the Mg anode reactivity as discussed above. For these reasons, 0.5 vol. % ethanol was used in further battery discharge tests (Fig. III-7 c) using different current densities (from 0.5 mA/cm^2 to 10 mA/cm^2) and the performances were compared to the electrolyte w/o ethanol. The discharge voltages decrease with increasing current densities in both electrolytes, however, the values are higher (+120 mV at 0.5 mA/cm^2, +150 mV at 2.5 mA/cm^2 and +140 mV at 5 mA/cm^2) in electrolyte with 0.5 vol. % ethanol. Only at the highest current density of 10 mA/cm^2, the discharge voltage in ethanol-containing electrolyte decreases more rapidly and shows even a slightly lower value than in the electrolyte without ethanol. This indicates that ethanol can significantly improve the cell discharge properties at wide range of current densities, but can have some limits in application at much higher current densities (*e.g.* > 10 mA/cm^2). A good stability of the high

discharge voltage can be also observed during the longer battery discharge test at elevated current density (5 mA/cm^2 in Fig. III-7 d). These phenomena are related to the organic-inorganic electrolyte, in which, the layer formed on the Mg surface is thin but stable enough to inhibit the Mg corrosion and at the same time allow for a good Mg reactivity.

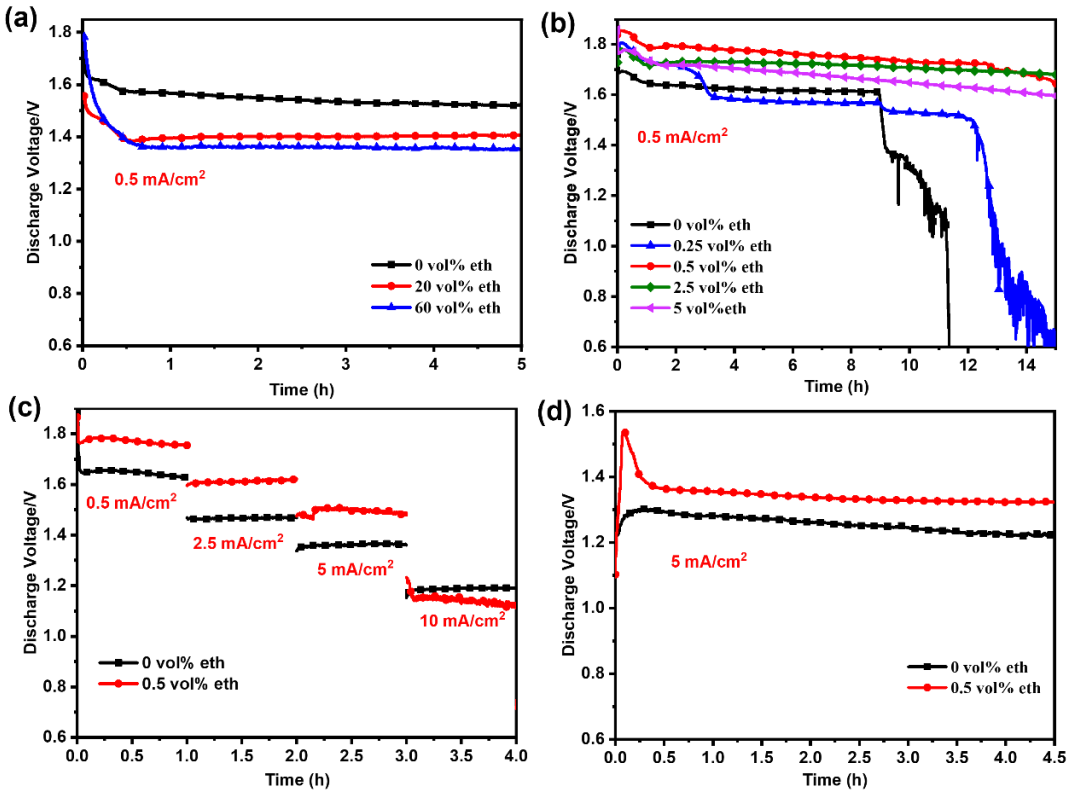

Fig. III-7 Discharge tests of Mg-air battery cell performed in 0.6 M NaCl-based electrolytes (a) with the high ethanol content (≥ 20 vol. %); (b) with low ethanol content (≤ 5 vol. %); (c) at current densities of 0.5, 2.5, 5, 10 mA/cm^2 during 1 h in 0 and 0.5 vol. % of ethanol; and (d) at currrent density of 5 mA/cm^2 during 4.5 h in 0 and 0.5 vol % of ethanol.

III-3.4 Influence of low fraction of ethanol on Mg corrosion

The hydrogen evolution test can be useful in rough estimation of corrosion rate and degradation of Mg anode [41, 42] as discussed in section III-3.1. Notably, a very fast increase of hydrogen evolution is observed in water-based electrolyte while much slower in electrolyte with low fraction of ethanol (0.5 vol. %), with a total mean value of 38.5 ml and 7.7 ml of H_2 during 500 min of immersion, respectively (Fig. III-8). It indicates that ethanol efficiently inhibits the

hydrogen evolution, which can be explained by a lower proton reactivity in ethanol than in water-based electrolyte. Concomitantly, the corrosion rate of Mg is significantly decreased. These results clearly confirm a much better behaviour and prolonged discharge time of Mg-air battery (showed in Fig. III-7 b).

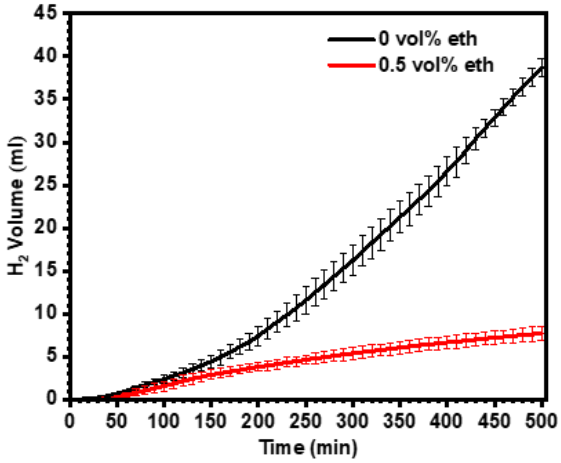

Fig. III-8 H_2 evolution in 0.6 M NaCl-based electrolytes with and without 0.5 vol. % ethanol at OCP for 500 min.

III-3.5 Surface morphological analysis of Mg electrodes after discharge tests

In order to better understand the influence of ethanol on discharge performance, surface morphologies of Mg anode after discharge tests for 15 min, 40 min and 12 hours in electrolytes without or with 0.5 vol. % ethanol at a current density of 0.5 mA/cm^2 were analysed by SEM (Fig. III-9). The Mg anode is less damaged when ethanol is added, which corresponds to the longer discharge time (Fig. III-7 b). ToF-SIMS depth profiles performed on Mg anodes after 15 minutes discharge in these two electrolytes (Fig. III-S1) do not show significant differences in surface modifications. For longer discharge times the surface is too damaged to be characterized by a surface sensitive technique such as ToF-SIMS. After discharge in electrolyte without ethanol, the surface of Mg anode is significantly deteriorated showing the important fraction of surface covered by black corrosion products (Fig. III-9 a) in comparision to the Mg anode discharged in electrolyte with ethanol (Fig. III-9 b). The amount of discharge products observed to the naked eye significantly increases with time of discharge and covers almost entirely the surface of anode (> 40 min). Thus, for longer discharge times, the surface corrosion products were removed by chromic acid (as described in the experimental overview section of III-2).

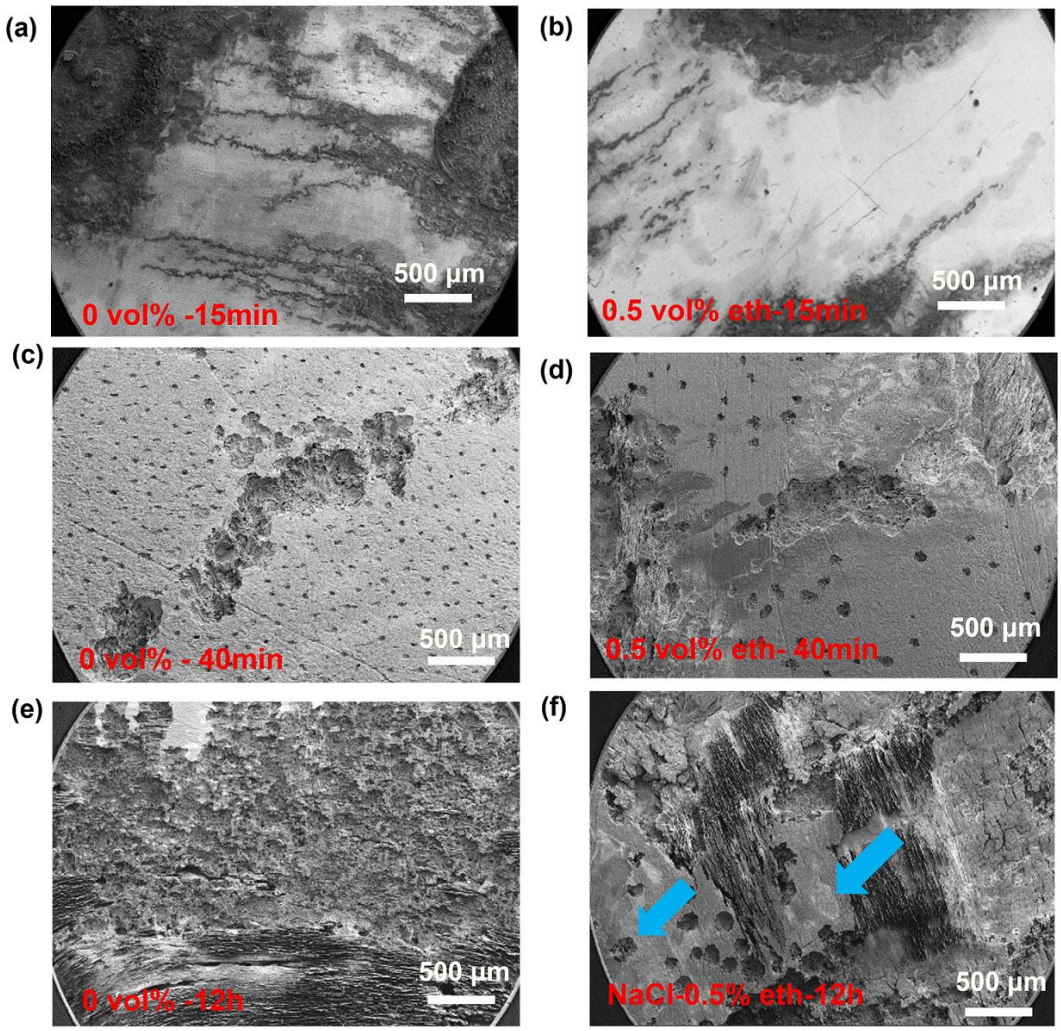

Fig. III-9 SEM images of Mg anode after degradation induced by different times of discharge at current density of 0.5 mA/cm^2 in 0.6 M NaCl without (a, c, e) or with 0.5 vol. % ethanol (b, d, f): (a) and (b) before removal of corrosion products after 15 min of discharge; after removal of corrosion layer products by chromic acid; and (c) and (d) after 40 min of discharge; (e) and (f) after 12 hours of discharge.

It can be easily noticed that a higher number of corrosion pits in metallic Mg substrate can be observed in blank NaCl electrolyte (Fig. III-9 c) than in electrolyte with ethanol (Fig. III-9 d). Degradation of Mg metallic substrate is even more significant after 12 hours of discharge in the electrolyte without ethanol (Fig. III-9 e), than in the ethanol-containing electrolyte, where the areas of apparently non-intact mettalic substrate are still visible (marked by blue arrows in Fig. III-9 f). Theses results indicate that ethanol can efficiently decrease the corrosion and improve the utilization efficiency of Mg anode in full Mg-air batteries. The SEM results agree with 3D

laser microscope analyses showing much flatter surface topography and lower roughness (Fig. III-S3) when ethanol is used (which can be deduced from lower peaks to valleys heights of around 195 ± 1.5 µm for ethanol-based *vs* 382.5 ± 60.5 µm for water-based electrolytes). Apparently, the addition of ethanol reduces the number and the depth of corrosion pits, as observed by SEM, avoids a perforation of Mg plate, and consequently, prolongs the Mg-air battery lifetime, as can be proved by the discharge test demonstrated in Fig. III-7 b.

III-4 Conclusions

This study aimed at investigating the influence of ethanol concentration in water solvent with 0.6 M NaCl on the corrosion behavior of Mg electrode and discharge performances of Mg-air battery. To better understand the influence of ethanol, the surface composition and morphology of Mg anode were thoroughly investigated. The results have shown that the Mg anode surface in high volume ratio of organic (ethanol) to inorganic (water) agents is much less destroyed, and its electrochemical properties significantly optimized. Meanwhile, it was demonstrated that the formed corrosion layer has a lower thickness, is less porous and denser and that the quantity of $Mg(OH)_2$ decreases, which is beneficial to corrosion behavior. Moreover, the corrosion inhibition was also attributed to higher quantity of $MgCO_3$ as demonstrated by XPS and ToF-SIMS. However, to improve the kinetics and reactivity of Mg anode in full battery cells the composition and properties of the passivating layer should be optimized. The high concentration of ethanol in the range of tens of percent (≥ 20 vol. %) demonstrated a lower discharge voltage, which was attributed to formation of the blocking surface layer leading to slower reaction kinetics. The following battery tests in electrolyte with a low quantity of ethanol (≤ 5 vol. %) showed to have a beneficial effect on the discharge voltage and the prolonged battery life. A significant inhibition of Mg anode corrosion at this low-content ethanol (0.5 vol. %) electrolytes was confirmed by a remarkable decrease of H_2 evolution. These results, taken together, suggest that using organic/inorganic agents the reactivity of Mg-based anode can be better controlled leading to improved performances of Mg-air batteries.

III-5 Supplementary information

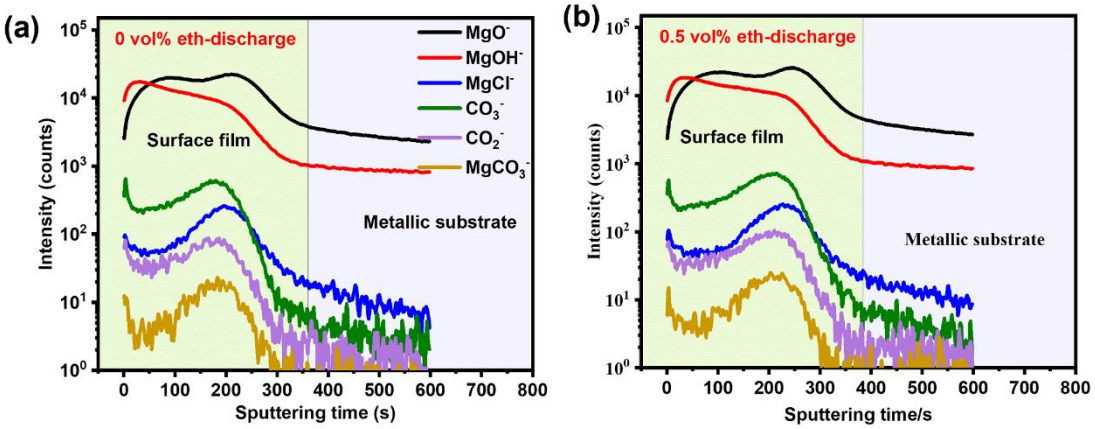

Fig. III-S1 ToF-SIMS depth profiles of the passive film formed on Mg anode surface (a) without ethanol; (b) with 0.5 vol. % ethanol after discharge test for 15min.

III-5.1 Static contact angle

Mg surface wettability in different solutions was investigated by contact angle measurements, as shown in Fig. III-6. Owing to the hydrophilic properties of ethanol solvent, the contact angle on Mg samples decreases from 67° to 30° for water and water-ethanol mixture electrolytes. To simulate the working environment of magnesium air batteries, the contact angle of different electrolyte droplets on Mg samples were tested using 0.6 M NaCl in pure H_2O and with addition of 0.5 vol. % and 50 vol. % ethanol as (Fig. III-6 d, e, f, respectively). With addition of 0.5 vol. % ethanol, the contact angle decreases from 66° to 45° and is even reduced to 38° when 50 vol. % ethanol is added to the electrolyte. The surface tension of a solvent on a solid substrate is affected by its dielectric constant. A broader difference between the dielectric constants of the solvent and the solid implies a higher surface tension between the phases, resulting in a bigger contact angle of liquid on solid's surfaces [43]. The relative static permittivity of water, ethanol and MgO are 80.1, 25.3, and 9.8, respectively. This can explain the strong decrease of the contact angle when ethanol is added to the electrolyte. As observed on the optical images (Fig. III-2 b), a smaller diameter of dark spots is observed on the Mg surface exposed to electrolyte with ethanol addition. This is attributed to the surface wetting of different electrolyte on Mg. The lower contact angle of electrolyte with ethanol on Mg could decrease the time of full infiltration and the electrolyte can be more homogeneously dispersed over the Mg surface.

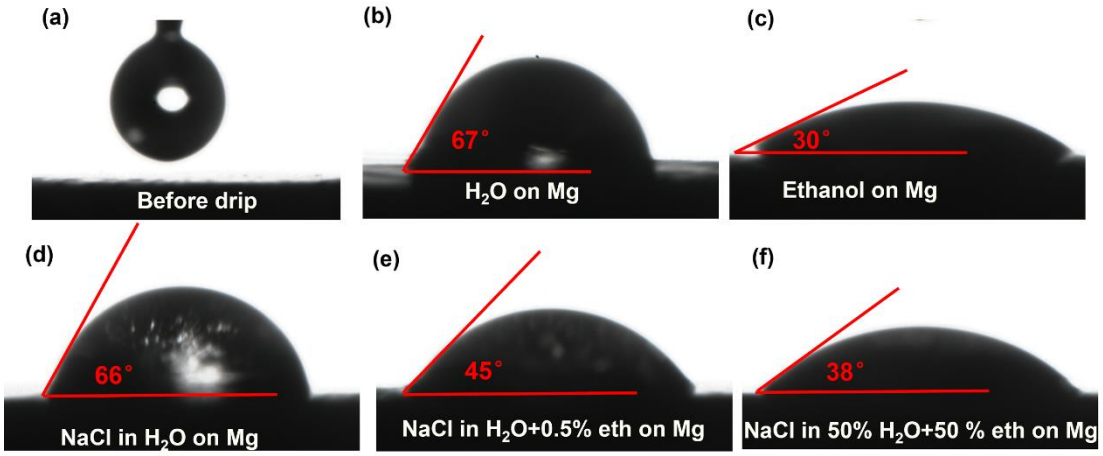

Fig. III-S2 Contact angle measurements on polished Mg samples for (b) pure H_2O, (c) pure ethanol, and electrolyte of 0.6M NaCl in (d) H_2O (e) 0.5 vol. % ethanol (f) 50 vol. % ethanol droplet.

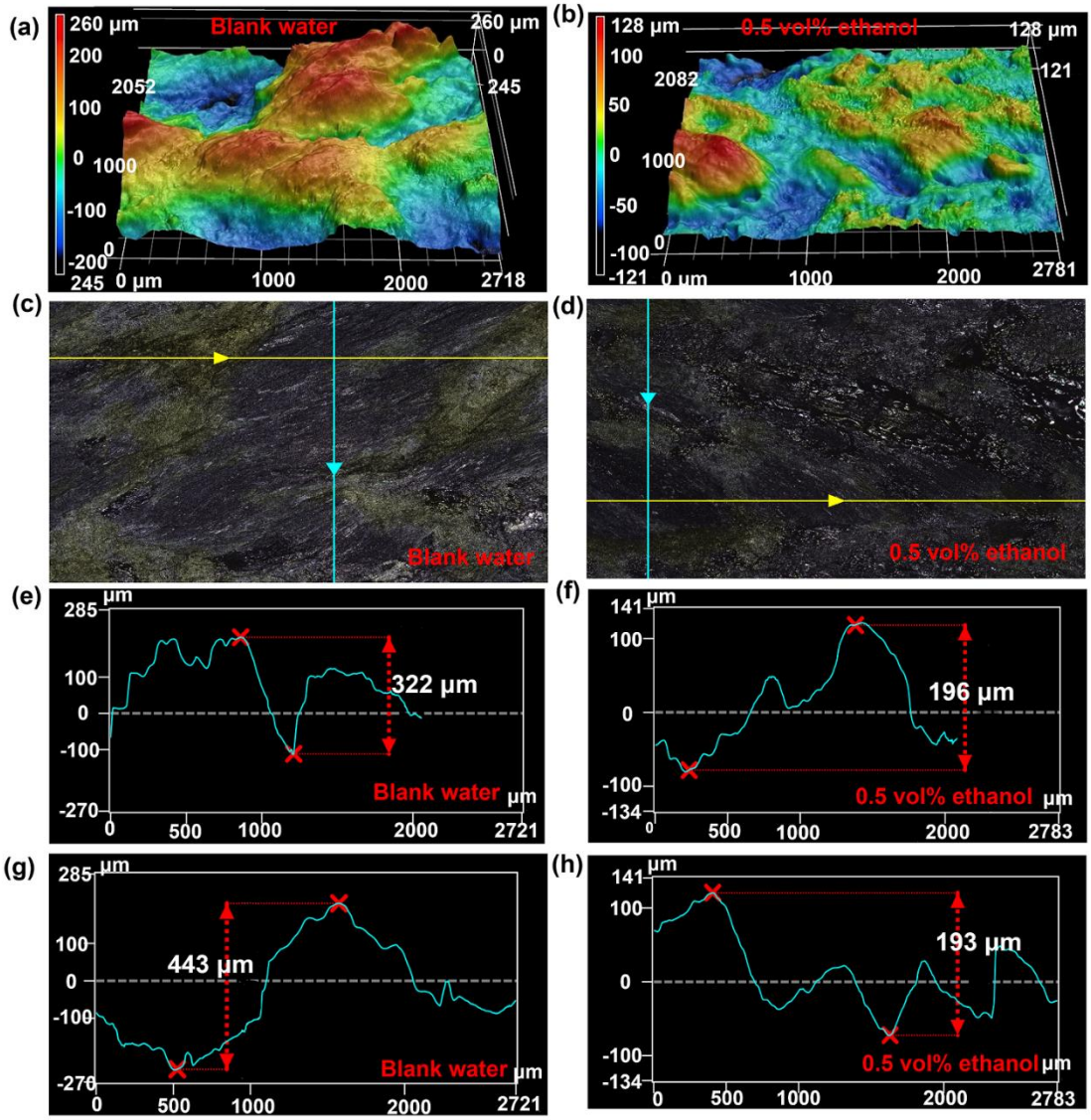

Fig. III-S3 Microscope images of Mg metallic substrate anodes after 5 h discharge in 0.6 M NaCl electrolyte with and without ethanol after removal of corrosion products by chromic acid, (a) and (b) three-dimensional (3D) laser scan microscope morphology images; (c) and (d) 2D light microscope images which noted the position of horizontal and vertical line; (e) and (f) horizontal line profiles and (g) and (h) vertical line profiles.

III-References

[1] B. Vaghefinazari, D. Höche, S.V. Lamaka, D. Snihirova, M.L. Zheludkevich, Tailoring the Mg-air primary battery performance using strong complexing agents as electrolyte additives, J Power Sources, 453 (2020) 227880.

[2] Y. Zhao, G. Huang, C. Zhang, C. Peng, F. Pan, Effect of phosphate and vanadate as electrolyte additives on the performance of Mg-air batteries, Materials Chemistry and Physics, 218 (2018) 256-261.

[3] J. Ma, J. Wen, H. Zhu, Q. Li, Electrochemical performances of Al–0.5Mg–0.1Sn–0.02In alloy in different solutions for Al–air battery, J Power Sources, 293 (2015) 592-598.

[4] J. Li, B. Zhang, Q. Wei, N. Wang, B. Hou, Electrochemical behavior of Mg-Al-Zn-In alloy as anode materials in 3.5 wt.% NaCl solution, Electrochimica Acta, 238 (2017) 156-167.

[5] N. Wang, W. Li, Y. Huang, G. Wu, M. Hu, G. Li, Z. Shi, Wrought Mg-Al-Pb-RE alloy strips as the anodes for Mg-air batteries, J Power Sources, 436 (2019) 226855.

[6] M.P. Gomes, I. Costa, N. J.L. Rossi, B. Tribollet, V. Vivier, On the corrosion mechanism of Mg investigated by electrochemical impedance spectroscopy, Electrochimica Acta, 306 (2019) 61-70.

[7] S. Leleu, B. Rives, J. Bour, N. Causse, N. e, On the stability of the oxides film formed on a magnesium alloy containing rare-earth elements, Electrochimica Acta, 290 (2018) 586-594.

[8] L. Wang, D. Snihirova, M. Deng, C. Wang, B. Vaghefinazari, G. Wiese, M. Langridge, D. Höche, S.V. Lamaka, M.L. Zheludkevich, Insight into physical interpretation of high frequency time constant in electrochemical impedance spectra of Mg, Corros Sci, 187 (2021) 109501.

[9] G.v. Baril, G. Galicia, C. Deslouis, N. e, B. Tribollet, V. Vivier, An Impedance Investigation of the Mechanism of Pure Magnesium Corrosion in Sodium Sulfate Solutions, J Electrochem Soc, 154 (2007) C108.

[10] T.N. Vu, D. Veys-Renaux, E. Rocca, Potential bioactivity of coatings formed on AZ91D magnesium alloy by plasma electrolytic anodizing, Journal of biomedical materials research. Part B, Applied biomaterials, 100 (2012) 1846-1853.

[11] G.-L. Song, Z. Shi, Corrosion mechanism and evaluation of anodized magnesium alloys, Corros Sci, 85 (2014) 126-140.

[12] J. Li, Q. Jiang, H. Sun, Y. Li, Effect of heat treatment on corrosion behavior of AZ63 magnesium alloy in 3.5 wt.% sodium chloride solution, Corros Sci, 111 (2016) 288-301.

[13] Y.Q. Zhou, B.S. Wu, G.H. Lin, Y. Li, D.C. Chen, P. Zhang, M.Y. Yu, B.B. Zhang, D.Q. Yun, Enhancing Performance and Uniformity of Perovskite Solar Cells via a Solution-Processed C70 Interlayer for Interface Engineering, ACS applied materials & interfaces, 9 (2017) 33810-33818.

[14] Y. Zhou, B. Wu, G. Lin, Z. Xing, S. Li, L. Deng, D. Chen, D. Yun, S. Xie, Interfacing Pristine C60 onto TiO2 for Viable Flexibility in Perovskite Solar Cells by a Low-Temperature All-Solution Process onto TiO2 for Viable Flexibility in Perovskite Solar Cells by a Low-Temperature All-Solution Process, Advanced Energy Materials, 8 (2018) 1800399.

[15] X. Liu, S. Liu, J. Xue, Discharge performance of the magnesium anodes with different

phase constitutions for Mg-air batteries, J Power Sources, 396 (2018) 667-674.

[16] B. Díaz, E. Härkönen, J. Światowska, V. Maurice, A. Seyeux, P. Marcus, M. Ritala, Low-temperature atomic layer deposition of Al2O3 thin coatings for corrosion protection of steel: Surface and electrochemical analysis, Corros Sci, 53 (2011) 2168-2175.

[17] I.L.M. Emilse M.A. Martini, Characterization of the film formed on iron in borate solution by electrochemical impedance spectroscopy, Corros Sci, 42 (2000) 433-454.

[18] S. Mirhashemihaghighi, J. Światowska, V. Maurice, A. Seyeux, L.H. Klein, E. Härkönen, M. Ritala, P. Marcus, Electrochemical and Surface Analysis of the Corrosion Protection of Copper by Nanometer-Thick Alumina Coatings Prepared by Atomic Layer Deposition, J Electrochem Soc, 162 (2015) C377-C384.

[19] N. Wang, R. Wang, C. Peng, B. Peng, Y. Feng, C. Hu, Discharge behaviour of Mg-Al-Pb and Mg-Al-Pb-In alloys as anodes for Mg-air battery, Electrochimica Acta, 149 (2014) 193-205.

[20] G. Song, Recent Progress in Corrosion and Protection of Magnesium Alloys, Advanced Energy Materials, 7 (2005) 563-586.

[21] A. Atrens, G.-L. Song, F. Cao, Z. Shi, P.K. Bowen, Advances in Mg corrosion and research suggestions, Journal of Magnesium and Alloys, 1 (2013) 177-200.

[22] C.R. S. Mathieu, J. Hazan, P. Steinmetz, Corrosion behaviour of high pressure die-cast and semi-solid cast AZ91D alloys, Corros Sci, 44 (2002) 2737–2756.

[23] M. Curioni, The behaviour of magnesium during free corrosion and potentiodynamic polarization investigated by real-time hydrogen measurement and optical imaging, Electrochimica Acta, 120 (2014) 284-292.

[24] G. Williams, N. Birbilis, H.N. McMurray, The source of hydrogen evolved from a magnesium anode, Electrochemistry Communications, 36 (2013) 1-5.

[25] D.K. Chanda, A. Samanta, A. Dey, P.S. Das, A.K. Mukhopadhyay, Nanoflower, nanoplatelet and nanocapsule Mg(OH)2 powders for adsorption of CO2 gas, Journal of Materials Science, 52 (2017) 4910-4922.

[26] S.H. Salleh, S. Thomas, J.A. Yuwono, K. Venkatesan, N. Birbilis, Enhanced hydrogen evolution on Mg (OH)2 covered Mg surfaces, Electrochimica Acta, 161 (2015) 144-152.

[27] M. Liu, S. Zanna, H. Ardelean, I. Frateur, P. Schmutz, G. Song, A. Atrens, P. Marcus, A first quantitative XPS study of the surface films formed, by exposure to water, on Mg and on the Mg–Al intermetallics: Al3Mg2 and Mg17Al12, Corros Sci, 51 (2009) 1115-1127.

[28] M. Santamaria, F. Di Quarto, S. Zanna, P. Marcus, Initial surface film on magnesium metal: A characterization by X-ray photoelectron spectroscopy (XPS) and photocurrent spectroscopy (PCS), Electrochimica Acta, 53 (2007) 1314-1324.

[29] G.-L.S. A Atrens, Z Shi, A Soltan, S Johnston, and MS Dargusch, Understanding the Corrosion of Mg and Mg Alloys, Chapter (2017) 515-532.

[30] A. Seyeux, M. Liu, P. Schmutz, G. Song, A. Atrens, P. Marcus, ToF-SIMS depth profile of the surface film on pure magnesium formed by immersion in pure water and the identification of magnesium hydride, Corros Sci, 51 (2009) 1883-1886.

[31] C. Xia, R. Black, R. Fernandes, B. Adams, L.F. Nazar, The critical role of phase-transfer catalysis in aprotic sodium oxygen batteries, Nature chemistry, 7 (2015) 496-501.

[32] Y.G. Zhu, Q. Liu, Y. Rong, H. Chen, J. Yang, C. Jia, L.J. Yu, A. Karton, Y. Ren, X. Xu, S. Adams, Q. Wang, Proton enhanced dynamic battery chemistry for aprotic lithium-oxygen batteries, Nature communications, 8 (2017) 14308.

[33] K. Duan, J. Ning, L. Zhou, S. Wang, Q. Wang, J. Liu, Z. Guo, Synergistic Inorganic-Organic Dual-Additive Electrolytes Enable Practical High-Voltage Lithium-Ion Batteries, ACS applied materials & interfaces, 14 (2022) 10447-10456.

[34] Y. Wang, B. Liu, X. Zhao, X. Zhang, Y. Miao, N. Yang, B. Yang, L. Zhang, W. Kuang, J. Li, E. Ma, Z. Shan, Turning a native or corroded Mg alloy surface into an anti-corrosion coating in excited CO2, Nature communications, 9 (2018) 4058.

[35] M. Danaie, R.M. Asmussen, P. Jakupi, D.W. Shoesmith, G.A. Botton, The role of aluminum distribution on the local corrosion resistance of the microstructure in a sand-cast AM50 alloy, Corros Sci, 77 (2013) 151-163.

[36] D. Mercier, J. Światowska, E. Protopopoff, S. Zanna, A. Seyeux, P. Marcus, Inhibition of Mg Corrosion by Sulfur Blocking of the Hydrogen Evolution Reaction on Iron Impurities, J Electrochem Soc, 167 (2020) 121504.

[37] V. Fournier, P. Marcus, I. Olefjord, Oxidation of magnesium, Surface and Interface Analysis, 34 (2002) 494-497.

[38] H. Saleh, T. Weling, J. Seidel, M. Schmidtchen, R. Kawalla, F.O.R.L. Mertens, H.P. Vogt, An XPS Study of Native Oxide and Isothermal Oxidation Kinetics at 300 °C of AZ31 Twin Roll Cast Magnesium Alloy, Oxidation of Metals, 81 (2013) 529-548.

[39] M. Santamaria, F. Di Quarto, S. Zanna, P. Marcus, The influence of surface treatment on the anodizing of magnesium in alkaline solution, Electrochimica Acta, 56 (2011) 10533-10542.

[40] L.T. Fan, X.G. Yuan, C.x. Zhou, A.W. Zeng, K.T. Yu, M. Kalbassi, K. Porter, Contact Angle of Ethanol and n-Propanol Aqueous Solutions on Metal Surfaces, Chemical Engineering & Technology, 34 (2011) 1535-1542.

[41] G. Song, K.A. Unocic, The anodic surface film and hydrogen evolution on Mg, Corros Sci, 98 (2015) 758-765.

[42] G.S. Frankel, A. Samaniego, N. Birbilis, Evolution of hydrogen at dissolving magnesium surfaces, Corros Sci, 70 (2013) 104-111.

[43] W. Xu, J. Xiao, D. Wang, J. Zhang, J.-G. Zhang, Effects of Nonaqueous Electrolytes on the Performance of Lithium/Air Batteries, Journal of The Electrochemical Society, 157 (2010) A219.

Chapter IV Influence of sodium 5-sulfosalicylate as a corrosion inhibitor in NaCl electrolyte on enhanced performances of Mg-air batteries

This work aims at employing sodium 5-sulfosalicylate (5-S-Sal) corrosion inhibitor into aqueous NaCl electrolyte to improve the discharge performance of Mg-air battery and decrease the side reactions of Mg anode. The corrosion tests at open circuit potentials show a significant decrease of hydrogen evolution when 5-S-Sal inhibitor is added into NaCl electrolyte. X-ray photoelectron spectroscopy and time-of-flight secondary ion mass spectrometry analyses demonstrate that due to presence of 5-S-Sal inhibitor, a corrosion resistant layer shows a lower quantity of $Mg(OH)_2$ than those formed in pure NaCl electrolyte. The surface enrichment in S-like species originating form inhibitor molecule, could have an important effect on decreased Mg corrosion and slower H_2 evolution. Within different concentrations of 5-S-Sal in NaCl electrolyte (0.05 M to 0.15 M), the best discharge performances are achieved in electrolyte with 0.1 M inhibitor. The discharge voltage of full Mg-air battery improves from ~1.58 V to ~1.82 V at a current density of 0.5 mA/cm^2, and the discharge lifetime from around 12.5 hours is prolonged to around 80 hours. Scanning electron microscopy and 3D topography laser microscopy clearly indicate that during the discharge tests much smaller surface degradation and more uniform surface layer is formed in the presence of the inhibitor in the NaCl electrolyte.

IV-1 Objectives and motivation

The discharge products such as MgO, $Mg(OH)_2$ and $MgCO_3$ accumulate on the Mg surface due to the magnesium corrosion [1, 2] and it can block the Mg anode surface. Thus, the working voltage, and consequently, the practical specific energy and the overall discharge performances of full Mg-air battery can be greatly lower [3] than their theoretical values.

To overcome these problems, we have proposed to apply the sodium 5-sulfosalicylate (5-S-Sal) as a corrosion inhibitor in 0.6 M NaCl electrolyte for Mg-air batteries. Different immersion times of Mg anode in electrolyte with and without inhibitors were applied to elucidate the progress of Mg corrosion and analyze the corrosion of Mg by linear sweep voltammetry and electrochemical impedance spectroscopy. The surface chemical composition of Mg anode was analyzed by X-ray Photoelectron Spectroscopy and Time-of-Flight Secondary Ion Mass Spectrometry. Then, after the corrosion studies, different concentrations of 5-S-Sal were used to compare the discharge behaviors with the objective to tune the best battery performances *i.e.*, the highest discharge voltage and the longest battery lifetime. The composition and morphology of the Mg anode was also analyzed after discharge tests to demonstrate its improved performance in electrolyte with inhibitor.

IV-2 Experimental overview

The electrolyte solutions were made of 0.6 M NaCl in ultra-pure H_2O with or without sodium 5-sulfosalicylate (5-S-Sal) acid. The Mg samples preparation and the chemical composition have been introduced in Chapter II-1. The specific experimental conditions used in this chapter are presented below:

- EIS and LSV were performed after Mg specimen immersion in the two kinds of electrolytes (with or without sodium 5-sulfosalicylate (5-S-Sal) acid) for different times (15, 30, 60, 300, 400 min).
- The conditions of volume of hydrogen evolution tests and full Mg-air battery tests are similar to those introduced in chapter III-2.
- Digital optical microscope, SEM and 3D-LSM were employed to analyze Mg anode surface morphologies after immersion in electrolyte with and without inhibitor. The details of the instruments were introduced in section of II-5.
- ToF-SIMS and XPS were combined to analyze the surface chemical composition of Mg anode. ToF-SIMS negative ion depth profiles and XPS spectra were obtained for Mg

after 15 min of immersion at OCP and discharge (in full cell) in blank 0.6M NaCl electrolyte and electrolyte with 0.1 M 5-S-Sal inhibitor, and the pristine Mg after polishing. The negative ion including $MgOH^-$, MgO^-, $MgCl^-$, MgH^-, $MgCO_3^-$, $^{34}S^-$ were selected.

IV-3 Results and discussion

IV-3.1 Influence of 0.1 M 5-S-Sal in NaCl electrolyte on corrosion behavior of pure Mg

First, the corrosion behavior analysis of pure Mg samples in NaCl electrolyte with and without inhibitor using the hydrogen evolution tests at OCP, LSV and EIS are demonstrated. The H_2 evolution reflects the corrosion rate of metallic Mg according to reactions (IV-1 and IV-2), where a dissolution of 1 mol of Mg generates 1 mol of H_2 [3-5]. Fig. IV-1 a shows the H_2 evolution at OCP in 0.6 M NaCl with or without inhibitor and Fig. IV-1 b is the corresponding OCP. In electrolyte without inhibitor, H_2 evolution shows a slow augmentation up to around 100 min, and then, a quasi exponential increase during the following 400 min of immersion. OCP curve also demonstrates an increase to –1.54 V (*vs* Ag/AgCl) during around 100 min of immersion. The OCP increase can be attributed to the cation adsorption (*e.g.* H_3O^+) on the Mg electrode surface, which potential of zero charge is more negative than its equilibrium potential [6]. Interestingly, with the first 100 min of H_2 evolution and potential increases, the concomitant development of black corrosion spots on the Mg electrode surface can be observed. The Mg electrode surface becomes almost fully covered by the black corrosion spots during this time of immersion (see the left-hand inset of digital camera image in Fig. IV-1 b). The corrosion spots can catalyze the hydrogen evolution reaction (HER) [7, 8], which can explain the exponential increase of H_2 volume in Fig. IV-1 a. Then, after 100 min, the OCP value stabilizes at around -1.56 V due to the equilibrium between the cation adsorption on the Mg surface and the full surface coverage by dark corrosion spots.

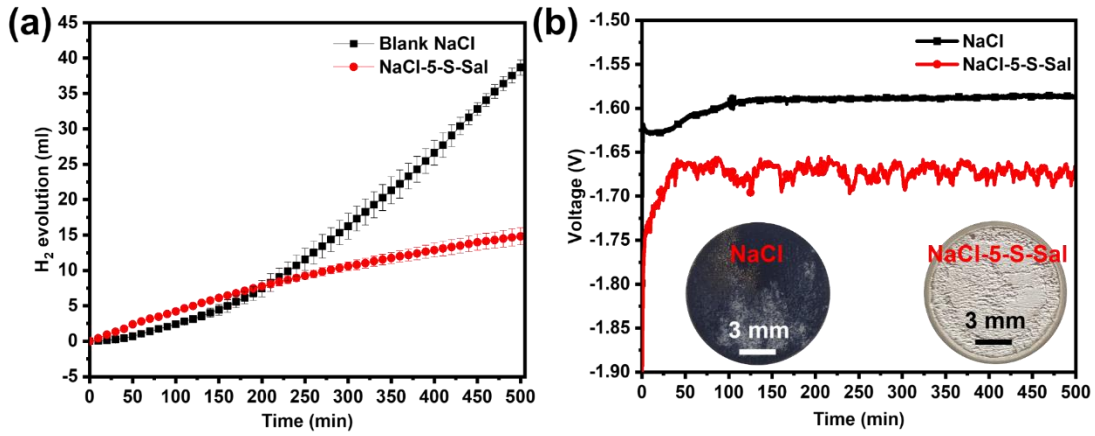

Fig. IV-1 Mg anode in 0.6 M NaCl electrolyte without and with 0.1 M 5-S-Sal (a) H_2 evolution test at open circuit potential (OCP); (b) OCP measurements and digital camera images of Mg samples after 300 min of immersion.

With 0.1 M 5-S-Sal inhibitor in the electrolyte, the stable OCP is reached at –1.68 V, which is 120 mV lower than in the blank NaCl electrolyte. More negative OCP of Mg in half cell configuration is beneficial for achieving a higher discharge potential in full Mg-air battery [4]. Although the volume of H_2 evolution is slightly higher in presence of inhibitor in electrolyte during the first 150 min, the linear and not exponential increase is observed in the following minutes of immersion resulting in around 13 ml of H_2 in comparison to almost four-fold volume of H_2 (40 ml) in a blank electrolyte at the end of the immersion tests (500 min). It was previously explained that 5-S-Sal inhibits the corrosion process on Fe-containing intermetallics and Fe impurities present in Mg sample and increases the solubility of $Mg(OH)_2$ leading to a significant decrease of the precipitates and of the dark corrosion spots formation [9], as it can be confirmed by the image of bright Mg surface in the inset of Fig. IV-1 b (right-hand image). The 5-S-Sal inhibitor can produce soluble complexes with Mg^{2+} of mild stability (log K_{Mg2+} is 5.1) [10, 11]. As cathodic inhibitor, it has the ability of complexing Fe^{3+} (log KFe_{3+} = 36.8). These properties can lead to significant improvement in the Mg corrosion properties and keep the Mg surface clean from dark corrosion spots. Consequently, the anodic and cathodic reactions of Mg dissolution [12-15] and HER, respectively, are significantly slowed down.

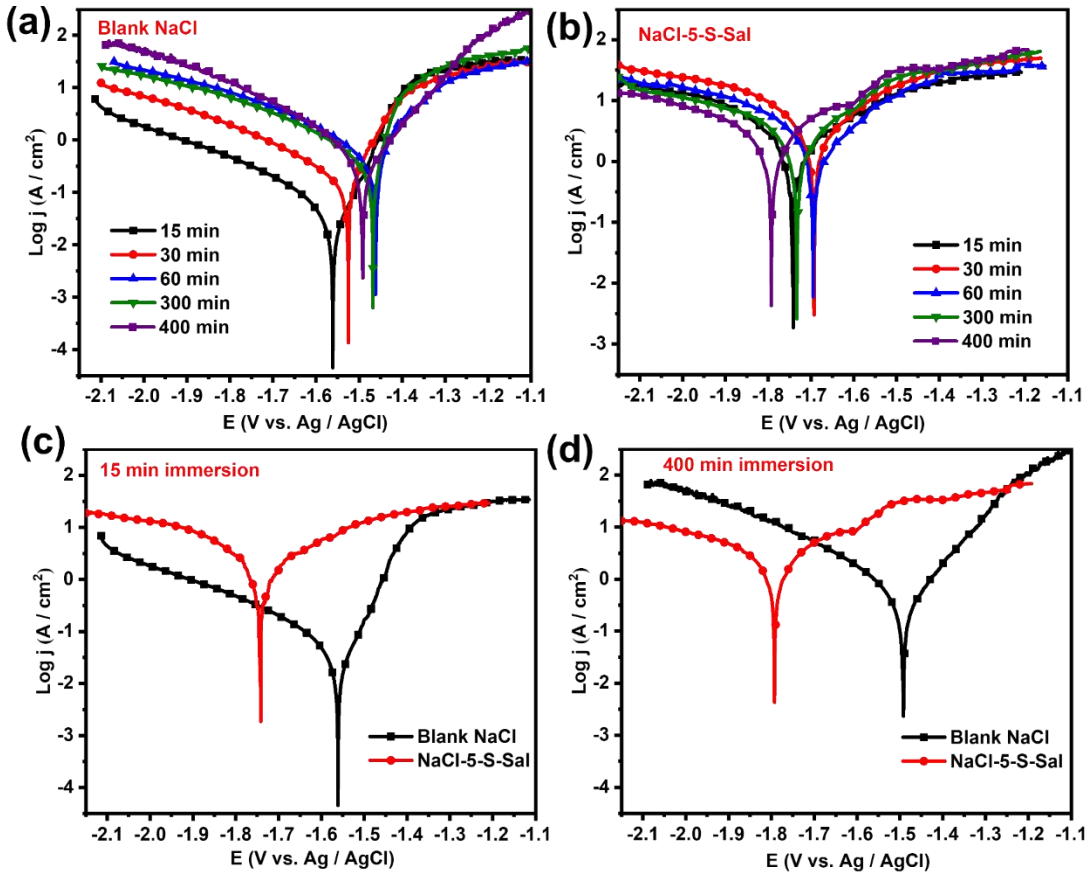

Fig. IV-2 LSV curves of Mg after different immersion times (15, 30, 60, 300 and 400 min) (a) in blank 0.6 M NaCl electrolyte; (b) in 0.6 M NaCl electrolyte with 0.1 M 5-S-Sal inhibitor; (c) comparison of 15 min immersion time; (d) and 400 min immersion time in the two electrolytes.

To better understand the influence of 5-S-Sal inhibitor on the corrosion performance of the Mg anode, potentiodynamic polarization curves (LSV) and electrochemical impedance spectroscopy were performed (Fig. IV-2 and Fig. IV-3, respectively) after different immersion times (15, 30, 60, 300 and 400 min).

The cathodic reaction corresponds to the hydrogen evolution reaction according to reaction (IV-1) and the anodic to Mg dissolution (IV-2):

$$\text{Cathodic reaction:} \quad 2H_2O + 2e^- \rightarrow H_2 \uparrow + 2OH^- \qquad \text{(IV-1)}$$

$$\text{Anodic reaction:} \quad Mg \rightarrow Mg^{2+} + 2e^- \qquad \text{(IV-2)}$$

These cathodic and anodic reactions correspond respectively to the cathodic and anodic branches of the polarization curves present in Fig. IV-2. In blank NaCl (Fig. IV-2 a), the increase of cathodic current density with immersion time indicates the augmentation of hydrogen evolution. As discussed above, the HER is catalysed by formation of dark corrosion spots [16], which formation can be easily observed on Mg electrode (as observed after immersion at OCP in Fig. IV-1 b and Fig. IV-4). With the inhibitor (Fig. IV-2 b), the cathode branch curves change scarcely as a function of immersion time indicating a stable corrosion behaviour of Mg anode. More significant slopes of the anodic branches in blank electrolyte (around 60 mV/decade) than in electrolyte with addition of 5-S-Sal inhibitor (around 20 mV/decade) are noticed. The higher Tafel slope denotes important dissolution of Mg anode (Fig. IV-2 a). This behaviour is less pronounced for longer immersion times and more particularly in the electrolyte with inhibitor addition (Fig. IV-2 a, b). In order to better see the influence of inhibitor on cathodic and anodic behaviour of Mg after short (15 min) and long (400 min) time of immersion, the LSV curves were superimposed (Fig. IV-2 c and d). Fig. IV-2 c shows up a much flatter anodic branch for electrolyte with inhibitor than blank electrolyte for 15 min of immersion. The limiting anodic current density remained almost unaltered with the presence of inhibitor at different times of immersion (Fig. IV-2 b). It means that the surface of the Mg anode is less active and better protected in the presence of 5-S-Sal inhibitor over different immersion times. Moreover after 400 min of immersion (Fig. IV-2 d), the cathodic current, higher in the electrolyte with 5-S-Sal at lower immersion times, decreases significantly, indicating much lower cathodic activity and lower HER than in blank electrolyte.

Fig. IV-3 shows the electrochemical impedance spectra performed at free corrosion potential after various immersion times and the equivalent circuits used for fitting the experimental data. The Nyquist plots show high and low-frequency loops. The capacitive loop at the high-frequency range with a charge transfer resistance (R_{ct}) and a double capacitance (CPE_{dl}), corresponds to the reactivity at the electrolyte / metallic substrate interface [17-21]. Another capacitive loop at the low-frequency range with a surface resistance (R_f) and the capacitance (CPE_f) can be attributed to the reactivity at the corrosion layer / electrolyte interface [22]. The constant phase elements (CPE) were usually adopted for fitting, to substitute the ideal capacitors in both frequencies (for n equals to 1, the CPE is a pure capacitor) [23, 24]. This deviation from the ideal dielectric behavior can be explained by a heterogenous and rough surface of the Mg electrode [39-41]. For Mg exposed to electrolyte with inhibitor, the fairly resolvable corrosion

products on Mg surface leads to appearance of the third time constant at low frequencies with an inductive loop. In the case of electrolyte without inhibitor, the scatter plot can be observed at these frequencies indicating less stable non-stationary conditions due to significantly rougher surface layer with a possible corrosion product flaking. The EIS spectra were fitted using the equivalent circuit shown in Fig. IV-3 e [25-29], the left part for Mg in blank NaCl and the right part for Mg in the electrolyte with inhibitor.

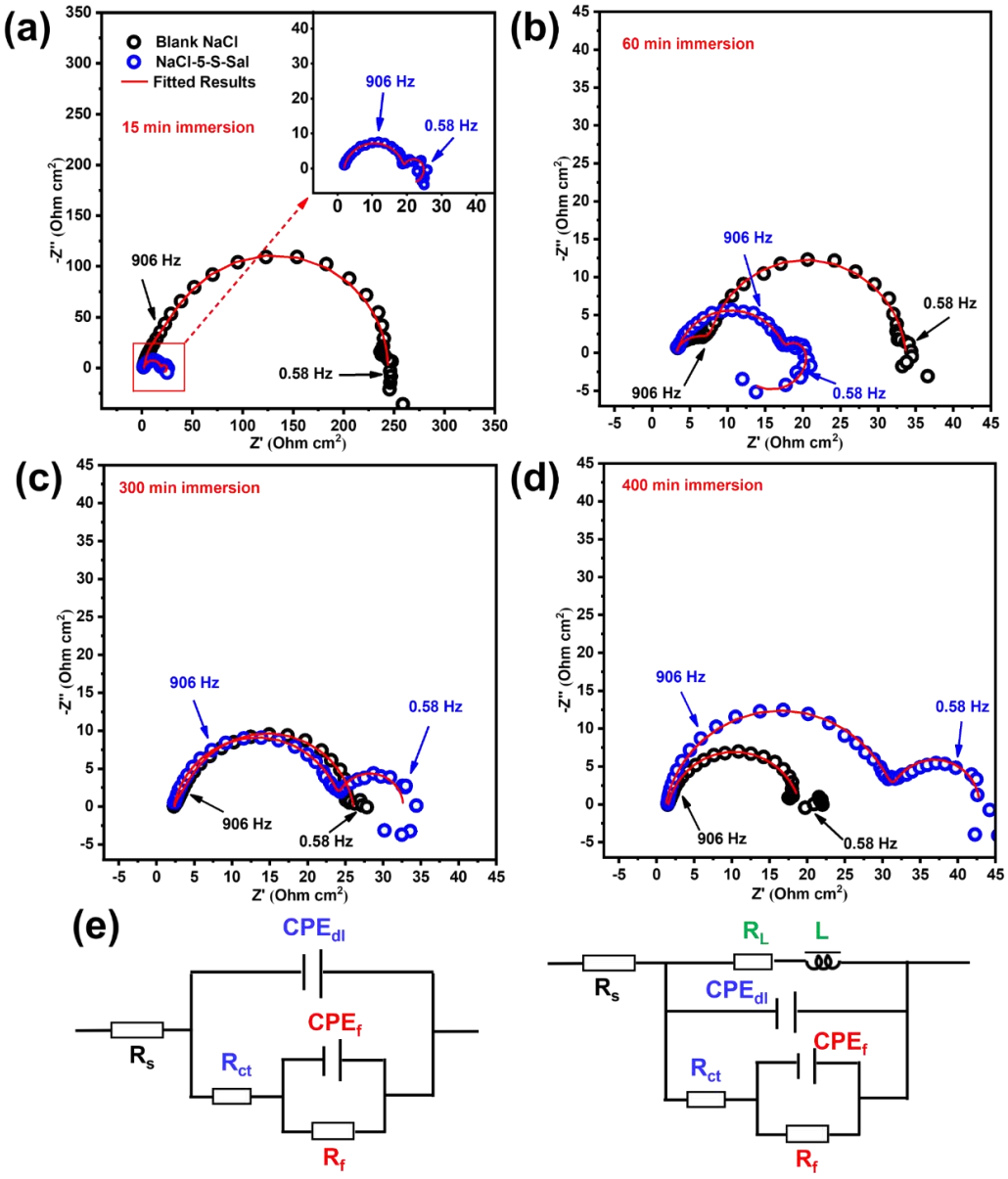

Fig. IV-3 Electrochemical impedance spectra of Mg anode in blank 0.6 M NaCl without and with and 0.1 M 5-S-Sal inhibitor after different times of immersion (a) 15 min; (b) 60 min; (c) 300 min; (d) 400 min; (e) equivalent circuits used for fitting the impedance spectra.

The fitting parameters (Table IV-1) show that the values of R_{ct} and R_f decrease in blank NaCl with immersion time particularly from 15 min to 60 min. These results corroborate the polarization results, *i.e.* the significant changes in the beginning of immersion. However, in the electrolyte with the inhibitor, R_{ct} and R_f values vary much less as a function of different time immersion. An opposite tendency can be observed as a function of immersion time for the charge transfer resistance (R_{ct}): a decrease in blank electrolyte and an increase in the electrolyte with the inhibitor. The Nyquist plots (Fig. IV-3 a-d) show that the *–Z"* in blank NaCl is far larger than in NaCl-5-S-S at 15 min, then very similar values can be observed at 300 min and finally *-Z"* value declines in blank NaCl electrolyte. This is even more clear in the Bode spectra (Fig. IV-S1) showing a significantly higher values of log |*Z*| (0.9 Ω.cm^2) at low frequencies in comparison to 5-S-Sal inhibitor at 15 min, which turn to lower values (0.3 Ω.cm^2 at 400 min). These results denote that the inhibitors can greatly reduce the effect of immersion time on the corrosion of Mg anode which is beneficial to the long discharge performance of Mg-air batteries.

Table IV-1. Parameters obtained from the EIS data fitting for Mg anode in blank 0.6 M NaCl and with 0.1 M 5-S-Sal inhibitor.

	NaCl				NaCl-5-S-Sal			
	15 min	**60 min**	**300 min**	**400 min**	**15 min**	**60 min**	**300 min**	**400 min**
R_s (Ω cm^2)	12	3	2	2	11	10	11	2
R_{ct} (Ω cm^2)	74	6	4	2	17	15	22	30
CPE_{dl} (Ω^{-1} cm^{-2} s^n)	8×10^{-6}	75×10^{-6}	0.2×10^{-3}	0.6×10^{-3}	23×10^{-6}	48×10^{-6}	46×10^{-6}	49×10^{-6}
n_1	1	0.80	0.93	0.86	0.88	0.84	0.88	0.87
R_f (Ω cm^2)	167	25	20	15	6	3	8	11
CPE_f (Ω^{-1} cm^{-2} s^n)	13×10^{-6}	0.2×10^{-3}	0.3×10^{-3}	0.3×10^{-6}	13×10^{-3}	16×10^{-3}	11×10^{-3}	11×10^{-3}
n_2	0.99	0.99	0.86	0.86	0.92	0.93	1	1
L (H)	/	/	/	/	150	32	/	/
R_L (Ω cm^2)	/	/	/	/	39	14	/	/

IV-3.2 Mg surface degradation induced by immersion tests

Fig. IV-4 presents the optical microscopy images of Mg anode after different immersion times

in electrolyte without or with 5-S-Sal inhibitor. In the blank NaCl electrolyte (Fig. IV-4 a-d), the obvious dark and non-reflective areas progressively grow on the Mg surface to finally cover the entire Mg electrode. However, there are not such dark corrosion spots on the surface immersed in 5-S-Sal additive (Fig. IV-4 e-h and digital pictures in the insets of Fig. IV-1 b), instead, the surface became rougher as time of immersion increases. As the hydrogen evolution is observed to evolve principally in the dark areas [5, 30], it can be confirmed from these optical images that the corrosion of Mg is significantly decreased in the electrolyte with inhibitor.

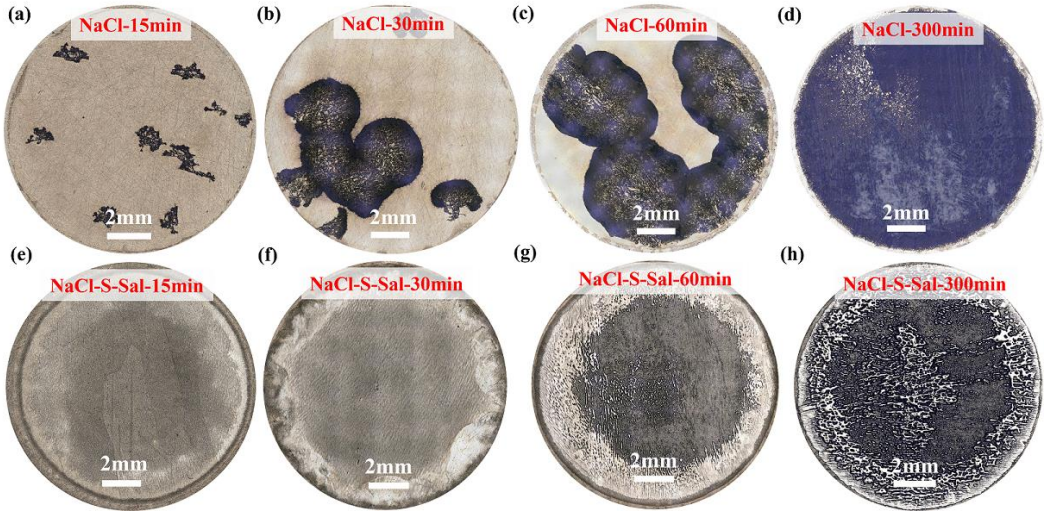

Fig. IV-4 Optical microscope images after different immersion times in 0.6 M NaCl electrolyte without (upper raw) and with 0.1 M S-Sal inhibitor (lower raw) (a) (e) 15 min; (b) (f) 30 min; (c) (g) 60 min; (d) (h) 300 min.

As shown by SEM, in blank NaCl (Fig. IV-5 a), the surface of Mg electrode is very heterogenous with areas of severe corrosion corresponding to black corrosion spots. These corrosion spots show also a cracked layer (inset image in Fig. IV-5 a). However, with the addition of 5-S-Sal inhibitor, a homogeneous surface layer can be observed at a micrometric level (Fig. IV-5 c). It indicates that 5-S-Sal inhibitor reduces the severe Mg corrosion and limits the formation of dark areas catalyzing the HER [7, 8]. However, the development of porous structures with characteristic nanoplatelets of magnesium oxide-hydroxide layer [31] can be observed in the areas out of black corrosion spots in both electrolytes (Fig. IV-5 b and d). A lower porosity and less developed flake-like structure are observed on the surface exposed to electrolyte containing 5-S-Sal inhibitor. One hypothesis is that 5-S-Sal inhibitor prevents the

formation of porous structure $Mg(OH)_2$ layer by adsorption of the organic molecules (*e.g.* inhibitor) on the Mg surface [9, 12] and another one is that the 5-S-Sal can induce a dissolution of hydroxide and/or precipitates. A mixed function of the inhibitor cannot be ruled out and it will be discussed here below.

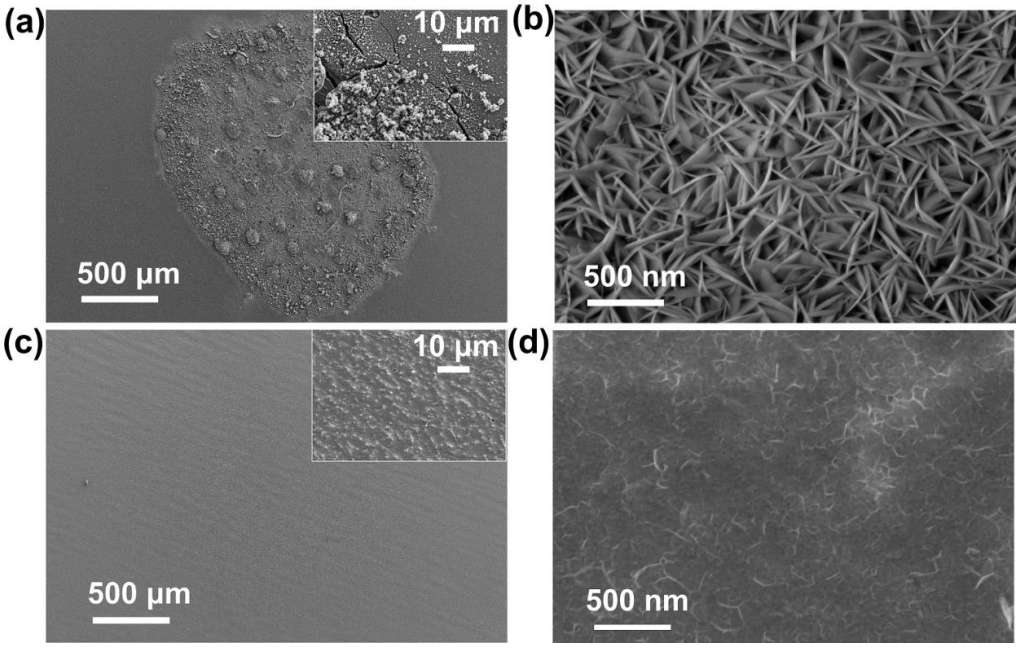

Fig. IV-5 SEM images of surface morphologies of Mg anode after 15 min immersion at OCP (a) in a blank 0.6 M NaCl electrolyte, (inset presents the magnified rough surface area corresponding to dark corrosion spots); (b) the magnified image of areas out of black corrosion spots (bright parts shown in optical microscopy in Fig. IV-4); (c) in 0.6 M NaCl with 0.1 M 5-S-Sal inhibitor; (d) the magnified image of sample present in c.

IV-3.3 Influence of 5-S-Sal inhibitor in NaCl electrolyte on discharge performance of Mg-air battery

Following the promising results obtained on Mg corrosion with 5-S-Sal inhibitor in NaCl electrolyte, a series of discharge tests of Mg-air battery in half and full cell configurations were performed. Fig. IV-6 presents the half-cell discharge performance of Mg in blank NaCl electrolyte with various concentration of 5-S-Sal (0.05, 0.1 and 0.15 M) at different current densities (0.5, 2.5, 5, and 10 mA/cm^2). In blank NaCl electrolyte at different current densities, the discharge potential decreases immediately and then increases to a stable value, which can

be attributed to a native oxide breakdown, the attack of Mg (dissolution) and rapid formation of a corrosion product layer. In the electrolyte with 5-S-Sal inhibitor, the discharge voltage increases slowly from the low potential (equivalent to OCP value of around –1.8 V, as also shown in Fig. IV-1 b) to the stable value and it can be explained by a slow layer growth, which is influenced by the reactivity of inhibitor at the electrolyte/metal interface (*e.g.* inhibitor adsorption on Mg surface). A slower kinetics of surface film growth is consistent with a more stable behavior observed by EIS (Fig. IV-3) and less significant morphological surface modifications demonstrated by SEM (Fig. IV-5 d). At 0.5 mA/cm^2 (Fig. IV-6 a), the most negative discharge potential for Mg is detected in 0.05 M 5-S-Sal. At 2.5 mA/cm^2 (Fig. IV-6 b) the same and stable discharge potential of –1.63 V is observed for all inhibitor concentrations. This potential is more negative than those observed in the blank NaCl electrolyte (-1.55 V). However, at higher current densities of 5 mA/cm^2 (Fig. IV-6 c), in electrolyte with the lower inhibitor concentration (0.05 M), an unstable discharge potential is observed (a potential jump at around 1750 s). In the same electrolyte, at higher current density discharge (10 mA/cm^2 in Fig. IV-6 d), the potential increase and its important fluctuation can be observed. At 10 mA/cm^2 the discharge potentials, are similar regardless of inhibitor concentration. Thus, it can be concluded that the addition of inhibitor at certain concentrations (not less than 0.1M) is beneficial for Mg discharge voltage when the low current densities are applied.

The half-cell's discharge voltage [11] can be expressed as:

$$E_{\text{anode}} = E_{\text{ocp}} - \eta_{\text{ct}} - \eta_{\text{diff}} - IR \qquad \text{(IV-3)}$$

where the E_{ocp} is the open circuit potential, η_{ct} and η_{diff} represent the potential drops, due to charge transfer process and diffusion overpotential, respectively, caused by discharge products. I and R are the loaded current and resistance of electrolyte between reference and working electrode [32-34]. Following this expression, it is clear that more negative OCP will contribute to lower discharge voltage assuming no modifications of other factors [1, 34, 35]. Furthermore, the clean Mg electrode with less corrosion products blocking the surface in electrolytes with inhibitor can lead to a lower resistance of the electrolyte between working electrode (Mg) and reference electrode and consequently to a smaller potential drop. The close discharge voltages at higher current densities (Fig. IV-6 d) can be significantly influenced by IR drop but also by diffusion overpotential and charge transfer process. Summarizing these results, the optimal

concentration of inhibitor for stable electrode behavior and discharge performance at different current densities is 0.1 M 5-S-Sal. For this reason, the battery performances in full cells and surface chemistry of Mg electrode in this electrolyte will be further studied in more details.

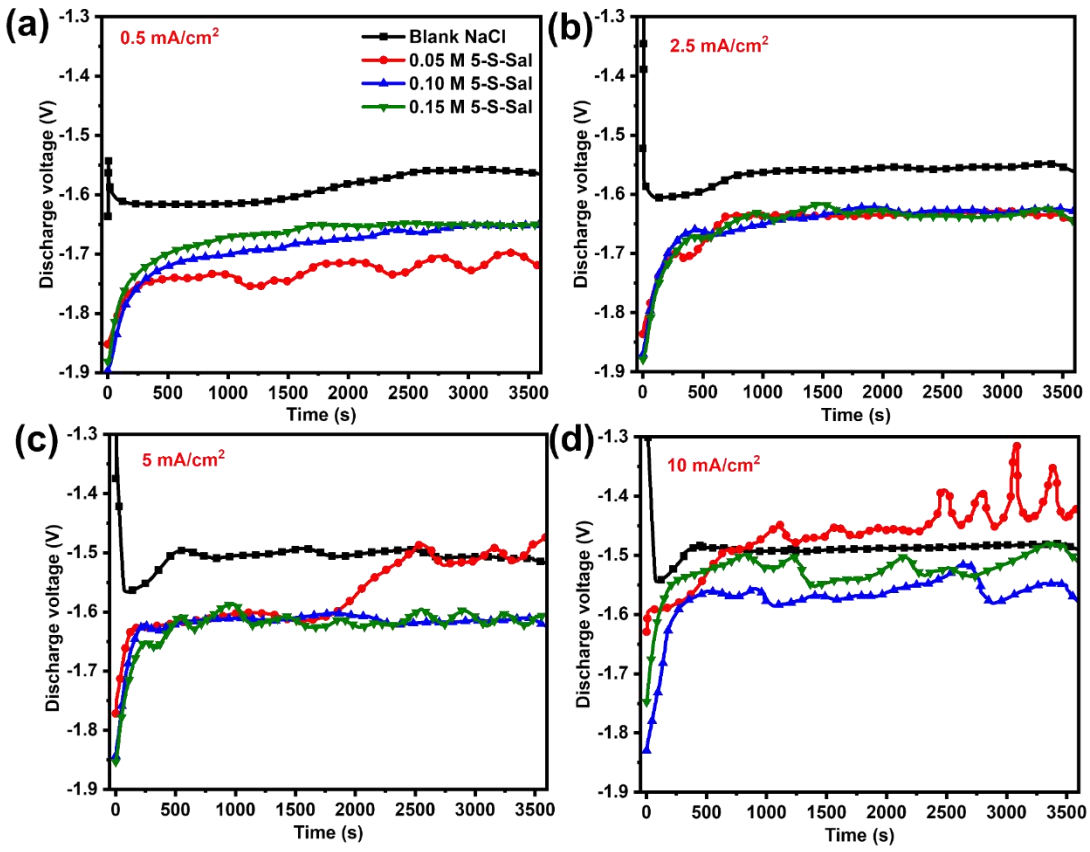

Fig. IV-6 Discharge performance of half Mg-air battery cells in blank 0.6 M NaCl and with 0.05 M, 0.1 M and 0.15 M 5-S-Sal inhibitor at different current densities (a) 0.5 mA/cm^2; (b) 2.5 mA/cm^2; (c) 5 mA/cm^2; (d) 10 mA/cm^2.

The discharge performances of full Mg-air batteries in electrolytes with or without inhibitors are presented in Fig. IV-7. The discharge voltage drops significantly after ~12.5 hours in blank NaCl (Fig. IV-7 a) and a serious corrosion damage and formation of large dark corrosion spots/holes were observed by eye on Mg plates. They can be attributed to the severe localized corrosion [36, 37] and local presence of other metallic inclusions and impurities such as Fe, Mn, as previously reported [38, 39]. In presence of 0.05, 0.15, and 0.1 M 5-S-Sal, the discharge times can be prolonged up to 30, 42, and 80 hours, respectively (Fig. IV-7 a). It indicates that the inhibitors can greatly increase the service time of Mg plates, which can be explained by a

significant decrease of Mg corrosion. Moreover, the discharge voltage in presence of inhibitor is higher by 275-470 mV than in blank NaCl electrolyte (Fig. IV-7 a), which can be attributed to the superior OCP and more homogenous surface that can reduce the influence of overpotentials (according to equation IV-3). Also, at higher current densities such as 5 mA/cm^2 (Fig.IV-7 b), the lifetime of Mg is significantly prolonged in presence of 0.1 M 5-S-Sal (28 hours in comparison to 12 hours in NaCl without inhibitor). Unfortunately, the discharge potential is not stable during the first hours and drops to 1.2 V after 6 hours. The 5-S-Sal can be consumed by continuous complexing with Mg^{2+} as a function of time and thus the advantage of inhibitors is reduced

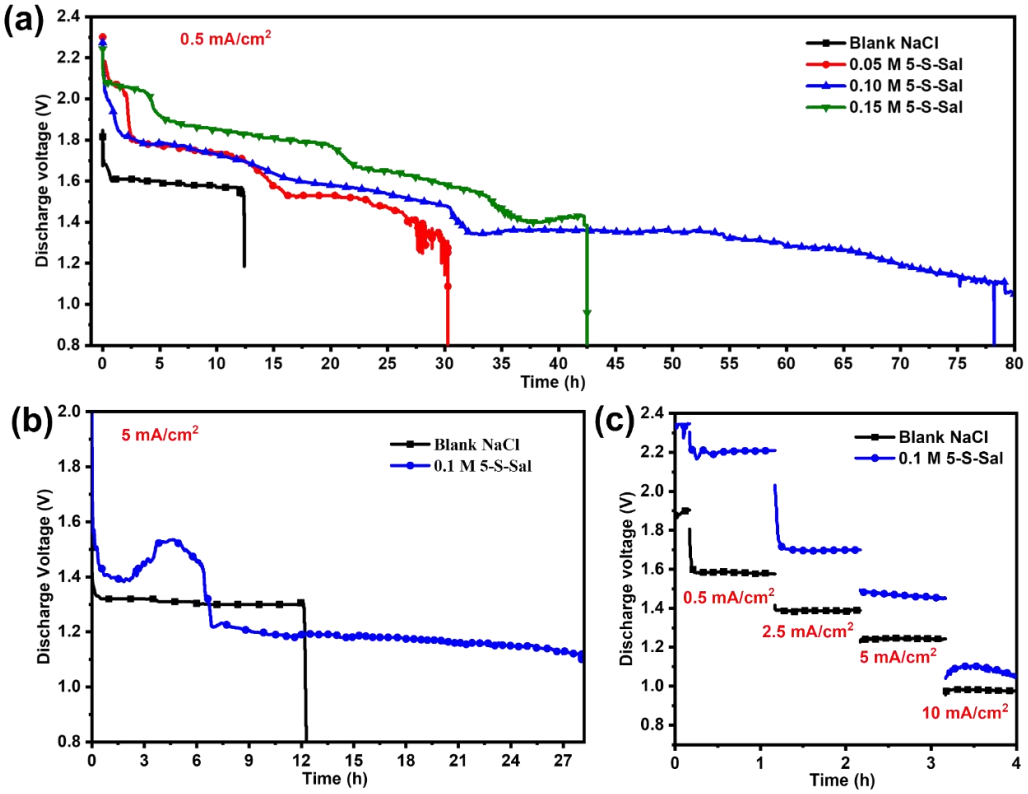

Fig. IV-7 Discharge curves of full Mg-air batteries obtained (a) in blank 0.6 M NaCl and with different concentration of 5-S-Sal electrolyte at current density of 0.5 mA/cm^2 for a long-time test, in blank NaCl and with 0.1 M 5-S-Sal inhibitor for comparison; (b) at different current densities; (c) at current density of 5 mA/cm^2.

Furthermore, the influence of different current densities on discharge curves in two electrolytes is demonstrated in Fig. IV-7 c. In presence of inhibitors, the discharge potential is higher by

about 620 mV (at 0.5 mA/cm^2), 310 mV (at 2.5 mA/cm^2), 230 mV (at 5 mA/cm^2) and 130 mV (at 10 mA/cm^2) with reference to the blank NaCl electrolyte. It indicates that the efficiency of inhibitor decreases slightly at higher current densities. The reaction of complexing with Mg^{2+} or other ions (*i.e.* metallic impurities) [11], for which 5-S-Sal inhibitor is responsible, can be the rate-limiting step. To efficiently protect the Mg surface and keep the surface free of black corrosion spots, a stronger complexation ability and faster kinetics are necessary.

IV-3.4 Influence of inhibitor on chemical composition of the surface layer on Mg anode

To better understand the working mechanism of 5-S-Sal inhibitor in NaCl electrolyte, chemical characterization was performed by ToF-SIMS negative ion depth profiles (Fig. IV-8 and Fig. IV-S2) after immersion at OCP and discharge tests of full Mg-air batteries. MgO^-, $MgOH^-$, MgH^-, $MgCl^-$, $MgCO_3^-$ ions [40] correspond to components of the passive or corrosion layer composition (magnesium oxide, hydroxide, hydride, chloride and carbonate, respectively) and $^{34}S^-$ ion to the presence of 5-S-Sal inhibitor. The very fast ion signal intensity increase observed during the first tens of seconds of sputtering corresponds to the time needed to reach the stationary conditions. The position of the metal/oxide interface was defined as the position where 80 % of maximum intensity of MgO^- signal is measured [41] . Based on the sputtering rate (0.1 nm/s estimated in our previous work [41]), the thickness of the layer formed on Mg surface in NaCl blank electrolyte is ~27.5 nm after immersion at OCP and ~33.5 nm after discharge test. First, it should be noted that the layers are much thicker than on the pristine electrode (~7.8 nm) indicating a significant growth of the oxide/hydroxide. Moreover, the thicker layer after discharge than after OCP indicates that the Mg dissolution and deposition of corrosion products is enhanced by the applied current. In the electrolyte containing the inhibitor (after OCP and discharge), the thickness of the layer is almost the same (~7.5 nm) as on the pristine Mg sample, which indicates much lower Mg corrosion when the inhibitor is present. Interestingly, the intensity of the MgO^- signal for Mg samples exposed to the electrolyte with inhibitor is higher than for the blank NaCl electrolyte, in contrast with the $MgOH^-$ signal intensities. This indicates that the inhibitor favors the formation of MgO over $Mg(OH)_2$. These results corroborate also with SEM (Fig. IV-5 d), showing less flake-like porous structure typical of $Mg(OH)_2$. The lower $^{18}OH^-$ and higher $^{18}O^-$ signals (Fig. IV-S2 a) in electrolytes with inhibitor agree well with this conclusion. Comparing the maximum intensity of MgO^-, $MgOH^-$ and MgH^- (Fig. IV-8 a, b and c) signals, it can be concluded that the MgH^- maximum is located

between MgO^- and $MgOH^-$. This can be more clearly viewed after superposition of all these signals for each sample in Fig. IV-S3. This indicates a multilayer structure of the film with magnesium hydrides embedded into magnesium hydroxide present on the extreme surface and the magnesium oxide present in the inner part of the layer, close to the interfacial region, as already reported by Seyeux *et al*. [40]. A high intensity $MgCl^-$ signal in blank NaCl electrolyte is observed within the whole thickness of the oxide/hydroxide layer, and particularly at the interface with the metallic substrate. Consequently, the high quantity of $Mg(OH)_2$, MgH_2 and/or $MgCl_2$ can catalyze the HER [7, 8] and enhance the rates of hydrogen evolution [42]. With 5-S-Sal inhibitor, the $MgCl^-$ signal is significantly weaker, close to the value observed for the pristine sample, and its intensity drops almost to zero in the interfacial region. This quasi absence of $MgCl^-$ species (representative of corrosion in chloride solution) confirms the efficient inhibition of Mg corrosion.

Besides, the S^- signal, which is a fingerprint of the sodium 5-sulfosalicylate molecule, is detected on Mg electrodes exposed to the electrolyte with inhibitor. As expected, a much higher S^- signal intensity (10 times) for Mg samples immersed at OCP or after discharge tests is observed for Mg surfaces exposed to electrolyte with inhibitor than without (Fig. IV-8 f). Apart the complexation effect of 5-S-Sal as described above [10, 11], the presence of sulfur can lead to corrosion inhibition of Mg according to our group's study [38] showing the sulfur adsorption (S_{ads}(Fe)) on Fe-rich sites, which are the catalytic sites for the HER.

Fig. IV-9 a shows the XPS Mg 2p core level spectra for the pristine Mg sample and Mg anode exposed to 0.6 M NaCl electrolyte without and with 0.1 M 5-S-Sal inhibitor at OCP and after discharge tests in full cells. Two peaks can be clearly distinguished for the pristine sample (Fig. IV-9 a_5) and for the Mg sample immersed at OCP in the electrolyte with 5-S-Sal inhibitor (Fig. IV-9 a_4): a peak at 49.8 eV, attributed to metallic Mg, and the other peak at higher binding energy, which corresponds to the magnesium compounds specified hereafter [21]. For other Mg samples (Fig. IV-9 (a_1), (a_2) and (a_3)), only one higher binding energy peak corresponding to compounds characteristic of corrosion layers are observed. This layer is too thick to detect the signal of metallic Mg, due to attenuation of the signal by the thick surface layer (probing depth of about 8 nm). Moreover, the Mg(II) components in the Mg 2p spectra show shifts towards higher binding energies, with reference to Mg 2p peak for pristine sample, of around +1.1 eV (after immersion at OCP), +2.1 eV (after discharge) in blank NaCl electrolyte and around +0.1 eV (after immersion at OCP), +0.5 eV (after discharge) in electrolyte with inhibitors. The more

positive binding energy indicates a chemical shift introduced by formation of thicker or less conductive surface layers [38, 43]. Much less significant Mg 2p shift observed in case of Mg exposed to electrolyte with inhibitor (Fig. IV-9 (a_3) and (a_4)) implies formation of much thinner layers. These results are consistent with the ToF-SIMS data presented above.

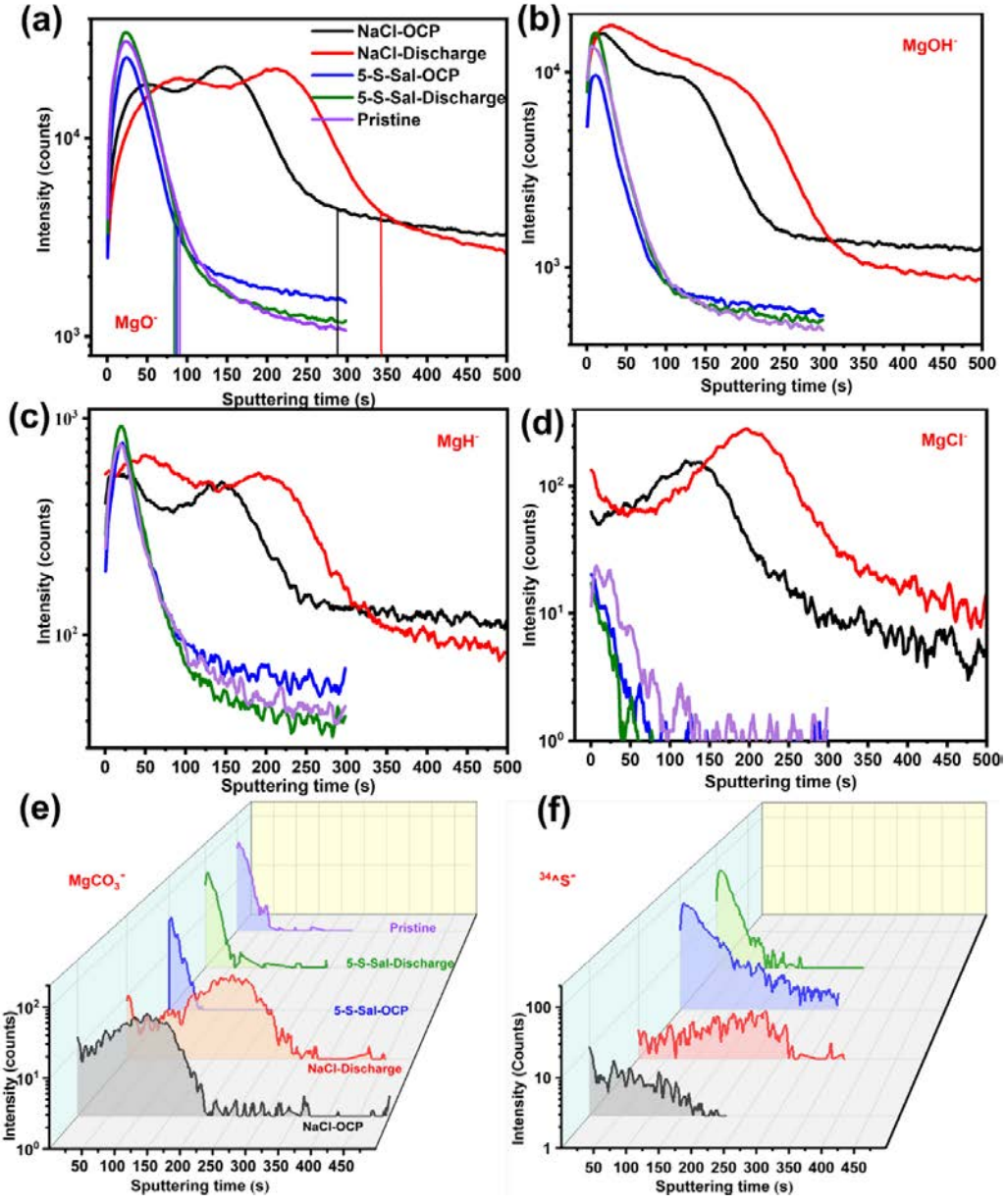

Fig. IV-8 ToF-SIMS (negative ions) in-depth profiles for the layers formed on the pristine Mg after polishing and after 15 min of immersion at OCP and discharge (full cell) in 0.6M NaCl electrolyte without and with 0.1 M 5-S-Sal inhibitor: (a) MgO^-, (b) $MgOH^-$, (c) MgH^-, (d) $MgCl^-$, (e) $MgCO_3^-$, (f) $^{34}S^-$.

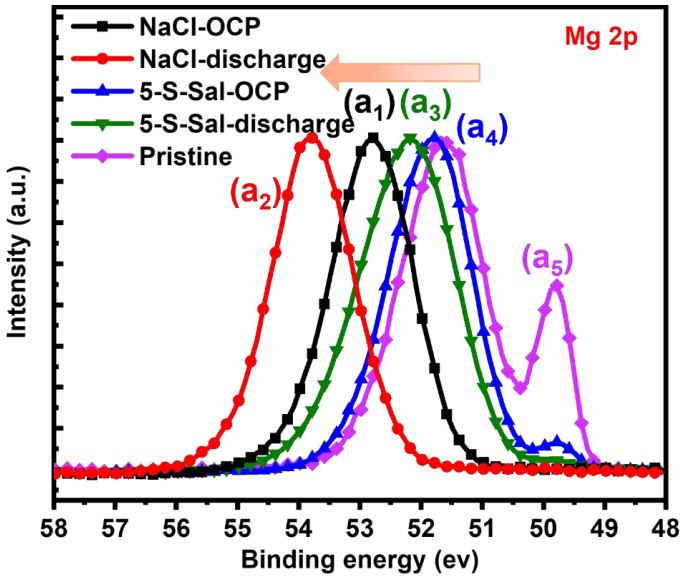

Fig. IV-9 XPS Mg 2p core level spectra for Mg anode in 0.6 M NaCl without or with 0.1 M 5-S-Sal inhibitor: (a_1) (a_3) after 15 min OCP; (a_2) (a_4) after 15 min discharge test (full cell); (a_5) Mg pristine after polishing.

A decomposition of Mg 2p and O 1s spectra was performed to determine the species present in the oxide layers (Fig. IV-10 and Fig. IV-S4). The binding energy was corrected using the position of the C 1s signal from hydrocarbons (-CH-CH-) (286 eV) [44]. Table IV-2 depicts different magnesium compounds, principally $Mg(OH)_2$ at 50.3 ± 0.2 eV, $MgCO_3$ at 51.3.± 0.4eV [45] and their corresponding atomic percentage calculated from Mg 2p spectra. The quantity of $Mg(OH)_2$ is reduced by almost half in 5-S-Sal-containing electrolyte as compared to blank NaCl electrolyte and an increase of $MgCO_3$ formation is observed leading to enhanced corrosion inhibition [46, 47]. The presence of $Mg(OH)_2$ and $MgCO_3$ in Mg 2p spectra is also confirmed by the decomposition of O 1s spectra (Fig. IV-10 b and d). The stoichiometry of these compounds was also calculated using the Mg 2p and O 1s peak intensities (corresponding to magnesium hydroxide or carbonate). The corrosion inhibition can be also governed by sodium 5-sulfosalicylate inhibitor, which presence is manifested by the S 2p signal (Fig. IV-11), which shows a spin-orbit doublet at 168.9 eV (S $2p_{1/2}$) and 167.7 eV (S $2p_{3/2}$) indicating the presence of -SO_3- corresponding to the inhibitor molecule [38, 48]. The sulfur species adsorbed on the Mg surface can reduce the anodic dissolution and hydrogen evolution as previously demonstrated [38]. The presence of S-containing species agrees also with ToF-SIMS data (Fig. IV-8 f).

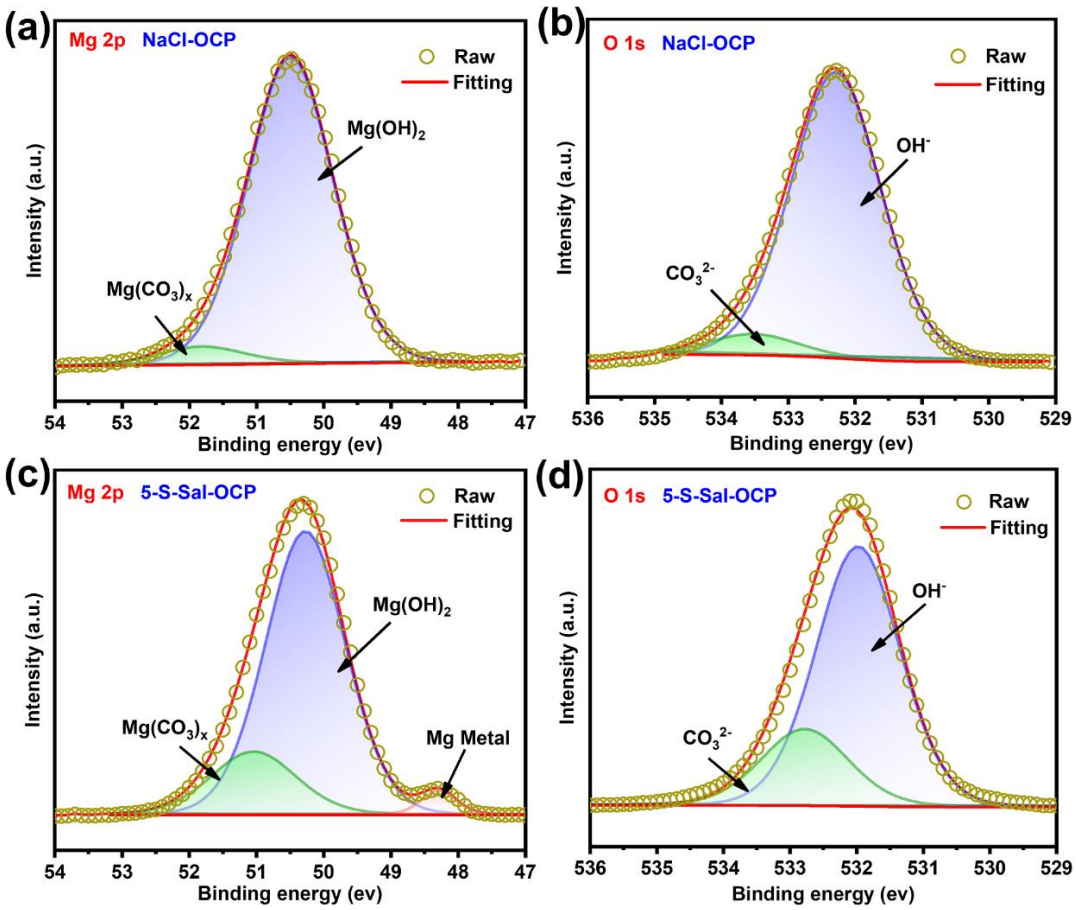

Fig. IV-10 XPS Mg 2p and O 1s core level spectra for Mg anode after 15 min of discharge at a current density of 0.5 mA/cm^2 in (a) (b) blank 0.6 M NaCl electrolyte; (c) (d) 0.6 M NaCl with 0.1 M 5-S-Sal inhibitor.

Table IV-2. Atomic % of Mg 2p and binding energies of Mg 2p and O 1s for different magnesium compounds calculated from XPS for Mg samples exposed to 0.6 M NaCl electrolyte with 0.1 M 5-S-Sal and without inhibitor (at OCP and after discharge test at current density of 0.5 mA/cm^2).

Atomic% Mg 2p	NaCl-OCP	NaCl-discharge	5-S-Sal-OCP	5-S-Sal-discharge	Peak position Mg 2p (eV)	Peak position O 1s (eV)
Mg metal	/	/	3	/	49.8*	/
$Mg(OH)_2$	95	96	79	79	50.3 ± 0.2	532.1 ± 0.2
$MgCO_3$	5	4	18	21	51.3 ± 0.4	533.2 ± 0.3

* No correction for charging effects.

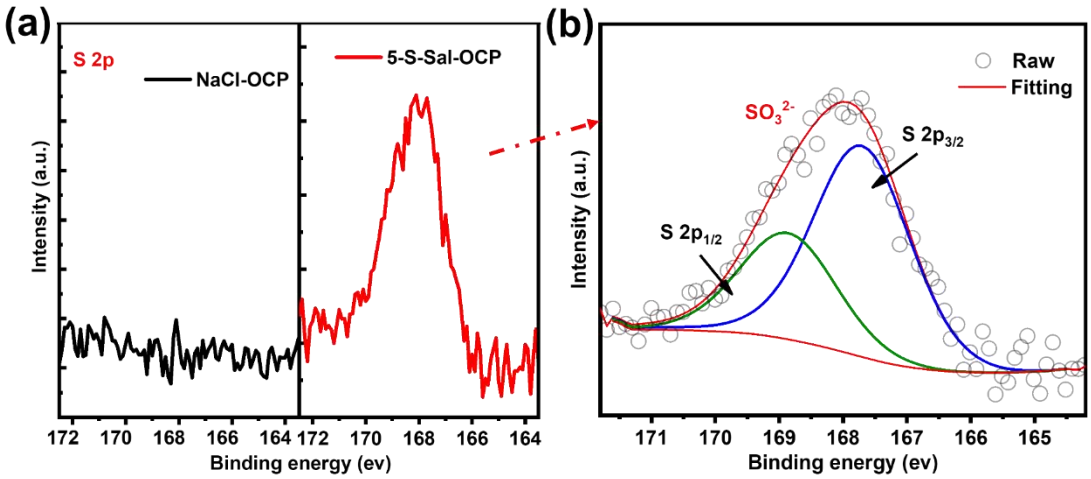

Fig. IV-11 (a) Comparison of S 2p core level spectra for Mg anodes in 0.6 M NaCl without or with 0.1 M 5-S-Sal inhibitor; (b) decomposition S 2p for Mg anode obtained in the electrolyte with 0.1 M 5-S-Sal.

IV-3.5 Mg negative electrode degradation after discharge tests as a function of used electrolyte

To observe the in-depth modifications and degradations of Mg plates, SEM analyses were performed on Mg anodes after 15 min discharge test at a current density of 0.5 mA/cm^2 in full battery cell (Fig. IV-S5). Apparently, several mm of diameter dark corrosion spots are present in the blank NaCl electrolyte (Fig. IV-S5 a), whereas no dark spots appear on Mg anode discharged under the same conditions in the electrolyte with 5-S-Sal inhibitor. At the nanometric level (Fig. IV-S5 b and d), it is shown that the discharge tests lead to formation of characteristic flake-like porous structure attributed to magnesium oxide-hydroxide layer [31, 49] in blank NaCl electrolyte. The presence of inhibitor leads to the formation of more homogenous layers without characteristic flake-like structure for the Mg samples with longer discharge time. These results are perfectly consistent with SEM observation of Mg after OCP tests (Fig. IV-5), which show no black areas when the inhibitor is added.

Cross-section SEM images of Mg after 5 hours of discharge tests (Fig. IV-12 (a-d)) show that the Mg samples are seriously damaged, and the Mg electrode is almost completely consumed in blank NaCl electrolyte. However, only slight dissolution of Mg sample in electrolyte with 5-S-Sal inhibitor is observed, with a little enrichment in corrosion products on the surface (Fig. IV-12 c, d, respectively). Consistent with the 3D laser microscope images, much flatter surface

topography (lower roughness) is observed (Fig. IV-S6) for Mg anode in presence of inhibitor (322 µm and 443 µm for blank NaCl *vs* 34 µm and 31 µm with 5-S-Sal additive). It indicates that the 5-S-Sal inhibitor effectively prevents the pitting corrosion of Mg anode exposed in long time discharge test. Thus, the service time of Mg-air batteries can be greatly prolonged.

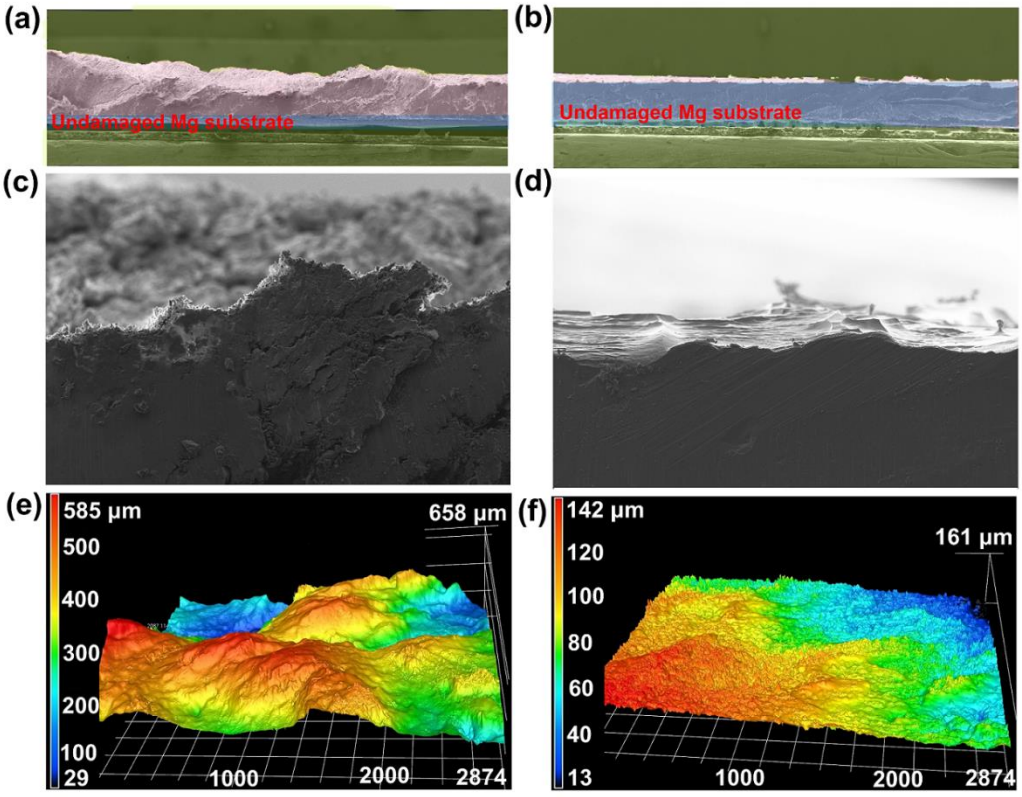

Fig. IV-12 Cross-section SEM images of Mg samples after 5 hours of discharge tests in (a and c) blank 0.6 M NaCl; (b and d) with 5-S-Sal inhibitor added to electrolyte. Three-dimensional topography laser microscope of Mg anode after 5 hours of discharge tests (full cell) (e) in blank 0.6 M NaCl; (f) in electrolyte with 5-S-Sal inhibitor.

IV-4 Conclusions

The influence of sodium 5-sulfosalicylate as an inhibitor in 0.6 M NaCl electrolyte on Mg-air battery performance and the stability of Mg electrode were thoroughly investigated by combining electrochemical, surface morphology and chemical surface characterization methods. A more negative OCP and an improved average discharge voltage by 275-470 mV (during the discharge test of full cells at a current density of 0.5 mA/cm^2) were observed in the

electrolyte with inhibitor. Moreover, a much less active cathode behavior of Mg electrode was observed by linear sweep voltammetry measurements and a stable impedance value after long-time immersion. The obtained data show that the inhibitor improves the stability and corrosion resistance of Mg anode and decreases the HER. The presence of inhibitor in the electrolyte provided almost a four-fold reduction of the hydrogen evolution in comparison to the blank electrolyte. Chemical surface characterizations by XPS and ToF-SIMS revealed the formation of a multilayer structure of the corrosion film with magnesium hydrides embedded into magnesium hydroxide on the extreme surface and magnesium oxide in the inner layer close to the interfacial region. A higher amount of MgO and lower amount of $Mg(OH)_2$ are observed on the Mg electrode exposed to the electrolyte with inhibitor. The surface layer did not show the presence of chlorides and a slight enrichment in sulfur species was also observed, which could be responsible for blocking the active, catalytic sites of HER. However, it should be noted that previously demonstrated complexation effect of Mg^{2+} or other ions (*i.e.* metallic impurities) by 5-S-Sal inhibitor is also responsible for the corrosion inhibition of Mg. The addition of inhibitor leads to formation of a layer with limited thickness as shown by ToF-SIMS in-depth profiles, which is also beneficial for discharge performance of full battery with high discharge potential and prolonged battery lifetime.

IV-5 Supplementary information

Table IV-S1. Chemical composition (wt. %) of pure Mg.

Chemical Composition (wt. %)										
Mg	**Si**	**Fe**	**Cu**	**Mn**	**Al**	**Ni**	**Zn**	**Sn**	**Pb**	**Ti**
Bal	**0.003**	**0.002**	**0.0005**	**0.002**	**0.004**	**0.0005**	**0.004**	**0.004**	**0.001**	**0.001**

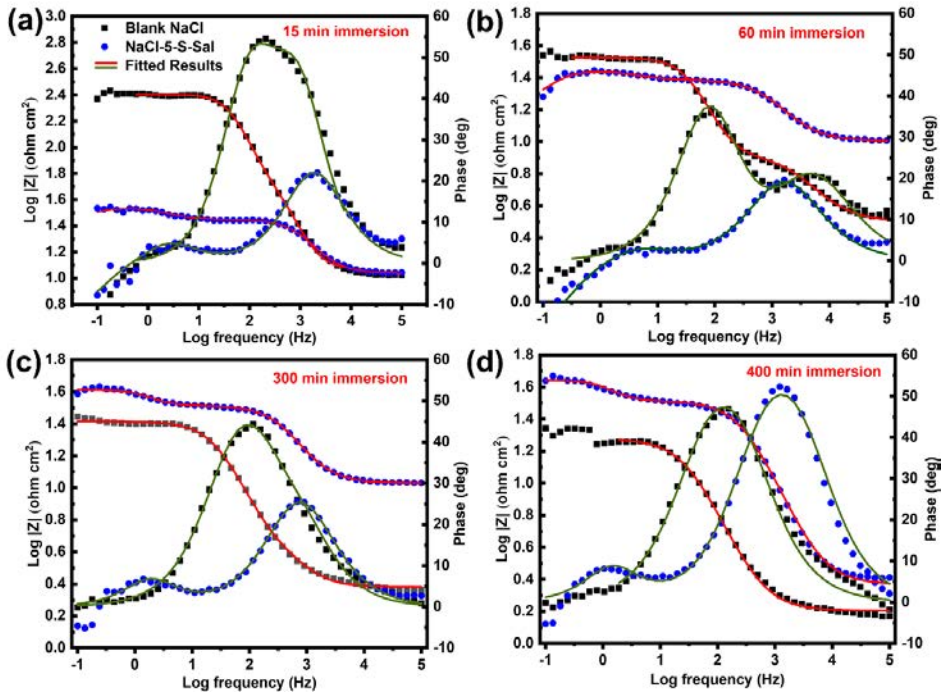

Fig. IV-S1 Bode spectra of impedance modulus *vs* log (Freq) and phase angles *vs* log (Freq) for Mg anode in NaCl electrolyte with and without 5-S-Sal after different times of immersion (a) 15 min; (b) 60 min; (c) 300 min; (d) 400 min.

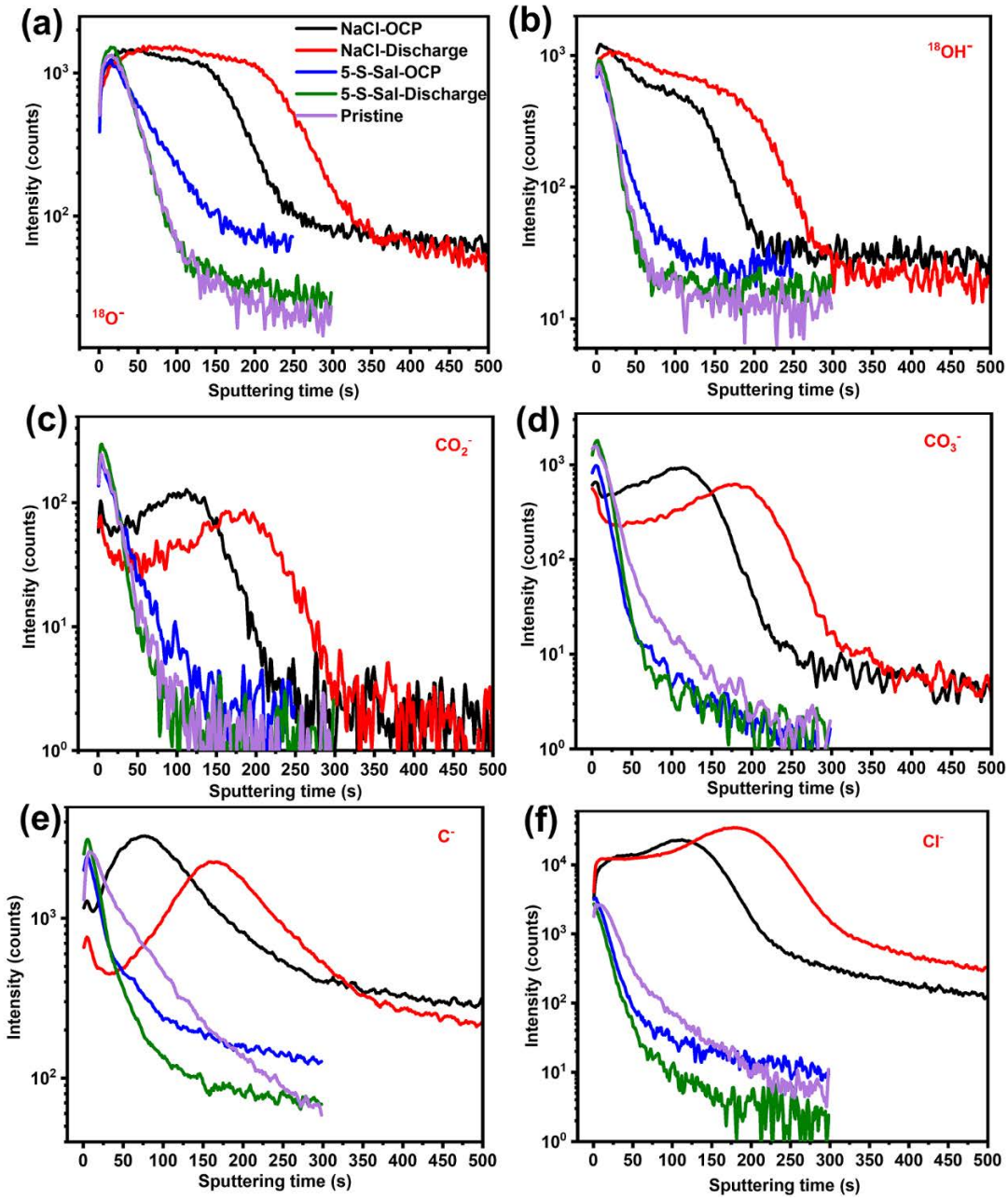

Fig. IV-S2 Comparison of different ToF-SIMS negative ion depth profiles obtained for the passive film formed on Mg anode pristine after polishing, and after 15 min of OCP or discharge test in NaCl electrolyte with and without 5-S-Sal (a) $^{18}O^-$; (b) $^{18}OH^-$; (c) CO_2^-; (c) Cl^-; (d) CO_3^-; (e) C^-; (f) Cl^-.

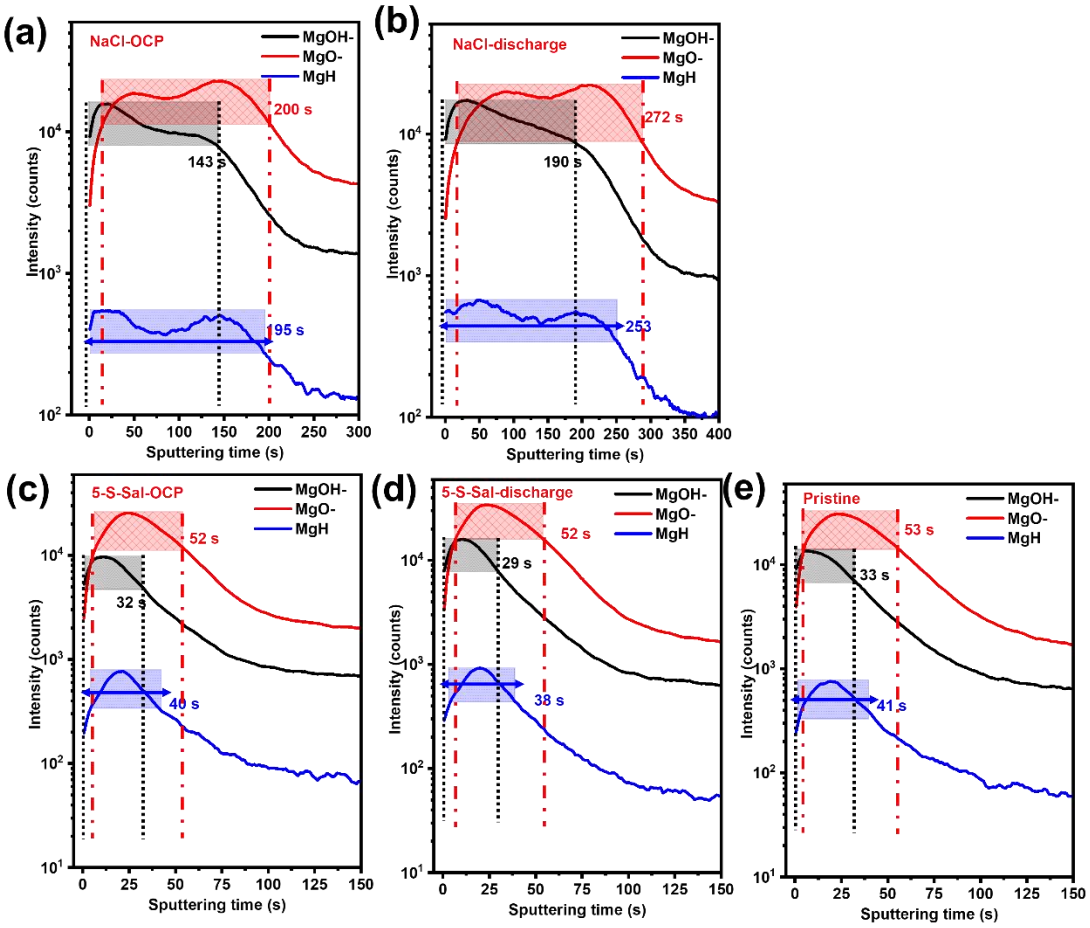

Fig. IV-S3 The comparation of the MgO^-, $MgOH^-$ and MgH^- ToF-SIMS negative ion depth profiles for Mg anode (a-d) 15 min of immersion at OCP and discharge (full cell) in blank 0.6 M NaCl electrolyte and electrolyte with 0.1 M 5-S-Sal inhibitor; (e) the pristine Mg after polishing.

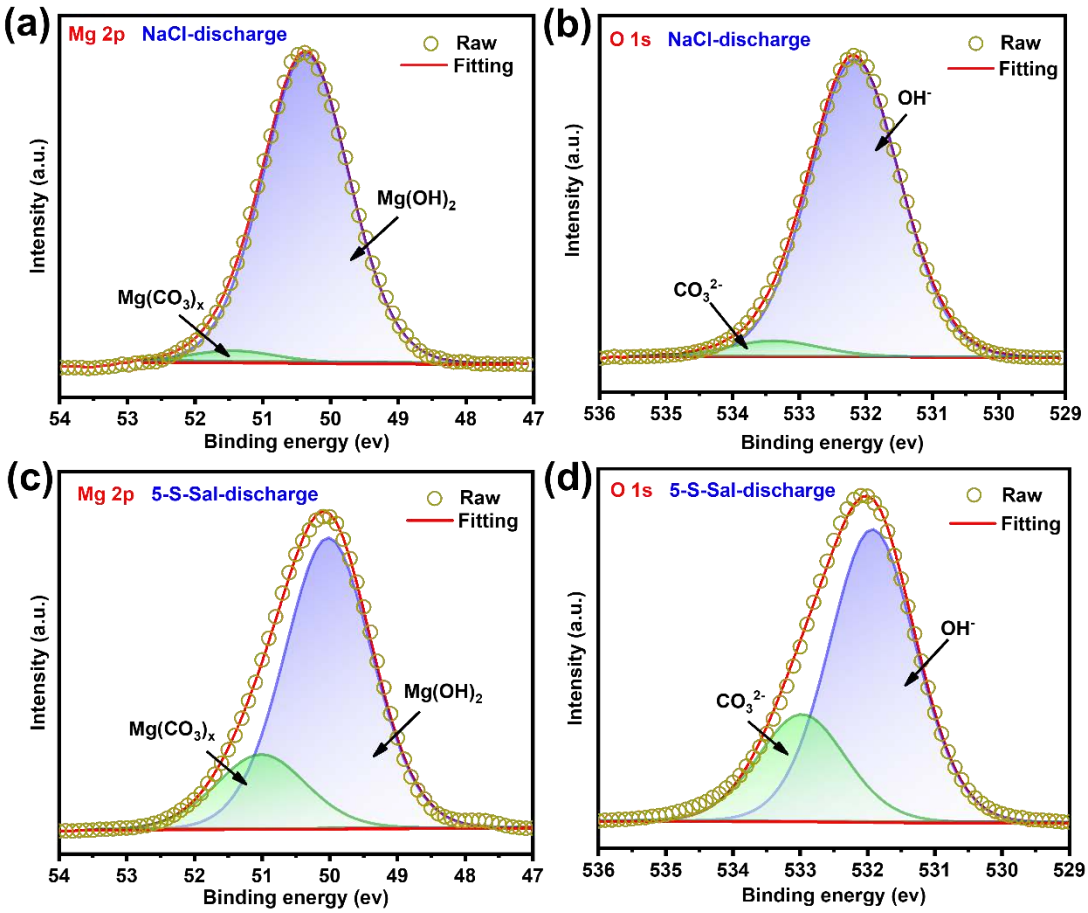

Fig. IV-S4 XPS spectra of Mg 2p core level and O1s core level for Mg anode (a) (b) in blank NaCl electrolyte; (c) (d) in NaCl electrolyte with 5-S-Sal after 15 min OCP test.

Table IV-S2 Atomic % calculated from O1s core level for Mg exposed to different electrolytes at OCP and discharge test.

Atomic% (O 1s)	NaCl-OCP	NaCl-discharge	5-S-Sal-OCP	5-S-Sal-Discharge
$Mg(OH)_2$	93	95	81	83
$MgCO_3$	7	5	19	27

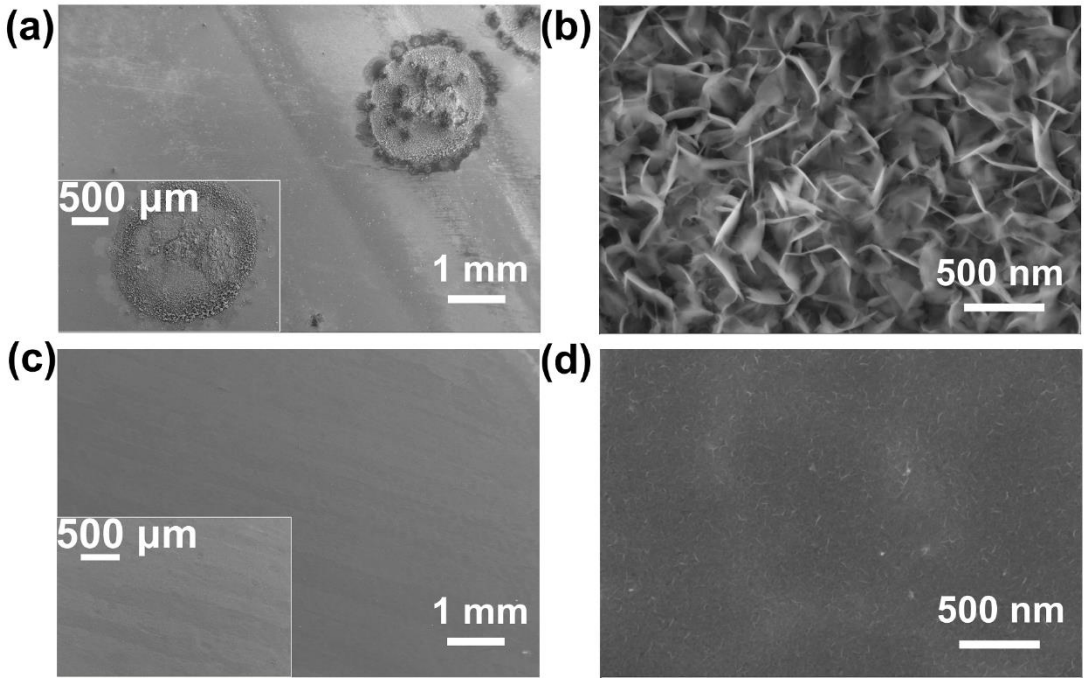

Fig. IV-S5 SEM image of Mg anode surface morphologies after 15 min of discharge test at current density of 0.5 mA/cm^2 (a) in blank NaCl electrolyte (inset figure is the magnification of dark part); (b) the magnified image of uncorroded bright part in a; (c) in NaCl with 5-S-Sal inhibitor (inset figure is the magnified image); (d) the magnified image of b.

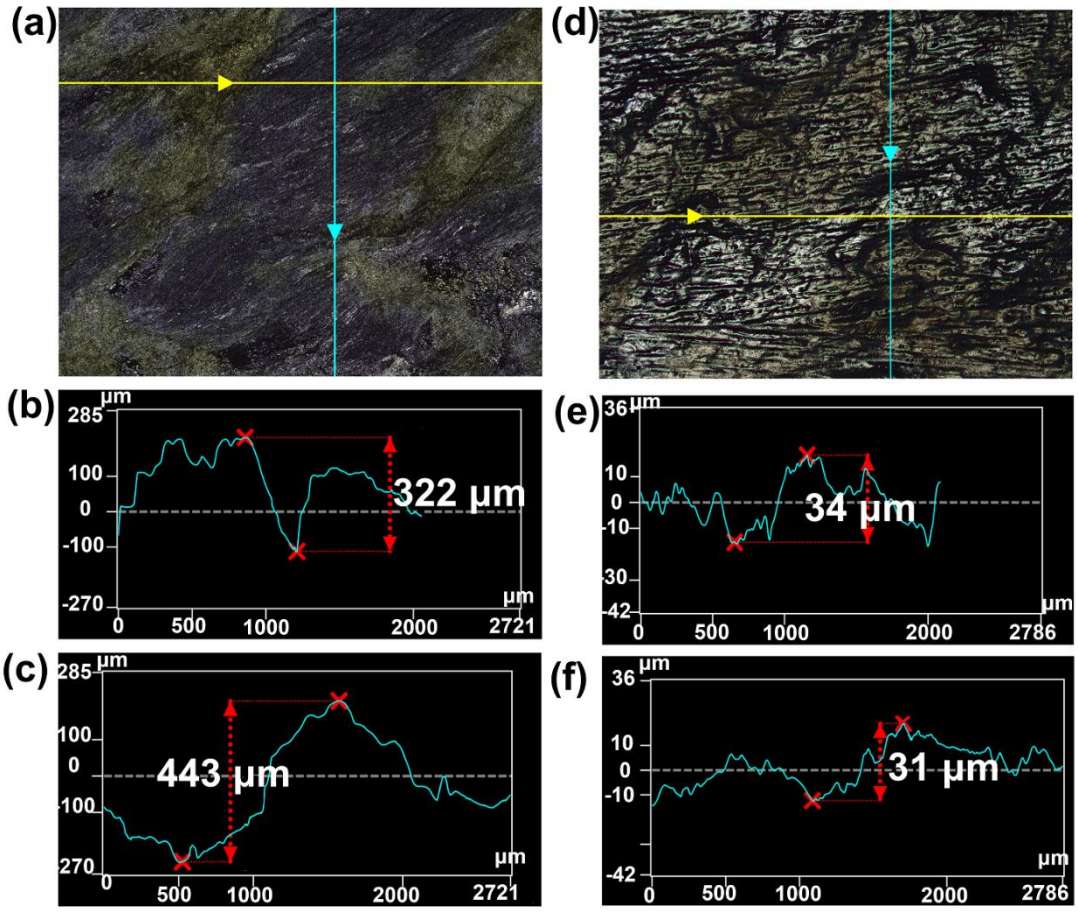

Fig. IV-S6. Three-dimensional (3D) laser microscope of Mg sample anode after 5 h discharge in 0.6 M NaCl without inhibitor (a-c); and (d-f) with 5-S-Sal inhibitor.

IV-References

[1] X. Chen, S. Ning, Q. Le, H. Wang, Q. Zou, R. Guo, J. Hou, Y. Jia, A. Atrens, F. Yu, Effects of external field treatment on the electrochemical behaviors and discharge performance of AZ80 anodes for Mg-air batteries, Journal of Materials Science & Technology, 38 (2020) 47-55.

[2] M. Deng, L. Wang, D. Höche, S.V. Lamaka, D. Snihirova, B. Vaghefinazari, M.L. Zheludkevich, Clarifying the decisive factors for utilization efficiency of Mg anodes for primary aqueous batteries, J Power Sources, 441 (2019) 227201.

[3] T. Zhang, Z. Tao, J. Chen, Magnesium–air batteries: from principle to application, Mater. Horiz., 1 (2014) 196-206.

[4] X. Chen, H. Wang, Q. Zou, Q. Le, C. Wen, A. Atrens, The influence of heat treatment on discharge and electrochemical properties of Mg-Gd-Zn magnesium anode with long period stacking ordered structure for Mg-air battery, Electrochimica Acta, 367 (2021) 137518.

[5] G. Song, Recent Progress in Corrosion and Protection of Magnesium Alloys, Advanced Energy Materials, 7 (2005) 563-586.

[6] J. Li, B. Zhang, Q. Wei, N. Wang, B. Hou, Electrochemical behavior of Mg-Al-Zn-In alloy as anode materials in 3.5 wt.% NaCl solution, Electrochimica Acta, 238 (2017) 156-167.

[7] M. Curioni, The behaviour of magnesium during free corrosion and potentiodynamic polarization investigated by real-time hydrogen measurement and optical imaging, Electrochimica Acta, 120 (2014) 284-292.

[8] G. Williams, N. Birbilis, H.N. McMurray, The source of hydrogen evolved from a magnesium anode, Electrochemistry Communications, 36 (2013) 1-5.

[9] K.A. Yasakau, A. Maltseva, S.V. Lamaka, D. Mei, H. Orvi, P. Volovitch, M.G.S. Ferreira, M.L. Zheludkevich, The effect of carboxylate compounds on Volta potential and corrosion inhibition of Mg containing different levels of iron, Corros Sci, 194 (2022) 109937.

[10] R.M.S. Arthur E. Martell, Critical Stability Constants, Springer, Second supplement (1989).

[11] L. Wang, D. Snihirova, M. Deng, B. Vaghefinazari, S.V. Lamaka, D. Höche, M.L. Zheludkevich, Tailoring electrolyte additives for controlled Mg-Ca anode activity in aqueous Mg-air batteries, J Power Sources, 460 (2020) 228106.

[12] S.V. Lamaka, B. Vaghefinazari, D. Mei, R.P. Petrauskas, D. Hoche, M.L. Zheludkevich, Comprehensive screening of Mg corrosion inhibitors, Corros Sci, 128 (2017) 224-240.

[13] A. Maltseva, S.V. Lamaka, K.A. Yasakau, D. Mei, D. Kurchavov, M.L. Zheludkevich, G. re, P. Volovitch, In situ surface film evolution during Mg aqueous corrosion in presence of selected carboxylates, Corros Sci, 171 (2020) 108484.

[14] J. Yang, C. Blawert, S.V. Lamaka, K.A. Yasakau, L. Wang, D. Laipple, M. Schieda, S. Di, M.L. Zheludkevich, Corrosion inhibition of pure Mg containing a high level of iron impurity in pH neutral NaCl solution, Corros Sci, 142 (2018) 222-237.

[15] S.V. Lamaka, D. Höche, R.P. Petrauskas, C. Blawert, M.L. Zheludkevich, A new concept for corrosion inhibition of magnesium: Suppression of iron re-deposition, Electrochemistry Communications, 62 (2016) 5-8.

[16] G.S. Frankel, A. Samaniego, N. Birbilis, Evolution of hydrogen at dissolving magnesium

surfaces, Corros Sci, 70 (2013) 104-111.

[17] V. Moutarlier, M.P. Gigandet, B. Normand, J. Pagetti, EIS characterisation of anodic films formed on 2024 aluminium alloy, in sulphuric acid containing molybdate or permanganate species, Corros Sci, 47 (2005) 937-951.

[18] N. Wang, W. Li, Y. Huang, G. Wu, M. Hu, G. Li, Z. Shi, Wrought Mg-Al-Pb-RE alloy strips as the anodes for Mg-air batteries, J Power Sources, 436 (2019) 226855.

[19] X. Chen, W. Tian, S. Li, M. Yu, J. Liu, Effect of temperature on corrosion behavior of 3003 aluminum alloy in ethylene glycol–water solution, Chinese Journal of Aeronautics, 29 (2016) 1142-1150.

[20] M. Anik, I.M. Guneşdoğdu, Corrosion characteristics of Alloy AZ63 in buffered neutral solutions, Mater Design, 31 (2010) 3100-3105.

[21] F. Zucchi, V. Grassi, A. Frignani, C. Monticelli, G. Trabanelli, Electrochemical behaviour of a magnesium alloy containing rare earth elements, Journal of Applied Electrochemistry, 36 (2005) 195-204.

[22] T.N. Vu, D. Veys-Renaux, E. Rocca, Potential bioactivity of coatings formed on AZ91D magnesium alloy by plasma electrolytic anodizing, Journal of biomedical materials research. Part B, Applied biomaterials, 100 (2012) 1846-1853.

[23] X. Liu, S. Liu, J. Xue, Discharge performance of the magnesium anodes with different phase constitutions for Mg-air batteries, J Power Sources, 396 (2018) 667-674.

[24] Y. Zhou, B. Wu, G. Lin, Z. Xing, S. Li, L. Deng, D. Chen, D. Yun, S. Xie, Interfacing Pristine C60 onto TiO2 for Viable Flexibility in Perovskite Solar Cells by a Low-Temperature All-Solution Process onto TiO2 for Viable Flexibility in Perovskite Solar Cells by a Low-Temperature All-Solution Process, Advanced Energy Materials, 8 (2018) 1800399.

[25] G.-L. Song, Z. Shi, Corrosion mechanism and evaluation of anodized magnesium alloys, Corros Sci, 85 (2014) 126-140.

[26] J. Li, Q. Jiang, H. Sun, Y. Li, Effect of heat treatment on corrosion behavior of AZ63 magnesium alloy in 3.5 wt.% sodium chloride solution, Corros Sci, 111 (2016) 288-301.

[27] Y.Q. Zhou, B.S. Wu, G.H. Lin, Y. Li, D.C. Chen, P. Zhang, M.Y. Yu, B.B. Zhang, D.Q. Yun, Enhancing Performance and Uniformity of Perovskite Solar Cells via a Solution-Processed C70 Interlayer for Interface Engineering, ACS applied materials & interfaces, 9 (2017) 33810-33818.

[28] A.D. King, N. Birbilis, J.R. Scully, Accurate Electrochemical Measurement of Magnesium Corrosion Rates; a Combined Impedance, Mass-Loss and Hydrogen Collection Study, Electrochimica Acta, 121 (2014) 394-406.

[29] M. Curioni, F. Scenini, T. Monetta, F. Bellucci, Correlation between electrochemical impedance measurements and corrosion rate of magnesium investigated by real-time hydrogen measurement and optical imaging, Electrochimica Acta, 166 (2015) 372-384.

[30] D.S. Guangling Song, The effect of zirconium grain refinement on the corrosion behaviour of magnesium-rare earth alloy MEZ, Journal of Light Metals, 2 (2002).

[31] D.K. Chanda, A. Samanta, A. Dey, P.S. Das, A.K. Mukhopadhyay, Nanoflower, nanoplatelet and nanocapsule Mg(OH)2 powders for adsorption of CO2 gas, Journal of Materials Science, 52 (2017) 4910-4922.

[32] T.B.R. D. Linden, Handbook of Batteries, McGraw-Hill, New York, Handbook of Batteries (2002).

[33] J.O.B. C. Daniel, Handbook of Battery Materials, John Wiley & Sons, Handbook of Battery Materials (2012).

[34] M. Deng, D. Hoche, S.V. Lamaka, D. Snihirova, M.L. Zheludkevich, Mg-Ca binary alloys as anodes for primary Mg-air batteries, J Power Sources, 396 (2018) 109-118.

[35] X. Liu, J. Xue, P. Zhang, Z. Wang, Effects of the combinative Ca, Sm and La additions on the electrochemical behaviors and discharge performance of the as-extruded AZ91 anodes for Mg-air batteries, J Power Sources, 414 (2019) 174-182.

[36] G.-L. Song, Z. Xu, Crystal orientation and electrochemical corrosion of polycrystalline Mg, Corros Sci, 63 (2012) 100-112.

[37] L.G. Bland, K. Gusieva, J.R. Scully, Effect of Crystallographic Orientation on the Corrosion of Magnesium: Comparison of Film Forming and Bare Crystal Facets using Electrochemical Impedance and Raman Spectroscopy, Electrochimica Acta, 227 (2017) 136-151.

[38] D. Mercier, J. Światowska, E. Protopopoff, S. Zanna, A. Seyeux, P. Marcus, Inhibition of Mg Corrosion by Sulfur Blocking of the Hydrogen Evolution Reaction on Iron Impurities, J Electrochem Soc, 167 (2020) 121504.

[39] D. Hoche, S.V. Lamaka, B. Vaghefinazari, T. Braun, R.P. Petrauskas, M. Fichtner, M.L. Zheludkevich, Performance boost for primary magnesium cells using iron complexing agents as electrolyte additives, Scientific reports, 8 (2018) 7578.

[40] A. Seyeux, M. Liu, P. Schmutz, G. Song, A. Atrens, P. Marcus, ToF-SIMS depth profile of the surface film on pure magnesium formed by immersion in pure water and the identification of magnesium hydride, Corros Sci, 51 (2009) 1883-1886.

[41] Y.Z. Y. Q. Zhou, J. T. Li, S. Zanna, A. Seyeux, P. Marcus, J. Światowska Organic/inorganic hybrid electrolyte for enhancing performance of Mg-air batteries Applied surface science, (Submitted) (2022).

[42] J.A. Yuwono, C.D. Taylor, G.S. Frankel, N. Birbilis, S. Fajardo, Understanding the enhanced rates of hydrogen evolution on dissolving magnesium, Electrochemistry Communications, 104 (2019) 106482.

[43] M. Santamaria, F. Di Quarto, S. Zanna, P. Marcus, Initial surface film on magnesium metal: A characterization by X-ray photoelectron spectroscopy (XPS) and photocurrent spectroscopy (PCS), Electrochimica Acta, 53 (2007) 1314-1324.

[44] M. Santamaria, F. Di Quarto, S. Zanna, P. Marcus, The influence of surface treatment on the anodizing of magnesium in alkaline solution, Electrochimica Acta, 56 (2011) 10533-10542.

[45] V. Fournier, P. Marcus, I. Olefjord, Oxidation of magnesium, Surface and Interface Analysis, 34 (2002) 494-497.

[46] Y. Wang, B. Liu, X. Zhao, X. Zhang, Y. Miao, N. Yang, B. Yang, L. Zhang, W. Kuang, J. Li, E. Ma, Z. Shan, Turning a native or corroded Mg alloy surface into an anti-corrosion coating in excited CO2, Nature communications, 9 (2018) 4058.

[47] D. Xue, Y. Yun, M.J. Schulz, V. Shanov, Corrosion protection of biodegradable magnesium implants using anodization, Materials Science and Engineering: C, 31 (2011) 215-223.

[48] B. Flamme, J. Światowska, M. Haddad, P. Phansavath, V. Ratovelomanana-Vidal, A. Chagnes, Sulfone Based-Electrolytes for Lithium-Ion Batteries: Cycling Performances and Passivation Layer Quality of Graphite and LiNi1/3Mn1/3Co1/3O2 Electrodes, J Electrochem Soc, 167 (2020) 070508.

[49] S.H. Salleh, S. Thomas, J.A. Yuwono, K. Venkatesan, N. Birbilis, Enhanced hydrogen evolution on Mg (OH)2 covered Mg surfaces, Electrochimica Acta, 161 (2015) 144-152.

Chapter V Influence of trace acetic acid in $NaNO_3$ aqueous electrolytes for long-lifetime Mg-air batteries

The high rate of hydrogen evolution in traditionally-used NaCl aqueous electrolytes largely impairs the performance of Mg-air batteries and leads to a low utilization, poor specific capacity and low energy density. Thus, the conventional NaCl solute was replaced by $NaNO_3$ and traces of acetic acid as inhibitor were employed. The resulting Mg-air batteries based on an optimized electrolyte show an improved discharge voltage reaching ~1.8 V at current density of 0.5 mA/cm^2 and significantly longer lifetime to more than 360 hours compare to only ~17 hours service time in NaCl electrolyte. The study of chemical composition and morphology of corrosion products allowed for thorough analysis of the working mechanism of Mg anode in this optimized electrolyte. X-ray photoelectron spectroscopy and time-of-flight secondary ion mass spectrometry were used to obtain chemical information on the surface film and scanning electron microscopy combined with transmission electron microscopy were applied to clarify the morphology changes of the surface layer

V-1 Objectives and motivation

The current work investigates the effects of replacing the usually used NaCl solute by $NaNO_3$ in aqueous solvent for Mg-air batteries. Moreover, in order to boost the discharge performance of full Mg-air battery, a low quantity of acetic acid agent as a corrosion inhibitor was added into $NaNO_3$-based electrolyte. The electrochemical measurements combined with the morphology analyses were used to thoroughly analyse the corrosion behaviour of Mg anode in different electrolytes (NaCl in H_2O, $NaNO_3$ in H_2O and $NaNO_3$ in H_2O mixed with acetic acid). Moreover, the composition of the surface film is also of great interest [1-4] in order to better understand the working mechanisms of the Mg-air battery and tailor the Mg anode/electrolyte interface. Thus, we combine analysis techniques such as X-ray photoelectron spectroscopy, time-of-flight secondary ion mass spectrometry,transmission electron microscope (TEM) and scanning electron microscopy to get a better insight into the influence of acetic-acid inhibitor on the corrosion inhibition of Mg in Mg-air batteries. TEM allowed to clarify the morphology and structure of corrosion layer on the Mg anode.

V-2 Experimental overview

The electrolytes were made of 0.6 M NaCl or 0.5 M $NaNO_3$ in ultra-pure H_2O with or without acetic acid (AC). The Mg samples preparation, the instruments and experimental conditions were introduced in chapter II. The specific experimental conditions used here are presented below:

- The EIS and LSV were used to compare the electrochemical performance of Mg in electrolyte of NaCl-H_2O, $NaNO_3$-H_2O and $NaNO_3$-H_2O/AC electrolyte at different times of immersion (15, 30, 60, 300 min).
- OM and 3D-LSM, and SEM were used to study the Mg anode surface morphology after the same times of immersion as aforementioned.
- The cross-section SEM were performed after Mg specimen's immersion in the NaCl-H_2O, $NaNO_3$-H_2O and $NaNO_3$-H_2O/AC electrolytes for 2 hours.
- The volumes of hydrogen evolution were measured during the discharge test in different electrolytes at current density of 5 mA/cm^2 in half cells.

- The same conditions of full Mg-air battery tests were applied that those introduced in chapter III-2.
- ToF-SIMS negative ion depth profiles and XPS spectra were performed after 5 min of immersion in $NaNO_3$ aqueous electrolyte with and without acetic acid.
- The conditions and samples preparation of TEM tests were introduced in the II-5.4.2 section

V-3. Results and discussion

V-3.1 Mg corrosion as a function of the electrolyte

The reactivity of Mg anode in NaCl-H_2O, $NaNO_3$-H_2O and $NaNO_3$-H_2O/AC electrolytes was systematically investigated using the electrochemical impedance spectroscopy (EIS) (Fig. V-1). The constant phase elements (CPE) instead of ideal capacitances were used for fitting all the EIS spectra (Fig. V-1 A). For *n* equal 1, the CPE is considered as a pure capacitor [5-7]. R_{ct} and CPE_{dl} represent a charge transfer resistance and a double capacitance at high-frequency range, respectively, which are related to the reactivity at the electrolyte / metallic substrate interface [6, 8-11]. R_f and CPE_f correspond to a surface resistance and the capacitance, respectively, and can be attributed to the reactivity at the corrosion layer / electrolyte interface [12]. The values of fitting parameters are depicted in Table V-1. As expected from bibliographic studies, a much higher R_{ct} or R_f (266 and 369 Ω.cm^2) can be observed in $NaNO_3$ electrolyte than in NaCl electrolyte (7 and 27 Ω.cm^2). The comparison of EIS as a function of immersion time is present in Fig. V-S1. In NaCl electrolyte a very quick decrease of R_{ct} is observed with the increase of immersion time (Table S1), which indicates the high reactivity of Mg anode in NaCl based electrolyte. However, the $NaNO_3$ electrolyte has clearly a significant beneficial effect on the corrosion properties of Mg anode. Meanwhile, much higher R_{ct} means a low transport properties and slow diffusion of Mg^{2+} through a dense/blocking surface film, which implies the poor discharge performance of full Mg-air battery and thus hinders the application of $NaNO_3$ electrolyte [13]. With the acetic acid added, the R_{ct} and R_f decrease to 79 and 92 Ω.cm^2, respectively, for 300 min of immersion. The corresponding Bode plots (Fig. V-S2) clearly show a decrease of the phase intensity and lower impedance (log |*Z*|) for Mg in $NaNO_3$ electrolyte with acetic acid than in pure $NaNO_3$, especially, for longer immersion times. The highest values

of log |*Z*| at low frequencies observed for all immersion times in $NaNO_3$ further confirms the formation of protective/blocking film on the Mg surface. After the addition of acetic acid, a lowest value of log |*Z*| (2.1 $\Omega.cm^2$) at low frequencies at initial immersion time (15 min) can be observed, which turns to higher value than in NaCl electrolyte at 60 min and close to 2.3 $\Omega.cm^2$ in $NaNO_3$ electrolyte at 300 min. These results denote that $NaNO_3$ as solute in aqueous electrolyte can greatly reduce the corrosion reactivity of Mg anode and the electrolyte containing acetic acid can decrease the charge transfer resistance. It can be concluded that the corrosion behavior of Mg anode in $NaNO_3$-based electrolytes is significantly improved in comparison to the NaCl-H_2O electrolyte.

The optical microscope (OM) images of Mg samples after immersion in different electrolytes are shown in Fig. V-1 B and Fig. V-S1. In NaCl-H_2O electrolyte, the dark spots completely cover the Mg surface after 60 min immersion, but no characteristic dark corrosion spots can be observed in $NaNO_3$-H_2O electrolyte and a very homogenous surface film is formed even after a long-time immersion (300 min). With the addition of acetic acid, the surface morphology is heterogeneous with some bright circles after the immersion time of 15 min and 60 min.

There are no darks spots formed on Mg specimens' surface even after 300 min immersion. As the dark regions are associated to the active Mg dissolution and hydrogen evolution [14-16], it can be concluded here that the corrosion of Mg anode was greatly reduced in $NaNO_3$-based electrolyte [14, 17]. Some white powder-like spots attributed to the corrosion products (such as a mixture of MgO and $Mg(OH)_2$) can be observed (Fig. V-1 b_3) on the Mg anode surface after the specimen drying by filtered compressed air. This layer can be also easy peeled-off, which illustrates that the acetic acid can limit the formation of dense/compact passive film as those formed in $NaNO_3$.

The potentiodynamic polarization curve (Fig. V-1 C) was employed to investigate the cathodic processes (principally the hydrogen evolution reaction) and the anodic reaction (related to the Mg dissolution) [18]. Obviously in $NaNO_3$ electrolyte, both of the cathodic and anodic branches show much lower current densities. Moreover, the corrosion potential is much higher, which indicates much slower dissolution of Mg anode, and it can be further confirmed by the less destroyed surface morphology. However, the $NaNO_3$-H_2O electrolyte can lead to the surface lugging and decrease the activity of Mg as anode in full Mg-air battery setup, such as the lower

discharge performances and battery voltage. With addition of acetic acid, the corrosion potential is almost the same as those observed for NaCl electrolyte, but the current densities of cathodic and anodic branches are lower. Furthermore, the polarization tests as a function of immersion time are shown in Fig. V-S1. The tendency is consistent with the EIS results for Mg immersion in NaCl-H_2O electrolyte, showing the cathodic current density significantly higher with the increase of immersion time from 15 min to 60 min. The scarce changes in electrolyte of $NaNO_3$-H_2O and $NaNO_3$-H_2O/AC denote the stable corrosion behaviors of Mg anode.

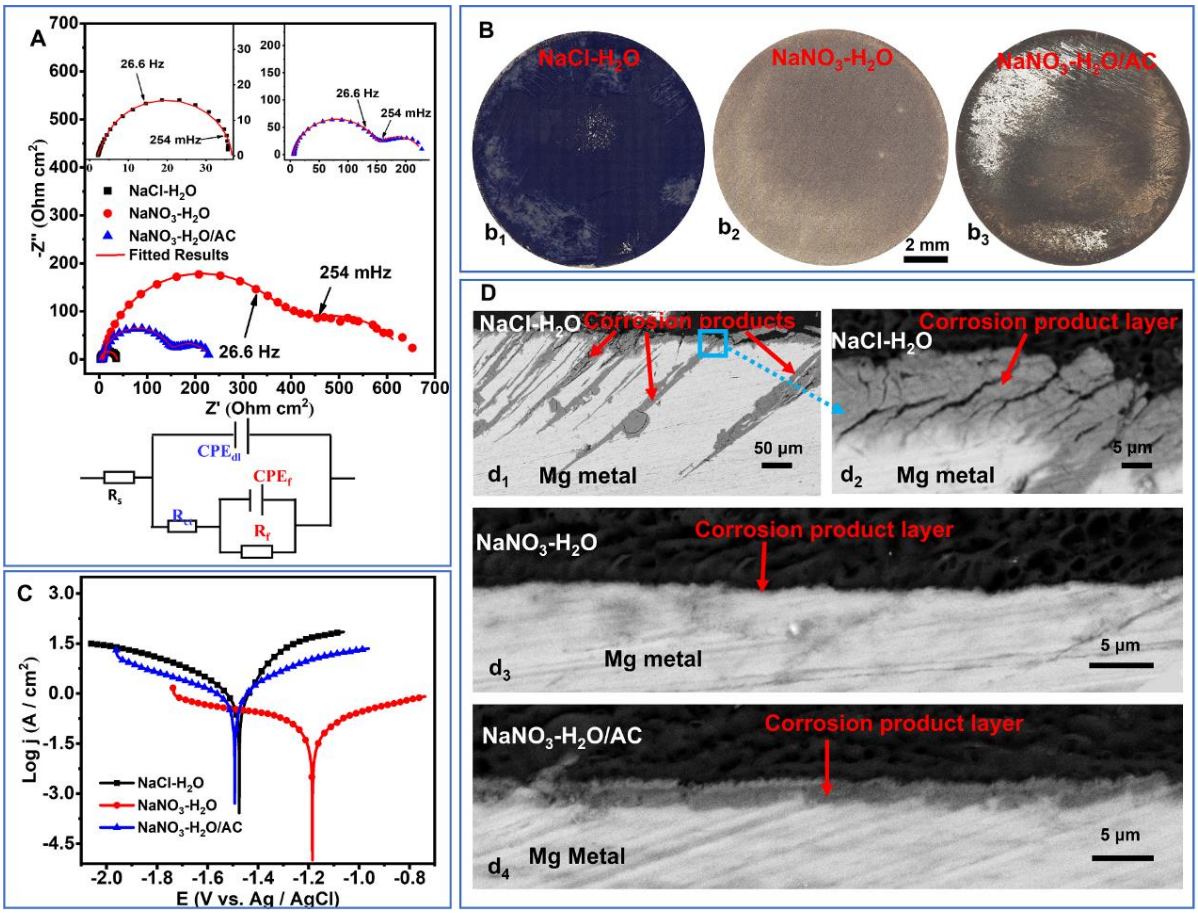

Fig. V-1 The corrosion behavior of Mg anode in NaCl-H_2O, $NaNO_3$-H_2 and $NaNO_3$-H_2O/AC electrolytes (A) electrochemical impedance spectra; (B) optical microscope images; (C) polarization curves; and (D) cross-sectional SEM image of Mg surface morphologies after 2 hours immersion.

To have a better insight into the corrosion evolution in the bulk of Mg electrode and a distribution of the corrosion products as a function of electrolyte, the cross-sectional SEM (in the BSE mode) of Mg specimens was performed after 2 hour-immersion in different electrolytes (Fig. V-1 D). In NaCl-H_2O electrolyte, several hundred microns of elongated (long strip) corrosion defects extend inside the Mg substrate. The higher magnification image (Fig. V-1 d_2) d_2) shows that the interface is pretty rough and loose with several deep pits and corrosion cavities. Interestingly, chlorides can be observed in these cavities as demonstrated by the EDS analysis in Fig. V-S3 A. A very thin corrosion film is observed in $NaNO_3$-H_2O electrolyte (Fig. V-1 d_3), and a slightly thicker but relatively homogenous layer in $NaNO_3$-H_2O/AC electrolyte, which is consistent whit the results of OM (Fig. V-1 b_3). Furthermore, the thickness of the corrosion product film was briefly estimated by the line scan EDS analysis of O, Mg, C and Cl elements (Fig. V-S4) showing thicknesses of around 12.2, 1.0 and 2.6 μm for Mg immersed in electrolytes of NaCl-HO_2, $NaNO_3$-H_2O and $NaNO_3$-H_2O/AC, respectively. These results are consistent with the impedance and polarization measurements.

Table V-1 EIS data fitting parameters retrieved from the spectra fitting obtained for Mg anode in NaCl-H_2O, $NaNO_3$-H_2O and $NaNO_3$-H_2O/AC electrolytes after 300 min of immersion.

	NaCl-H_2O	$NaNO_3$-H_2O	$NaNO_3$-H_2O/AC
R_s (Ω cm^2)	8	9	6
R_{ct} (Ω cm^2)	7	266	79
CPE_{dl} (Ω^{-1} cm^{-2} s^n)	0.2×10^{-3}	0.9×10^{-3}	3.4×10^{-3}
n_1	0.96	0.69	0.83
R_f (Ω cm^2)	27	369	92
CPE_f (Ω^{-1} cm^{-2} s^n)	0.2×10^{-3}	10×10^{-6}	24×10^{-6}
n_2	0.95	0.93	0.92

V-3.2 Effect of electrolyte on full cells properties

The above comprehensive analysis has clarified the influence of electrolytes on Mg anode corrosion behavior. In the following part, the performance of full Mg-air battery and the hydrogen evolution test during the discharge test as function of electrolyte are demonstrated.

The hydrogen evolution during the battery discharge is one of the serious problems, which causes the decrease of anode utilization [19]. Thus, the volume of evolved hydrogen during the

half cells discharge test in different electrolytes was performed (Fig. V-2 A). A quasi-exponential increase of H_2 evolution in the NaCl aqueous electrolyte with a total mean value of 43 ml/cm^2 at 400 min is observed. However, the significantly lower amount of H_2 can be detected in electrolyte of $NaNO_3$-H_2O with less than 10 ml/cm^2 after 1400 min. With addition of the acetic acid, the mean value is slightly lower than in $NaNO_3$ electrolyte. These results illustrate the low corrosion of Mg anode in $NaNO_3$-based electrolytes, which agrees with previous reports [13, 20, 21]. Besides, the acetic acid is beneficial for the Mg corrosion inhibition and prolong the discharge service time of Mg-air battery.

The discharge curves of full Mg-air batteries (in Fig. V-2 B) show much lower discharge voltage (1.3 V) in $NaNO_3$ in comparison to NaCl electrolyte at current density of 0.5 mA/cm^2. Even though, the discharge lifetime of Mg anode is significantly prolonged while Mg specimens are completely damaged only after 17.5 hours in NaCl electrolyte. The severe corrosion areas with black discharge products covering the Mg surface after only 5 min of discharge test (the cracked and heterogenous layer in the inset images) are observed by SEM (Fig. V-C-E). The surface completely covered by the discharge products with several huge cracks (inset image), allowing for the diffusion of chlorides into the magnesium metal substrate, was observed after 30 min of discharge test (Fig. V-S5 A). After 5-hour discharge test, the specimens were seriously damaged (Fig. V-S6 A). These results, showing very deep defects and heterogenous corrosion in NaCl electrolyte, confirm cross-section SEM results (Fig. V-1 d_1). Consequently, the severe corrosion leads to the short discharge service time of full Mg-air battery. Notably, in $NaNO_3$-H_2O/AC, the discharge potential increases to around 1.8 V for the initial 5 hours' test which is of around 500 mV higher than in $NaNO_3$-H_2O electrolyte. Unfortunately, the discharge potential is unstable and drop to 1.59 V after 10 hours, which may be attributed to a decrease of acetic acid content. From one side the acetic acid is easy to volatilize in the open battery system, from another side, it can be consumed by absorbtion on the Mg surface. In $NaNO_3$-H_2O electrolyte (Fig. V-2 c_2), Mg anode surface is homogenous and clean without dark areas, which is consistent with the OM images. A dense flake-like structure characteristic of magnesium oxide-hydroxide [22, 23] can be observed as illustrated in the inset figure. The surface morphology after longer discharge tests (30 min and 5 hours) is shown in Fig. V-S5 B and Fig. V-S6 B (b_3 and b_4). The modifications of morphology are less significant in comparison to the initial 5 min of discharge. Combining these results with the electrochemical analysis (EIS and LSV), it can be confirmed,

that a very dense protective surface film is formed on Mg anode. In the electrolyte with acetic acid added, SEM image (Fig. V-2 c_3) illustrates a different grayscale color images and the inset image shows no flake-like $Mg(OH)_2$ structure on the surface. It can indicate some differences in the composition of the corrosion product layer, which will be further investigated by XPS, ToF-SIMS and TEM.

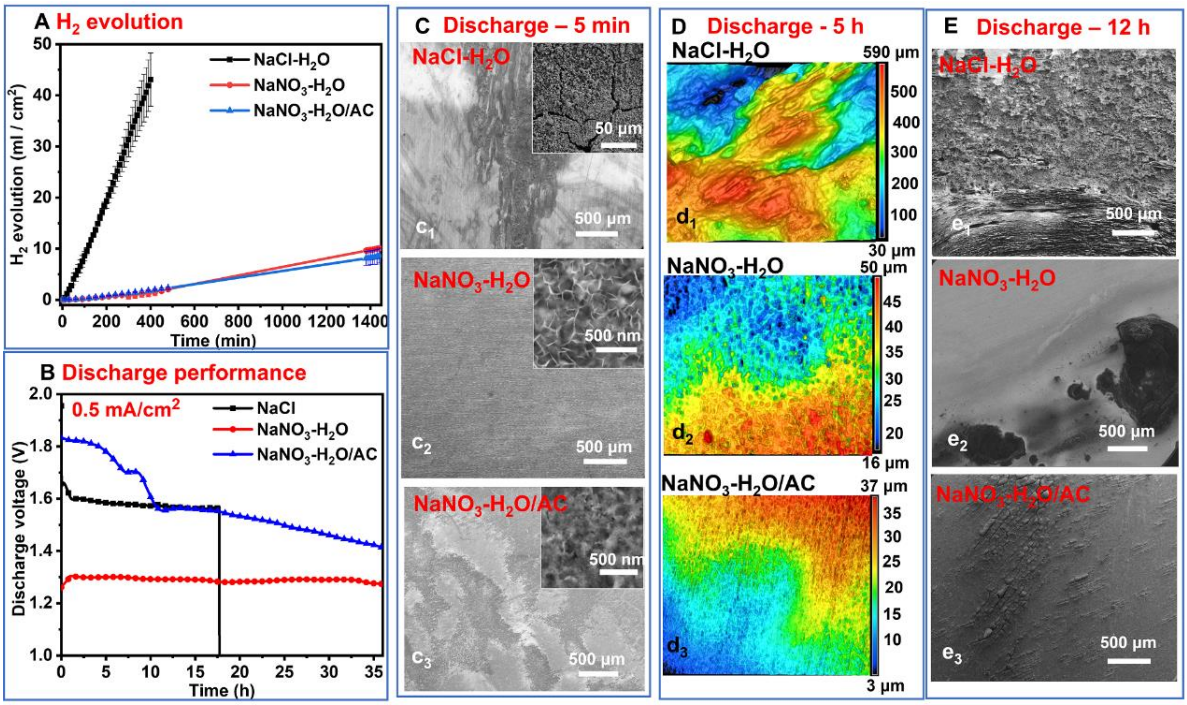

Fig. V-2 Mg-air battery tests in NaCl-H_2O, $NaNO_3$-H_2O and $NaNO_3$-H_2O/AC electrolytes A) H_2 evolution test of half Mg-air battery at current density of 5 mA/cm^2; (B) discharge tests of full Mg-air batteries at current density of 0.5 mA/cm^2; (C) surface SEM image of Mg anodes after 5 min of discharge; (D) the three-dimensional topography laser microscope of Mg anode surface after 5 hours of discharge test; and (E) surface SEM image of Mg samples after 12 hours of discharge test.

To demonstrate the influence of electrolyte on the roughness of surface corrosion, the 3D laser microscope images were performed (Fig. V-2 D). The z scale span is significantly lower for $NaNO_3$-H_2O (from 16 to 50 µm) and $NaNO_3$-H_2O/AC (from 3 to 37 µm) electrolytes than for NaCl-H_2O electrolyte (30 µm to 590 µm), implying much lower surface roughness of the Mg

anode exposed to the $NaNO_3$-based electrolytes. It indicates a significant corrosion inhibition in these electrolytes. Despite a formation of some dark discharge products on the Mg surface after longer discharge times tests (12 hours) in $NaNO_3$-H_2O electrolyte (Fig. V-2 E), a homogenous layer without darks corrosion products can be observed in $NaNO_3$-H_2O/AC electrolyte. It means that the acetic acid can prevent the formation of black corrosion products, which is beneficial to discharge behaviour of Mg-air battery. The analyses of morphology corroborate with the H_2 evolution measurements discussed hereabove.

3.3 Influence of acetic acid inhibitor on discharge performance

The above investigations have proved that the $NaNO_3$ based electrolyte can significantly decrease the Mg corrosion and prolong the lifetime of Mg-air batteries. However, few researches have been devoted to investigate the influence of inhibitors on the discharge behaviour of Mg-air batteries. Thus, this part presents more details about the discharge performance of Mg anode in $NaNO_3$ electrolyte with and without acetic acid. The discharge performance of half-cells as function of current density (0.5, 5, 10, and 20 mA/cm^2) is present in Fig. V-2 A. It is interesting to note a rapid change of the discharge voltage at initial stages of discharge at different current densities in $NaNO_3$ electrolyte. It can be attributed to the native oxide surface film breakdown and can be a detrimental factor for stability of Mg anode [13]. However, in presence of acetic acid, the modifications of the discharge potentials are less abrupt, which can point to a better surface stability of Mg anode and easier ionic (Mg^{2+}) transfer. The surface film reactivity and the surface film properties were already discussed on the basis of EIS results showing a little lower R_{ct}. Therefore, the addition of acetic acid is beneficial for the discharge voltages (the average values were more negative by about 90, 60, 40 and 30 mV at current densities of 0.5, 5, 10, and 20 mA/cm^2 than without acetic acid, respectively). The smaller voltage differences with the increase of current densities can be influenced by IR drop but also by diffusion overpotential and charge transfer process as shown in our previous studies [24].

The influence of different quantity of acetic acid in 0.5 M $NaNO_3$ (0.1, 0.5, 0.75 and 1 vol%) on the discharge performance of full Mg-air cells at 0.5 mA/cm^2 was studied (Fig. V-3 B). Notably, the battery can keep more than 360 hours of discharge time in presence of 0.5 vol% acetic acid, which is a huge improvement in comparison to the NaCl-H_2O electrolyte (only ~17

hours in Fig. V-2 B). The acetic acid is a principal responsible for the decreased of Mg anode corrosion [25-27]. Unfortunately, the discharge potential is not stable as already discussed above. The discharge voltage can return to higher values upon addition of the acetic acid during the experiment, however these results are not shown here and can be the object of future investigations. For the low quantity of acetic acid (0.1 vol%), the discharge potential drops down immediately and the similar values can be observed as for electrolyte without AC after 23 hours. Too low concentrations of acetic acid cause the unstable discharge voltage due to its fast evaporation. For the slightly higher concentration of acetic acid (0.75 vol% and 1 vol%) the battery lifetime is significantly prolonged to 277 hours and 191 hours, respectively. However, a decrease of lifetime with higher concentrations can lead to Mg metal dissolution. It indicates that there is a concentration threshold. It seems that 0.5 vol % acetic acid in $NaNO_3$ electrolyte is a good compromise between the sufficiently high cell voltage and long battery lifetime. Furthermore, for this concentration of acetic acid, the discharge voltage increases from ~1.13 V to ~1.35 V at higher current densities (2.5 mA/cm^2) with reference to electrolyte without AC (Fig. V-3 C). The discharge voltages decrease with increase of current density in both electrolytes (Fig. V-3 D). It is worth to note, that at high current densities *e.g.* 20 mA/cm^2, the discharge voltage is only 0.2 V in $NaNO_3$ electrolyte, which indicates that this electrolyte is not suitable for application at the high current discharge tests. However, the addition of acetic acid, greatly improves the discharge voltage to around 0.8 V. The voltage increase in electrolyte with the presence of AC is also observed for lower current densities of around +400 mV (for 0.5 mA/cm^2), +200 mV (for 2.5 mA/cm^2), +280 mV (for 5 mA/cm^2) and +450 mV (for 10 mA/cm^2). These results indicate that the acetic acid can significantly improve the battery discharge performance especially at higher current densities.

The corresponding SEM morphology analysis of Mg samples after discharge test (Fig. V-3 E and F) shows that the surface morphology is totally different after the addition of acetic acid. Notably, after 12 hours discharge test, a more homogenous surface is observed in electrolyte with acetic acid, which indicates a better stability of Mg anode and a reduced corrosion. The analysis of working mechanism of acetic acid in $NaNO_3$-based electrolyte will be further investigated by XPS and ToF-SIMS and combined with high-magnification morphology and crystallographic structure analysis (TEM, XRD).

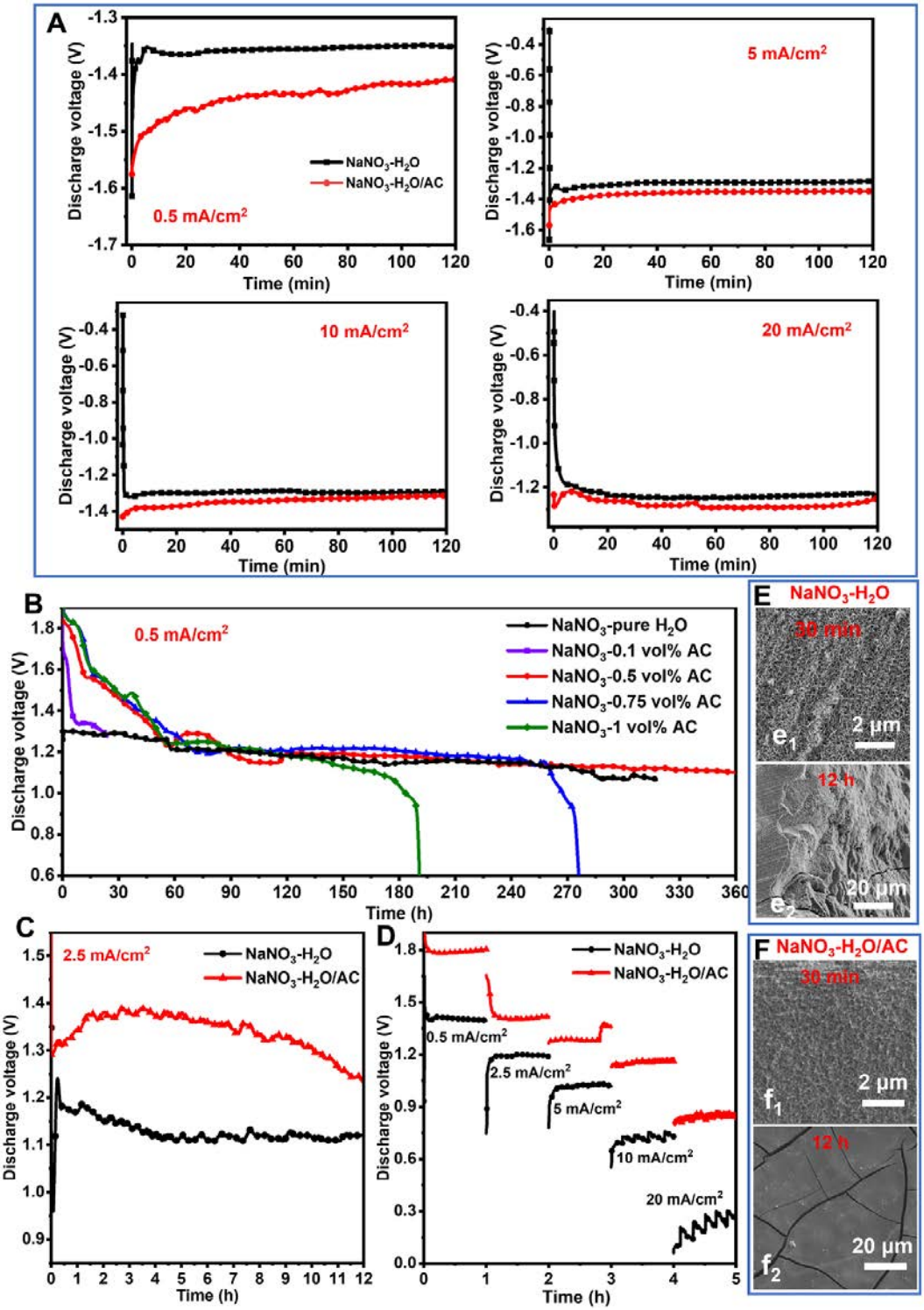

Fig. V-3 Discharge curves of Mg-air battery in $NaNO_3$-H_2O and $NaNO_3$-H_2O/AC electrolytes and corresponding SEM morphology (A) a comparison of the discharge performance in half Mg-air battery cell at different current densities; (B) influence of different concentrations of

acetic acid in $NaNO_3$-H_2O electrolyte for long discharge time in full Mg-air battery; (C) discharge performances of full Mg-air batteries at current density of 2.5 mA/cm^2; (D) influence of different current densities on performance of full Mg-air battery; (E) SEM images of Mg anode after different immersion times (30 min and 12 h) of discharge tests of Mg-air full battery in $NaNO_3$-H_2O; and (F) in $NaNO_3$-H_2O/AC electrolytes.

The FIB-SEM images of Mg electrode in $NaNO_3$ electrolyte with and without acetic acid are shown in Fig. V-4 A. In $NaNO_3$-H_2O electrolyte, the magnesium hydroxide grows vertically upwards on Mg metal substrate, but the flake-like $Mg(OH)_2$ seems to be collapsed due to the focused ion beam. The surface morphology is totally different when acetic acid is added to electrolyte and shows the lamellar-like morphology.

For a better understanding of the role of acetic acid, ToF-SIMS negative ion depth profiles were performed in $NaNO_3$ and $NaNO_3$ with AC electrolytes (Fig. V-4 E and Fig. V-4 F). Fig. V-4 D shows a superposition of all profiles for both samples. The ions attributed to the corrosion products (MgO^-, $MgOH^-$, $MgCO_3^-$, MgH^-, NO_2^-) were selected for comparison. All depth profiles (expect for NO_2^-) for $NaNO_3$-H_2O and $NaNO_3$-H_2O/AC electrolytes are almost overlapped in the range from 250 to 650 s of sputtering time (Fig. V-4 D). It indicates that the chemical composition and distribution of species within the corrosion films are very similar. However, an extra and/or thicker layer with some new species such as $COOH^-$ and NO_2^- is present over the Mg anode surface in electrolyte with acetic acid (shown in Fig. V-4 F). The significant changes in the surface morphology (Fig. V-4 A) can confirm the formation of the new compounds on the surface and the additional and/or thicker surface layer. The details of surface morphology will be further investigated by TEM. The MgO^-, $MgOH^-$, $MgCO_3^-$ and MgH^- ions correspond to the components of passive or corrosion layer (magnesium oxide, hydroxide, carbonate and hydride, respectively). A rapid ion intensity change during the first tens of seconds of sputtering, is attributed to the time needed to reach a stationary condition. Similarly to the previous studies, 80 % of maximum intensity of MgO^- signal decrease was employed to define the position of the metal/oxide interface [24, 28]. The thicknesses of the surface layer in $NaNO_3$ electrolyte without and with acetic acid are ~25 nm and ~54 nm, respectively. The calculation was performed by assuming the sputtering rate of 0.1 nm/s estimated for the same measurements conditions in our previous work [24]. These results

confirm the cross-sectional SEM (in Fig. V-1 d_3 and d_4) demonstrating that the addition of acetic acid leads to the thickness increase of the surface layer. It should be noted that the thicknesses are much smaller here due to the much shorter immersion time (5 min for ToF-SIMS *vs* 2 h for cross-section SEM analysis). The ToF-SIMS ion depth profiles indicate the formation of the typical duplex layer structure with an outer Mg hydroxide and an inner Mg oxide layer (with the maximum intensity of $MgOH^-$ signal in the beginning of sputtering time and MgO^- maximum intensity shifted to longer sputtering time). Interestingly, the sudden intensity of $MgOH^-$ signal decrease in electrolyte of $NaNO_3$ (as well as $^{\wedge 18}OH^-$ signal in Fig. V-S8), can indicate a lower corrosion rate of Mg anode in $NaNO_3$ electrolyte. As already discussed previously, the high quantity of $Mg(OH)_2$ can catalyze the HER [29, 30] and enhance the rates of hydrogen evolution [31]. Besides, Fig. V-S9 A and B show that after 15 min of immersion, the total oxide-hydroxide layer thickness in $NaNO_3$ is far thinner than in NaCl, which also indicates that Mg is less prone to corrosion in $NaNO_3$ electrolyte. For $NaNO_3$ electrolyte with acetic acid, the $COOH^-$ and NO_2^- signals are located in the outer part of the oxide surface, while MgH^- is located between MgO^- and $MgOH^-$ as already observed in our former studies [24]. It should be noted that, that a low NO_2^- signal intensity was detected on the surface of Mg anode despite the application of $NaNO_3$-based electrolyte (see also Fig. V-S8). In agreement with these results, XPS spectra of N 1s core level region (Fig. V-S7) shows that there is no N-like species detected in $NaNO_3$ electrolyte however some traces of N-like species (most probably nitrites and nitrates) can be detected in electrolyte with AC. The increase of the surface layer thickness with the prolonged immersion time (1, 7, and 15 min) in the electrolyte with acetic acid is demonstrated in Fig. V-S 9 C-D. Furthermore, after the discharge tests (Fig. V-S10) more significant layer thickness can be observed in electrolyte with acetic acid, which illustrates that the Mg anode can easily react in this electrolyte, which results in the improvement of discharge performance.

Fig. V-4 B and C show the XPS spectra of Mg 2p and O 1s core level regions for the Mg anode exposed to $NaNO_3$ electrolyte without and with acetic acid after 5 min OCP. Obviously, in electrolytes with acetic acid, the peaks width becomes larger, indicating a presence of several, additional components. The identification of magnesium compounds was performed using a decomposition of Mg 2p and O 1s and combined with the ToF-SIMS results. The position of the hydrocarbons from C 1s signal (-CH-CH-) in the contamination layer was used for the

binding energy correction. Table V-2 depicts the atomic % and the binging energies of all compounds (from Mg 2p and O 1s peak fitting). However, this quantitative analysis (atomic %) can remain affected by error, due to very rough surfaces on which usually the surface analysis by XPS has serious limitations. It is also possible that around 10 % higher quantity of hydroxide *vs* oxide species observed on the surface exposed to electrolyte with AC inhibitor is in the range of error. The Mg 2p spectra show signals at 50.5 eV and 51.3 eV corresponding to $Mg(OH)_2$ and $Mg(CO_3)_x$ compounds in agreement with the previous studies [1, 32, 33]. Besides, the O 1s spectrum shows peaks corresponding to OH^- (532.2 ± 0.1 eV) and CO_3^{2-} (533.6 ± 0.1 eV). However, the binding energy shift of around -1 eV can be observed for the MgO for Mg peaks in electrolytes with AC compared to electrolyte without AC. The explanation of this shift will be further discussed in the TEM part (Fig. V-S 11). It is interesting to note that an extra peak can be observed at higher binding energies of 52.4 eV for Mg 2p and 534.6 eV for O 1s. This peak can be attributed to the new species formed on the Mg surface origination from carboxylic acid ($COOH^-$) or NO_x^- species from $NaNO_3$, as shown by ToF-SIMS results. As previously demonstrated most of the organic inhibitors can adsorb on the metal surface [26, 34-36], among others, the -COOH from acetic acid [37].

Table V-2. Atomic % and binding energies of Mg 2p and O1s for Mg anode after 5 min of immersion in $NaNO_3$-H_2O and $NaNO_3$-H_2O/AC electrolytes.

		$NaNO_3$-H_2O			$NaNO_3$-H_2O/AC			
		$Mg(CO_3)_x$	$Mg(OH)_2$	MgO	Oxide film-NO_x-$(COOH)_x$	$Mg(CO_3)_x$	$Mg(OH)_2$	MgO
O 1s	Binding energy (ev)	533.5	532.1	531.8	534.6	533.7	532.2	530.8
Mg 2p	Binding energy (ev)	51.3	50.5	50.2	52.4	51.3	50.5	49.2
	Atomic (%)	49.2	10	40.8	20.7	11.2	18.3	49.8

Summarizing the surface morphology analysis by FIB-SEM and chemical analysis by ToF-SIMS and XPS, it can be concluded that the traces of acetic acid inhibitor in $NaNO_3$ electrolyte significantly influences the surface morphology and the surface layer thickness. The principal layer compounds such as MgO, $Mg(OH)_2$, $MgCO_3$ and their distribution in the oxide surface film is not significantly modified. However, with the addition of acetic acid, the nitrate/nitrites

can decompose and adsorb together with carboxylic acid leading to formation of more robust and corrosion resistant layer, but sufficiently permeable for ion diffusion allowing to improve the electrochemical performances of Mg-air battery.

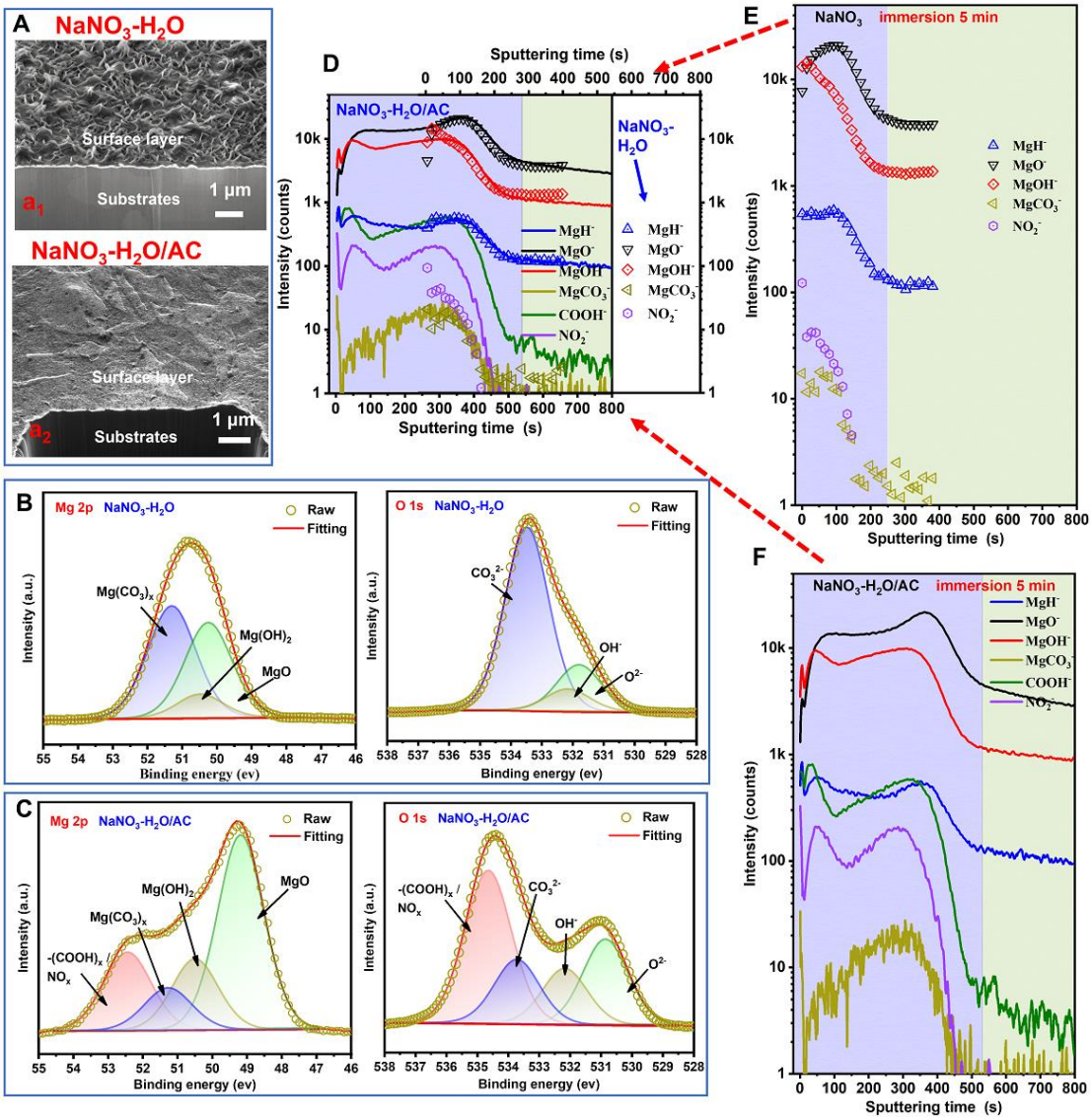

Fig. V-4 (A) Cross-sectional SEM images after focused-ion beam (FIB) milling, and the chemical compositional characterization of Mg anode in $NaNO_3$ and $NaNO_3$ with AC electrolytes after 5 min of immersion. XPS spectra of Mg 2p and O1s core levels; (B) $NaNO_3$-H_2O; (C) $NaNO_3$-H_2O/AC electrolyte; ToF-SIMS negative ion depth profiles; (D) the superposition of E and F; (E) $NaNO_3$-H_2O (F) $NaNO_3$-H_2O/AC electrolyte.

Fig. V-5 A and D show the X-ray diffraction (XRD) patterns of the Mg corrosion products obtained after immersed in $NaNO_3$-H_2O and of $NaNO_3$-H_2O/AC electrolytes. Two kinds of diffraction peaks are related to Mg metal and $Mg(OH)_2$, respectively. All diffraction peaks correspond to $Mg(OH)_2$ trigonal system (PDF#04-016-4785). Transmission electron microscopy (TEM) was further applied to characterize the corresponding corrosion products and the trigonal crystal system of $Mg(OH)_2$ is explicitly verified by the electron diffraction pattern (inset of Fig. V-1 B and E) in accordance with lattice planes of the trigonal system. However, the morphology of the specimens demonstrates significant differences, as shown by the bright field images in Fig. V- 5 B and E. Each of this morphology is well consistent with the SEM observations (Fig. V-4 a_1 and 4 a_2), respectively. The typical flake-like $Mg(OH)_2$ morphology is shown after exposition to $NaNO_3$-H_2O electrolyte and the lamellar-like morphology is characteristic for the sample exposed to electrolyte with acetic acid. The higher magnification (in Fig. V-5 C and F) clearly indicates the differences in morphology. Fig. V-S 11 shows the diffraction patterns of MgO at zone axis in Fig. V-S 11 a_1 and b_1. Although they are the same kind of MgO as the lattice parameters are the same, the crystal orientation distributions are quite different. The high-resolution imaging (Fig. V-S 11) reveals that the MgO precipitates are of nanometric sizes dispersed in the parent $Mg(OH)_2$ phase. It was observed that the MgO precipitation happened in $Mg(OH)_2$ phase due to the heating by electron beam. The MgO precipitation process took less than 5 minutes until the total disappearance of the diffraction spots of $Mg(OH)_2$ phase. During the precipitation, the parent $Mg(OH)_2$ crystalline phase transforms into crystalized MgO nano-precipitates in an amorphous matrix (Fig. V-S11 a_4, a_5, b_4, b_5). As the building block of flack-like or lamellar structure of the corrosion products, it is evidenced that each flack or lamella of $Mg(OH)_2$ phase is a single crystal. In the $NaNO_3$-H_2O specimen, the diffraction pattern (Fig. V-S11 a_1) of the corrosion product (Fig. V-S11 a_2) demonstrates a series of diffraction rings, indicating that the product has a polycrystalline structure. The $Mg(OH)_2$ flacks are almost randomly orientated in the bulk of corrosion product. A dark field image (Fig. V-S11 a_3) shows the morphology and distribution of a set of flacks in the same orientation. In the case of $NaNO_3$-H_2O/AC specimen, the microstructure of the corrosion product is composed by stacking of lamellar layers. The electron diffraction (Fig. V-S11 b_1) along the axis normal to the lamella stack (Fig. V-S11 b_2) shows a single crystal pattern. It suggests that the lamellae in the stack are of similar crystalline orientation.

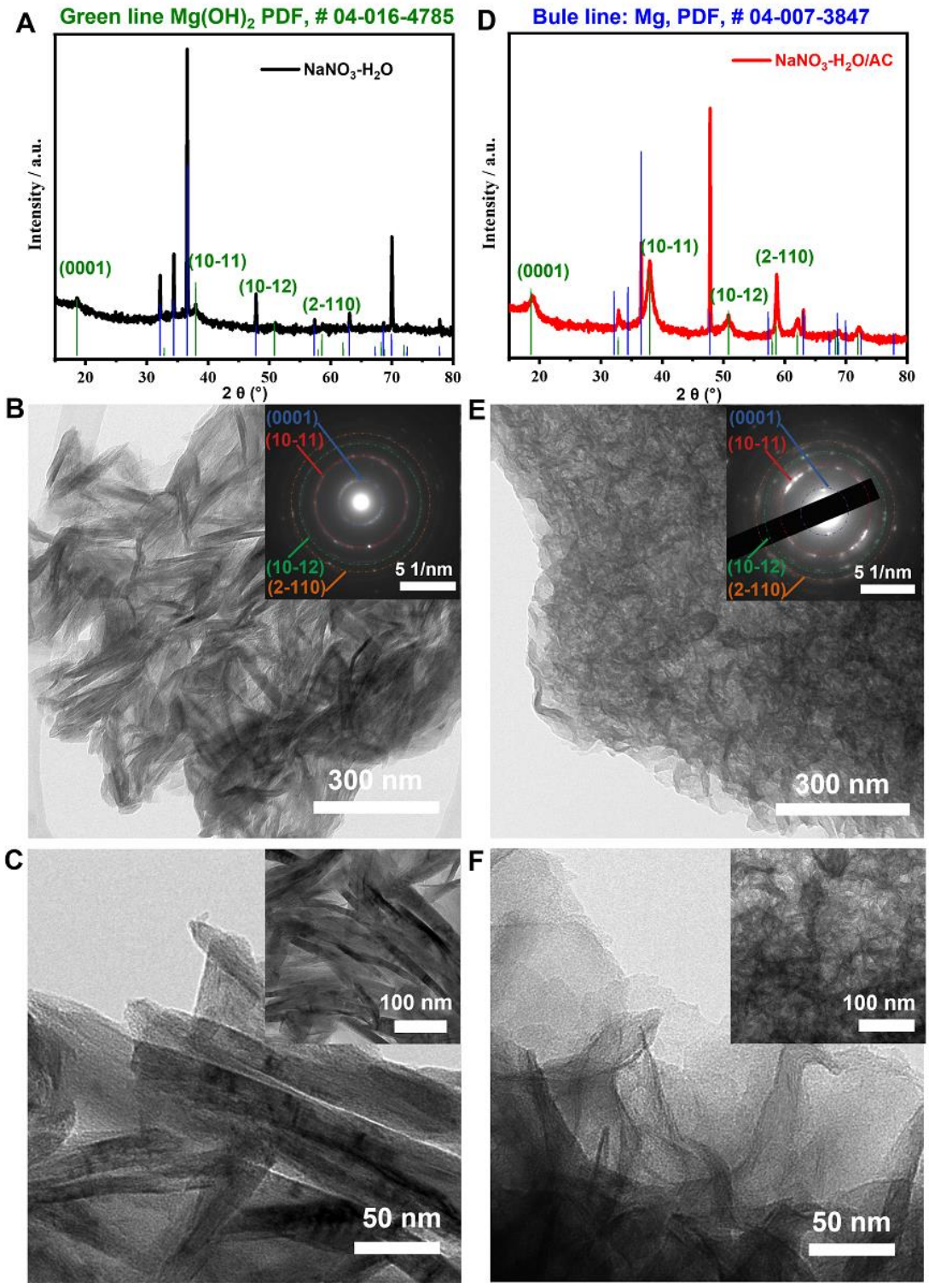

Fig. V-5 Morphology and structure of Mg corrosion products obtained in $NaNO_3$ without and with acetic acid: (A-C) XRD patterns; and (D-F) TEM views of Mg anode in electrolyte $NaNO_3$-H_2O and electrolyte $NaNO_3$-H_2O/AC

The dark field image (Fig. V-S11 b_3) highlights one of the single crystal lamella in the corrosion product. The lamella exhibits a plate shape in the size of 500 nm in width. The thickness of the single layer of the lamellae is estimated to be a few nanometers, according to that the contrast at the transparent part of the product is close to that of the carbon film of the grid. About the crystallographic orientation of MgO nano-precipitates, unique variant was observed in a single flack or a single lamella. The important differences between the microstructures of the corrosion products of the two specimens should result from the different corrosion environments. The differences in the reaction environment and product chemistry could probably lead to the changes on interfacial energies of the $Mg(OH)_2$ phase and the subsequent variation in growth kinetics responsible for microstructure changes. However, the crystallographic analysis by TEM and XRD is not able to distinguish the differences on the chemistry of the $Mg(OH)_2$ phase and that of MgO precipitates. Indeed, the signatures of the chemical differences can be detected by XPS, where the binding energy differences of O 1s peaks corresponding to MgO precipitates are observed when comparing the results of the two specimens (Fig. V-4). Therefore, the changes of the chemical states and the microstructures of the corrosion products induced by the changes of the electrolytic environment could probably be the reasons of different electrochemical behaviors of the battery.

V.4 Conclusions

In summary, we developed a suitable electrolyte based on $NaNO_3$ with traces of acetic acid for Mg-air batteries. The application of this electrolyte led to the high anode efficiency and significantly prolonged the cells lifetime to more than 360 hours and improved the discharge voltage to 1.8 V. According to the systematic analyses, we demonstrated that already the application of $NaNO_3$ instead of NaCl greatly decreases the corrosion of Mg, however a decrease of the discharge voltage was possible via addition of small quantities of acetic acid. It attributed to dominant cathodic corrosion reaction of NO_3^- to NO_2^- replacing the HER and formation of a denser surface film. The addition of acetic acid, lead to the surface morphology modifications as demonstrated by SEM and TEM. However, the chemical distribution of MgO, $Mg(OH)_2$ and $MgCO_3$ in the inner layer/substrate interface remained similar regardless of electrolyte according to the ToF-SIMS depth profiles. Furthermore, on the outer part of the layer the presence of carboxylic groups probably combining with the nitrates/nitrites were observed

by the XPS. As a result, the structure, thickness and the chemical composition of the surface film was optimized to be more favorable to Mg^{2+} transfer resulting in the higher discharge voltage and significantly prolonged lifetime of Mg-air battery.

V-5 Supplementary information

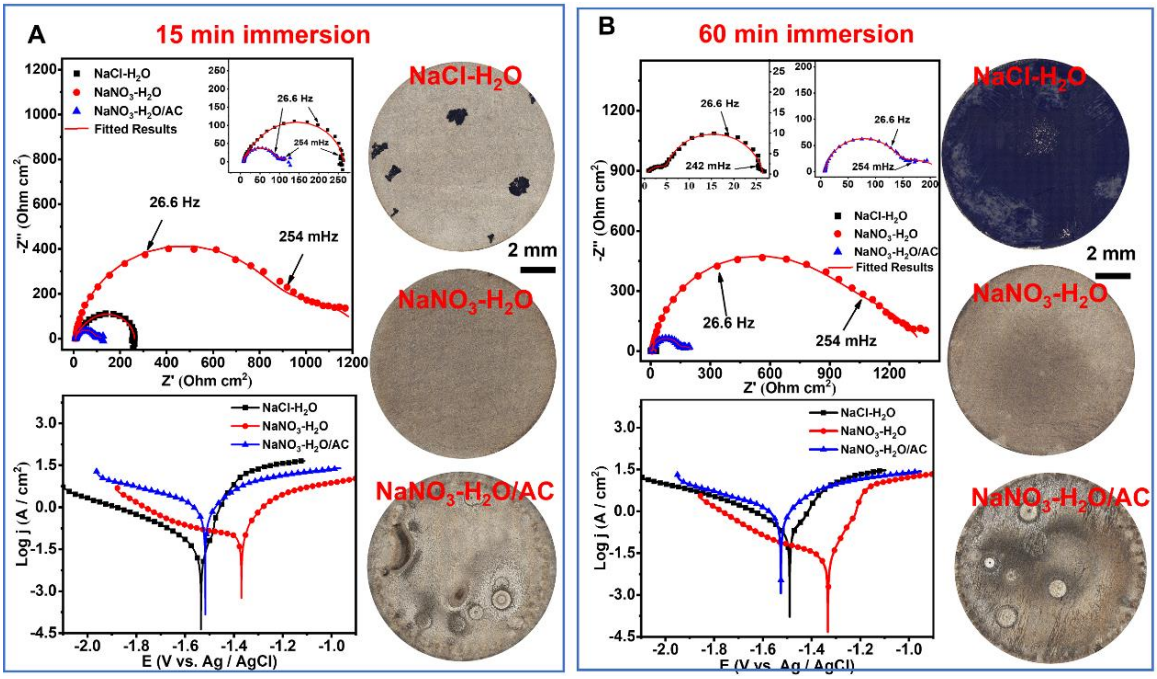

Fig. V-S1 The electrochemical impedance spectra, polarization curves and optical microscope morphologies of Mg anode after immersion in NaCl-H_2O, $NaNO_3$-H_2 and $NaNO_3$-H_2O/AC electrolytes for different times (A) 15 min; (b) 60 min.

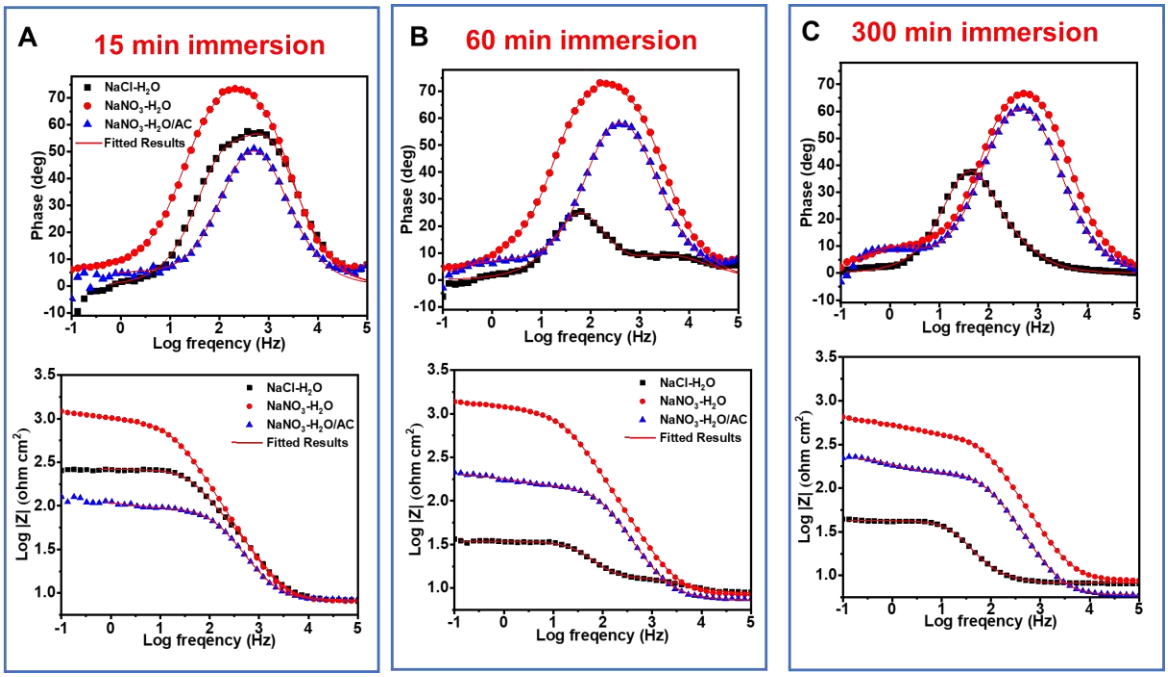

Fig. V-S2 Bode spectra of impedance modulus *vs* log (Freq) and phase angle *vs* log (Freq) of Mg anode in in electrolyte of NaCl-H_2O, $NaNO_3$-H_2 and $NaNO_3$-H_2O/AC after different times of immersion (a) 15 min; (b) 60 min; (c) 300 min; (d) 400 min.

Table. V-S1 Parameters obtained from the EIS data fitting for Mg anode in of NaCl-H_2O, $NaNO_3$-H_2O and $NaNO_3$-H_2O/AC electrolytes for 15 min and 60 min of immersion times.

	15 min			60 min		
	NaCl-H_2O	$NaNO_3$-H_2O	$NaNO_3$-H_2O/AC	NaCl-H_2O	$NaNO_3$-H_2O	$NaNO_3$-H_2O/AC
R_s (Ω cm^2)	8	8	8	9	8	7
R_{ct} (Ω cm^2)	121	407	30	6	494	91
CPE_{dl} (Ω^{-1} cm^{-2} s^n)	14×10^{-6}	1×10^{-3}	8.8×10^{-3}	0.2×10^{-3}	0.4×10^{-6}	3.4×10^{-3}
n_1	0.92	0.72	0.65	0.7	0.7	0.53
R_f (Ω cm^2)	133	847	83	203	879	124
CPE_f (Ω^{-1} cm^{-2} s^n)	12×10^{-6}	14×10^{-6}	25×10^{-6}	0.2×10^{-3}	13×10^{-6}	20×10^{-6}
n_2	1	0.94	0.91	0.98	0.94	0.95

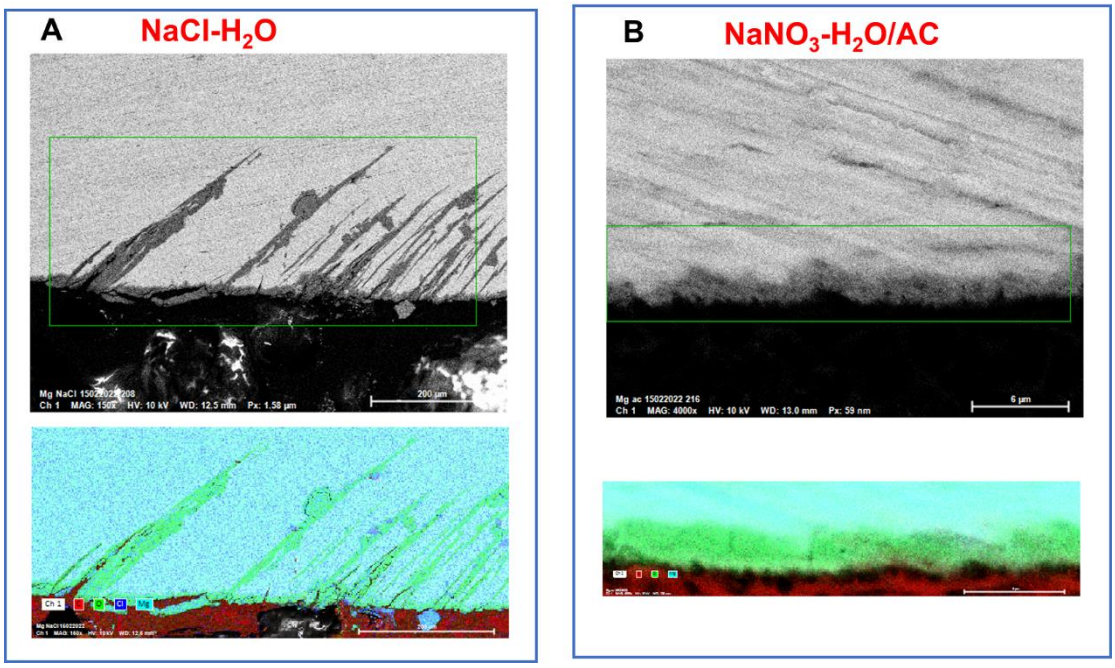

Fig. V-S3 The cross-sectional SEM images of Mg surface morphologies and corresponding energy dispersive spectroscopy (EDS) mapping for Mg anode in (A) NaCl-H_2O; (B) $NaNO_3$-H_2O/AC for 120 min of immersion.

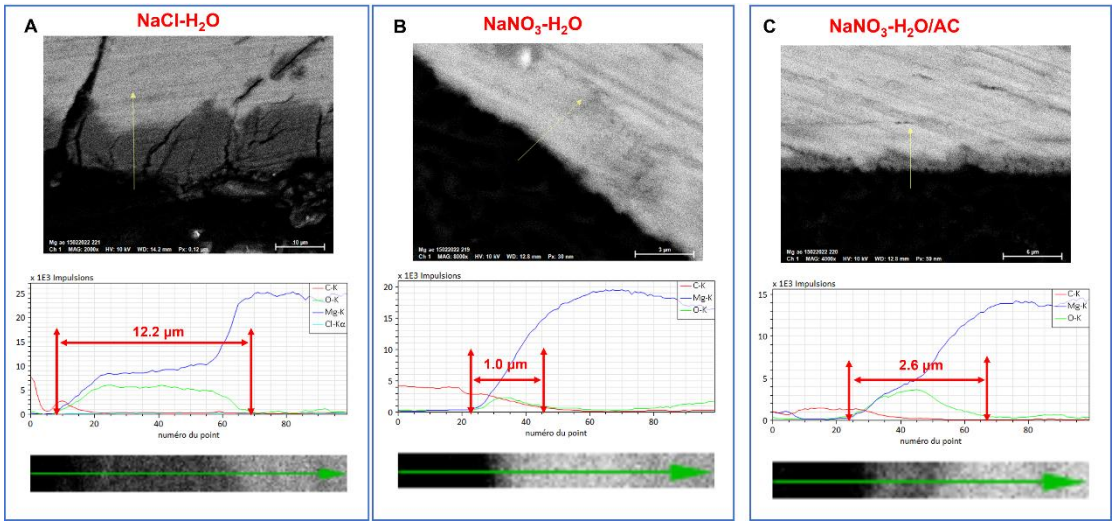

Fig. V-S4 The cross-sectional SEM image of Mg surface morphologies and corresponding EDS liner scan and element mapping for Mg anode in of (A) NaCl-H_2O; (B) $NaNO_3$-H_2O; (C) $NaNO_3$-H_2O/AC electrolytes for 120 min immersion.

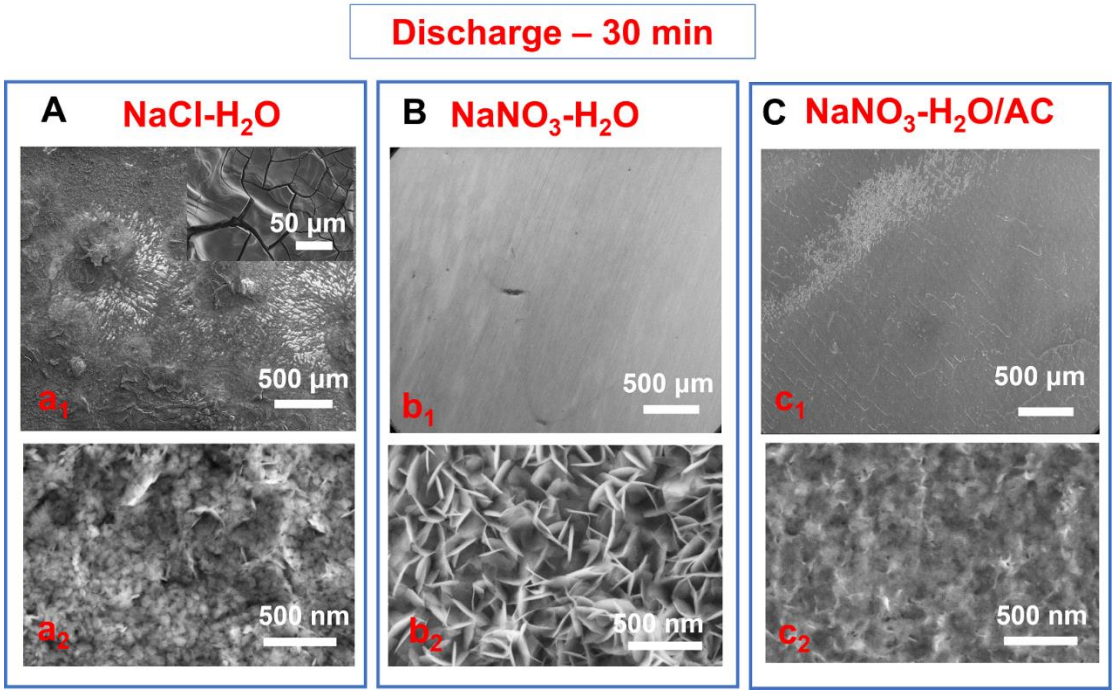

Fig. V-S5 The surface SEM images of Mg samples after 30 min discharge test in electrolyte of (A) NaCl-H_2O; (B) $NaNO_3$-H_2O; (C) $NaNO_3$-H_2O/AC.

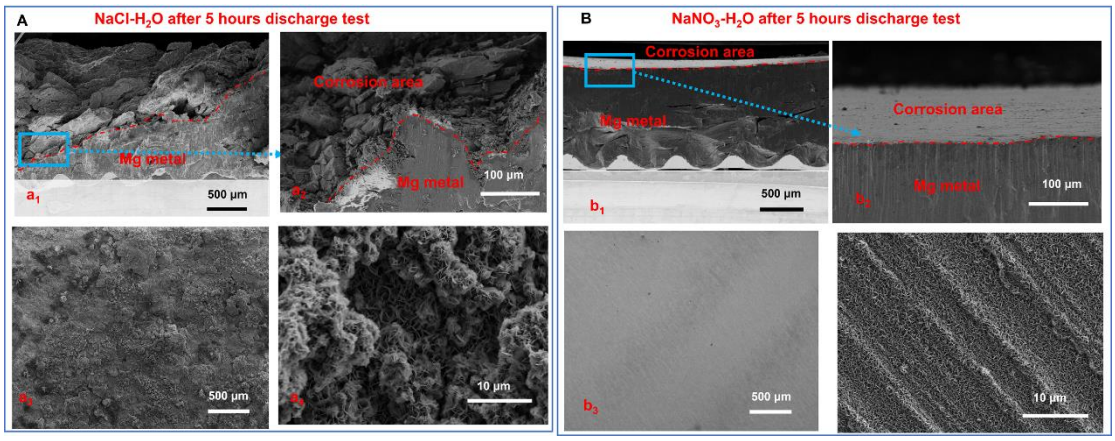

Fig. V-S6 The cross-sectional and corrosponding surface SEM images of Mg samples after 5 hours discharge test in electrolyte of (A) NaCl-H_2O; (B) $NaNO_3$-H_2O.

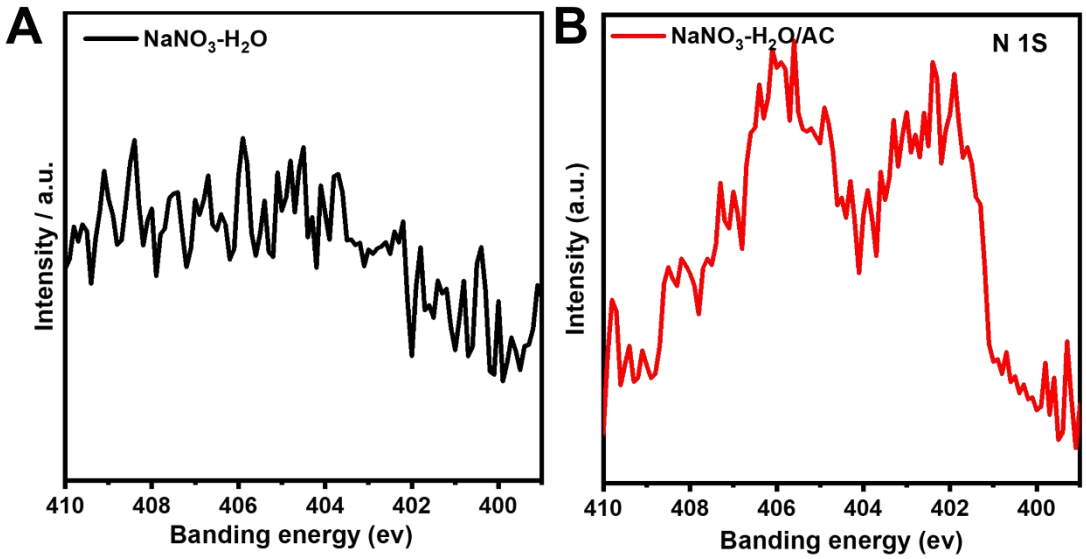

Fig. V-S7 XPS (XPS) spectra of N 1s core level for Mg samples after 15 min immersion in of (A) $NaNO_3$-H_2O; (B) $NaNO_3$-H_2O/AC.

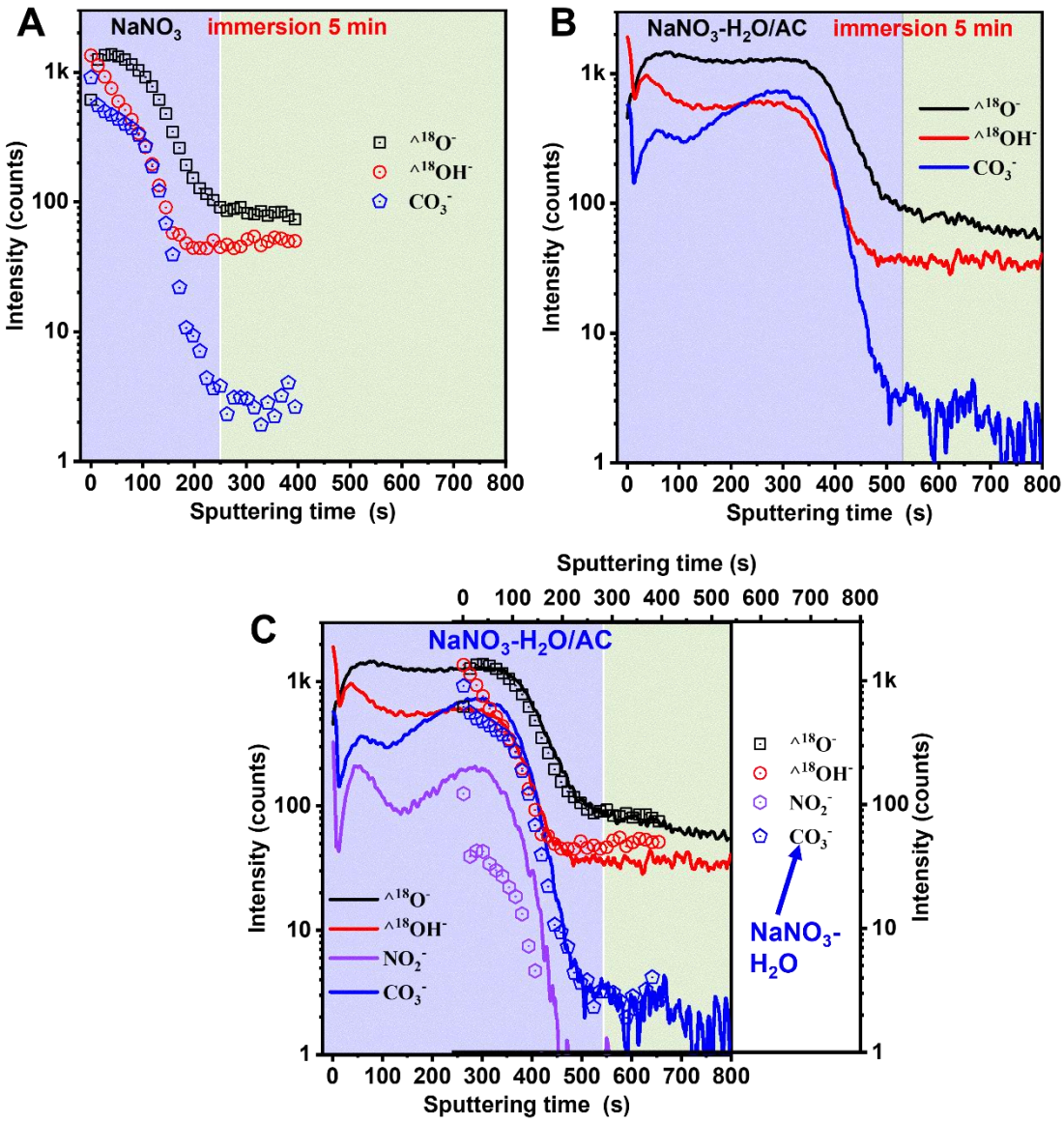

Fig. V-S8 ToF-SIMS negative ion depth profiles of Mg samples after 15 min of immersion in (A) $NaNO_3$-H_2O; (B) $NaNO_3$-H_2O/AC electrolytes ;and (C) the comparation of A and B.

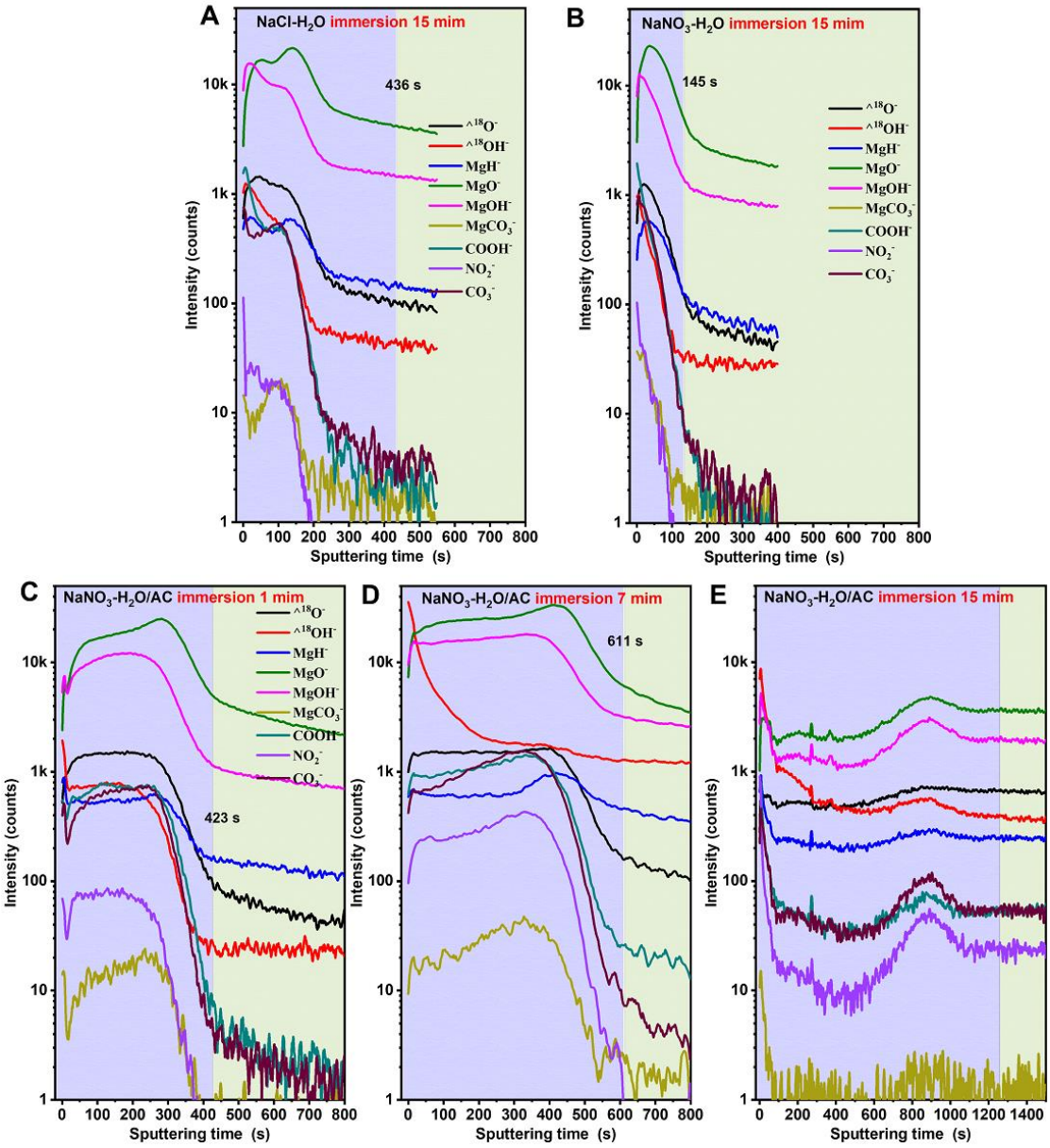

Fig. V-S9 ToF-SIMS negative ion depth profiles of Mg samples after different times of immersion: (A) 15 min immersion in NaCl-H_2O; (B) 15 min immersion in $NaNO_3$-H_2O; (C) 1 min immersion, $NaNO_3$-H_2O/AC (D) 7 min immersion in $NaNO_3$-H_2O/AC; (E) 15 min immersion in $NaNO_3$-H_2O/AC.

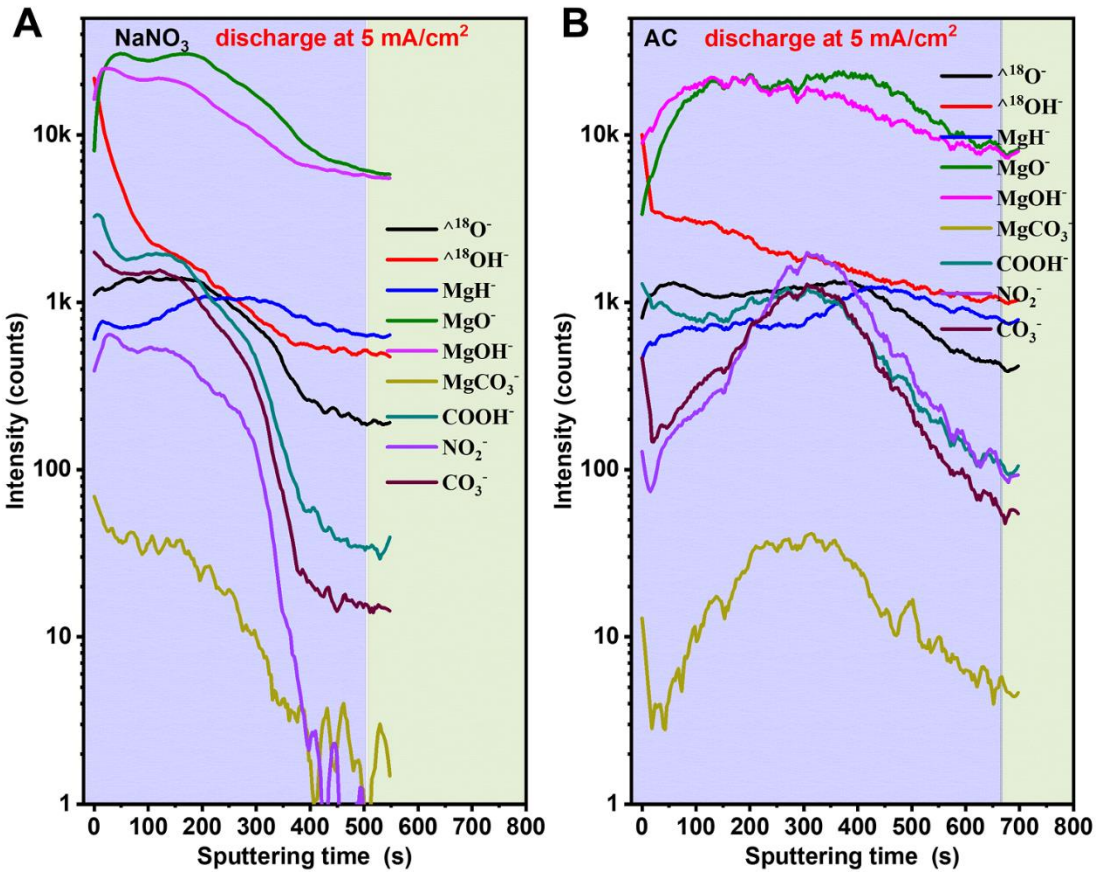

Fig. V-S10 ToF-SIMS negative ion depth profiles of Mg samples after 5 min discharge tests at current density of 5 mA/cm^2 in (A) $NaNO_3$-H_2O; (B) $NaNO_3$-H_2O/AC.

Table V-S2. Atomic % of Mg 2p core levels for Mg anode in electrolyte of $NaNO_3$-H_2O and $NaNO_3$-H_2O/AC after 5 min immersion.

atomic (%)		oxide film-$(COOH)_x$	$Mg(CO_3)_x$	$Mg(OH)_2$	MgO
Mg2p	$NaNO_3$-H_2O	/	49.2	10	40.8
	$NaNO_3$-H_2O/AC	20.7	11.2	18.3	49.8

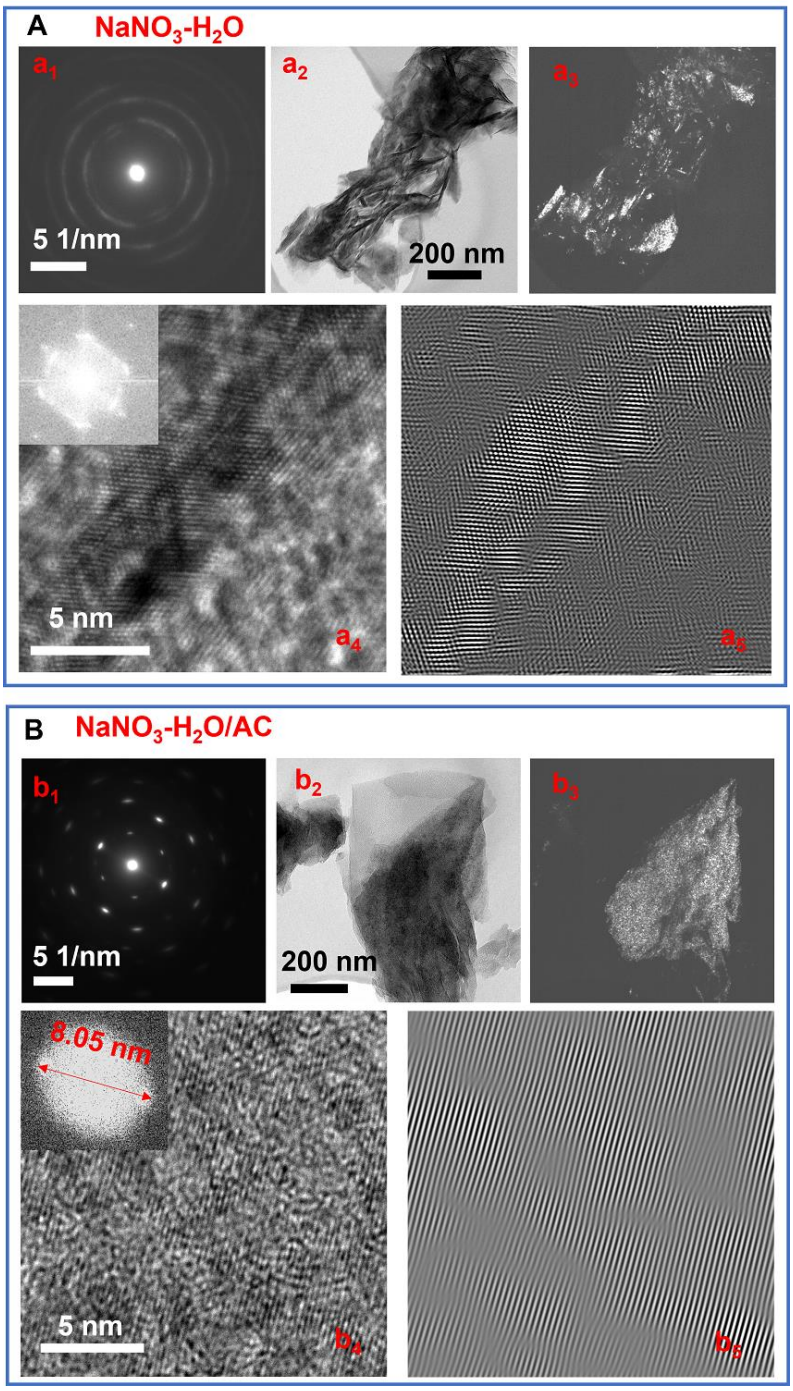

Fig. V-S11 The transmission electron microscopy of Mg corrosion products as function of acetic acid in electrolyte $NaNO_3$, (A) in electrolyte $NaNO_3$-H_2O; and (B) electrolyte $NaNO_3$-H_2O/AC (a_1 and b_1, the electron diffraction pattern; a_2 and b_2 TEM morphology; a_3 and b_3, dark-field TEM image; a_4 and b_4, high-resolution TEM view; a_5 and b_5, inverse fast Fourier transforms (FFTs) images.)

V-References

[1] M. Santamaria, F. Di Quarto, S. Zanna, P. Marcus, Initial surface film on magnesium metal: A characterization by X-ray photoelectron spectroscopy (XPS) and photocurrent spectroscopy (PCS), Electrochimica Acta, 53 (2007) 1314-1324.

[2] M. Santamaria, F. Di Quarto, S. Zanna, P. Marcus, The influence of surface treatment on the anodizing of magnesium in alkaline solution, Electrochimica Acta, 56 (2011) 10533-10542.

[3] G.-L.S. Jufeng Huang, Yixing Zhu, Dajiang Zheng, Ziming Wang, The anodically polarized Mg surface products and accelerated hydrogen evolution, Journal of Magnesium and Alloys, Available online (2021).

[4] G. Zhang, L. Wu, A. Tang, X.-B. Chen, Y. Ma, Y. Long, P. Peng, X. Ding, H. Pan, F. Pan, Growth behavior of MgAl-layered double hydroxide films by conversion of anodic films on magnesium alloy AZ31 and their corrosion protection, Applied Surface Science, 456 (2018) 419-429.

[5] N.S.V. Narayanan, B.V. Ashok Raj, S. Sampath, Physicochemical, spectroscopic and electrochemical characterization of magnesium ion-conducting, room temperature, ternary molten electrolytes, J Power Sources, 195 (2010) 4356-4364.

[6] F. Zucchi, V. Grassi, A. Frignani, C. Monticelli, G. Trabanelli, Electrochemical behaviour of a magnesium alloy containing rare earth elements, Journal of Applied Electrochemistry, 36 (2005) 195-204.

[7] Y. Zhou, B. Wu, G. Lin, Z. Xing, S. Li, L. Deng, D. Chen, D. Yun, S. Xie, Interfacing Pristine C60 onto TiO2 for Viable Flexibility in Perovskite Solar Cells by a Low-Temperature All-Solution Process onto TiO2 for Viable Flexibility in Perovskite Solar Cells by a Low-Temperature All-Solution Process, Advanced Energy Materials, 8 (2018) 1800399.

[8] V. Moutarlier, M.P. Gigandet, B. Normand, J. Pagetti, EIS characterisation of anodic films formed on 2024 aluminium alloy, in sulphuric acid containing molybdate or permanganate species, Corros Sci, 47 (2005) 937-951.

[9] N. Wang, W. Li, Y. Huang, G. Wu, M. Hu, G. Li, Z. Shi, Wrought Mg-Al-Pb-RE alloy strips as the anodes for Mg-air batteries, J Power Sources, 436 (2019) 226855.

[10] X. Chen, W. Tian, S. Li, M. Yu, J. Liu, Effect of temperature on corrosion behavior of 3003 aluminum alloy in ethylene glycol–water solution, Chinese Journal of Aeronautics, 29 (2016) 1142-1150.

[11] M. Anik, I.M. Guneşdoğdu, Corrosion characteristics of Alloy AZ63 in buffered neutral solutions, Mater Design, 31 (2010) 3100-3105.

[12] T.N. Vu, D. Veys-Renaux, E. Rocca, Potential bioactivity of coatings formed on AZ91D magnesium alloy by plasma electrolytic anodizing, Journal of biomedical materials research. Part B, Applied biomaterials, 100 (2012) 1846-1853.

[13] F.W. Richey, B.D. McCloskey, A.C. Luntz, Mg Anode Corrosion in Aqueous Electrolytes and Implications for Mg-Air Batteries, J Electrochem Soc, 163 (2016) A958-A963.

[14] A.A. G. Song, D. Stjohn, J. Nairn, Y. Li, The electrochemical corrosion of pure magnesium

in 1 N NaCl, Corros. Sci. , 39 (1997) 855-875.

[15] G. Song, Recent Progress in Corrosion and Protection of Magnesium Alloys, Advanced Energy Materials, 7 (2005) 563-586.

[16] D.S. G. Song, The effect of zirconium grain refinement on the corrosion behaviour of magnesium-rare earth alloy MEZ, J. Light Met, 2 (2002) 1-16.

[17] G.-L.S. Jufeng Huang, Andrej Atrens, Matthew Dargusch, What activates the Mg surface—A comparison of Mg dissolution mechanisms, Journal of Materials Science & Technology, 54 (2020) 207-220.

[18] N. Wang, R. Wang, C. Peng, B. Peng, Y. Feng, C. Hu, Discharge behaviour of Mg-Al-Pb and Mg-Al-Pb-In alloys as anodes for Mg-air battery, Electrochimica Acta, 149 (2014) 193-205.

[19] J. Ma, G. Wang, Y. Li, F. Ren, A.A. Volinsky, Electrochemical performance of Mg-air batteries based on AZ series magnesium alloys, Ionics, 25 (2018) 2201-2209.

[20] W. Li, C. Li, C. Zhou, H. Ma, J. Chen, Metallic magnesium nano/mesoscale structures: their shape-controlled preparation and mg/air battery applications, Angewandte Chemie, 45 (2006) 6009-6012.

[21] E.N. El Sawy, H.A. El-Sayed, H.A. El Shayeb, Corrosion of Mg, AS31 and AZ91 alloys in nitrate solutions, J Alloy Compd, 492 (2010) 69-76.

[22] D.K. Chanda, A. Samanta, A. Dey, P.S. Das, A.K. Mukhopadhyay, Nanoflower, nanoplatelet and nanocapsule Mg(OH)2 powders for adsorption of CO2 gas, Journal of Materials Science, 52 (2017) 4910-4922.

[23] S.H. Salleh, S. Thomas, J.A. Yuwono, K. Venkatesan, N. Birbilis, Enhanced hydrogen evolution on Mg (OH)2 covered Mg surfaces, Electrochimica Acta, 161 (2015) 144-152.

[24] S.Z. Yaqing Zhou, Antoine Seyeux, Luntao Wang, Philippe Marcus, Jolanta Światowska, Influence of sodium 5-sulfosalicylate as a corrosion inhibitor in NaCl electrolyte on enhanced performances of Mg-air batteries, J Power Sources, (submitted) (2022).

[25] A.O. Yüce, R. Solmaz, G. Kardaş, Investigation of inhibition effect of rhodanine-N-acetic acid on mild steel corrosion in HCl solution, Materials Chemistry and Physics, 131 (2012) 615-620.

[26] G. Avci, Corrosion inhibition of indole-3-acetic acid on mild steel in 0.5M HCl, Colloids and Surfaces A: Physicochemical and Engineering Aspects, 317 (2008) 730-736.

[27] R. S. Abdel Hameed1, *, H. I. AlShafey4, A. H. Abu-Nawwas, 2-(2, 6-dichloranilino) phenyl acetic acid Drugs as Eco-Friendly Corrosion Inhibitors for Mild Steel in 1M HCl, Int. J. Electrochem. Sci., 9 (2014).

[28] Y.Z. Y. Q. Zhou, J. T. Li, S. Zanna, A. Seyeux, P. Marcus, J. Światowska Organic/inorganic hybrid electrolyte for enhancing performance of Mg-air batteries Applied surface science, (Submitted) (2022).

[29] M. Curioni, The behaviour of magnesium during free corrosion and potentiodynamic polarization investigated by real-time hydrogen measurement and optical imaging, Electrochimica Acta, 120 (2014) 284-292.

[30] G. Williams, N. Birbilis, H.N. McMurray, The source of hydrogen evolved from a

magnesium anode, Electrochemistry Communications, 36 (2013) 1-5.

[31] J.A. Yuwono, C.D. Taylor, G.S. Frankel, N. Birbilis, S. Fajardo, Understanding the enhanced rates of hydrogen evolution on dissolving magnesium, Electrochemistry Communications, 104 (2019) 106482.

[32] V. Fournier, P. Marcus, I. Olefjord, Oxidation of magnesium, Surface and Interface Analysis, 34 (2002) 494-497.

[33] D. Mercier, J. Światowska, E. Protopopoff, S. Zanna, A. Seyeux, P. Marcus, Inhibition of Mg Corrosion by Sulfur Blocking of the Hydrogen Evolution Reaction on Iron Impurities, J Electrochem Soc, 167 (2020) 121504.

[34] R.S.A.M.S.E. Din, Efficiency of organic acids and their anions in retarding the dissolution of aluminium, Corros Sci, 12 (1972) 689-697.

[35] M. Bouklah, A. Ouassini, B. Hammouti, A.E. Idrissi, Corrosion inhibition of steel in sulphuric acid by pyrrolidine derivatives, Applied Surface Science, 252 (2006) 2178-2185.

[36] D.L. P. Kern, Adsorption of organic corrosion inhibitors on iron in the active and passive state. A replacement reaction between inhibitor and water studied with the rotating quartz crystal microbalance, Electrochimica Acta, 47 (2001) 589-598.

[37] S.K.S.a.A.K. Mukherjee, Kinetics of Mild Steel Corrosion in Aqueous Acetic Acid Solutions, J. Mater. Sci. Technol., 26 (2010) 264-269.

Conclusions and perspectives

This thesis has been focused on engineering new electrolytes and their additives for primary aqueous Mg-air batteries and in-depth characterization of the Mg electrode/electrolyte interface. The chemical surface and in-depth analyses on Mg anode have been performed by XPS and ToF-SIMS characterization techniques and combined with the morphological characterization by microscopic techniques such as SEM, OM and 3D-SLM. The electrochemical techniques (OCP, LSV, EIS and galvanostatic discharge tests) have been employed to investigate the corrosion behavior of Mg anode and discharge performance of full Mg-air battery as a function of electrolyte and/or electrolyte additive. The work is split into three parts.

Modification of the background solvent

This part has been focused on a modification of solvent for Mg-air batteries. To do so, a part of water was replaced by ethanol solvent and mixed with 0.6 M NaCl. The influence of ethanol concentration in water solvent with 0.6 M NaCl on the corrosion behavior of Mg electrode and discharge performances of Mg-air battery has been investigated. To better understand the influence of ethanol, the surface composition and morphology of Mg anode were thoroughly investigated. The following conclusions are drawn from this part:

1) In high volume ratio of organic (ethanol) (≥ 20 vol %) to inorganic (water) agents the Mg anode is much less corroded.
2) With the ethanol addition, the potentiodynamic polarization curves shows a more positive corrosion potential (E_{corr}), a decrease of the corrosion current (I_{corr}) and an increase of polarization resistance (R_p) in the ethanol containing electrolyte; the EIS analysis confirms the improved corrosion resistance of Mg.
3) The results of XPS and ToF-SIMS demonstrate that the improved corrosion behavior of Mg is attributed to the higher quantity of $MgCO_3$ and the lower quantity of $Mg(OH)_2$. SEM further demonstrates that the formed corrosion layer thickness is lower, denser and with the morphology characteristics different than the pallet-like morphologu of $Mg(OH)_2$, confirming its decrease.

4) However, the high concentration of ethanol in the range of tens of percent (≥ 20 vol %) demonstrats a lower discharge voltage, which has been attributed to formation of the dense surface layer, blocking the ion transfer and leading to sluggish reaction kinetics. This indicates that too high ethanol to water ratio is not suitable for application in Mg-air batteries.
5) The following battery tests in electrolyte with a low quantity of ethanol (≤5 vol%) has shown to have a beneficial effect on the discharge voltage and the prolonged battery life. A significant inhibition of Mg anode corrosion at this low-content ethanol (0.5 vol%) electrolytes has been confirmed by a remarkable decrease of H_2 evolution.
6) A decreased reactivity of Mg-based anode and lower HER is the most probably attributed to the lower proton reactivity in ethanol than in water. The hybrid electrolyte significantly modifies the composition and structure of surface layer and finally leads to improved performances of Mg-air batteries.

Application of the electrolyte additives

The modification of electrolyte has been performed by application of sodium 5-sulfosalicylate (5-S-Sal) as a corrosion inhibitor in 0.6 M NaCl electrolyte. The most important results are as follows:

1) A significantly less active cathodic behavior of Mg electrode has been observed by LSV measurements and a relative stable impedance value after different time immersion. The hydrogen evolution test shows only a four-fold of H_2 volume with reference to the blank electrolyte (w/o inhibitor) and a more negative OCP has been observed leading to the improved discharge voltage of full Mg-air battery.
2) Chemical surface characterizations by XPS and ToF-SIMS demonstrate a formation of the multilayer structure of the surface film with the magnesium hydrides embedded into magnesium hydroxide present on the extreme surface and the magnesium oxide present in the inner layer close to the layer/substrate interface.
3) A higher quantity of MgO and lower quantity of $Mg(OH)_2$ is formed on Mg electrode exposed to electrolyte with inhibitor. The chlorides are not detected in the surface layer confirming a decreased corrosion.

4) A slight enrichment in sulfur species (corresponding to the inhibitor molecule) is observed, which could be responsible for blocking the active, catalytic sites of HER.
5) Within different concentrations of 5-S-Sal in NaCl electrolyte (0.05 M to 0.15 M), the best discharge performances have been achieved in electrolyte with 0.1 M inhibitor.
6) And finally, the discharge voltage of full Mg-air battery is improved from ~1.58 V to ~1.82 V (at current density of 0.5 mA/cm^2), and the discharge lifetime from around 12.5 hours is prolonged to around 80 hours.
7) This 5-S-Sal inhibitor can from one side be responsible for a complexation of Mg^{2+} or other ions (i.e. metallic impurities) like previously demonstrated. Moreover, formation of a thinner surface layer (as shown by ToF-SIMS in-depth profiles), is also responsible for the higher discharge potential and the prolonged battery lifetime.

Modifications of the background solutes and application of the electrolyte additive

The most frequently used NaCl solute in aqueous primary Mg-air batteries has been replaced by $NaNO_3$. Besides, a low quantity of acetic acid as an inhibitor has been used to improve the cells discharge voltage. Different mixtures of electrolytes such as NaCl in H_2O, $NaNO_3$ in H_2O and $NaNO_3$ in H_2O mixed with acetic acid have been compared. The following results can be listed:

1) Comparing to the electrolyte with NaCl solute, the corrosion rate of Mg and H_2 evolution is decreased in $NaNO_3$-based electrolyte, however, the discharge voltage of full Mg-air batteries is also lowered.
2) The surface of Mg anode in $NaNO_3$-H_2O electrolyte has a morphology characteristics of $Mg(OH)_2$, and it changes gradually with increase of acetic acid concentration as observed by SEM and TEM.
3) ToF-SIMS depth profiles show that the chemical distribution of MgO, $Mg(OH)_2$ and $MgCO_3$ compounds at the layer/metallic substrate interface is very similar in $NaNO_3$-based electrolyte with and without acetic acid, but a higher thickness and/or an extra outer surface layer is formed when the acetic acid is added. These results corroborate also with XPS data showing higher binding energy peaks in the Mg 2p and O 1s regions corresponding to the carboxylic acid ($COOH^-$) or NO_x^- species from $NaNO_3$.

4) The tests in full Mg-air battery in this new optimized electrolyte show the higher discharge voltage reaching ~1.8 V at 0.5 mA/cm^2 with reference to 1.3 V in $NaNO_3$ w/o acetic acid or 1.59 V in NaCl electrolyte and tremendous increase of battery lifetime to more than 360 hours comparing to only ~17 hours service time in NaCl electrolyte.
5) As a result, by the modification electrolyte, the structure, thickness and the chemical composition of the surface film was optimized to be more favourable to Mg^{2+} transfer resulting in the higher discharge voltage and long lifetime of full Mg-air batteries.

These results indicate that the corrosion rate of Mg electrode can be inhibited and the discharge performances of primary Mg-air batteries can be significantly improved by the electrolyte engineering and the electrolyte/electrode interface. The thorough understanding of metals corrosion and their surface chemistry, the surface modifications induced by the electrochemical processes and the metal/electrolyte interfaces are primordial in development of Mg-air batteries. In order to better tune the surface and electrolyte/electrode interface properties, several future studies need to be undertaken:

1) Concerning the modifications of the background solvents, some other efficient solvents or their mixtures can be developed. It will be interesting to search for a suitable mixed solvent, which can simultaneously decrease the Mg corrosion and improve the discharge voltage of full Mg-air batteries. Aqueous mixed ionic liquid electrolytes will be one the interesting candidates. Certain types of the ionic liquids can have a reasonable ionic conductivity and they are known to have very good electrochemical stability, high thermal and chemical stability. Besides, the mixed electrolyte based on water and ionic liquid can play role in supporting high rate capability and improving the discharge performance of Mg-air batteries.
2) A large number of Mg corrosion inhibitors have been investigated so far for corrosion protection application of Mg and Mg alloys, such as salicylaldehide, 3-Methylsalicylate Na, 2,5-pyridinedicarboxylate Na, 8-Hydroxyqeinoline and so on, but very few of them was actually used as inhibitors for Mg-air batteries. The further work can focus on the inhibitors more suitable for Mg batteries. Based on the current results it can be concluded that it is very difficult to balance the decrease of Mg corrosion and increase the discharge voltage at the same time. Thus, it is meaningful to develop the mixed

inhibitors for Mg-air batteries.

3) The influence of other solutes, such as KNO_3, Na_2SO_4, Na_3PO_4 in the aqueous solvents will be interesting to study. The usually used NaCl solute can seriously damage the Mg metal, but new types of solutes such as bi- or trinary solutes can be developed in aqueous electrolytes.
4) To further go beyond this limit, the Mg alloys development is feasible, such as AZ31, AZ91, A/Ca, Mg/Li etc. As Al alloyed with Mg forms the secondary phase, which can reduce anodic reaction kinetics and increase the corrosion resistance. Mg alloyed with Li benefits to their lightest structure, extremely negative OCP and good Faradic capacities. The Ca-based alloys used as anode materials in Mg-based-air batteries show the superior energy densities.
5) Due to all above reasons, a high-throughput experimentation (HTE) development in Me-air batteries is necessary in order to be able to perform a rapid screening of different battery compounds and accelerate the battery discovery.

Acknowledgements

The work in this thesis was carried out in the laboratory of Physico-Chimie des Surfaces (PCS) Team in the Institut de Recherche de Chimie Paris (IRCP) / CNRS (UMR 8247) at Chimie ParisTech (L'École nationale rieure de chimie de Paris), Univers de recherche Paris Sciences et Lettres (PSL). Some parts of the experiments were done in the group of Prof. Shi-gang Sun and Pro Jun-tao Li in the College of Energy, Xiamen University.

First and foremost, I am particularly grateful to my supervisor, Jolanta Światowska for her offering me this great opportunity to conduct my PhD work. She is very kind and enthusiastic to help me. She is willing to share her opinion to us and giving the helpful suggestion for the experiments and writing. Then, I would like to thank my co-supervisors, Philippe Marcus, for his enthusiastic support and concern.

Moreover, I would like to express my sincere regards to the jury members, Eric De Vito, Cristina Iojoiu, and Nadine re for devoting their precious time to the review of my thesis manuscript and for their scientific evaluation

Next, I would like to thank Sandrine Zanna, Antoine Seyeux, Luntao Wang and Fan Sun for the experiment tests of XPS, ToF-SIMS and TEM, and the discussion of data analyzations.

Furthermore, I would express my sincere appreciation to Jun-tao Li, Yao Zhou and many other people of the Prof. Shi-gang Sun's group in Xiamen University, for their kind help and useful suggestions. Many thanks to the c Wiame and Zhanyu Wu, for sharing their knowledge and help me daily life. Also, thanks Meicheng Li, Zuocheng Wang, Zhiheng Zhang, Xueying Wang, Xiaocui Wu and all of the other members in laboratory of PCS, for sharing the good times together in the lab.

Sincerely I am grateful to the fellowship from China Scholarship Council (CSC) for supporting the whole work of this thesis (NO. 201806310116).

In the end, I would like to express my deepest thanks to my family and my friends, especially my parents and my boyfriend Guanhua Lin. Thanks for my parents to support me everything in my life. And my particular thanks to Guanhua always encourage me and take care of me, support me do what I want to do all the time.

Appendix-Résumé étendu de thèse

Cette thèse de doctorat est composée de 5 chapitres. Le chapitre I présente l'état de l'art et les objectifs de la thèse. Le chapitre II détaille les techniques expérimentales utilisées dans cette thèse. Les méthodes électrochimiques (OCP, SIE, LSV et galvanostatique), d'analyse de surface (XPS, ToF - SIMS) et de microscopie (MEB, MO, 3D-LSM, MET) y sont expliquées. Les chapitres III à V présentent les résultats de recherche. Le chapitre III décrit une nouvelle méthode améliorant les performances électrochimiques des batteries Mg-air grâce à l'utilisation d'un électrolyte hybride organique/inorganique (éthanol/eau). Dans le chapitre IV, le recours au 5-sulfosalicylate de sodium (5-S-Sal) comme inhibiteur de corrosion dans l'électrolyte NaCl 0,6 M pour les batteries Mg-air est présenté. Le chapitre V démontre l'influence positive d'une faible quantité d'acide acétique dans l'électrolyte aqueux $NaNO_3$ sur les performances de décharge des batteries Mg-air.

Chapitre I : Etat de l'art et objectifs de la thèse

De nos jours, le monde fait face à une demande croissante de sources d'énergie renouvelables, de grande capacité, de puissance élevée, de faible coût et sûres. Ainsi, de nouvelles technologies de stockage sont amenées à se développer. En particulier, les batteries métal-air possèdent une plus grande capacité de stockage d'énergie et une grande densité d'énergie théorique, qui est parfois supérieure à celle des batteries lithium-ion les plus performantes. Les batteries métal-air telles que les batteries lithium-air (Li-air), les batteries zinc-air (Zn-air), les batteries magnésium-air (Mg-air) et les batteries aluminium-air (Al-air) promettent d'être appliquées à la prochaine génération de véhicules électriques (VE). Les batteries Mg-air ont une capacité spécifique théorique importante (2,2 Ah/g), une grande densité d'énergie spécifique (6,8 kWh/kg) et une tension théorique élevée (3,09 V) [1-3]. En outre, le magnésium possède des propriétés bien équilibrées telles qu'un potentiel redox hautement négatif, une capacité volumétrique plus élevée et un faible coût. Le Mg est également un matériau écologique et non toxique. C'est le huitième élément le plus abondant et il constitue environ 2 % de la croûte terrestre.

Les batteries Mg-air primaires ont déjà été utilisées dans de nombreuses applications : l'Institut Coréen des Sciences et Technologies (KIST) a présenté en 2013 une voiture électrique équipée de batteries Mg-air complètes avec une autonomie de 800 km [4]. La société Magpower systems Inc. [5] au Canada a développé un type de batteries MAFC de secours qui peut équiper les canots de sauvetage, les maisons, les écoles et les hôpitaux. La Furukawa Battery Co., Ltd. [6] au Japon a développé une petite batterie MgBOX d'urgence portable qui peut être stockée pendant de longues périodes et ensuite activée en ajoutant simplement de l'eau douce ou salée pour ensuite être utilisée pour charger de petites lampes ou des téléphones portables.

La réaction globale dans les batteries Mg-air est la suivante :

$$2\ Mg + O_2 + 2\ H_2O \rightarrow 2\ Mg(OH)_2 \qquad E°= -3{,}09\ V\ vs\ SHE \qquad (1)$$

L'anode Mg est oxydée en Mg^{2+}, produisant deux électrons (Fig. Annexe 1), O_2 traverse la cathode à air et s'adsorbe sur la surface du catalyseur, puis une réaction avec H_2O se produit

pour former OH^- [7-9].

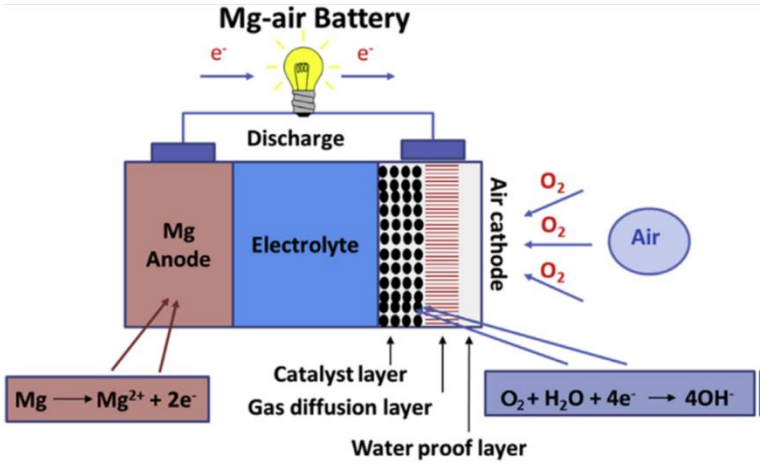

Fig. Annexe 1. Structure et principe de fonctionnement d'une batterie Mg-air [10].

Une batterie Mg-air est une cellule ouverte qui consomme l'oxygène de l'air. Le Mg métallique utilisé comme une anode peut être remplacé par une nouvelle plaque de Mg lorsque celui-ci est épuisé, ainsi la batterie Mg-air peut être "ravitaillée" [11]. L'anode métallique la plus courante est constituée de Mg pur (Mg commercial ou nano/mesoscale) ou d'alliages de Mg (Mg/Al/Zn, AZ31, AZ61, AZ91, Mg/Al/Mn, AM50, AM60, MA8M06 et Mg/Li). Des solutions aqueuses de NaCl, $KHCO_3$, NH_4NO_3, $NaNO_3$, HNO_3, $NaNO_2$, $Mg(NO_3)_2 \cdot 6H_2O$ + $NaNO_2$, Na_2SO_4, ou $MgCl_2$ sont couramment utilisées comme électrolytes [10]. La cathode à air est composée d'oxygène de l'air combiné à une couche imper-respirante, la couche de diffusion des gaz et la couche de catalyseur déposée sur le collecteur de courant.

Cependant, le Mg est très réactif et souffre de l'auto-corrosion due à la présence de certaines impuretés métalliques dans le Mg et d'un « chunk effect », qui est causé par le détachement de particules métalliques [12]. De plus, l'effet « negative difference effect » (NDE) [11, 13-16], au cours duquel, les courants cathodiques et anodiques augmentent avec le potentiel imposé, accélère la corrosion lors de la décharge des batteries Mg-air et conduit à un dégagement d'hydrogène. En raison de la corrosion du Mg, les produits de décharge tels que MgO, $Mg(OH)_2$ et $MgCO_3$ peuvent s'accumuler sur la surface du Mg et bloquer la surface de l'anode [17, 18]. Ces inconvénients entravent grandement les applications pratiques et la commercialisation des batteries Mg-air, et conduisent à une faible tension de décharge et à une densité d'énergie

spécifique insuffisante. Pour pallier ces problèmes, des développements visant à augmenter les performances électrochimiques des batteries peuvent être envisagés sur certains composants des batteries Mg-air tels que l'anode, les électrolytes et la cathode.

Un grand nombre de recherches se sont concentrées sur la mise au point d'alliages adaptés aux applications dans les batteries Mg-air. L'Al allié au Mg forme une phase secondaire ($Mg_{17}Al_{12}$) [19, 20], qui peut réduire la cinétique de réaction anodique et augmenter la résistance à la corrosion ; le Zn allié au Mg peut accélérer la dissolution des produits de décharge (tels que $Mg(OH)_2$) en raison de la diminution du pH par l'hydrolyse du Zn^{2+} dissous dans l'électrolyte aqueux à base d'eau de mer [21] ; les alliages Mg-Li sont également couramment étudiés pour des applications dans les batteries Mg-air en raison de leur structure plus légère, de leur OCP extrêmement négatif et de leurs bonnes capacités faradiques. En outre, en ce qui concerne la modification de l'anode à base de Mg, la modification de la microstructure comme le traitement thermique et le processus de corroyage (laminage et extrusion) peuvent également être utilisés pour améliorer les performances des batteries Mg-air.

Il convient de noter que les modifications des électrolytes ont récemment attiré l'attention des chercheurs. L'électrolyte peut être modifié par l'utilisation d'un mélange de sels ou l'ajout d'additifs (inhibiteurs) ou en employant deux solvants ou plus.

Choix de l'électrolyte : L'électrolyte joue un rôle critique dans l'efficacité de la réaction et le transport ionique dans les batteries Mg-air. Il peut déterminer l'efficacité d'utilisation de l'anode Mg et la composition des produits de décharge. Un électrolyte approprié peut réduire efficacement le taux d'auto-corrosion du Mg et améliorer les performances de décharge de la batterie Mg-air complète. Un électrolyte idéal doit être un bon conducteur ionique, il doit également réduire l'influence de la chute ohmique. En outre, la stabilité chimique et électrochimique élevée, l'impact sur l'environnement limité et le faible prix sont également des facteurs importants. Afin d'améliorer les performances de décharge des batteries Mg-air, des modifications des solutés et des solvants peuvent être réalisées.

Modifications de solutés : Elles comprennent le mélange de différents sels dans des

électrolytes aqueux et des additifs électrolytiques. Les sels de sodium d'acides pyridine-dicarboxyliques et plusieurs dérivés d'acides salicyliques présentent des efficacités inhibitrices parmi les plus élevée. Par ailleurs, des quinaldates et des nitrates avec des fumarates et des nitrobarbiturates, possédant une bonne efficacité d'inhibition, ont également été testés. L'effet du phosphate et du vanadate en tant qu'additifs électrolytiques s'est avéré bénéfique pour l'efficacité anodique des batteries Mg-air, tandis que le phosphate a un effet inhibiteur plus fort. Une série d'agents complexants en tant qu'additifs électrolytiques ont été rapportés par le groupe de Zheludkevich [22, 23]. L'objectif des agents complexants est de former un complexe avec Fe^{3+} pour empêcher la redéposition de Fe et la formation d'un complexe soluble avec Mg^{2+} dans le but d'augmenter l'utilisation anodique.

Modification des solvants : Concernant les solvants, les réactifs aqueux et non aqueux peuvent être utilisés pour les batteries Mg-air [24, 25]. À titre d'exemple, les solutions doubles organique/inorganique avec une partie organique : 0,5 M $Mg(ClO_4)_2$-N,N-diméthylformamide (DMF) ou acétonitrile (AN) ont été utilisées du côté de l'anode de Mg et une partie inorganique : NaCl-H_2O 0,6 M a été employé du côté de la cathode à air. Un électrolyte double avec une configuration acide-sel pour améliorer les performances de de la batterie Mg-air (tension et puissance) a également été proposé. Presque au même moment, une batterie Mg-air à haute densité d'énergie basée sur un électrolyte gel à double couche a été démontrée dans la littérature. Seuls quelques types d'électrolytes organiques/inorganiques ont été utilisés pour les batteries Mg-air. Cependant, d'autres batteries métal-air montrent des performances prometteuses en électrolytes doubles organiques/inorganiques [26-28].

Dans cette thèse, afin d'améliorer la stabilité de l'électrode négative Mg et les performances de la batterie Mg-air, des études approfondies des modifications à l'interface électrode/électrolyte en fonction de la composition de l'électrolyte ont été réalisées. Voici les questions plus spécifiques qui ont été abordées dans ce travail :

1) Les propriétés de corrosion accrues du Mg peuvent-elles être bénéfiques pour le comportement électrochimique de l'électrode négative Mg utilisée dans les batteries Mg-air ?

2) Les inhibiteurs de corrosion peuvent-ils être utilisés dans les systèmes de batterie Mg-air pour améliorer la durée de vie de l'électrode négative Mg ou le potentiel de décharge ?
3) Quelle est la nature et la composition chimique de la couche superficielle formée sur l'électrode négative Mg responsable des propriétés électrochimiques améliorées du Mg-air ?
4) Comment ajuster la composition de l'électrolyte à l'aide de sel, de solvant et d'additif pour mieux contrôler l'interface électrode/électrolyte dans des batteries Mg-air et quels sont les mécanismes correspondants ?

Afin d'y répondre, nous avons centré ce travail sur les modifications des électrodes Mg en fonction de la composition de l'électrolyte (sel, solvant ou additif) induites par des processus électrochimiques (immersion, polarisation, décharge). Pour mieux comprendre la réactivité de l'interface électrode Mg/électrolyte et être plus complémentaire par rapport à l'état de l'art, la composition en surface et en profondeur de l'électrode Mg a été caractérisée par des techniques physico-chimiques d'analyse de surface telles que la spectroscopie de photoélectrons induits par rayons X (XPS) et la spectrométrie de masse d'ions secondaires à temps de vol (ToF-SIMS).

Chapitre II. Partie expérimentale

Dans ce chapitre, les techniques analytiques et les conditions expérimentales sont introduites. Une batterie complète Mg-air a été utilisée pour les tests de performance de décharge. La cellule était composée d'une anode commerciale en Mg pur (≥ 99,9 % en poids, la composition chimique détaillée donnée dans le Tableau Annexe 1), d'un électrolyte (~17,5 ml) et d'une cathode à air Pt/C (20 % en poids de Pt acheté chez Alfa Aesar, France) .

Tableau Annexe 1. Composition chimique de l'anode en Mg (% en poids).

Composition chimique (% en poids)										
mg	Si	Fe	Cu	Mn	Al	Ni	Zn	Sn	Pb	Ti
bal	0,003	0,002	0,0005	0,002	0,004	0,0005	0,004	0,004	0,001	0,001

La demi-cellule était composée d'une électrode de référence Ag/AgCl (RE), d'une feuille de

platine comme contre-électrode (CE) et d'une plaque de Mg comme électrode de travail (WE). Les échantillons de Mg ont été polis mécaniquement sous l'eau avec des papiers abrasifs SiC pour la mesure électrochimique ou ensuite polis avec une pâte abrasive diamantée jusqu'à 0,25 µm pour la caractérisation de surface par XPS et ToF-SIMS. Les différents électrolytes de cette thèse ont été répertoriés dans le Tableau Annexe 2.

Tableau Annexe 2. Électrolytes (solvants, sels, additifs) et leurs fournisseurs utilisés dans ce travail (chapitres III, IV et V).

	Chapitre III	**Chapitre IV**	**Chapitre V**
Électrolyte aqueux de base	0,6 M NaCl	0,6 M NaCl	0,6 M NaCl / 0,5 M $NaNO_3$
Sel/solvant, fournisseur	NaCl : AnalaR Normapur, réactif d'analyse, VMR H_2O ultra pur : Millipore, résistivité > 18,5 MΩ·cm $NaNO_3$: AnalaR Normapur, réactif d'analyse, VMR		
Additifs, fournisseur	Éthanol : > 99,97 %, AnalaR Normapur , VMR	Acide 5-sulfosalicylate de sodium : Sinopharm Chemical Reagent Co. Ltd	Acide acétique glacial : 100 %, AnalaR Normapur , VMR

Les mesures électrochimiques telles que le potentiel de circuit ouvert (OCP), la spectroscopie d'impédance électrochimique (SIE), la voltamétrie à balayage linéaire (LSV) et la décharge galvanostatique ont été utilisées. Le dégagement d'hydrogène au cours des tests d'immersion ou de décharge de Mg a été mesuré dans différents électrolytes. La reproductibilité a été vérifiée au moins trois fois.

Les compositions chimiques du film de surface et les produits de corrosion de l'anode de Mg ont été obtenus par des techniques d'analyse de surface telles que la spectroscopie de photoélectrons induits par rayons X (XPS) et la spectrométrie de masse d'ions secondaires à temps de vol (ToF-SIMS). L'XPS peut également être utilisé pour l'analyse semi-quantitative telle que l'évaluation de l'épaisseur du film de surface et le pourcentage atomique (rapport) d'espèces chimiques. Le ToF-SIMS est une technique d'analyse beaucoup plus sensible à la

surface que l'XPS et tous les éléments, y compris l'hydrogène, peuvent être détectés. La limite de détection du ToF-SIMS est de l'ordre du ppm pour une monocouche pour les éléments et sous-femtomole pour les molécules. Par ailleurs, la zone d'analyse peut varier de quelques μm à une centaine de μm, et la profondeur d'analyse est inférieure à 10 Å.

Les caractérisations morphologiques permettent de mieux comprendre la relation entre le comportement à la corrosion et les performances du Mg en tant qu'anode dans les batteries Mg-air. Les caractérisations ont été réalisées après des tests d'immersion dans différents électrolytes et après des tests de décharge. Les principales techniques d'analyse de la morphologie de surface sont introduites, notamment la microscopie électronique à balayage (MEB), le microscope optique (MO) et la microscopie à balayage laser tridimensionnelle (3D-LSM). Pour l'analyse approfondie des produits de corrosion de l'anode de Mg dans différents électrolytes, l'analyse par microscopie électronique à transmission (MET) a été appliquée. Les conditions expérimentales sont détaillées dans ce chapitre.

Chapitre III : **Electrolyte hybride organique/inorganique pour améliorer les performances des batteries Mg-air**

Dans ce chapitre, l'effet de différentes fractions d'éthanol dans l'eau avec 0,6 M de NaCl sur les performances de décharge des batteries Mg-air complètes et les comportements de corrosion de l'électrode Mg a été étudié en détails. Le déroulement de l'étude expérimentale est illustré à la Fig. Annexe 2.

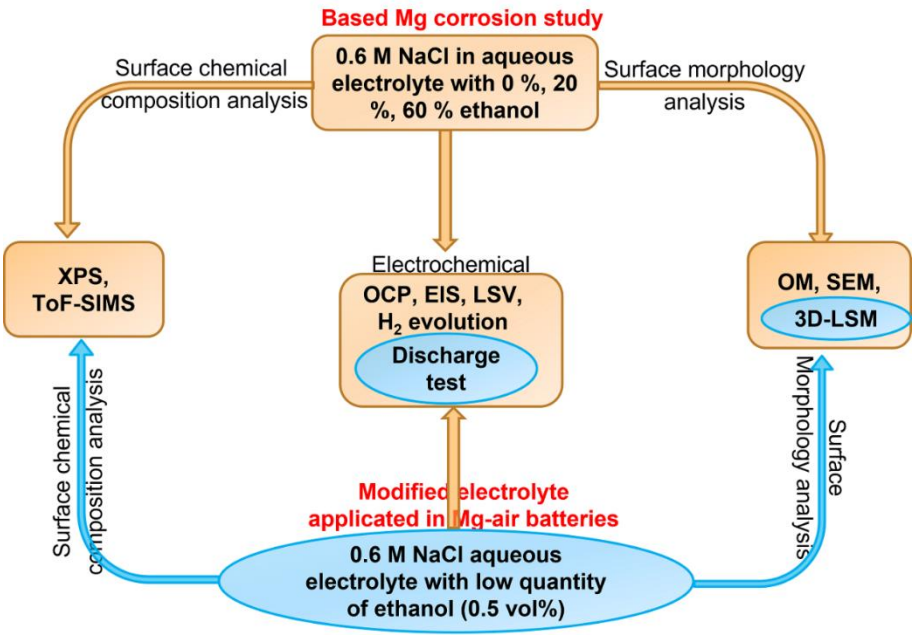

Fig. Annexe 2. Schéma d'étude expérimentale des tests de corrosion et de décharge du Mg dans du NaCl 0,6 M pour différentes concentrations en éthanol.

La première partie du chapitre est focalisée sur l'étude du comportement à la corrosion de l'électrode Mg en fonction de l'électrolyte organique/inorganique (forte teneur en éthanol de plus de 20% en volume) :

Tests électrochimiques : Les résultats de l'OCP montrent que le E_{ocp} final se déplace vers des valeurs négatives avec une augmentation de la concentration en éthanol (environ –15 mV pour 20 vol% et –26 mV pour 60 vol% éthanol). Dans le test SIE, R_{ct} augmente beaucoup avec l'ajout d'éthanol (2 fois pour 20 vol% d'éthanol) indiquant une réactivité décroissante à l'interface électrolyte/substrat métallique. R_f augmente de 183 Ω cm^2 de le cas de l'électrolyte sans éthanol à 393 Ω cm^2 pour 20 vol% et 7917 pour 60 vol% d'éthanol, ce qui indique que l'inhibition de la corrosion du Mg est nettement améliorée dans les électrolytes contenant de l'éthanol. Les courbes de polarisation potentiodynamique, illustrent le fait que l'augmentation de la concentration en éthanol diminue les densités de courant cathodique et anodique, indiquant respectivement un dégagement d'hydrogène plus faible et une dissolution réduite du Mg. L'ajout d'éthanol résulte en potentiel de corrosion plus positif (E_{corr}), une diminution du courant

de corrosion (I_{corr}) et une augmentation de la résistance de polarisation (R_p).

Morphologie de surface : Les résultats des images de microscopie optique ont montrés plusieurs grandes taches sombres qui couvrent presque toute la surface des échantillons de Mg dans l'électrolyte sans éthanol, mais, la taille et la densité des taches diminuent avec l'augmentation de la teneur en éthanol dans l'électrolyte. Les images MEB ont montrées des fissures apparaissant sur la couche de corrosion correspondant aux taches de corrosion sombres sur la surface de Mg exposée à l'électrolyte sans éthanol. La taille des taches de corrosion noires est nettement réduite dans l'électrolyte contenant de l'éthanol, indiquant une inhibition significative de la corrosion du Mg.

Analyses de surface : À partir des profils en profondeur d'ions négatifs ToF-SIMS (sur la Fig. Annexe 3), on peut conclure que l'épaisseur totale de la couche d'oxyde-hydroxyde et la quantité de produits de corrosion insolubles diminuent avec l'augmentation de la concentration en éthanol [29-31], ce qui peut être essentiel pour les performances de décharge de la batterie. De plus, avec l'augmentation de la teneur en éthanol, l'intensité du signal $MgCl^-$ est légèrement réduite, ce qui est cohérent avec la diminution de la corrosion. Les spectres XPS de niveau de cœur du Mg 2p montrent un déplacement progressif des pics vers les énergies de liaison plus faibles, qui diminuent avec l'augmentation de la concentration en éthanol, indiquant une diminution de l'épaisseur de la couche de surface. La légère diminution du rapport OH/Mg avec l'augmentation de la fraction d'éthanol est cohérente avec l'appauvrissement en hydroxyde sur la surface du Mg [32]. Une très faible quantité de $MgCO_3$ a été détectée sur la surface de Mg après immersion dans un électrolyte aqueux, bien qu'une augmentation significative de 3 à 26 at% ait été observée avec l'augmentation de la concentration en éthanol.

Dans la deuxième partie de ce chapitre, l'influence de l'électrolyte organique/inorganique sur le comportement de décharge d'une batterie Mg-air complète (pour une faible teneur en éthanol de moins de 5% en volume) a été etudié.

Performances de décharge : Dans les électrolytes avec 0,5-5 vol % d'éthanol, des tensions supérieures (~1,7 V) et stables avec le temps de décharge ont été observées pendant des durées

beaucoup plus longues (~15 heures) que dans les électrolytes sans éthanol. Parmi eux, la tension la plus élevée d'environ 1,76 V a été remarquée pour 0,5 vol% d'éthanol, cependant les tensions de décharge diminuent avec l'augmentation des densités de courant, mais elles restent toujours plus élevées que dans l'électrolyte sans éthanol. Une bonne stabilité de la tension de décharge a également été observée pendant le test de décharge de batterie plus long à une densité de courant élevée de 5 mA/cm^2.

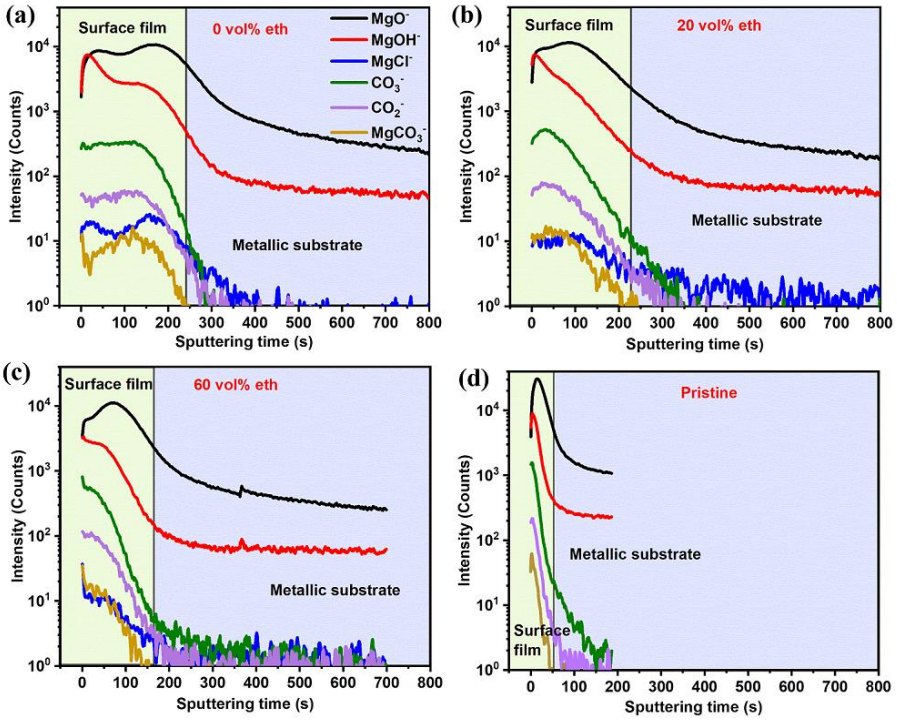

Fig. Annexe 3. Profils en profondeur d'ions négatifs ToF-SIMS obtenus pour Mg après immersion dans du NaCl 0,6 M à OCP pendant 10 min, (a) sans éthanol, (b) avec 20 vol %, (c) 60 vol % d'éthanol et (d) Mg intacte après polissage.

Dégagement de H_2 : Un dégagement d'hydrogène beaucoup plus lent (7,7 ml de H_2 pendant 500 min) a été observé dans l'électrolyte avec une faible fraction d'éthanol (0,5 vol%) que dans l'électrolyte sans éthanol (38,5 ml) montrant une diminution de la corrosion.

Morphologie de surface : Les analyses MEB et au microscope laser 3D montrent que la surface de l'anode Mg est moins abîmée et beaucoup plus plate, lorsque l'éthanol est ajouté, ce qui peut expliquer le temps de décharge plus long. De plus, la surface couverte par les produits de corrosion noire est beaucoup plus faible dans un électrolyte avec l'éthanol.

Ce chapitre montre que l'inhibition significative de la corrosion pour une teneur élevée en éthanol ($\geqslant$ 20 vol%) a été observée. En faisant varier la fraction éthanol-eau dans l'électrolyte d'une batterie complète, il a été démontré que même une faible teneur en éthanol ($\leq$ 5 vol%), peut significativement améliorer les performances électrochimiques de l'anode Mg. Entre plusieurs teneurs en éthanol, la valeur de 0,5 vol% montre les meilleures performances avec un taux de corrosion limité et montre une amélioration considérable des performances de décharge et de la durée de vie de la batterie.

Chapitre IV : Influence du 5-sulfosalicylate de sodium comme inhibiteur de corrosion dans l'électrolyte NaCl sur l'amélioration des performances des batteries Mg-air

Ce chapitre vise à utiliser l'inhibiteur de corrosion 5-sulfosalicylate de sodium (5-S-Sal) dans l'électrolyte aqueux de NaCl. Le déroulement de l'étude expérimentale est illustré dans la Fig. Annexe 4.

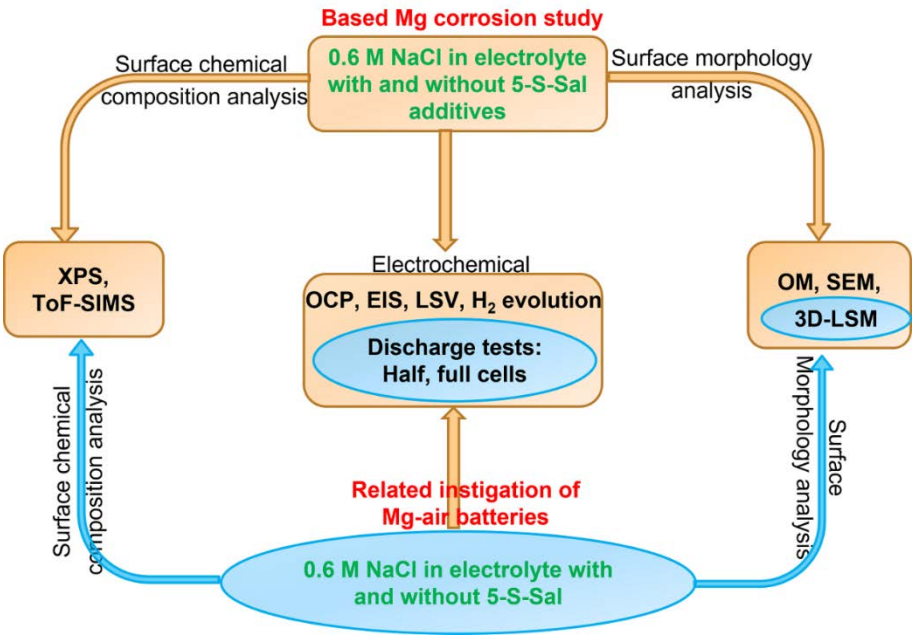

Fig. Annexe 4. Schéma d'étude expérimentale des tests de corrosion du Mg et des tests de décharge dans du NaCl 0,6 M avec et sans inhibiteur 5-S-Sal.

Tests électrochimiques : Avec 0,1 M d'inhibiteur de 5-S-Sal dans l'électrolyte, un OCP stable a été atteint à –1,68 V, soit 120 mV de moins que dans l'électrolyte NaCl sans inhibiteur. Une augmentation linéaire et non exponentielle du dégagement d'hydrogène a été observée lors de l'immersion dans l'électrolyte contenant l'inhibiteur. Un volume presque quatre fois plus élevé de H_2 a été mesuré dans un électrolyte sans inhibiteur que dans l'électrolyte avec inhibiteur. Les courbes LSV ont montré que la surface de l'anode Mg est moins active et mieux protégée en présence d'inhibiteur 5-S-Sal sur différents temps d'immersion. Les mesures SIE effectuées en fonction du temps d'immersion dans l'électrolyte sans et avec inhibiteur ont respectivement montré une diminution et une augmentation de la résistance de transfert de charge (R_{ct}). Cela indique que les propriétés de corrosion de la couche de surface sont améliorées lorsque l'inhibiteur est utilisé.

Morphologie de surface (après tests OCP) : Dans l'électrolyte avec NaCl sans inhibiteur, la formation progressive des zones sombres et opaques conduisant à la couverture complète de la surface a été observée. Cependant, en présence d'inhibiteur de 5-S-Sal, aucune de ces taches de corrosion sombres n'a été observée. Une surface plus homogène avec une porosité plus faible

et une structure en forme « de flocon » moins développée a été observée sur la surface exposée dans l'électrolyte contenant l'inhibiteur 5-S-Sal.

Performances de décharge : À 0,5 mA/cm^2, le potentiel de décharge le plus négatif pour une demi-pile de Mg-air a été détecté dans 0,05 M 5-S-Sal. À 2,5 mA/cm^2, le même potentiel de décharge stable de –1,63 V a été observé pour toutes les concentrations d'inhibiteur, ce qui était plus négatif que dans l'électrolyte NaCl blanc (–1,55 V). Cependant, à des densités de courant plus élevées de 5 mA/cm ^{2}, un potentiel de décharge instable a été observé dans l'électrolyte avec la plus faible concentration d'inhibiteur (0,05 M), indiquant qu'il existe des limites d'utilisation de cet inhibiteur à des densités de courant plus élevées. De plus, en présence de 0,05, 0,15 et 0,1 M 5-S-Sal, les temps de décharge des batteries Mg-air complètes peuvent être prolongés jusqu'à 30, 42 et 80 heures, respectivement (Fig. Annexe 5 a). Cela indique que les inhibiteurs peuvent augmenter considérablement le temps de service de l'anode de Mg. De plus, à des densités de courant plus élevées telles que 5 mA/cm^2 (Fig. Annexe 5 b), la durée de vie du Mg peut être considérablement prolongée (jusqu'à 28 heures contre 12 heures). En présence d'inhibiteur, les potentiels de décharge sont également plus élevés comme le montre la Fig. Annexe 5 c.

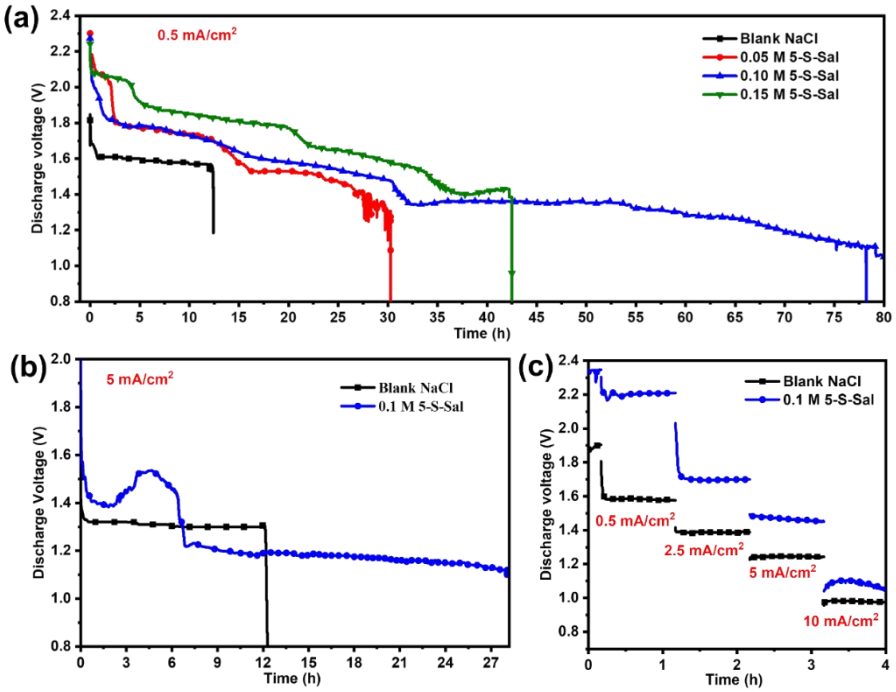

Fig. Annexe 5. Courbes de décharge de batteries Mg-air complètes obtenues (a) dans du NaCl 0,6 M sans et avec différentes concentrations d'inhibiteur 5-S-Sal à une densité de courant de 0,5 mA/cm^2 pour un test de longue durée, (b) NaCl sans et avec 0,1 M d'inhibiteur 5-S-Sal à une densité de courant de 5 mA/cm^2 (c) NaCl sans et avec 0,1 M d'inhibiteur 5-S-Sal à différentes densités de courant.

Analyses de surface : Les profils en profondeur d'ions négatifs ToF-SIMS montrent que l'intensité du signal MgO^- pour les échantillons Mg exposés à l'électrolyte avec inhibiteur est plus élevée que pour l'électrolyte sans inhibiteur, contrairement aux intensités du signal $MgOH^-$. Cela indique que l'inhibiteur favorise la formation de MgO par rapport à $Mg(OH)_2$. Avec l'inhibiteur 5-S-Sal, le signal $MgCl^-$ est significativement plus faible, voire quasi absent, confirmant l'efficacité de l'inhibition de la corrosion du Mg. Comme pour les résultats du chapitre précédent, les spectres Mg 2p ont montré des changements vers des énergies de liaison plus élevées pour les échantillons exposés à l'électrolyte sans inhibiteur que pour les échantillons exposés à l'électrolyte avec inhibiteur. De plus, une quantité inférieure de $Mg(OH)_2$ (réduite presque de moitié) et une augmentation de la formation de $MgCO_3$ dans l'électrolyte contenant du 5-S-Sal ont également été observées par XPS [21, 33].

Morphologie de surface (après tests de décharge) : Les images de coupe transversale MEB de Mg après 5 heures de tests de décharge ont montré que l'électrode de Mg est presque complètement consommée dans l'électrolyte NaCl sans inhibiteur. Cependant, seule une légère dissolution de l'échantillon de Mg dans l'électrolyte avec l'inhibiteur 5-S-Sal est observée, avec un faible enrichissement en produits de corrosion à la surface. Conformément aux images au microscope laser 3D, une topographie de surface beaucoup plus plane (rugosité inférieure) est observée pour l'anode Mg en présence d'inhibiteur.

On peut conclure que les tests de corrosion aux potentiels de circuit ouvert ont montré une diminution significative du dégagement d'hydrogène lorsque l'inhibiteur 5-S-Sal a été ajouté à l'électrolyte NaCl. Les caractérisations de surface par XPS et ToF-SIMS ont également mis en évidence une plus faible quantité de $Mg(OH)_2$ en présence d'inhibiteur 5-S-Sal que dans l'électrolyte NaCl pur sans inhibiteur. Dans une gamme de concentrations de 5-S-Sal dans

l'électrolyte NaCl (0,05 M à 0,15 M), les meilleures performances de décharge ont été obtenues avec concentration de 0,1 M d'inhibiteur. La tension de décharge de la batterie Mg-air complète est passée de ~1,58 V à ~1,82 V à une densité de courant de 0,5 mA/cm^2, et la durée de vie de la décharge a été prolongée d'environ 12,5 heures à environ 80 heures.

Chapitre V : Traces d'acide acétique dans l'électrolyte aqueux $NaNO_3$ pour les batteries Mg-air à longue durée de vie

Dans ce chapitre, le soluté de NaCl conventionnel a été remplacé par du $NaNO_3$ et des traces d'acide acétique comme inhibiteurs ont été utilisées.

Corrosion du Mg en fonction des formulations d'électrolyte :

Les résultats de SEI indiquent que le $NaNO_3$ en tant que soluté dans l'électrolyte aqueux peut réduire considérablement la réactivité à la corrosion de l'anode de Mg et que l'électrolyte contenant de l'acide acétique entraîne une diminution de la résistance de transfert de charge. Les images au microscope optique ont montré des modifications mineures du métal Mg testé dans l'électrolyte $NaNO_3$-H_2O/AC, indiquant que l'acide acétique peut limiter la formation de film de surface dense/compact comme ceux formés dans $NaNO_3$. Le LSV a montré une diminution des densités de courant cathodique et anodique dans l'électrolyte $NaNO_3$. Cependant, l'électrolyte $NaNO_3$ peut entraîner le colmatage de surface Mg et par conséquent diminuer l'activité de l'anode Mg dans la configuration complète de la batterie Mg-air. L'image du MEB en coupe transversale (en mode BSE) a montré plusieurs centaines de microns de défauts allongés (longue bande de corrosion) à l'intérieur du substrat Mg dans l'électrolyte NaCl, et la présence de Cl dans ces cavités. Un film très mince de produit de corrosion a été observé sur l'anode de Mg immergée dans l'électrolyte de $NaNO_3$, et une couche un peu plus épaisse mais relativement homogène sur l'anode de Mg immergée dans du $NaNO_3$ avec l'acide acétique.

Effet de l'électrolyte sur les propriétés des cellules complètes :

Une quantité significativement plus faible de H_2 a été détectée dans l'électrolyte de $NaNO_3$-H_2O que dans l'électrolyte de NaCl. Aucune diminution significative n'a été observée après addition de l'acide acétique. Cependant, dans cet électrolyte, l'augmentation du potentiel de décharge a été observée à environ 1,8 V pour le test initial de 5 heures dans l'électrolyte de $NaNO_3$-H_2O/AC (500 mV de plus que dans l'électrolyte $NaNO_3$-H_2O). Malheureusement, le potentiel de décharge était instable et chute à 1,59 V après 10 heures, ce qui peut être attribué à une consommation progressive de l'acide acétique dans l'électrolyte.

Tests de décharge en fonction des inhibiteurs :

Les performances de décharge des demi-cellules en fonction de la densité de courant ont prouvé que l'ajout d'acide acétique est bénéfique pour les tensions de décharge (les valeurs moyennes étaient plus négatives d'environ 90, 60, 40 et 30 mV à des densités de courant de 0,5, 5, 10 et 20 mA/cm^2 que sans acide acétique, respectivement). Les tests dans des cellules complètes Mg-air effectuées à 0,5 mA/cm^2 ont montré que la batterie peut fonctionner environ 360 heures en présence d'acide acétique à 0,5 vol%, ce qui est une énorme amélioration par rapport au NaCl-H_2O électrolyte qui montre seulement ~17 heures de décharge. Pour cette concentration d'acide acétique, la tension de décharge est passée d'environ 1,13 V à environ 1,35 V à des densités de courant plus élevées (2,5 mA/cm^2). L'analyse de la morphologie de surface par FIB-MEB et l'analyse chimique par ToF -SIMS et XPS ont montré que les traces de molécule d'inhibiteur d'acide acétique influencent de manière significative la morphologie de surface et l'épaisseur de la couche de surface. Les composés de la couche principale tels que MgO, $Mg(OH)_2$, $MgCO_3$ et leur distribution dans la partie interne du film de surface d'oxyde ne sont pas significativement modifiés. Cependant, avec l'ajout d'acide acétique, les nitrates/nitrites peuvent se décomposer et s'adsorber avec l'acide carboxylique, entraînant la formation d'une couche plus robuste et résistante à la corrosion mais suffisamment perméable pour la diffusion des ions, ce qui permet d'améliorer les performances électrochimiques de l'anode de Mg. La morphologie typique en forme de « flocons » de $Mg(OH)_2$ a été observée par MET après exposition à l'électrolyte $NaNO_3$-H_2O. La morphologie lamellaire a été observée à la surface de Mg avec l'ajout d'acide acétique.

En conclusion de ce chapitre, un électrolyte optimisé a montré une tension de décharge améliorée atteignant ~ 1,8 V à une densité de courant de 0,5 mA/cm^2 et une durée de vie de la batterie nettement plus longue (360 heures contre seulement environ 17 heures dans l'électrolyte NaCl). L'XPS et le ToF-SIMS ont été utilisés pour analyser la composition du film de surface et le MEB combiné avec le MET pour clarifier les changements de morphologie de la couche de surface avec ajout d'acide acétique.

Conclusions générales et perspectives

Ces résultats indiquent que la corrosion de l'électrode Mg peut être inhibée et que les performances de décharge des batteries primaires Mg-air peuvent être considérablement améliorées par les modifications de l'électrolyte et de l'interface électrolyte/électrode. La connaissance approfondie de la corrosion des métaux et de leur chimie de surface, des modifications de surface induites par les processus électrochimiques et des interfaces métal/électrolyte sont primordiales dans le développement des batteries Mg-air. Afin de mieux ajuster les propriétés de surface et d'interface électrolyte/électrode, plusieurs études futures doivent être entreprises :

1) Concernant les modifications des solvants, d'autres solvants efficaces ou leurs mélanges peuvent être développés. Il sera intéressant de rechercher un solvant mixte approprié, qui puisse simultanément diminuer la corrosion du Mg et améliorer la tension de décharge des batteries complètes Mg-air. En outre, les électrolytes aqueux et liquides ioniques seront l'un des candidats intéressants. Certains types de liquides ioniques peuvent avoir une conductivité ionique raisonnable et ils sont connus pour avoir une très bonne stabilité électrochimique, thermique et chimique.

2) Un grand nombre d'inhibiteurs de corrosion de Mg ont été étudiés jusqu'à présent pour leur utilisation dans la protection contre la corrosion du Mg et de ses alliages. On peut citer, par exemple, le salicylaldéhide, le 3-méthylsalicylate de sodium, le 2,5-pyridine dicarboxylate de sodium, la 8-hydroxyqeinoline, mais très peu d'entre eux ont été utilisés comme inhibiteurs pour les batteries Mg-air. La suite des travaux pourra

porter sur des inhibiteurs plus adaptés aux batteries Mg. Sur la base des résultats actuels, on peut conclure qu'il est très difficile de diminuer la corrosion du Mg et d'augmenter la tension de décharge en même temps. Ainsi, il est important de développer les inhibiteurs mixtes pour les batteries Mg-air.

3) L'influence d'autres sels, tels que KNO_3, Na_2SO_4, Na_3PO_4 dans les solvants aqueux sera intéressante à étudier. Le NaCl habituellement utilisé peut sérieusement endommager le Mg métallique, mais de nouveaux types de sels bi- ou trinaires peuvent être développés dans les électrolytes aqueux.

4) Pour dépasser cette limitation, le développement d'alliages de Mg tels que AZ31, AZ91, A/Ca, Mg/Li est envisageable. Par exemple, l'Al allié avec le Mg forme une phase secondaire, qui peut réduire la cinétique de réaction anodique et augmenter la résistance à la corrosion. Le Mg allié au Li bénéficie de sa structure plus légère, d'un OCP extrêmement négatif et de bonnes capacités faradiques. Les alliages à base de Ca utilisés comme matériaux d'anode dans les batteries à base de Mg-air présentent des densités d'énergie supérieures.

5) Pour toutes ces raisons, le développement d'expérimentation à haut débit (EHD) est nécessaire afin de pouvoir effectuer un criblage rapide de différents composés de batterie et augmenter les performances de batteries Mg-air.

Appendix-Références :

[1] X. Liu, S. Liu, J. Xue, Discharge performance of the magnesium anodes with different phase constitutions for Mg-air batteries, J Power Sources 396 (2018) 667-674.
[2] X. Liu, J. Xue, The role of Al2Gd cuboids in the discharge performance and electrochemical behaviors of AZ31-Gd anode for Mg-air batteries, Energy 189 (2019) 116314.
[3] Y. Li, X. Zhang, H.-B. Li, H.D. Yoo, X. Chi, Q. An, J. Liu, M. Yu, W. Wang, Y. Yao, Mixed-phase mullite electrocatalyst for pH-neutral oxygen reduction in magnesium-air batteries, Nano Energy 27 (2016) 8-16.
[4] C. Byung-wo, http://www.electric-vehiclenews.com/2013/01/kist-develop-magnesium-air-battery-with.html, [Cited January, 2013] (2013).
[5] MAGPOWER, http://www.magpowersystems.com/.
[6] M.M.A. Battery, 2019, https://www.ecomarinepower.com/en/mgbox-air-battery ([cited 2020 September]).
[7] T. Zhang, Z. Tao, J. Chen, Magnesium–air batteries: from principle to application, Mater. Horiz. 1(2) (2014) 196-206.
[8] W. Li, C. Li, C. Zhou, H. Ma, J. Chen, Metallic magnesium nano/mesoscale structures: their shape-controlled preparation and mg/air battery applications, Angewandte Chemie 45(36) (2006) 6009-12.
[9] Y.S. Chun-Sheng Li, Florian Gebert, and Shu-Lei Chou, Current Progress on Rechargeable Magnesium–Air Battery, Adv. Energy Mater 7 (2017) 1700869.
[10] L. Zhang, Q. Shao, J. Zhang, An overview of non-noble metal electrocatalysts and their associated air cathodes for Mg-air batteries, Materials Reports: Energy 1(1) (2021) 100002.
[11] F. Cheng, J. Chen, Metal-air batteries: from oxygen reduction electrochemistry to cathode catalysts, Chem Soc Rev 41(6) (2012) 2172-92.
[12] M. Esmaily, J.E. Svensson, S. Fajardo, N. Birbilis, G.S. Frankel, S. Virtanen, R. Arrabal, S. Thomas, L.G. Johansson, Fundamentals and advances in magnesium alloy corrosion, Progress in Materials Science 89 (2017) 92-193.
[13] G. Song, Recent Progress in Corrosion and Protection of Magnesium Alloys, Advanced Energy Materials 7 (2005) 563-586.
[14] J. Li, B. Zhang, Q. Wei, N. Wang, B. Hou, Electrochemical behavior of Mg-Al-Zn-In alloy as anode materials in 3.5 wt.% NaCl solution, Electrochimica Acta 238 (2017) 156-167.
[15] M. Curioni, The behaviour of magnesium during free corrosion and potentiodynamic polarization investigated by real-time hydrogen measurement and optical imaging, Electrochimica Acta 120 (2014) 284-292.
[16] K.A. Yasakau, A. Maltseva, S.V. Lamaka, D. Mei, H. Orvi, P. Volovitch, M.G.S. Ferreira, M.L. Zheludkevich, The effect of carboxylate compounds on Volta potential and corrosion inhibition of Mg containing different levels of iron, Corros Sci 194 (2022) 109937.
[17] X. Chen, S. Ning, Q. Le, H. Wang, Q. Zou, R. Guo, J. Hou, Y. Jia, A. Atrens, F. Yu, Effects of external field treatment on the electrochemical behaviors and discharge performance of AZ80 anodes for Mg-air batteries, Journal of Materials Science & Technology 38 (2020) 47-55.
[18] M. Deng, L. Wang, D. Höche, S.V. Lamaka, D. Snihirova, B. Vaghefinazari, M.L. Zheludkevich, Clarifying the decisive factors for utilization efficiency of Mg anodes for primary aqueous batteries, J Power Sources 441 (2019) 227201.
[19] G. Song, A. Atrens, M. Dargusch, Influence of microstructure on the corrosion of diecast AZ91D, Corros Sci 41(2) (1998) 249-273.
[20] G.S.a.A. Atrens, Understanding Magnesium Corrosion—A Framework for Improved Alloy Performance, Adv. Eng. Mater. 5 (2003) 837-858.
[21] N. Wang, R. Wang, C. Peng, Y. Feng, B. Chen, Effect of hot rolling and subsequent annealing on

electrochemical discharge behavior of AP65 magnesium alloy as anode for seawater activated battery, Corros Sci 64 (2012) 17-27.
[22] B. Vaghefinazari, D. Höche, S.V. Lamaka, D. Snihirova, M.L. Zheludkevich, Tailoring the Mg-air primary battery performance using strong complexing agents as electrolyte additives, J Power Sources 453 (2020) 227880.
[23] L. Wang, D. Snihirova, M. Deng, B. Vaghefinazari, S.V. Lamaka, D. Höche, M.L. Zheludkevich, Tailoring electrolyte additives for controlled Mg-Ca anode activity in aqueous Mg-air batteries, J Power Sources 460 (2020) 228106.
[24] P.H. J. Ma, X. Jia, C. Zhanga, G. Wang, Organic/inorganic double solutions for magnesium - air batteries, RSC Advances 11 (2021) 7502-7510.
[25] J. Ma, X. Jia, M. Ma, C. Zhang, F. Ren, G. Wang, Mg(ClO4)2-N,N-Dimethylformamide (Acetonitrile)/NaCl Double Electrolytes for Magnesium–Air Batteries, Journal of Materials Engineering and Performance 30(2) (2021) 1567-1576.
[26] S. Clark, A.R. Mainar, E. Iruin, L.C. Colmenares, J.A. Blázquez, J.R. Tolchard, Z. Jusys, B. Horstmann, Designing Aqueous Organic Electrolytes for Zinc–Air Batteries: Method, Simulation, and Validation, Advanced Energy Materials 10(10) (2020) 1903470.
[27] S. Hosseini, S. Masoudi Soltani, Y.-Y. Li, Current status and technical challenges of electrolytes in zinc–air batteries: An in-depth review, Chemical Engineering Journal 408 (2021) 127241.
[28] T.M. Di Palma, F. Migliardini, D. Caputo, P. Corbo, Xanthan and kappa-carrageenan based alkaline hydrogels as electrolytes for Al/air batteries, Carbohydrate polymers 157 (2017) 122-127.
[29] C. Xia, R. Black, R. Fernandes, B. Adams, L.F. Nazar, The critical role of phase-transfer catalysis in aprotic sodium oxygen batteries, Nature chemistry 7(6) (2015) 496-501.
[30] Y.G. Zhu, Q. Liu, Y. Rong, H. Chen, J. Yang, C. Jia, L.J. Yu, A. Karton, Y. Ren, X. Xu, S. Adams, Q. Wang, Proton enhanced dynamic battery chemistry for aprotic lithium-oxygen batteries, Nature communications 8 (2017) 14308.
[31] K. Duan, J. Ning, L. Zhou, S. Wang, Q. Wang, J. Liu, Z. Guo, Synergistic Inorganic-Organic Dual-Additive Electrolytes Enable Practical High-Voltage Lithium-Ion Batteries, ACS applied materials & interfaces 14(8) (2022) 10447-10456.
[32] M. Santamaria, F. Di Quarto, S. Zanna, P. Marcus, The influence of surface treatment on the anodizing of magnesium in alkaline solution, Electrochimica Acta 56(28) (2011) 10533-10542.
[33] D. Xue, Y. Yun, M.J. Schulz, V. Shanov, Corrosion protection of biodegradable magnesium implants using anodization, Materials Science and Engineering: C 31(2) (2011) 215-223.

RÉSUMÉ

Le monde a été témoin de la demande croissante de sources d'énergie à combustibles non fossiles de grande capacité, de puissance élevée, à faible coût et de sécurité fiable. Parmi les différents nouveaux systèmes de stockage d'énergie, les batteries Mg-air ont attiré une attention particulière en raison de leur capacité spécifique théorique élevée (2,2 Ah/g), de leur densité d'énergie spécifique élevée (6,8 kWh/kg), d'une capacité volumétrique élevée de Mg (3833 mAh /cm^3), et tension théorique élevée (3,09 V). Cependant, dans les électrolytes aqueux, Mg subit une auto-corrosion et une grande quantité de H_2 est générée. Le faible rendement coulombique et les faibles tensions de fonctionnement sont les principaux inconvénients des batteries Mg-air. Pour surmonter ces problèmes, cette thèse se concentre principalement sur la modification de l'électrolyte pour améliorer les performances de décharge des batteries Mg-air. Premièrement, les travaux visaient à appliquer un électrolyte hybride organique/inorganique à l'anode de magnésium pur dans la batterie Mg-air pour réduire sa corrosion et améliorer les performances de décharge associées. Deuxièmement, nous avons utilisé l'inhibiteur de corrosion 5-sulfosalicylate de sodium (5-S-Sal) dans l'électrolyte aqueux de NaCl pour améliorer les performances de décharge de la batterie Mg-air et diminuer les réactions secondaires de l'anode Mg. Enfin, le soluté de NaCl conventionnel a été remplacé par du $NaNO_3$, puis une trace d'acide acétique comme inhibiteur a été utilisée dans la batterie à électrolyte aqueux Mg-air. Dans cette thèse, les analyses de profils de surface et de profondeur (au moyen de XPS et ToF-SIMS) combinées à la caractérisation morphologique à l'aide de techniques microscopiques (SEM, OM et 3D-SLM) ont été utilisées pour étudier la réactivité de l'anode Mg. Les techniques électrochimiques (OCP, LSV, EIS et tests de décharge galvanostatique) ont été utilisées pour étudier le comportement à la corrosion de l'anode Mg et les performances de décharge d'une batterie Mg-air complète en fonction de l'électrolyte et/ou de l'additif électrolytique. Ces techniques d'analyse ont permis d'améliorer significativement les performances des batteries Mg-air en mettant au point de nouveaux électrolytes et leurs additifs et en caractérisant en profondeur l'interface électrode/électrolyte.

MOTS CLÉS

processus interfaciaux ; batterie magnésium-air; auto-corrosion ; propriétés de décharge ; électrolytes ; couche de surface, caractérisation de surface

ABSTRACT

The world has witnessed the increasing demand for non-fossil fuel power sources with large capacity, high power, low cost and reliable safety. Among different new energy storage systems, Mg-air batteries attracted significant attention due to their high theoretical specific capacity (2.2 Ah/g), high specific energy density (6.8 kWh/kg), a high volumetric capacity of Mg (3833 mAh/cm^3), and high theoretical voltage (3.09 V). However, in aqueous electrolytes, Mg undergoes self-corrosion and a large amount of H_2 is generated. Low coulombic efficiency and low operating voltages are the major drawbacks of Mg-air batteries. To overcome these problems, this thesis mainly focusses on the electrolyte modification for improving the discharge performance of Mg-air batteries. Firstly, the part of this work aimed at applying an organic/inorganic hybrid electrolyte to pure magnesium anode in Mg-air battery to reduce its corrosion and improve related discharge performance. Secondly, we employed sodium 5-sulfosalicylate (5-S-Sal) corrosion inhibitor into aqueous NaCl electrolyte to improve the discharge performance of Mg-air battery and decrease the side reactions of Mg anode. Lastly, the conventional NaCl solute was replaced by $NaNO_3$, then a trace of acetic acid as inhibitor was employed into the aqueous electrolyte Mg-air battery. In this thesis, the surface and depth profiles analyses (by means of XPS and ToF-SIMS) combined with the morphological characterization using microscopic techniques (SEM, OM and 3D-SLM) were used to study the reactivity of Mg anode. The electrochemical techniques (OCP, LSV, EIS and galvanostatic discharge tests) were employed to investigate the corrosion behavior of Mg anode and discharge performance of full Mg-air battery as a function of electrolyte and/or electrolyte additive. These analysis techniques performed that the performances of Mg-air batteries has been significantly improved by enginering new electrolytes and their additives and in-depth characterization of the electrode/electrolyte interface.

KEYWORDS

interfacial processes; magnesium-air battery; self-corrosion; discharge properties; electrolytes; surface layer, surface characterization